ANALYSIS AND COMPUTATION OF THE CROSS-FLOW PAST AN OSCILLATING CYLINDER WITH TWO DEGREES OF FREEDOM

QASEM M. AL-MDALLAL

ANALYSIS AND COMPUTATION OF THE CROSS-FLOW PAST AN OSCILLATING CYLINDER WITH TWO DEGREES OF FREEDOM

By

Qasem M. Al-Mdallal

SUBMITTED IN PARTIAL FULFILLMENT OF THE
REQUIREMENTS FOR THE DEGREE OF
DOCTOR OF PHILOSOPHY
AT
MEMORIAL UNIVERSITY OF NEWFOUNDLAND
ST. JOHN'S, NEWFOUNDLAND
OCTOBER 2004

Table of Contents

List of Tables

List of Figures

Abstract

The present thesis deals with analysis and numerical simulation of a new class of wake flows created by combined recti-linear (translational) and rotational oscillation of a cylinder placed in a steady uniform flow. The flow is incompressible and two-dimensional, and recti-linear and rotational oscillations are harmonic. The instantaneous translation and rotation start at the same moment and the development of the flow is studied in a coordinate frame which moves with the cylinder but does not rotate. The analysis is carried out for combined phase-locked translation and rotation with a single frequency. The results are presented for five set of the four dimensionless groups which characterize this flow. The resulting vortex formation modes and synchronization (lock-on) phenomena behind the cylinder (in the near-wake region) as well as the fluid forces acting on the cylinder are analyzed. In addition, a series of one-degree-of-freedom (1-DoF) forced vibration calculations are carried out to better understand what differences result from the addition of rotational oscillations to streamwise (in-line) or cross-stream (transverse) motion and to see which effects a transverse-only or in-line-only simulations miss. The numerical scheme is verified by applying it to the special cases of uniform flow past a stationary cylinder; a steadily rotating cylinder; a cylinder undergoing (1-DoF) forced (recti-linear or rotational) oscillations. Exceptionally good comparisons with previous experimental and numerical results are obtained. Furthermore, the simulations of the start-up flow for the case of combined (2-DoF) forced recti-linear and rotational cylinder oscillations at a moderate Reynolds number are consistent with the results of the analytical solution.

Acknowledgements

I would like to express my gratitude to my supervisor, Dr. Serpil Kocabiyik, for her guidance and support throughout the course of this work. I thank her for all her efforts and concern for my academic progress at Memorial. Her expert advice, common-sense and perceptiveness played a major role in my successes at Memorial. Throughout the thesis-writing period, she provided encouragement, sound advice and great guidance.

Financial support for this work was provided by Natural Sciences and Engineering Research Council of Canada (NSERC) research grant received by Dr. Kocabiyik, and in the form of a graduate fellowship offered by Memorial University of Newfoundland.

I am grateful to the faculty, staff and colleagues of the Department of Mathematics and Statistics, especially for providing the computing facilities that this research heavily depend upon.

Special thanks go to Drs. M. Haddara, M. H. Ahmed and F. M. Mahfouz for their valuable time and discussions throughout this work.

I would also like to express my appreciation to Dr. Gary Sneddon for proof-reading parts of this thesis.

Lastly from the bottom of my heart I wish to thank my family, in particular my wife, for her patience, support and understanding throughout this work.

Chapter 1

Introduction

Flow around cylindrical body has been a research topic in fluid mechanics for decades because of its complex physical phenomena, such as separation and vortex shedding, and also its practical importance in many industrial fields. In practice, the problem arise from the interest in predicting loads on structures due to the fluid motion. The study of vortex shedding from an oscillating cylindrical body has fascinated researchers for a long time. The occurrence of this flow phenomena is due to instabilities and depends on the geometry of the body and the Reynolds number. It has been the cause of flow-induced failure of structures in various fields of engineering. The study of periodic vortex shedding and wake development behind a cylindrical body remains one of the most challenging problems in fluid mechanics, since it can lead to better understanding of the cause of flow-induced vibration and its subsequent suppression and control.

It is well known that at Reynolds numbers in excess of approximately 40 the wake of a cylindrical body in uniform flow consists of a Kármán vortex street, the vortices

being shed alternatively from either side of the body. As the vortices are shed, a periodic force is exerted on the body, whose component in the transverse direction (lift force) has the same frequency as the vortex-shedding cycle, while the component in the streamwise direction (drag force) has a frequency equal to twice the shedding frequency. Vortex shedding and the consequent fluctuating forces may cause flow-induced vibrations. In turn, a number of significant changes occur in both the wake structure and the dynamic of fluid forces acting on the cylinder when the cylinder oscillates. Thus, the flow-induced motion of a body in a free stream is important from the standpoint of fundamental research and in the design and maintenance of engineering structures.

A common approach to studying fluid-structure interactions is to force the body to oscillate with a predefined motion that approximates the flow-induced motion. The wake of the oscillating body and the flow-induced motion are intrinsically interdependent; thus the relationship between these two factors is complicated and difficult to determine. Many investigations have been made of the near-wake flow structure subject to controlled one-degree of freedom (1-DoF) forcings. In general, relatively simple forcing methods on the cylinder have been employed e.g. in-line (streamwise) oscillation [Griffin and Ramberg (1976), Ongoren and Rockwell (1988b), Badr, Dennis, Kocabiyik and Nguyen (1995b), Iliadis and Anagnostopoulos (1998), Mittal and Kumar (1999), Cetiner and Rockwell (2001), Guilmineau and Queutey (2002)]; transverse (cross-stream) oscillation [Bishop and Hassan (1964), Koopman (1967), Stansby (1976), Williamson and Roshko (1988), Ongoren and Rockwell (1988a), Lu

and Dalton (1996), Blackburn and Henderson (1999), Carberry, Sheridan and Rockwell (2001)]; oblique translational oscillation at angles $0^o < \eta < 90^o$ with respect to the free-stream [Ongoren and Rockwell (1988b), Kocabiyik and Al-Mdallal (2003a,b) and Kocabiyik, Mahfouz and Al-Mdallal (2004)]; and rotational oscillation about cylinder axis [Tokumaru and Dimotakis (1991); Beak and Sung (1998; 2000); Dennis, Nguyen and Kocabiyik (2000), Mahfouz and Badr (2000), Cheng, Chew and Luo (2001), Beak, Lee and Sung (2001)]. In the cases of in-line and transverse oscillations, the cylinder oscillates translationally at an angle of 0^0 or 90^0 with respect to the free stream, respectively.

Despite the large number of papers dedicated to the problem of a cylinder vibrating transverse to a fluid flow there is only one paper which also allows the body to perform rotational oscillations about its axis in a quiescent fluid (swimming motion): Blackburn, Elston and Sheridan (1999). In their work the incompressible Navier-Stokes equations were solved using a two-dimensional direct simulation technique. The numerical technique employs a spectral element spatial discretization in conjunction with a second-order time integration scheme based on operator splitting and backwards differencing. Their calculations were performed at the fixed values of the Keulegan-Carpenter (U_tT/d: period parameter) and Reynolds numbers for the transverse oscillation, $KC = \pi$ and $R = 200 \times 2^{1/2}$, respectively, where d is the cylinder diameter. Here U_t and T are the maximum transverse oscillatory velocity and the associated period of cylinder oscillation. The frequency of the rotational oscillation is the same as for the transverse oscillation, while the amplitude of the rotational motion is set so that the peak tangential speed on the surface of the cylinder is the same as

the peak transverse oscillatory speed. The transverse and rotational oscillations are out of phase and the phase angle between the two motions was set to π. In the work by Blackburn *et al.*, the generation of streaming flow normal to the axis of transverse oscillation was reported. We note that for moderately low KC values, a cylinder oscillating in a quiescent fluid results in a streaming flow along the translation axis, with reflectional symmetry about this line (Tatsuno and Bearman (1990)). At higher KC, a variety of two-dimensional symmetry breaking bifurcations are observed in resulting flow patterns (Tatsuno and Bearman (1990); Williamson (1985)).

Riley (1991) made a very careful numerical study to investigate the flow induced by a circular cylinder (placed in a quiescent fluid) performs, simultaneously and with a single frequency, transverse, torsional and axial vibrations. It was assumed that the three superposed oscillations are out of phase. For large values of a suitably defined Reynolds number, such a flow induces a steady streaming in the fluid that is confined in a thin boundary-layer at the cylinder surface. A collision of these steady-streaming boundary layers was investigated by Riley for small amplitude of transverse vibrations, resulting in jets of fluid erupting symmetrically from the cylinder surface along the axis of the vibration. The steady streaming associated with purely transverse vibrations of the cylinder is significantly modified by the presence of, and interaction with, torsional oscillations. As the amplitude of the torsional oscillations increases the jets are deflected, symmetrically, away from the axis of oscillation until they merge to form a single jet which is perpendicular to that axis. The direction, and there is a choice of two, of this jet depends upon the phase difference between transverse and torsional oscillations. The axial flow is unaffected directly by the torsional oscillations

of the cylinder whereas the interaction with the transverse vibrations does affect it. The interaction between the transverse and axial vibrations introduces a modification to the axial flow, which results in a steady streaming motion in the axial direction. The direction of this streaming, at any particular angular location, depends crucially on the phase difference between the transverse and the axial vibrations. Thus, Riley's work demonstrated that in the complete absence of transverse vibrations the flow is relatively uninteresting and phase difference between the three superimposed oscillations play a crucial role in determining the flow structure. In Riley's work numerical solutions were obtained both infinite and large but finite Reynolds numbers using boundary-layer equations and viscous-inviscid interactive procedure.

A literature survey reveals that there are no papers studying the more practical case of flow-induced vibrations in which a circular cylinder forced to move with the combined (2-DoF) forced recti-linear and rotational oscillations in a uniform flow. If both motions are simple harmonic, the flow is characterized by five dimensionless groups, which correspond to two sets of oscillation amplitudes and frequencies, and Reynolds number: (i) Reynolds number, $R = Ud/\nu$; (ii) amplitudes of two simple harmonic motions, A and θ_m; (iii) frequency ratios, f/f_0 and f_θ/f_0; where U is the free-stream velocity, d is the cylinder diameter, ν is the kinematic viscosity of the fluid, and A, θ_m and f, f_θ are the amplitudes and the frequencies of recti-linear and rotational displacements of the cylinder, respectively. The vortex shedding (Strouhal) frequency for the stationary cylinder is denoted by $2f_0^*$ and, dimensionlessly quantified as the classical (natural) Strouhal frequency $S_0 = f_0^* d/U$ so that $S_0 = 2f_0$ i.e., $f_0 = f_0^* a/U$ where a is the cylinder radius.

In the case of a cylinder performing 1-DoF forced recti-linear or rotational cylinder oscillations when the oscillation frequency is near the natural shedding frequency, $f/f_0 \approx 1$ or $f/f_\theta \approx 1$ (for transverse or rotational oscillation) or twice the natural shedding frequency, $f/f_0 \approx 2$ (for in-line oscillation) vortices start shedding at the same frequency. Thus, in the forced wake flows vortex shedding is entrained by the cylinder motion i.e., the vortex shedding frequency changes to match the cylinder forcing frequency. This is the lock-on phenomenon, where the self-excited oscillation synchronizes with the forcing frequency of the cylinder oscillation. The concept of vortex lock-on and the modes of vortex formation for the flows generated by 1-DoF cylinder motions are discussed in the comprehensive reviews of Sarpkaya (1979; 2004); Griffin and Hall (1991); Bearman (1984); Matsumoto (1999); Pier and Huerre (2001), Williamson and Govardhan (2004); in book chapters by Anagnostoppoulos (2002) and Zdravkovich (1997) and in a book by Sumer and Fredsøe (1997).

Only one experimental study has been made on the (1-DoF) forced recti-linear oscillations of a cylinder at an arbitrary angle η with respect to the free stream: Ongoren and Rockwell (1988b). Visual observations were made in the Reynolds number and frequency ratio ranges $584 \leq R \leq 1300$ and $0.5 \leq f/f_0 \leq 4.0$, respectively, at angle of inclination $\eta = 0^0, 45^0, 60^0, 90^0$ of cylinder oscillation with respect to the free stream. For most experiments, a constant value of dimensionless amplitude, $A = 0.26$, was chosen. They showed that if the cylinder is excited at an angle other than the cross-stream or streamwise direction, then there is mixed-mode excitation: the perturbation from the cylinder motion contains both symmetrical and anti-symmetrical

contributions and the potential for exciting both types of modes. Moreover, these modes either can be synchronized, i.e. phase-locked, with the cylinder motion, or they can compete with each other. In their investigation, they addressed under which conditions these modes occur, for both synchronized and non-synchronized vortex formation. Particular remarkable finding by Ongoren and Rockwell is that the occurrence of synchronized vortex formation in the asymmetric mode when the cylinder motion produces purely symmetrical perturbations of large amplitude. Basic modes of vortex formation from the cylinder undergoing (1-DoF) forced recti-linear oscillations at angle η with respect to the free stream are summarized in Figure 1.1 (see Ongoren and Rockwell (1988b), p. 227). The modes of vortex formation can be categorized into two basic groups: an asymmetric mode of vortex formation and a symmetric mode of vortex formation. There is a single symmetric **2S** mode: a pair of vortices are shed in phase from both sides of the cylinder during one oscillation cycle (i.e., a clockwise rotating single vortex is shed from one side of the cylinder and a counter-clockwise rotating single vortex is shed from the other side of the cylinder during one oscillation cycle). There are three basic asymmetric, **2S**, **S+P** and **2P**, modes where **S** and **P** refer to a shed single vortex and a pair of shed vortices, respectively. In the asymmetric **2S** mode there is alternate, out-of-phase shedding of vortices from either side of the cylinder over one or two periods of an oscillation cycle (i.e., a clockwise rotating single vortex is shed from one side of the cylinder and a counter-clockwise rotating single vortex is shed from the other side of the cylinder over one or two periods of an oscillation cycle). The asymmetric **2S** mode over one oscillation cycle corresponds to the classical mode of vortex shedding leading to the formation of Kármán vortex street. The other two asymmetric modes show period

doubling relative to the classical Kármán vortex mode. These modes arise from the symmetrical perturbation component induced by oscillations at all inclination angles to the free-stream except 90^0. Moreover, the asymmetric **S+P** and **2P** modes involve formation of counter-rotating vortex pairs. Specifically, in the asymmetric **S+P** mode two clockwise rotating vortices are shed from one side of the cylinder and a counter-clockwise rotating single vortex is shed from the other side of the cylinder over two oscillation cycles; in the asymmetric **2P** mode a pair of clockwise rotating vortices are shed from one side of the the cylinder and a pair counter-clockwise rotating vortices are shed from the other side of the cylinder over two oscillation cycles. According to the experimental work of Ongoren and Rockwell (1988b) symmetric mode can occur at any value of inclination angle to the free-stream except 90^0. The asymmetric, **2S**, **S+P** and **2P**, modes over two oscillation cycles occur only for $0^0 \leq \eta < 90^0$ where there is a symmetrical component in the flow perturbation. In fact the effect of the symmetrical component of the perturbation is to double the period of the asymmetrical vortex formation. The asymmetric **2S** mode over two periods of the cylinder oscillation occurs only for $\eta \neq 0^0$. The asymmetric **S+P** and **2P** occur only for $\eta = 0^0$. We note that generalization of occurrence of these modes are restricted to the relatively small amplitudes of cylinder oscillation. Ongoren and Rockwell (1988b) showed that the cylinder at an angle other than 0^0 or 90^0 can cause vortex lock-on. In their work it was reported that phase locking of vortex shedding with the cylinder motion is possible for all the modes described earlier.

A class of flows which has not received attention until now is that created by a rigid circular circular cylinder moving with combined (2-DoF) forced recti-linear (in-line or

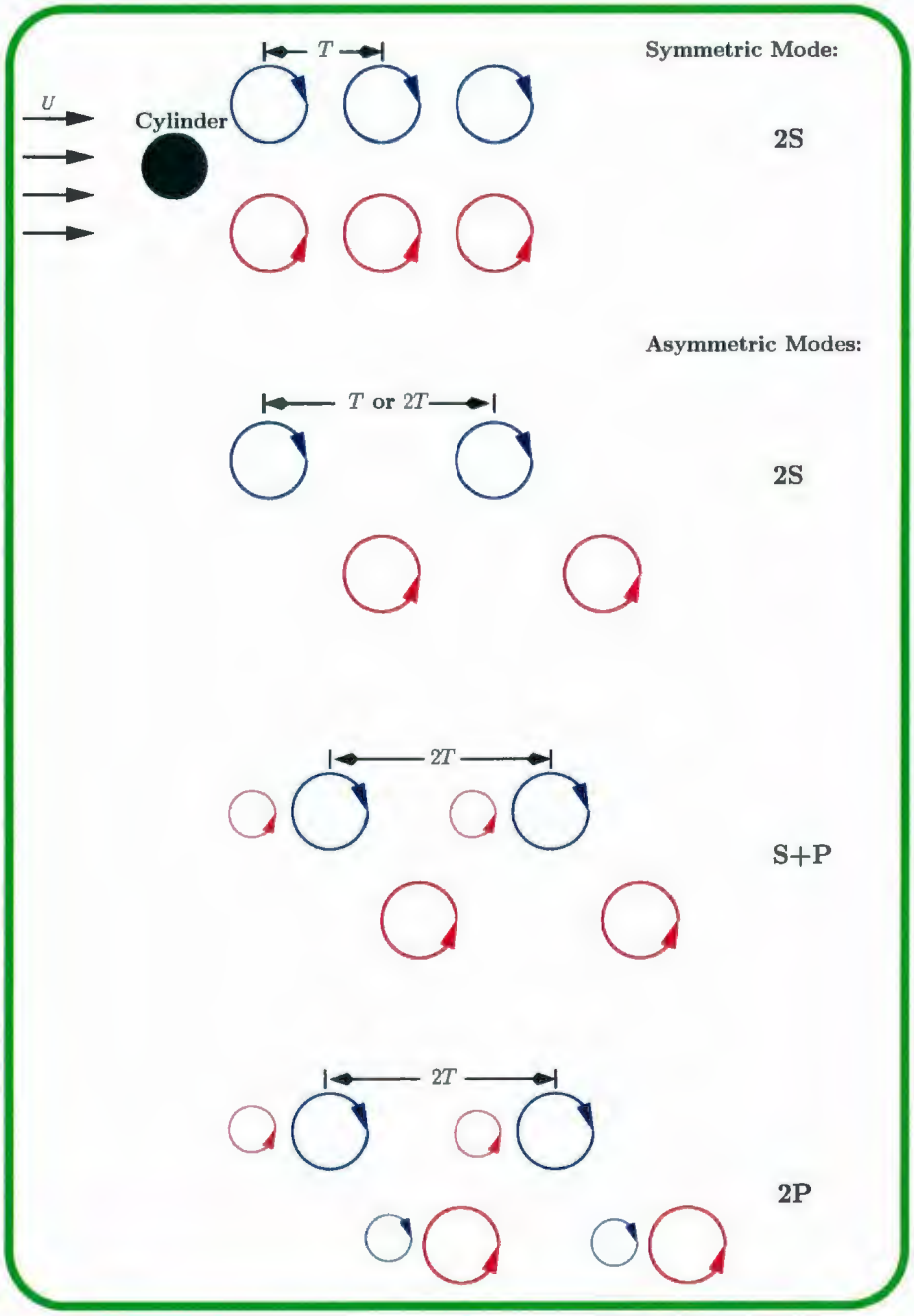

Figure 1.1: Representation of basic modes of vortex formation from cylinder oscillating with 1-DoF at angle η with respect to the free stream.

transverse) and rotational oscillations in a uniform stream of viscous incompressible flow. The present thesis deals with this class of wake flows to analyze the vortex formation modes and synchronization (lock-on) phenomena behind the cylinder (in the near-wake region) as well as the fluid forces acting on the cylinder. The flow is incompressible and two-dimensional, and recti-linear and rotational oscillations are harmonic. The motion is assumed to be laminar and governed by the unsteady Navier-Stokes equations and the mass conservation equation. The associated conditions are no-slip and impermeability conditions on the cylinder surface and free stream conditions far away from the surface.

The method of analysis adopted here is based on the use of truncated Fourier representations for the stream function and vorticity in the angular polar coordinate. Two types of solutions are obtained. A series expansion for small times is developed, using boundary-layer theory for impulsively started flows and an exact analysis. The initial flow is determined by means of analytical expressions. The governing Navier-Stokes equations are also integrated to obtain the velocity field for longer times using an accurate spectral-finite difference method, but with the boundary vorticity calculated using global vorticity conditions, termed *integral conditions* rather than local finite-difference approximations. An implicit Crank-Nicolson method is employed in the time advancements and a second-order central difference scheme is used for spatial derivatives. The discretized nonlinear vorticity equations are solved using a Gauss-Seidel iterative method. It is shown that the correct satisfaction of integral conditions is the required condition to ensure that the pressure in the fluid is periodic in θ with 2π. Thus, the correct satisfaction of integral conditions is considered as a

very important part of the solution procedure since they ensure both the free stream is approached far from the cylinder and satisfaction of the physically essential results for the existence of the flow. Special care is taken to account for the impulsive start of the motion. This is done by implementing the special starting procedure using similarity coordinates later replaced by physical coordinates. The numerical technique has previously been described and applied to simulations of flows past a stationary cylinder; a steadily rotating cylinder; a cylinder undergoing (1-DoF) forced oscillations: Collins (1971); Collins and Dennis (1973b); Badr and Dennis (1985); Badr, Dennis, Kocabiyik and Nguyen (1995b); Dennis, Nguyen and Kocabiyik (2000) to name a few. However, in these studies the calculations were carried out only for moderate values of the times ($t \leq 40$). In this thesis the numerical simulations are carried out for longer times ($t \leq 120$) to analyze the wake flow generated by combined (2-DoF) recti-linear and rotational cylinder oscillations.

The numerical scheme is verified by applying it to the special cases of (i) a stationary cylinder (no forced oscillations) (ii) a steadily rotating cylinder (no forced oscillations); (iii) a cylinder undergoing 1-DoF forced recti-linear oscillations at angles of 0^0, 60^0, 90^0 with respect to the uniform free-stream. The numerical simulations are carried out at $R = 100,\ 106,\ 10^3$ for the case of a stationary cylinder and tested against existing numerical and experimental results. Good agreement with these results is found. The flow around a steadily rotating cylinder is calculated for the constant rotating rates $\Omega = 1,\ 3$ at $R = 500,\ 10^3$ and good qualitative agreement with the findings of [Chou (2000): numerical] and [Badr *et. al.* (1990), Coutanceau and Pineau (1997): experimental] are found. The numerical simulations are carried out at

$R = 855$ under the same oscillation conditions as the experimental study of Ongoren and Rockwell (1988b) for the case of a cylinder undergoing 1-DoF forced recti-linear oscillations at angles of 0^0, 60^0, 90^0 with respect to the uniform free-stream. The resulting near-wake structures are compared with those obtained experimentally by Ongoren and Rockwell (1988b). Good qualitative agreement between these results is found. Furthermore, the numerical method is used to calculate the unsteady initial flow for the case of combined (2-DoF) forced recti-linear and rotational cylinder oscillations at a Reynolds number of $R = 855$ to check the analytical solutions obtained at small times. The surface pressure distribution is also calculated for the same (2-DoF) motion case to verify the correct implementation of the surface pressure periodicity in the numerical scheme for large values of the time.

For the combined (2-DoF) forced recti-linear (in-line or transverse) and rotational cylinder oscillation case numerical simulations are carried out for combined phase-locked translation and rotation with a single frequency, i.e., $f = f_\theta$. It is assumed that the instantaneous translation and rotation start at the same moment and the development of the flow is studied in a coordinate frame which moves with the cylinder but does not rotate. The calculations are performed for large values of the time in the cases $R = 855$ and $A = 0.26$: $f/f_0 = 0.5,\ 1,\ 2,\ 3,\ 4$ and $\Theta_m = 15^o,\ 30^o,\ 60^o; 75^o$. The resulting vortex formation modes and synchronization (lock-on) phenomena behind the cylinder (in the near-wake region) as well as the fluid forces acting on the cylinder are analyzed. In addition, a series of 1-DoF forced vibration calculations are carried out to better understand what differences result from the addition of rotational oscillations to streamwise or cross-stream motion and to see which effects a transverse-only or in-line-only simulations miss.

Chapter 2

The formulation of the problem

2.1 Basic equations and boundary conditions

In this thesis we consider the unsteady motion of a viscous incompressible fluid past an oscillating circular cylinder of infinite length and constant cross-section. We take a Cartesian coordinate system (x, y, z) with origin fixed in the cylinder and the z-axis being the axis of the cylinder. The surface of the cylinder is enclosed by an impermeable boundary C. The cylinder is of radius a and is placed horizontally in a cross-stream of an infinite extend. The fluid moves past the cylinder with uniform velocity U in the positive x-direction of the Cartesian coordinates. At $t^* = 0$, the cylinder suddenly starts to move with combined (2-DoF) harmonic oscillatory translation and rotation. We note that t^* denotes the time. We have assigned the imposed translational oscillatory motion along the translation axis at an arbitrary angle η to the free-stream direction, so that translational oscillatory motion has the form

$$Y^*(t^*) = Y_m \cos(2\pi f^* t^*), \tag{2.1.1}$$

while the rotational oscillatory motion of the cylinder about its axis is described by

$$\Theta^*(t^*) = -\Theta_m \cos(2\pi f_\theta^* t^*), \tag{2.1.2}$$

where f^* and f_θ^*; Y_m and Θ_m are, respectively, the frequencies and amplitudes of the two simple harmonic motions. Here Y^* and Θ^* are, respectively, the instantaneous dimensional linear and angular cylinder displacement with counterclockwise rotation corresponding to positive $d\Theta^*/dt^*(= \Omega^*(t^*))$ and with upward rectilinear motion direction along the axis of oscillation corresponding to positive $dY^*/dt^*(= V^*(t^*))$. The physical model and coordinate system considered is shown in Figure 2.1.

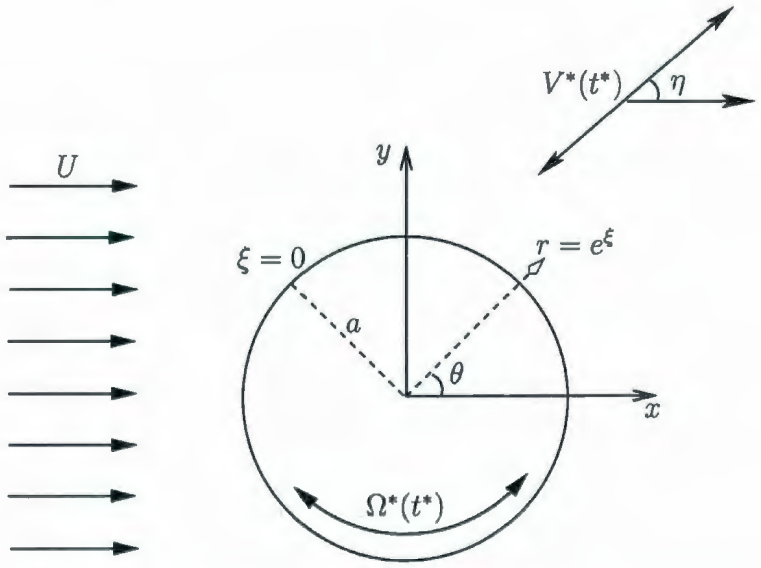

Figure 2.1: The physical model and coordinate system

The governing equations of motion for a viscous fluid are obtained by a consideration of the forces acting upon a fluid particle. The resulting momentum or Navier-Stokes

equations in dimensional form are

$$\frac{\partial \vec{v}_I^*}{\partial t^*} + (\vec{v}_I^* \cdot \vec{\nabla})\vec{v}_I^* = -\frac{1}{\rho}\vec{\nabla}p^* + \nu\nabla^2\vec{v}_I^* \tag{2.1.3}$$

where the subscript I denotes the inertial frame of reference. Here $\vec{v}_I^*$ is the velocity vector, p^* is the fluid pressure, ρ is the density of the fluid and ν is the coefficient of kinematic viscosity defined by

$$\nu = \frac{\mu}{\rho}, \tag{2.1.4}$$

where μ is the dynamic viscosity of the fluid. In addition to these equations, conservation of mass of the fluid gives rise to the equation of continuity. For an incompressible fluid this equation is

$$\vec{\nabla} \cdot \vec{v}_I^* = 0. \tag{2.1.5}$$

Equations (2.1.3) and (2.1.5) together govern the unsteady motion of a viscous incompressible fluid and must be solved subject to appropriate boundary conditions. For the flow past a cylinder these conditions are the no slip of the fluid on the cylinder surface and the fluid velocity approaching the uniform stream at large distances from the cylinder.

It is well known that the major problem associated with a numerical computation of viscous flow around an oscillating cylinder is describing the boundary conditions at the continuously accelerating solid wall within a discrete finite difference or finite element grid system. To overcome this difficulty and achieve a fixed grid with respect to the cylinder, it is necessary to use a non-inertial reference frame attached to the cylinder so that the cylinder axis coincides with z-axis. The present study considers a frame of reference which translates and oscillates with the cylinder but does not

rotate relative to the cylinder, where the axes of inertial and non-inertial frames are parallel to each other as shown in Figure 2.2.

The relation between the two frames can easily be obtained by considering any point

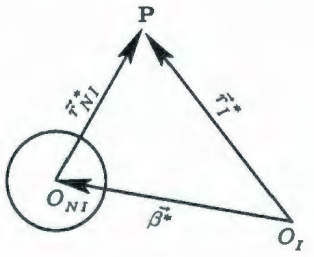

Figure 2.2: Change of origin of coordinates.

P which is located by the vectors $\vec{r}^*_I$ and $\vec{r}^*_{NI}$ with respect to inertial and non-inertial frames, respectively. It is assumed that O_I and O_{NI} are, respectively, the origins of the inertial and non-inertial frames so that O_{NI} is located by a vector $\vec{\beta}^*$ with respect to O_I. Thus the relation between the vectors $\vec{r}^*_I$ and $\vec{r}^*_{NI}$ is given by

$$\vec{r}^*_I(t^*) = \vec{r}^*_{NI}(t^*) + \vec{\beta}^*(t^*). \tag{2.1.6}$$

Since the origin O_{NI} is moving with respect to the fixed origin O_I the relation between the velocities relative to the two frames is obtained by differentiating (2.1.6) with respect to t^*

$$\begin{aligned} \frac{d\vec{r}^*_I}{dt^*} &= \vec{v}^*_I = \frac{\vec{r}^*_{NI}}{dt^*} + \frac{d\vec{\beta}^*}{dt^*} \\ \vec{v}^*_I &= \vec{v}^*_{NI} + \vec{v}^*_S, \end{aligned} \tag{2.1.7}$$

where $\vec{v}^*_I$ and $\vec{v}^*_{NI}$ represent velocities in the inertial and non-inertial frames, respectively, and $\vec{v}^*_S$ represents the velocity of the moving frame (or the cylinder) with respect to the inertial frame.

By direct substitution of (2.1.7) into the equations (2.1.3) and (2.1.5), we obtain the governing equations in the non-inertial reference frame as follows (after dropping all the subscripts)

$$\frac{\partial \vec{v}^*}{\partial t^*} + (\vec{v}^* \cdot \vec{\nabla})\vec{v}^* = -\frac{1}{\rho}\vec{\nabla}p^* + \nu\nabla^2\vec{v}^* + \vec{a}^*, \tag{2.1.8}$$

$$\vec{\nabla} \cdot \vec{v}^* = 0, \tag{2.1.9}$$

where the vectors $\vec{v}^*$ and $\vec{a}^*$ represent respectively the velocity in the moving frame of reference and the acceleration of the moving coordinate system.

As the cylinder is of infinite length and constant cross-section, the flow is assumed to be two-dimensional in the xy-plane. The velocity and acceleration vectors are then of the form

$$\vec{v}^* = (u^*, v^*, 0) \tag{2.1.10}$$

$$\vec{a}^* = -\frac{d\vec{v}_S^*}{dt^*} = \dot{V}^*(t^*)(\cos(\eta), \sin(\eta), 0). \tag{2.1.11}$$

Here

$$\vec{v}_S^* = (-U - V^*(t^*)\cos(\eta), -V^*(t^*)\sin(\eta), 0), \tag{2.1.12}$$

and $V^*(t^*)(= dY^*/dt^*)$ is the dimensional rectilinear oscillatory velocity of the cylinder and $\dot{V}^*(t^*) = dV^*/dt^*$. Throughout this thesis we use superscript dot to denote ordinary differentiation with respect to time. All quantities in these equations are dimensional, their dimensionless counterparts being given by

$$\vec{v}^* = U\,\vec{v}, \qquad p^* = 1/2\,\rho U^2 p \tag{2.1.13}$$

$$x^* = a\,x, \qquad y^* = a\,y, \qquad z^* = a\,z, \qquad t^* = a\,t/U. \tag{2.1.14}$$

Since the flow is assumed two dimensional in the xy-plane the equations (2.1.8) and (2.1.9), in the dimensionless form, become

$$\frac{\partial \vec{v}}{\partial t} + (\vec{v} \cdot \vec{\nabla})\vec{v} = -\frac{1}{2}\vec{\nabla}p + \frac{2}{R}\nabla^2\vec{v} + \vec{a}, \tag{2.1.15}$$

$$\vec{\nabla} \cdot \vec{v} = 0. \tag{2.1.16}$$

where $\vec{v} = (u, v, 0)$ and $\nabla^2 = \partial^2/\partial x^2 + \partial^2/\partial y^2$. Here u, v, p are functions of (x, y) and R is the Reynolds number defined by

$$R = \frac{2\,a\,U}{\nu}. \tag{2.1.17}$$

The problem as formulated here involves three equations in the three unknowns u, v and p. The Poisson's equation for pressure can be obtained by taking the divergence of the momentum equation (2.1.15) and then using the continuity equation (2.1.16). The boundary conditions for this equation are the Neumann conditions obtained from the momentum equations. The difficulty in solving this equation numerically leads us to formulate the problem in terms of the stream function , ψ, and (negative) scalar vorticity , ζ, defined by

$$u(x, y) = \frac{\partial \psi}{\partial y}, \qquad v(x, y) = -\frac{\partial \psi}{\partial x}, \tag{2.1.18}$$

$$\zeta(x, y) = \frac{\partial u}{\partial y} - \frac{\partial v}{\partial x}. \tag{2.1.19}$$

As a consequence of two dimensional flow, the dimensionless vorticity vector, $\vec{w}$, is given by

$$\vec{w} = \vec{\nabla} \times \vec{v} = (0, 0, -\zeta). \tag{2.1.20}$$

The dimensional stream function and vorticity are given by

$$\psi^* = 2\,a\,U\,\psi, \qquad \zeta^* = U\,\zeta/2\,a. \tag{2.1.21}$$

It can be easily seen from equations (2.1.16) and (2.1.18) that the continuity equation is automatically satisfied by the stream function. Also, taking the curl of the

momentum equations eliminates the pressure from them and gives equations for ψ and ζ in the form

$$\frac{\partial \zeta}{\partial t} = \frac{2}{R}\left(\frac{\partial^2 \zeta}{\partial x^2} + \frac{\partial^2 \zeta}{\partial y^2}\right) + \left(\frac{\partial \psi}{\partial x}\frac{\partial \zeta}{\partial y} - \frac{\partial \psi}{\partial y}\frac{\partial \zeta}{\partial x}\right), \tag{2.1.22}$$

$$\frac{\partial^2 \psi}{\partial x^2} + \frac{\partial^2 \psi}{\partial y^2} = \zeta. \tag{2.1.23}$$

The problem now consists of a coupling of two second-order nonlinear partial differential equations.

The boundary conditions for ψ and ζ must now be given. ψ and $\partial\psi/\partial n$ are known on the contour C of the cylinder, where $\partial/\partial n$ is differentiation in the normal direction to the cylinder. Since the flow field is unbounded, conditions at infinity must be imposed. Generally these reduce to the fact that the asymptotic behavior of both ψ and ζ is known as infinity is approached. If $\mathcal{D}$ denotes the infinite region outside the cylinder, then the conditions on ψ and ζ are

$$\text{for } t = 0: \ \zeta = 0 \ \text{ throughout } \mathcal{D}, \ \zeta \neq 0 \ \text{ on } C, \tag{2.1.24a}$$

$$\text{for } t \geq 0: \ \psi = 0, \quad \frac{\partial \psi}{\partial n} = -\Omega(t) \quad \text{on } C \tag{2.1.24b}$$

and

$$\frac{\partial \psi}{\partial y} \to 1 + V(t)\cos(\eta), \quad \frac{\partial \psi}{\partial x} \to -V(t)\sin(\eta) \quad \text{as } x^2 + y^2 \to \infty. \tag{2.1.24c}$$

We note that $D \cup C$ forms the closure of the fluid domain. Here $V(t) = V^*(t^*)/U$ and $\Omega(t) = \Omega^*(t^*)a/U$ are the dimensionless recti-linear and rotational oscillatory velocities of the cylinder, respectively. Conditions (2.1.24b) and (2.1.24c) are the mathematical statements of no-slip and impermeablity conditions at the cylinder

surface and uniform flow at infinity, respectively. The use of the condition of uniform flow at infinity for impulsively started motion can be justified on the basis that the vorticity generated on the surface of the cylinder is diffused and convected away at finite rate. Thus after any finite interval of time, the uniform flow at infinity will remain undisturbed. Implicit in condition (2.1.24c) is that

$$\zeta(x,y) \to 0 \quad \text{as} \quad x^2+y^2 \to \infty \tag{2.1.25}$$

which is obtained from the asymptotic form of the stream function at infinity

$$\psi = (1+V(t)\cos(\eta))\, y - V(t)\, \sin(\eta)\, x \tag{2.1.26}$$

together with the stream function equation (2.1.23).

The difficulty which accompanies the numerical simulation of stationary and moving cylinders in uniform flow lies in the representation of the cylinder geometry to allow for accurate application of these numerical integration methods. The use of coordinate transformations and mapping techniques for this problem is possible and have been successfully used by numerous researchers [see for example, Jordan and Fromm (1972), Braza *et al.* (1986) and Badr and Dennis (1985)]. In this work modified polar coordinates (ξ,θ), where $\xi = \ln(r)$, are adopted by considering a conformal transformation of the form

$$x + iy = \exp(\xi + i\theta) \tag{2.1.27}$$

which transforms the surface of the cylinder to $\xi = 0$ and the region outside the cylinder to the semi-infinite strip $\xi > 0$, $0 \le \theta < 2\pi$ as shown in Figure 2.3. The same line segments $\theta = 0$, $\theta = 2\pi$ ultimately approach the direction of the uniform stream as $\xi \to \infty$.

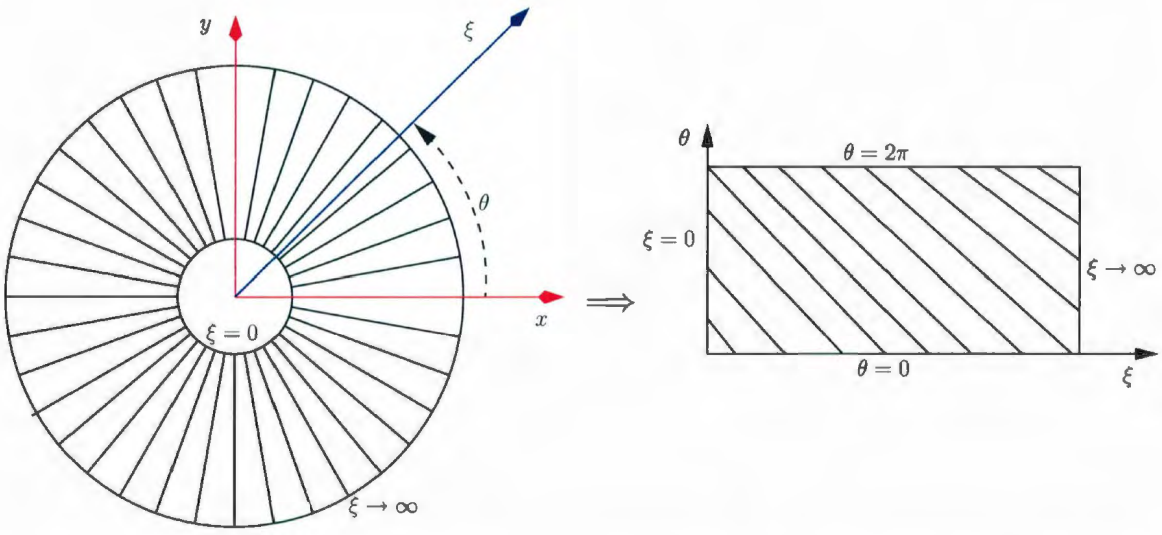

Figure 2.3: The Cartesian and modified Polar coordinate systems (left) and the transformed domain (right).

The dimensionless velocity components (u_ξ, v_θ) in the directions of increase of (ξ, θ) are related to the stream function by

$$u_\xi(\xi,\theta,t) = e^{-\xi}\frac{\partial\psi}{\partial\theta}, \quad v_\theta(\xi,\theta,t) = -e^{-\xi}\frac{\partial\psi}{\partial\xi}. \tag{2.1.28}$$

The equation (2.1.19) for the vorticity then becomes

$$\zeta(\xi,\theta,t) = e^{-2\xi}\left[\frac{\partial}{\partial\theta}(e^{\xi}u_\xi) - \frac{\partial}{\partial\xi}(e^{\xi}v_\theta)\right]. \tag{2.1.29}$$

The component equations of momentum from (2.1.15) can be written in the form

$$\frac{\partial u_\xi}{\partial t} + v_\theta\,\zeta = -\frac{e^{-\xi}}{2}\frac{\partial(p+|\vec{v}|^2)}{\partial\xi} + \frac{2\,e^{-\xi}}{R}\frac{\partial\zeta}{\partial\theta} + \vec{a}\cdot\mathbf{e}_\xi, \tag{2.1.30}$$

$$\frac{\partial v_\theta}{\partial t} - u_\xi\,\zeta = -\frac{e^{-\xi}}{2}\frac{\partial(p+|\vec{v}|^2)}{\partial\theta} - \frac{2\,e^{-\xi}}{R}\frac{\partial\zeta}{\partial\xi} + \vec{a}\cdot\mathbf{e}_\theta \tag{2.1.31}$$

where

$$\vec{a} \cdot \mathbf{e}_\xi = \dot{V}(t)\cos(\eta)\,\cos(\theta) + \dot{V}(t)\sin(\eta)\,\sin(\theta),$$

$$\vec{a} \cdot \mathbf{e}_\theta = -\dot{V}(t)\cos(\eta)\,\sin(\theta) + \dot{V}(t)\sin(\eta)\,\cos(\theta)$$

and $\mathbf{e}_\xi$, $\mathbf{e}_\theta$ are the unit vectors in the ξ, θ directions respectively. However, the governing equations for ψ and ζ become

$$e^{2\xi}\frac{\partial \zeta}{\partial t} = \frac{2}{R}\left(\frac{\partial^2 \zeta}{\partial \xi^2} + \frac{\partial^2 \zeta}{\partial \theta^2}\right) + \frac{\partial \psi}{\partial \xi}\frac{\partial \zeta}{\partial \theta} - \frac{\partial \psi}{\partial \theta}\frac{\partial \zeta}{\partial \xi}, \tag{2.1.32}$$

$$\frac{\partial^2 \psi}{\partial \xi^2} + \frac{\partial^2 \psi}{\partial \theta^2} = e^{2\xi}\zeta. \tag{2.1.33}$$

The no-slip and impermeability conditions at the cylinder surface become

$$\psi = 0, \qquad \frac{\partial \psi}{\partial \xi} = -\Omega(t) \quad \text{when} \quad \xi = 0. \tag{2.1.34}$$

The condition of the velocity approaching the uniform stream at large distances from the cylinder becomes

$$e^{-\xi}\frac{\partial \psi}{\partial \xi} \to (1 + V(t)\cos(\eta))\sin\theta - V(t)\sin(\eta)\cos\theta \quad \text{as} \quad \xi \to \infty, \tag{2.1.35a}$$

$$e^{-\xi}\frac{\partial \psi}{\partial \theta} \to (1 + V(t)\cos(\eta))\cos\theta + V(t)\sin(\eta)\sin\theta \quad \text{as} \quad \xi \to \infty. \tag{2.1.35b}$$

We also have from equation (2.1.25)

$$\zeta(\xi, \theta, t) \to 0 \quad \text{as} \quad \xi \to \infty. \tag{2.1.36}$$

All flow variables must be periodic functions of the angular coordinate θ with period 2π. For the stream function and vorticity we then have

$$\zeta(\xi, \theta, t) = \zeta(\xi, \theta + 2\pi, t), \qquad \psi(\xi, \theta, t) = \psi(\xi, \theta + 2\pi, t). \tag{2.1.37}$$

From the definition of the stream function (2.1.28) it is obvious that the velocity components u_ξ and v_θ are also periodic functions of θ with period 2π. Since the difficulty in ensuring the pressure is likewise periodic in θ arises only in asymmetric flows, care must be exercised in order for the pressure to remain periodic in θ with period 2π for all t, this will be considered in Section 2.3.

By examining the boundary conditions, we see that there are two conditions for the stream function on the cylinder surface while none for the vorticity. The absence of the surface vorticity condition causes a major difficulty in solving equations (2.1.22) and (2.1.23) [see for example, Peyret and Taylor (1983)]. In numerical computations it is common practice to estimate, in the course of iterative processes, the vorticity boundary values using equation (2.1.23) on the boundaries, taking into account the conditions for ψ and $\partial\psi/\partial n$ given in (2.1.24b) and (2.1.24c). The convergence properties of any computational scheme based on this approach strongly depend on the treatment which is adopted in approximating the vorticity boundary values. Moreover, even when converging solutions are obtained, still great discrepancies of local and global quantities are found between apparently comparable calculations due to the existence of large velocity gradients near the cylinder surface. These computational results can be understood by considering that the rate of change of the total vorticity in the fluid domain is controlled by the values of the gradient of the vorticity on the boundary. Dennis and Chang (1969), Dennis and Walker (1971), Glowinski and Pironneau (1979) and Quatapelle and Valz-Gris (1981) specified vorticity boundary values by complementing the vorticity transport equation (2.1.33) with conditions of an integral character, so that numerical solutions of vorticity stream function

equations can be obtained by means of finite differences [see for example Dennis and Quartapelle (1989)], finite elements [see for example Quartapelle and Napolitano (1984)] and spectral methods [see for example Dennis and Quartapelle (1983)]. In this work, global vorticity conditions, termed *integral conditions* are used to predict the surface vorticity. These integral conditions can be derived by applying the local conditions for the stream function in Green's second identity for the Laplacian operator, namely

$$\iint_{\mathcal{D}} \left(\phi \nabla^2 \psi - \psi \nabla^2 \phi\right) d\mathcal{D} = \oint_S (\phi \frac{\partial \psi}{\partial n} - \psi \frac{\partial \phi}{\partial n}) ds, \tag{2.1.38}$$

to the flow region $\mathcal{D}$ outside the cylinder following the work by Dennis and Quartapelle (1989) and Dennis and Kocabiyik (1991). Here the boundary S of the flow domain is the contour of the cylinder, C, together with a contour at a large distance from it, C_∞, $\vec{n}$ refers to the outward normal to the boundary S of the flow domain, and s is measured along it. Choosing ϕ to be harmonic functions $\phi \in \{1, e^{-p\xi}\cos(p\theta), e^{-p\xi}\sin(p\theta), p = 1, 2, 3, \cdots\}$ and using $\nabla^2 \phi = 0$, (2.1.33), (2.1.34), (2.1.35a) and (2.1.35b) we arrive at the following integral conditions

$$\int_0^\infty \int_0^{2\pi} e^{2\xi} \zeta(\xi, \theta, t) d\theta d\xi = 2\pi \Omega(t), \tag{2.1.39a}$$

$$\int_0^\infty \int_0^{2\pi} e^{(2-p)\xi} \zeta(\xi, \theta, t) \cos(p\theta) d\theta d\xi = -2\pi V(t) \sin(\eta) \delta_{1,p}, \tag{2.1.39b}$$

$$\int_0^\infty \int_0^{2\pi} e^{(2-p)\xi} \zeta(\xi, \theta, t) \sin(p\theta) d\theta d\xi = 2\pi (V(t) \cos(\eta) + 1) \delta_{1,p}, \tag{2.1.39c}$$

for all integers $p \geq 1$ and $\delta_{s,p}$ is the Kronecker delta symbol defined by

$$\delta_{s,p} = 1 \text{ if } s = p, \ \delta_{s,p} = 0 \text{ if } s \neq p.$$

2.2 The method of analysis

The method of analysis is based on the solutions of the unsteady Navier-Stokes equations by means of Fourier analysis. Two types of solutions are obtained. A series expansion for small times is developed using an exact analysis. The governing Navier-Stokes equations are also integrated to obtain the velocity field by a spectral-finite difference method. The details of the method of solutions will be given in subsequent chapters. In this section we focus on the the method of analysis adopted by Collins and Dennis (1973a,b) and Badr and Dennis (1985). A brief description is as follows.

The periodicity condition on the vorticity ζ and stream function ψ given in (2.1.37) is implemented using a truncated Fourier series expansion

$$\zeta(\xi,\theta,t) \simeq \zeta_N(\xi,\theta,t) = \frac{1}{2}G_0(\xi,t) + \sum_{n=1}^{N}\left[G_n(\xi,t)\cos(n\theta) + g_n(\xi,t)\sin(n\theta)\right], \quad (2.2.1a)$$

$$\psi(\xi,\theta,t) \simeq \psi_N(\xi,\theta,t) = \frac{1}{2}F_0(\xi,t) + \sum_{n=1}^{N}\left[F_n(\xi,t)\cos(n\theta) + f_n(\xi,t)\sin(n\theta)\right], \quad (2.2.1b)$$

where N is the order of truncation in the Fourier series and the functions G_0, G_n, g_n, F_0, F_n and f_n are Fourier coefficients with independent variables ξ and t. Substituting (2.2.1a,b) into (2.1.32) and (2.1.33), respectively, we obtain two equations in terms of ψ_N and ζ_N, given in terms of their residuals as

$$R_1(\zeta_N,\psi_N) = e^{2\xi}\frac{\partial\zeta_N}{\partial t} - \frac{2}{R}\left(\frac{\partial^2\zeta_N}{\partial\xi^2} + \frac{\partial^2\zeta_N}{\partial\theta^2}\right) - \frac{\partial\psi_N}{\partial\xi}\frac{\partial\zeta_N}{\partial\theta} + \frac{\partial\psi_N}{\partial\theta}\frac{\partial\zeta_N}{\partial\xi}, \quad (2.2.2)$$

$$R_2(\zeta_N,\psi_N) = \frac{\partial^2\psi_N}{\partial\xi^2} + \frac{\partial^2\psi_N}{\partial\theta^2} - e^{2\xi}\zeta_N. \quad (2.2.3)$$

Substitution of the series given in (2.2.1) in equations (2.2.2) and (2.2.3), and following the works of Collins and Dennis (1973b), and Badr and Dennis (1985) we obtain the

following set of differential equations for the coefficients of ζ_N and ψ_N, after the standard use of orthogonal functions,

$$e^{2\xi}\frac{\partial G_0}{\partial t} = \frac{2}{R}\frac{\partial^2 G_0}{\partial \xi^2} + \sum_{m=1}^{N} m\frac{\partial}{\partial \xi}\left(F_m g_m - f_m G_m\right), \tag{2.2.4a}$$

$$e^{2\xi}\frac{\partial G_n}{\partial t} = \frac{2}{R}\left(\frac{\partial^2 G_n}{\partial \xi^2} - n^2 G_n\right) - \frac{1}{2}n f_n\frac{\partial G_0}{\partial \xi} + \frac{1}{2}S_n, \tag{2.2.4b}$$

$$e^{2\xi}\frac{\partial g_n}{\partial t} = \frac{2}{R}\left(\frac{\partial^2 g_n}{\partial \xi^2} - n^2 g_n\right) + \frac{1}{2}n F_n\frac{\partial G_0}{\partial \xi} + \frac{1}{2}T_n, \tag{2.2.4c}$$

$$\frac{\partial^2 F_0}{\partial \xi^2} = e^{2\xi}G_0, \qquad \frac{\partial^2 F_n}{\partial \xi^2} - n^2 F_n = e^{2\xi}G_n, \qquad \frac{\partial^2 f_n}{\partial \xi^2} - n^2 f_n = e^{2\xi}g_n, \quad \text{(2.2.5a, b, c)}$$

where

$$S_n = \sum_{m=1}^{N}\left\{\left[(m-n)F_k + lF_l\right]\frac{\partial g_m}{\partial \xi} - \left[kf_k + lf_l\right]\frac{\partial G_m}{\partial \xi} + mg_m\left[\frac{\partial F_k}{\partial \xi} + \frac{\partial F_l}{\partial \xi}\right]\right.$$
$$\left. -mG_m\left[sgn(m-n)\frac{\partial f_k}{\partial \xi} + \frac{\partial f_l}{\partial \xi}\right]\right\}, \tag{2.2.6}$$

and

$$T_n = \sum_{m=1}^{N}\left\{\left[lf_l - kf_k\right]\frac{\partial g_m}{\partial \xi} - \left[(m-n)F_k - lF_l\right]\frac{\partial G_m}{\partial \xi} - mG_m\left[\frac{\partial F_k}{\partial \xi} - \frac{\partial F_l}{\partial \xi}\right]\right.$$
$$\left. - mg_m\left[sgn(m-n)\frac{\partial f_k}{\partial \xi} - \frac{\partial f_l}{\partial \xi}\right]\right\}. \tag{2.2.7}$$

for all integers $1 \le n \le N$ with $k = |m-n|$ and $l = m+n$. Here, f_0 and g_0 are identically zero. Equations (2.2.4) and (2.2.5) define two sets of $2N+1$ differential equations produced originally from (2.2.2) and (2.2.3), respectively. These two sets of equations will be solved simultaneously at each time step in order to determine ζ and ψ. The boundary conditions associated with equations (2.2.4) and (2.2.5) follow directly from (2.1.34)-(2.1.36) and (2.1.39). At the cylinder surface, when $\xi = 0$, the

equations must be solved subject to

$$F_0 = F_n = f_n = \frac{\partial F_n}{\partial \xi} = \frac{\partial f_n}{\partial \xi} = 0, \quad \frac{\partial F_0}{\partial \xi} = -2\Omega(t), \tag{2.2.8}$$

for all integers $1 \leq n \leq N$ and as $\xi \to \infty$

$$e^{-\xi} F_0,\ e^{-\xi}\frac{\partial F_0}{\partial \xi} \to 0, \quad e^{-\xi} F_n,\ e^{-\xi}\frac{\partial F_n}{\partial \xi} \to -V(t)\sin(\eta)\delta_{n,1}, \tag{2.2.9a}$$

$$e^{-\xi} f_n,\ e^{-\xi}\frac{\partial f_n}{\partial \xi} \to (1 + V(t)\cos(\eta))\delta_{n,1}, \tag{2.2.9b}$$

$$G_0,\ G_n,\ g_n \to 0, \tag{2.2.9c}$$

for all integers $1 \leq n \leq N$.

Integrating both sides of each of the equations (2.2.5) with respect to ξ from $\xi = 0$ to $\xi = \infty$, after multiplying both sides of equations (2.2.5b) and (2.2.5c) by $e^{-n\xi}$ $(n = 1, ..., N)$, gives the following integral conditions

$$\int_0^\infty e^{2\xi} G_0(\xi, t)d\xi = 2\pi\Omega(t), \tag{2.2.10a}$$

$$\int_0^\infty e^{(2-n)\xi} G_n(\xi, t)d\xi = -2\pi V(t)\sin(\eta)\delta_{1,n}, \tag{2.2.10b}$$

$$\int_0^\infty e^{(2-n)\xi} g_n(\xi, t)d\xi = 2\pi(V(t)\cos(\eta) + 1)\delta_{1,n}, \tag{2.2.10c}$$

for all integers $1 \leq n \leq N$.

Furthermore, an initial condition is necessary to obtain the numerical solutions of (2.2.4) and (2.2.5). Boundary-layer theory for impulsively started flows is used to provide this by introducing the boundary-layer coordinates (z, θ, t) and using the following transformation

$$\xi = kz, \quad \psi = k\Psi, \quad \zeta = \omega/k; \quad k = (8t/R)^{\frac{1}{2}}. \tag{2.2.11}$$

This transformation maps the initial flow onto the scale of the boundary-layer thickness, k, and has been used by several researchers, some of which include Collins and Dennis (1973a), Badr and Dennis (1985), and Dennis, Nguyen and Kocabiyik (2000).

The Fourier coefficients for w and Ψ are related to the Fourier coefficients for ζ and ψ as follows

$$F_0 = kF_0^*,\ F_n = kF_n^*,\ f_n = kf_n^*,\ G_0 = G_0^*/k,\ G_n = G_n^*/k,\ g_n = g_n^*/k, \qquad (2.2.12)$$

for all integers $1 \le n \le N$. Consequently, the corresponding equations for (2.2.4) and (2.2.5) in the boundary-layer coordinates are given by (suppressing all stars)

$$4t\frac{\partial G_0}{\partial t} = e^{-2kz}\frac{\partial^2 G_0}{\partial z^2} + 2z\frac{\partial G_0}{\partial z} + 2G_0 + te^{-2kz}\sum_{m=1}^{N} m\frac{\partial}{\partial z}\left(F_m g_m - f_m G_m\right), \qquad (2.2.13a)$$

$$4t\frac{\partial G_n}{\partial t} = e^{-2kz}\frac{\partial^2 G_n}{\partial z^2} + 2z\frac{\partial G_n}{\partial z} + (2 - n^2k^2e^{-2kz})G_n - 2te^{-2kz}(n\frac{\partial G_0}{\partial z}f_n - S_n), \qquad (2.2.13b)$$

$$4t\frac{\partial g_n}{\partial t} = e^{-2kz}\frac{\partial^2 g_n}{\partial z^2} + 2z\frac{\partial g_n}{\partial z} + (2 - n^2k^2e^{-2kz})g_n + 2te^{-2kz}(n\frac{\partial G_0}{\partial z}F_n + T_n), \qquad (2.2.13c)$$

and

$$\frac{\partial^2 F_0}{\partial z^2} = e^{2kz}G_0, \quad \frac{\partial^2 F_n}{\partial z^2} - n^2k^2F_n = e^{2kz}G_n \quad \frac{\partial^2 f_n}{\partial z^2} - n^2k^2 f_n = e^{2kz}g_n, \qquad (2.2.14a, b, c)$$

for all integers $1 \le n \le N$. Here S_n and T_n are the same as (2.2.6) and (2.2.7) with ξ replaced by z and all unstarred functions F_n, f_n, G_n, g_n replaced by starred functions F_n^*, f_n^*, G_n^*, g_n^*, respectively. The boundary conditions associated with equations (2.2.13) and (2.2.14) are

$$F_0 = F_n = f_n = \frac{\partial F_n}{\partial z} = \frac{\partial f_n}{\partial z} = 0,\ \frac{\partial F_0}{\partial z} = -2\Omega(t), \quad \text{when} \quad z = 0 \qquad (2.2.15)$$

and as $z \to \infty$

$$k\, e^{-kz} F_0,\ e^{-kz}\frac{\partial F_0}{\partial z} \to 0, \quad k\, e^{-kz} F_n,\ e^{-kz}\frac{\partial F_n}{\partial z} \to -V(t)\sin(\eta)\delta_{n,1}, \tag{2.2.16a}$$

$$k\, e^{-kz} f_n,\ e^{-kz}\frac{\partial f_n}{\partial z} \to (1+V(t)\cos(\eta))\delta_{n,1}, \tag{2.2.16b}$$

$$G_0,\ G_n,\ g_n \to 0, \tag{2.2.16c}$$

and

$$\int_0^\infty e^{2kz} G_0(z,t)d\xi = 2\pi\Omega(t), \tag{2.2.17a}$$

$$\int_0^\infty e^{(2-n)kz} G_n(z,t)dz = -2\pi V(t)\sin(\eta)\delta_{1,n}, \tag{2.2.17b}$$

$$\int_0^\infty e^{(2-n)kz} g_n(z,t)dz = 2\pi(V(t)\cos(\eta)+1)\delta_{1,n}, \tag{2.2.17c}$$

for all integers $1 \le n \le N$. Closely following the methodology of Collins and Dennis (1973a), and Badr and Dennis (1985), the initial solutions for F_0, F_n, f_n, G_0, G_n and g_n at $t = 0$ are obtained as follows

$$G_0(z,0) = \frac{2}{\sqrt{\pi}}\Omega(0)e^{-z^2}, \quad G_n(z,0) = -\frac{4}{\sqrt{\pi}}V(0)\sin(\eta)e^{-z^2}\delta_{n,1}, \tag{2.2.18a, b}$$

$$g_n(z,0) = \frac{4}{\sqrt{\pi}}(1+V(0)\cos(\eta))e^{-z^2}\delta_{n,1}; \tag{2.2.18c}$$

$$F_0(z,0) = -\Omega(0)[\frac{1-e^{-z^2}}{\sqrt{\pi}} + z(1-\mathrm{erf}(z))], \tag{2.2.18d}$$

$$F_n(z,0) = -2V(0)\sin(\eta)[z\,\mathrm{erf}(z) + \frac{1}{\sqrt{\pi}}(e^{-z^2}-1)]\delta_{n,1}, \tag{2.2.18e}$$

$$f_n(z,0) = 2(1+V(0)\cos(\eta))[z\,\mathrm{erf}(z) + \frac{1}{\sqrt{\pi}}(e^{-z^2}-1)]\delta_{n,1} \tag{2.2.18f}$$

for all integers $n \ge 1$. Here, $\Omega(0)$ and $V(0)$ are initial oscillatory velocities of the cylinder at $t = 0$. The use of initial solution (2.2.18) is essential for obtaining accurate results at small times.

It is noted that the equations (2.1.32) and (2.1.33), and the conditions (2.1.34), (2.1.36), (2.1.37) and (2.1.39) can be written for ω and Ψ in the boundary-layer coordinates as follows

$$\frac{\partial^2\omega}{\partial z^2} + 2\mathrm{e}^{2kz}\left(z\frac{\partial\omega}{\partial z} + \omega\right) = 4t\left(\mathrm{e}^{2kz}\frac{\partial\omega}{\partial t} + \frac{\partial\Psi}{\partial\theta}\frac{\partial\omega}{\partial z} - \frac{\partial\Psi}{\partial z}\frac{\partial\omega}{\partial\theta}\right) - k^2\frac{\partial^2\omega}{\partial\theta^2}, \tag{2.2.19}$$

$$\frac{\partial^2\Psi}{\partial z^2} + k^2\frac{\partial^2\Psi}{\partial\theta^2} = e^{2kz}\omega, \tag{2.2.20}$$

and

$$\Psi = 0, \qquad \frac{\partial\Psi}{\partial z} = -\Omega(t) \text{ when } z = 0, \tag{2.2.21}$$

$$\omega \to 0 \quad \text{as } z \to \infty, \tag{2.2.22}$$

$$\omega(z,\theta,t) = \omega(z,\theta+2\pi,t), \qquad \Psi(z,\theta,t) = \Psi(z,\theta+2\pi,t), \tag{2.2.23}$$

$$\int_0^\infty\int_0^{2\pi} e^{2kz}\omega(z,\theta,t)d\theta dz = 2\pi\Omega(t), \tag{2.2.24a}$$

$$\int_0^\infty\int_0^{2\pi} e^{(2-p)kz}\omega(z,\theta,t)\cos(p\theta)d\theta dz = -2\pi V(t)\sin(\eta)\delta_{p,1}, \tag{2.2.24b}$$

$$\int_0^\infty\int_0^{2\pi} e^{(2-p)kz}\omega(z,\theta,t)\sin(p\theta)d\theta dz = 2\pi(V(t)\cos(\eta)+1)\delta_{p,1}, \tag{2.2.24c}$$

for all integers $p \geq 1$. The initial expressions for ω and Ψ at $t = 0$ can be obtained from (2.2.19) and (2.2.20) and are given by

$$\omega(z,\theta,0) = \frac{2\,e^{-z^2}}{\sqrt{\pi}}\left(\Omega(0) - 2\,V(0)\sin(\eta)\cos(\theta) + 2\left(V(0)\cos(\eta)+1\right)\sin(\theta)\right), \tag{2.2.25}$$

$$\begin{aligned}\Psi(z,\theta,0) &= \left[2\,V(0)\sin(\eta)\cos(\theta) - 2\left(V(0)\cos(\eta)+1\right)\sin(\theta) - \Omega(0)\right] \\ &\quad\times\left[\frac{1-e^{-z^2}}{\sqrt{\pi}} - z\,\mathrm{erf}(z)\right] - z\,\Omega(0).\end{aligned} \tag{2.2.26}$$

The mathematical derivations of these expressions and their forms in terms of Fourier components (F_0, F_n, f_n, G_0, G_n and g_n) are given in Appendix A.1.

2.3 Pressure distribution over the cylinder surface

The dimensionless pressure distribution over the cylinder surface is defined as

$$\tilde{p_0}(\theta) = \frac{p_0^*(\theta,t) - p_0^*(0,t)}{\rho U^2/2} = p_0(\theta,t) - p_0(0,t),$$

where p_0 represents the dimensionless pressure at $\xi = 0$.

Applying the θ-momentum equation given in (2.1.31) on the cylinder surface and using the boundary conditions $\psi = 0$, $\partial\psi/\partial\xi = -\Omega(t)$ when $\xi = 0$, we obtain

$$\left.\frac{\partial p}{\partial\theta}\right|_{\xi=0} = -\frac{4}{R}\left.\frac{\partial\zeta}{\partial\xi}\right|_{\xi=0} + 2\left[\dot{V}(t)\sin(\eta)\cos(\theta) - \dot{V}(t)\cos(\eta)\sin(\theta) - \dot{\Omega}(t)\right]. \quad (2.3.1)$$

Integrating (2.3.1) with respect to θ from $\theta = 0$ to an arbitrary angle θ gives

$$\tilde{p_0}(\theta) = \frac{-4}{R}\int_0^\theta \left.\left(\frac{\partial\zeta}{\partial\xi}\right)\right|_{\xi=0} d\theta + 2[\dot{V}(t)\sin(\theta) + \dot{V}(t)\cos(\eta)(\cos(\theta)-1) - \dot{\Omega}(t)\theta]. \quad (2.3.2)$$

Substituting the Fourier expansion (2.2.1a) for ζ and 2π for θ in (2.3.2) we see that the periodicity of the surface pressure requires that

$$\frac{2}{R}\frac{\partial G_0}{\partial\xi}(0,t) + 2\dot{\Omega}(t) = 0, \quad (2.3.3)$$

which may be written as

$$\frac{\partial G_0}{\partial\xi}(0,t) = -R\dot{\Omega}(t). \quad (2.3.4)$$

Alternatively, following the methodology of Badr and Dennis (1985) it can be shown that the condition (2.3.4) is implicitly satisfied by the satisfaction of the integral condition (2.2.10a) correctly in the numerical solution procedure. To see this we integrate equation (2.2.4a), with respect to ξ from $\xi = 0$ to $\xi = \xi_\infty$

$$\frac{\partial}{\partial t}\left[\int_o^{\xi_\infty} e^{2\xi} G_0\, d\xi\right] = \frac{2}{R}\left(\left.\frac{\partial G_0}{\partial\xi}\right|_{\xi=\xi_\infty} - \left.\frac{\partial G_0}{\partial\xi}\right|_{\xi=0}\right) + \sum_{m=1}^{N} m\left(F_m g_m - f_m G_m\right)\Big|_{\xi=0}^{\xi=\xi_\infty}, \quad (2.3.5)$$

where ξ_∞ is the value of ξ at which the conditions $g_n(\xi_\infty, t) = g_n(\xi_\infty, t) = 0$ are assumed. Thus, (2.2.10a) is established for any value of t by replacing the upper limit by ξ_∞ at any t provided that the value of the outer boundary ξ_∞ is chosen so that the vorticity, by the mechanism of convection, does not reach the outer boundary. Thus (2.3.5) reduces to (2.3.4) and hence the correct satisfaction of (2.2.10a) is the required condition to ensure that the pressure in the fluid is periodic with period 2π in θ.

The periodicity result of the pressure on the surface of the cylinder can be extended to all the flow domain points since the pressure at any point in the flow domain can be obtained from the surface pressure. This can be done by integrating the momentum equation (2.1.30) in the radial direction with respect to ξ from $\xi = 0$ to ξ and then using the fact that ψ, ζ and the surface pressure are all periodic functions in θ with period 2π. Thus, all the periodicity conditions of the problem are satisfied. In this sense we consider the satisfaction of (2.2.10) as a very important part of the solution procedure. The condition (2.2.10a) must be satisfied to ensure that the periodicity conditions are satisfied. The conditions (2.2.10b,c) ensure that the free stream is approached far from the cylinder just as the satisfaction of (2.2.10c) when $V(t) = 0$ gave this assurance in the uniform translation case without oscillation (i.e. $V(t) = \Omega(t) = 0$: Collins and Dennis (1973a,b)). Lastly, Dennis and Kocabiyik (1990) have shown that imposing (2.2.9) is inadequate, rather what must be enforced is that the vorticity decays rapidly enough. This can be achieved by examining the asymptotic solution for ζ.

It is noted that a numerical solution to the Navier-Stokes equations (vorticity/stream

function formulation) was reported by Lugt and Haussling (1974), who studied the problem of flow development for abruptly accelerated elliptic cylinder at 45° incidence for the Reynolds number values in the range 15 to 200. Comparisons between the obtained location of the first vortex and the flow visualization results reported by Honji (1972) show good agreement. However, the surface pressure distribution reported in Lugt and Haussling's paper shows some discrepancies since the pressure periodicity is not fully satisfied ($\tilde{p_0}(0) \neq \tilde{p_0}(2\pi)$). The same problem was also reported by Pannikker and Lavan (1975).

2.4 The drag, lift and moment coefficients

The main forces exerted on the cylinder surface are represented by the drag, lift and moment coefficients, defined as

$$C_D = \frac{D}{\rho U^2 a}, \qquad C_L = \frac{L}{\rho U^2 a}, \qquad C_M = \frac{M}{4\pi\mu a^2 f_\theta^*}, \tag{2.4.1}$$

where D, L and M are the drag, lift and moment forces exerted on a unit length of the cylinder respectively. Drag and lift forces consist of components due to the frictional forces and the pressure where the dimensionless viscous and pressure drag coefficients, C_{DF} and C_{DP}, are given by

$$C_{DF} = \frac{2}{R}\int_0^{2\pi} \zeta|_{\xi=0} \sin(\theta) d\theta, \tag{2.4.2}$$

$$C_{DP} = \frac{-2}{R}\int_0^{2\pi} \left.\frac{\partial\zeta}{\partial\xi}\right|_{\xi=0} \sin\theta d\theta - \pi\dot{V}(t)\cos(\eta), \tag{2.4.3}$$

respectively, and the dimensionless viscous and pressure lift coefficients, C_{LF} and C_{LP}, are given by

$$C_{LF} = -\frac{2}{R}\int_0^{2\pi} \zeta|_{\xi=0} \cos(\theta) d\theta \tag{2.4.4}$$

$$C_{LP} = \frac{2}{R}\int_0^{2\pi} \left.\frac{\partial \zeta}{\partial \xi}\right|_{\xi=0} \cos(\theta) d\theta - \pi \dot{V}(t)\sin(\eta), \tag{2.4.5}$$

respectively. The mathematical derivation of the these formulas is given in Appendix A.2. Consequently, the lift and drag coefficients are given by

$$C_D = C_{DP} + C_{DF}, \qquad C_L = C_{LP} + C_{LF}. \tag{2.4.6}$$

Thus, the total drag and lift coefficients can be rewritten in terms of the Fourier coefficients as

$$C_D = \frac{2\,\pi}{R}\left(g_1(0,t) - \frac{\partial g_1}{\partial \xi}(0,t)\right) - \pi \dot{V}(t)\cos(\eta), \tag{2.4.7}$$

$$C_L = -\frac{2\,\pi}{R}\left(G_1(0,t) - \frac{\partial G_1}{\partial \xi}(0,t)\right) - \pi \dot{V}(t)\sin(\eta). \tag{2.4.8}$$

Here C_{DF}, C_{DP}, C_{LF} and C_{LP} are defined by

$$C_{DF} = \frac{2\,\pi}{R}\, g_1(0,t), \tag{2.4.9}$$

$$C_{DP} = -\frac{2\,\pi}{R}\,\frac{\partial g_1}{\partial \xi}(0,t) - \pi \dot{V}(t)\cos(\eta), \tag{2.4.10}$$

$$C_{LF} = -\frac{2\,\pi}{R}\, G_1(0,t), \tag{2.4.11}$$

$$C_{LP} = \frac{2\,\pi}{R}\,\frac{\partial G_1}{\partial \xi}(0,t) - \pi \dot{V}(t)\sin(\eta). \tag{2.4.12}$$

The time-averaged drag coefficient is calculated by

$$\overline{C_D} = \frac{1}{n\,T}\int_{t_0}^{t_0+n\,T} C_D\, dt, \tag{2.4.13}$$

where T is the oscillation period defined by

$$T = 1/f \tag{2.4.14}$$

and n is the number of periods taking into account. Thus the time period between t_0 and $t_0 + nT$ is taken after reaching the quasi-steady state and covering more than one cycle of cylinder oscillation.

The mathematical derivation of the formula for the moment coefficient,

$$C_M = -\frac{1}{4\pi f_\theta}\int_0^{2\pi} \zeta|_{\xi=0} d\theta - \frac{\Omega(t)}{f_\theta}, \tag{2.4.15}$$

is given in Appendix A.2 which can be rewritten in terms of the Fourier coefficients as

$$C_M = -\frac{1}{4f_\theta} G_0(0,t) - \frac{\Omega(t)}{f_\theta}. \tag{2.4.16}$$

Chapter 3

Determination of the initial flow

As we mentioned earlier one of the basic difficulties in the direct use of numerical methods is the specification of the initial conditions corresponding to the impulsive start. In fact the most troublesome flow to calculate is the initial flow because of the rapid diffusion of vorticity into the flow field throughout the initial stages of the motion. In this chapter solutions for ψ and ζ in the form of time series, valid for small times after the impulsive start, are obtained for both the boundary-layer case and for finite Reynolds numbers using an exact analysis. The essential point here is that the small time series expansions can be used to check the accuracy of the numerical results at small times. These analytical solutions could be used to start the numerical integration procedure without the necessity of taking a large number of time steps near $t = 0$.

3.1 Explicit expansions for the scaled stream function and vorticity

The initial flow is governed by the usual boundary-layer theory in which a layer of thickness $(t/R)^{1/2}$ surrounds the cylinder following the sudden start. We therefore

use the initial solutions (2.2.25) and (2.2.26) for $\omega(z,\theta,0)$ and $\Psi(z,\theta,0)$ are obtained based on boundary layer theory, using (2.2.11), to build up a perturbation solution in powers of t following the methodology of Collins and Dennis (1973a). The expressions for the scaled stream function Ψ and ω can be made in powers of both k and t as follows

$$\omega(z,\theta,t)=\sum_{n=0}^{\infty}\sum_{m=0}^{\infty}\omega_{n,m}(z,\theta)t^m k^n, \qquad \Psi(z,\theta,t)=\sum_{n=0}^{\infty}\sum_{m=0}^{\infty}\Psi_{n,m}(z,\theta)t^m k^n. \quad (3.1.1)$$

If we substitute expressions (3.1.1) into the equations (2.2.19) and (2.2.20) and then equate the coefficients of the successive powers of k and t to zero we obtain equations for both $\omega_{n,m}$ and $\Psi_{n,m}$

$$\frac{\partial^2\omega_{n,m}}{\partial z^2}+2z\frac{\partial\omega_{n,m}}{\partial z}-[4m+2(n-1)]\omega_{n,m}=\mathrm{R}_{n,m}(z,\theta), \quad (3.1.2)$$

$$\frac{\partial^2\Psi_{n,m}}{\partial z^2}=-\frac{\partial^2\Psi_{n-2,m}}{\partial\theta^2}+\sum_{q=0}^{n}\frac{(2z)^{n-q}}{(n-q)!}\omega_{q,m}, \quad (3.1.3)$$

where

$$\mathrm{R}_{n,m}(z,\theta)=-\frac{\partial^2\omega_{n-2,m}}{\partial\theta^2} -2\sum_{q=0}^{n-1}\left[\frac{(2z)^{n-q}}{(n-q)!}\left\{z\frac{\partial\omega_{q,m}}{\partial z}-(2m+q-1)\omega_{q,m}\right\}\right] +\sum_{q=0}^{n}\left[4\sum_{j=0}^{m-1}\left\{\frac{\partial\Psi_{q,j}}{\partial\theta}\frac{\partial\omega_{n-q,m-j-1}}{\partial z}-\frac{\partial\Psi_{q,j}}{\partial z}\frac{\partial\omega_{n-q,m-j-1}}{\partial\theta}\right\}\right]. \quad (3.1.4)$$

In these equations the functions with a negative subscript are taken to be identically zero. The associated boundary and integral conditions on $\Psi_{n,m}$ and $\omega_{n,m}$ are deduced from (2.2.21)-(2.2.24), by replacing exponential term by its power series and using the expansions in (3.1.1) and the small time series expansions for oscillatory velocities

$$V(t)=\sum_{m=0}^{\infty}\sigma_m t^m, \qquad \Omega(t)=\sum_{m=0}^{\infty}\alpha_m t^m \quad (3.1.5)$$

where $\alpha_m, \sigma_m \in \mathbb{R}$. They are given by

$$\Psi_{n,m} = 0, \quad \frac{\partial \Psi_{n,m}}{\partial z} = -\alpha_m \delta_{n,0} \text{ when } z = 0, \tag{3.1.6}$$

$$\omega_{n,m} \to 0 \text{ when } z \to \infty, \tag{3.1.7}$$

$$\int_0^\infty \int_0^{2\pi} \left[\sum_{q=0}^{n} \frac{(2z)^{n-q}}{(n-q)!} \omega_{q,m} \right] d\theta dz = 2\pi \alpha_m \delta_{n,0}, \tag{3.1.8a}$$

$$\int_0^\infty \int_0^{2\pi} \left[\sum_{q=0}^{n} \frac{((2-l)z)^{n-q}}{(n-q)!} \omega_{q,m} \right] \cos(l\theta) d\theta dz = -2\pi \sin(\eta) \sigma_m \delta_{l,1} \delta_{n,0}, \tag{3.1.8b}$$

$$\int_0^\infty \int_0^{2\pi} \left[\sum_{q=0}^{n} \frac{((2-l)z)^{n-q}}{(n-q)!} \omega_{q,m} \right] \sin(l\theta) d\theta dz = 2\pi \left[\cos(\eta) \sigma_m + \delta_{m,0} \right] \delta_{l,1} \delta_{n,0}. \tag{3.1.8c}$$

We note that equations (3.1.2) and (3.1.3) are those considered by Collins and Dennis (1973a) in the case of the sudden translation of a circular cylinder without oscillations. In the present case oscillation of the cylinder enters through the coefficients σ_m and α_m in the small time series expansions (3.1.5) for oscillatory velocities $V(t)$ and $\Omega(t)$ and they appear in the boundary and integral conditions (3.1.6)-(3.1.8)

3.2 Reduction of the scaled stream function/vorticity equations to component form

The periodicity of Ψ and ω in θ with period 2π given in condition (2.1.37) implies periodicity of the functions $\Psi_{n,m}$ and $\omega_{n,m}$ appearing in the coefficient of $t^m k^n$ in the series (3.1.1). Thus, $\omega_{n,m}$ and $\Psi_{n,m}$ can be decomposed into a finite set of Fourier

cosine and sine components in the coordinate θ such that

$$\omega_{n,m}(z,\theta) = \sum_{p=0}^{m+1} \left[G^p_{n,m}(z)\cos(p\theta) + g^p_{n,m}(z)\sin(p\theta) \right], \tag{3.2.1}$$

$$\Psi_{n,m}(z,\theta) = \sum_{p=0}^{m+1} \left[F^p_{n,m}(z)\cos(p\theta) + f^p_{n,m}(z)\sin(p\theta) \right]. \tag{3.2.2}$$

The equations and conditions for which the Fourier cosine and sine components, $G^p_{n,m}(z)$, $F^p_{n,m}(z)$ and $g^p_{n,m}(z)$, $f^p_{n,m}(z)$, can be obtained by substituting (3.2.1) and (3.2.2) in (3.1.2)-(3.1.8) and using standard orthogonality conditions. Rotational oscillation of the cylinder appear only in the terms (when $p = 0$) in these expansions. The solutions for each $\omega_{n,m}$ and $\Psi_{n,m}$ can be determined by solving $4\,m + 6$ ordinary differential equations for $G^p_{n,m}(z)$, $F^p_{n,m}(z)$ and $g^p_{n,m}(z)$, $f^p_{n,m}(z)$. These components satisfy a typical set of ordinary differential equations of the form

$$\frac{d^2\mathcal{Y}^p_{n,m}}{dz^2} + 2z\frac{d\mathcal{Y}^p_{n,m}}{dz} - [2n + 4m - 2]\mathcal{Y}^p_{n,m} = \overline{\mathcal{R}}^p_{n,m}, \tag{3.2.3}$$

$$\frac{d^2\mathcal{X}^p_{n,m}}{dz^2} = p^2\,\mathcal{X}^p_{n-2,m} + \sum_{s=0}^{n} \frac{(2z)^{n-s}}{(n-s)!}\mathcal{Y}^s_{n,m} \tag{3.2.4}$$

where the functions $\mathcal{Y}^p_{n,m}$ and $\mathcal{X}^p_{n,m}$ represent either $G^p_{n,m}$ and $F^p_{n,m}$ or $g^p_{n,m}$ and $f^p_{n,m}$. Here $\overline{\mathcal{R}}^p_{n,m}$ represents Fourier sine and cosine components, $\mathrm{RC}^p_{n,m}$ and $\mathrm{RS}^p_{n,m}$, in the Fourier series expansion for $\mathrm{R}_{n,m}$ defined in terms of equation (3.1.4)

$$\mathrm{R}_{n,m}(z,\theta) = \mathrm{RC}^0_{n,m}(z) + \sum_{p=1}^{m+1} \left[\mathrm{RC}^p_{n,m}(z)\cos(p\,\theta) + \mathrm{RS}^p_{n,m}(z)\sin(p\,\theta) \right] \tag{3.2.5}$$

and are given by

$$\begin{aligned} \mathrm{RC}^0_{n,m} &= -2\sum_{q=0}^{n-1}\left[\frac{(2z)^{n-q}}{(n-q)!}\left\{z\frac{dG^0_{q,m}}{dz}-(2m+q-1)G^0_{q,m}\right\}\right]+\sum_{q=0}^{n}\sum_{j=0}^{m-1}\sum_{s=1}^{m_1}2s \\ &\times \left[F^s_{q,j}\frac{dg^s_v}{dz}-G^s_{q,j}\frac{df^s_v}{dz}-f^s_{q,j}\frac{dG^s_v}{dz}+g^s_{q,j}\frac{dF^s_v}{dz}\right], \end{aligned} \tag{3.2.6a}$$

$$\mathrm{RC}^p_{n,m} = p^2\, g^p_{n-2,m} - 2\sum_{q=0}^{n-1}\left[\frac{(2z)^{n-q}}{(n-q)!}\left\{z\frac{dg^p_{q,m}}{dz}-(2m+q-1)g^p_{q,m}\right\}\right]+\mathcal{A}1^p_{n,m}+\mathcal{A}2^p_{n,m} \tag{3.2.6b}$$

and

$$\mathrm{RS}^p_{n,m} = p^2\, G^p_{n-2,m} - 2\sum_{q=0}^{n-1}\left[\frac{(2z)^{n-q}}{(n-q)!}\left\{z\frac{dG^p_{q,m}}{dz}-(2m+q-1)G^p_{q,m}\right\}\right]+\mathcal{B}1^p_{n,m}+\mathcal{B}2^p_{n,m} \tag{3.2.6c}$$

where $\mathcal{A}1^p_{n,m}$, $\mathcal{A}2^p_{n,m}$, $\mathcal{B}1^p_{n,m}$ and $\mathcal{B}2^p_{n,m}$ are defined by

$$\mathcal{A}1^p_{n,m} = \begin{cases} 4\,p\displaystyle\sum_{j=p-1}^{m-1}\sum_{q=0}^{n}\left[F^p_{q,j}\frac{dG^0_v}{dz}-G^p_{q,j}\frac{dF^0_v}{dz}\right] & \text{if} \quad 1\le p\le m \\ 0 & \text{elsewhere} \end{cases} \tag{3.2.7a}$$

$$\mathcal{A}2^p_{n,m} = \begin{cases} \left\{\displaystyle\sum_{j=p}^{m-1}\sum_{s=M_1}^{m_2}2\,s\sum_{q=0}^{n}\left[F^s_{q,j}\frac{dg^{s-p}_v}{dz}-G^s_{q,j}\frac{df^{s-p}_v}{dz}-f^s_{q,j}\frac{dG^{s-p}_v}{dz}\right.\right. \\ \left.\left.+\,g^s_{q,j}\frac{df^{s-p}_v}{dz}\right]\right\}-\left\{\displaystyle\sum_{j=0}^{m-p-1}\sum_{s=1}^{m_3}2\,s\sum_{q=0}^{n}\left[F^s_{q,j}\frac{dg^{s+p}_v}{dz}\right.\right. \\ \left.\left.-G^s_{q,j}\frac{df^{s+p}_v}{dz}-f^s_{q,j}\frac{dG^{s+p}_v}{dz}+g^s_{q,j}\frac{dF^{s+p}_v}{dz}\right]\right\}+\left\{\displaystyle\sum_{j=0}^{m-1}\right. \\ \displaystyle\sum_{s=M_3}^{m_4}2\,s\sum_{q=0}^{n}\left[F^s_{q,j}\frac{dg^{p-s}_v}{dz}-G^s_{q,j}\frac{df^{p-s}_v}{dz}-g^s_{q,j}\frac{dF^{p-s}_v}{dz}\right. \\ \left.\left.+f^s_{q,j}\frac{dG^{p-s}_v}{dz}\right]\right\} & \text{if} \quad 2\le p\le m+1 \\ 0 & \text{elsewhere} \end{cases} \tag{3.2.7c}$$

$$\mathcal{B}1^{p}_{n,m} = \begin{cases} 4\,p \displaystyle\sum_{j=p-1}^{m-1} \sum_{q=0}^{n} \left[g^{p}_{q,j} \frac{dF^{0}_{v}}{dz} - f^{p}_{q,j} \frac{dG^{0}_{v}}{dz} \right] & \text{if } 1 \le p \le m \\ 0 & \text{elsewhere} \end{cases} \tag{3.2.7b}$$

and

$$\mathcal{B}2^{p}_{n,m} = \begin{cases} \left\{ \displaystyle\sum_{j=p}^{m-1} \sum_{s=M_1}^{m_2} 2\,s \sum_{q=0}^{n} \left[g^{s}_{q,j} \frac{df^{s-p}_{v}}{dz} - f^{s}_{q,j} \frac{dg^{s-p}_{v}}{dz} - F^{s}_{q,j} \frac{dG^{s-p}_{v}}{dz} \right.\right. \\ \left. + G^{s}_{q,j} \frac{dF^{v}_{s-p}}{dz} \right] \Bigg\} - \left\{ \displaystyle\sum_{j=0}^{m-p-1} \sum_{s=1}^{m_3} 2\,s \sum_{q=0}^{n} \left[g^{s}_{q,j} \frac{df^{s+p}_{v}}{dz} \right.\right. \\ \left. - f^{s}_{q,j} \frac{dg^{s+p}_{v}}{dz} - F^{s}_{q,j} \frac{dG^{s+p}_{v}}{dz} + G^{s}_{q,j} \frac{dF^{s+p}_{v}}{dz} \right] \Bigg\} + \left\{ \displaystyle\sum_{j=0}^{m-1} \right. \\ \displaystyle\sum_{s=M_3}^{m_4} 2\,s \sum_{q=0}^{n} \left[g^{s}_{q,j} \frac{df^{p-s}_{v}}{dz} - f^{s}_{q,j} \frac{dg^{p-s}_{v}}{dz} + F^{s}_{q,j} \frac{dG^{p-s}_{v}}{dz} \right. \\ \left. \left. - G^{s}_{q,j} \frac{dF^{p-s}_{v}}{dz} \right] \right\} \\ 0 \end{cases} \quad \begin{array}{l} \text{if} \quad 2 \le p \le m+1 \\ \\ \\ \\ \\ \\ \\ \text{elsewhere} \end{array} \tag{3.2.7d}$$

Here $m_1 = \min(j+1, m-j)$, $m_2 = \min(j+1, m-j+p)$, $m_3 = \min(j+1, m-j-p)$, $m_4 = \min(j+1, p-1)$, $v = n-q, m-j-1$, $M_1 = \max(1, p+1)$, $M_3 = \max(1, p+j-m)$. It is noted that a special care must be exercised in determining the exact expressions (3.2.6) for the functional coefficients, $\mathrm{RC}^{0}_{n,m}$, $\mathrm{RC}^{p}_{n,m}$, $\mathrm{RS}^{p}_{n,m}$, of periodic terms in (3.1.4). This is due to the nonlinear term

$$\sum_{j=0}^{m-1} \left\{ \frac{\partial \Psi_{q,j}}{\partial \theta} \frac{\partial \omega_{n-q,m-j-1}}{\partial z} - \frac{\partial \Psi_{q,j}}{\partial z} \frac{\partial \omega_{n-q,m-j-1}}{\partial \theta} \right\},$$

in the expression (3.1.4) for $\mathrm{R}_{n,m}(z,\theta)$. To do this we use an analysis similar to convolution analysis [see for example Vretblad (2003)]. The details are not given

because they are complicated and require use of formulas given in Appendix B.1. The boundary conditions utilized in conjunction with (3.2.3) and (3.2.4) are the transformed conditions (3.1.6)-(3.1.8) after (3.2.1) and (3.2.2) have been applied. This gives

$$\mathcal{X}^p_{n,m}(0) = 0, \qquad \frac{d\mathcal{X}^p_{n,m}}{dz}(0) = \begin{cases} -\alpha_m\, \delta_{n,0}\, \delta_{p,0}, & \text{if} \quad \mathcal{X}^p_{n,m} = F^p_{n,m} \\ 0 & \text{if} \quad \mathcal{X}^p_{n,m} = f^p_{n,m} \end{cases} \tag{3.2.8}$$

$$\mathcal{Y}^p_{n,m} \to 0 \text{ as } z \to 0, \tag{3.2.9}$$

$$\int_0^\infty \mathcal{Y}^p_{n,m}\, dz = \begin{cases} -2\sin(\eta)\sigma_m\delta_{p,1}\delta_{n,0} + 2\alpha_m\delta_{p,0}\delta_{n,0} - a_1 & \text{if} \quad \mathcal{Y}^p_{n,m} = G^p_{n,m} \\ 2\left[\cos(\eta)\sigma_m + \delta_{m,0}\right]\delta_{p,1}\delta_{n,0} - a_1 & \text{if} \quad \mathcal{Y}^p_{n,m} = g^p_{n,m} \end{cases} \tag{3.2.10}$$

where

$$a_1 = \begin{cases} \displaystyle\int_0^\infty \sum_{s=0}^{n-1} \frac{((2-p)z)^{n-s}}{(n-s)!} G^p_{s,m}(z)dz & \text{if} \quad \mathcal{Y}^p_{n,m} = G^p_{n,m} \\ \displaystyle\int_0^\infty \sum_{s=0}^{n-1} \frac{((2-p)z)^{n-s}}{(n-s)!} g^p_{s,m}(z)dz & \text{if} \quad \mathcal{Y}^p_{n,m} = g^p_{n,m}. \end{cases}$$

The procedure is to solve equations (3.2.3) and (3.2.4) successively subject to the boundary and integral conditions (3.2.8)-(3.2.10). The method of solution and some analytical results will be given in subsequent sections.

3.3 Exact solution of the governing equations in their component form

A solution of (3.2.3) which satisfies (3.2.9) and (3.2.10) is found by combining a particular solution of the full equation with a solution of homogenous equation obtained

by putting $\overline{\mathcal{R}}^p_{n,m} = 0$ in (3.2.3). The homogeneous solution of equation (3.2.3) is obtained using $\mathcal{Y}^p_{n,m}(z) = e^{-1/2z}Y_h(z)$ to transform the homogenous form of (3.2.3) to

$$\frac{d^2Y_h}{dZ^2} - (\frac{Z^2}{4} + a)Y_h = 0 \tag{3.3.1}$$

where $Z = \sqrt{\pi}\, z$, $a = 2m + n - \frac{1}{2}$. This is the well-known differential equation [see Abramowitz and Stegun (1972), p. 687] whose solutions are the parabolic cylinder functions, $U(a, Z)$ and $V(a, Z)$, defined by

$$\begin{aligned} U(a,Z) &= D_{-a-\frac{1}{2}}(Z), \\ V(a,Z) &= \frac{1}{\pi}\Gamma\left(\frac{1}{2}+a\right)\left\{\sin(a\pi)D_{-a-\frac{1}{2}}(Z) + D_{-a-\frac{1}{2}}(-Z)\right\}, \end{aligned}$$

where

$$D_{-a-\frac{1}{2}}(Z) = \sqrt{\frac{\pi}{2}}\frac{(-1)^{a-\frac{1}{2}}}{(a-\frac{1}{2})!}e^{-Z^2/4}\frac{d^{a-\frac{1}{2}}}{dZ^{a-\frac{1}{2}}}\left[e^{Z^2/2}\mathrm{erfc}(\frac{Z}{\sqrt{2}})\right].$$

Here erfc is the complementary error function defined by

$$\mathrm{erfc}(z) = \frac{2}{\pi}\int_z^\infty e^{-s^2}ds.$$

Thus

$$Y_h(z) = C_1\, U(a, Z) + C_2\, V(a, Z). \tag{3.3.2}$$

Particular solution of the full equation (3.2.3) is determined by using the method of variation of parameters. These equations (3.2.3) can now be solved explicitly by repeating the process $2m + 1$ times until all the Fourier components, $G^p_{n,m}$ and $g^p_{n,m}$, of $\omega_{n,m}$, are completely determined. The solution for corresponding stream function components, $\Psi_{n,m}$, is found by simply integrating equation (3.1.3) twice with respect to z and then applying (3.1.6).

It is found in practice that the right-hand side of equation (3.1.2) becomes increasingly more complicated with the increase of either n or m.

3.3.1 The boundary-layer expansion

The boundary-layer expansion is obtained by considering the case of $n = 0$ in (3.1.1). This gives an expansion in powers of time for ω_0 and Ψ_0 when $k = 0$ of the form

$$\Psi_0(z, \theta, t) = \sum_{m=0}^{\infty} \Psi_{0,m}(z, \theta) t^m, \tag{3.3.3}$$

$$\omega_0(, \theta, t) = \sum_{m=0}^{\infty} \omega_{0,m}(z, \theta) t^m \tag{3.3.4}$$

where the solutions for both $\Psi_{0,m}$ and $\omega_{0,m}$, according to (3.1.2)-(3.1.4) and (3.1.6)-(3.1.8), can be determined by solving the following equations

$$\frac{\partial^2 \Psi_{0,m}}{\partial z^2} = \omega_{0,m}, \tag{3.3.5}$$

$$\frac{\partial^2 \omega_{0,m}}{\partial z^2} + 2z \frac{\partial \omega_{0,m}}{\partial z} - (4m - 2)\omega_{0,m} = \mathrm{R}_{0,m}(z, \theta) \tag{3.3.6}$$

where

$$\mathrm{R}_{0,m}(z, \theta) = 4 \sum_{j=0}^{m-1} \left[\frac{\partial \Psi_{0,j}}{\partial \theta} \frac{\partial \omega_{0,m-j-1}}{\partial z} - \frac{\partial \Psi_{0,j}}{\partial z} \frac{\partial \omega_{0,m-j-1}}{\partial \theta} \right] \tag{3.3.7}$$

subject to

$$\Psi_{0,m} = 0, \quad \frac{\partial \Psi_{0,m}}{\partial z} = -\alpha_m, \text{ when } \quad z = 0, \tag{3.3.8}$$

$$\int_0^{\infty} \int_0^{2\pi} \omega_{0,m} d\theta dz = 2\pi \alpha_m, \tag{3.3.9a}$$

$$\int_0^{\infty} \int_0^{2\pi} \omega_{0,m} \cos(p\theta) d\theta dz = -2\pi \sin(a_0) \sigma_m \delta_{p,1} \quad (p = 1, \cdots, m+1), \tag{3.3.9b}$$

$$\int_0^{\infty} \int_0^{2\pi} \omega_{0,m} \sin(p\theta) d\theta dz = 2\pi \left[\cos(a_0) \sigma_m + \delta_{m,0} \right] \delta_{p,1} \quad (p = 1, \cdots, m+1), \tag{3.3.9c}$$

$$\omega_{0,m} \to 0 \text{ when } z \to \infty. \tag{3.3.10}$$

The non-homogenous term $R_{0,m}(z,\theta)$ in equation (3.3.7) for $m = 0$ is identically zero. It can be shown that $\omega_{0,0}$ can be represented in terms of Fourier components as follows

$$\omega_{0,0}(z,\theta) \;=\; G^0_{0,0}(z) + G^1_{0,0}(z)\cos(\theta) + g^1_{0,0}(z)(\sin\theta), \tag{3.3.11}$$

using (3.2.1). The exact solutions for $G^0_{0,0}, G^1_{0,0}$ and $g^1_{0,0}$ are determined by solving (B.2.1), (B.2.2) and (B.2.3) subject to (B.2.1a), (B.2.2a) and (B.2.3a), respectively, given in Appendix B.2. The solution for $\omega_{0,0}$ is presented in Appendix A.1 and found to be

$$\omega_{0,0}(z,\theta) = 2\,\frac{e^{-z^2}\,(\alpha_0 - 2\,A_0\cos(\theta) + 2\,B_0\sin(\theta))}{\sqrt{\pi}} \tag{3.3.12}$$

where

$$A_0 = \sin(a_0)\sigma_0, \qquad B_0 = (1 + \cos(a_0)\sigma_0), \tag{3.3.13}$$

and $\mathrm{erf}(z)$ is the error function defined by

$$\mathrm{erf}(z) \;=\; \frac{2}{\sqrt{\pi}}\int_0^z e^{-s^2}ds.$$

The corresponding solution for $\Psi_{0,0}$ is determined by integrating (3.3.5) twice subject to the boundary conditions (3.3.8) when $m = 0$. It is found that

$$\Psi_{0,0}(z,\theta) = [2\,A_0\cos(\theta) - 2\,B_0\sin(\theta) - \alpha_0]\left(\frac{1-e^{-z^2}}{\sqrt{\pi}} - z\,\mathrm{erf}(z)\right) - z\,\alpha_0. \tag{3.3.14}$$

As previously noted, $\omega_{0,0}$ and $\Psi_{0,0}$ represent the initial expressions for ω and Ψ at $t = 0$ and form the starting point of numerical solution of (2.2.19) and (2.2.20). We note that these initial expressions for $\omega_{0,0}$ and $\Psi_{0,0}$ are identical to the ones, (2.2.25) and (2.2.26), that were given in the previous chapter when $V(0) = \sigma_0$ and $\Omega(0) = \alpha_0$.

The non-homogenous term $R_{0,m}(z,\theta)$ in equation (3.3.7) for $m = 1$ is given by

$$
\begin{aligned}
R_{0,1}(z,\,\theta) \;=\;& 16(B_0\cos(\theta)+\sin(\theta)\,A_0)\alpha_0\,\{[(\operatorname{erfc}(z)-2\,z^2\operatorname{erf}(z))\pi^{-\frac{1}{2}}+2\,z\pi^{-1}]\,e^{-z^2}\\
-\;& 2e^{-2\,z^2}z\pi^{-1}\}+16[-2A_0B_0\cos(2\,\theta)+({B_0}^2-{A_0}^2)\sin(2\theta)]\{[-(1+2z^2)\\
\times\;& \operatorname{erf}(z)\pi^{-\frac{1}{2}}+2\,z\pi^{-1}]\,e^{-z^2}-2\,e^{-2\,z^2}\,z\pi^{-1}\}
\end{aligned}
$$

and the form of the second term, $\omega_{0,1}(z,\theta)$, in the boundary-layer expansion, in terms of Fourier components are obtained from (3.2.1) when $n=0$ and $m=1$. It is found that

$$
\begin{aligned}
\omega_{0,1}(z,\theta) = G^0_{0,1}(z) + G^1_{0,1}(z)\cos(\theta) + G^2_{0,1}(z)\cos(2\theta)\\
+ g^1_{0,1}(z)\sin(\theta) + g^2_{0,1}(z)\sin(2\theta).
\end{aligned}
\tag{3.3.15}
$$

The exact solutions for $G^0_{0,1}, G^1_{0,1}, G^2_{0,1}$ and $g^1_{0,1}, g^2_{0,1}$ have been determined by solving (B.2.4), (B.2.5), (B.2.6) and (B.2.7), (B.2.8) subject to (B.2.4a), (B.2.5a), (B.2.6a) and (B.2.7a), (B.2.8a), respectively, given in Appendix B.2. Thus exact expression for $\omega_{0,1}$ is

$$
\begin{aligned}
\omega_{0,1}(z,\,\theta) =\;& 4\,(-z\operatorname{erfc}(z)+e^{-z^2}\pi^{\frac{-1}{2}})\,\alpha_1+\frac{1}{3}\Big[12\operatorname{erf}(z)\,z\operatorname{erfc}(z)+6\operatorname{erf}(z)\,(2\,z^2-1)\\
&\times e^{-z^2}\pi^{\frac{-1}{2}}+\Big(-16\,z\,e^{-z^2}+12\,z\,e^{-2\,z^2}+16\,z\operatorname{erfc}(z)\Big)\,\pi^{-1}-16\,e^{-z^2}\pi^{\frac{-3}{2}}\Big]\\
&\times(\sin(\theta)\,A_0+B_0\cos(\theta))\,\alpha_0+8\,(-z\operatorname{erfc}(z)+e^{-z^2}\pi^{\frac{-1}{2}})\,(B_1\sin(\theta)-A_1\cos(\theta))\\
&+\frac{1}{3}\Big[-12\,z\,(\operatorname{erf}(z)+2)\operatorname{erfc}(z)-6\,[(2\,z^2-1)\operatorname{erf}(z)-2]\,e^{-z^2}\pi^{\frac{-1}{2}}+(16\,e^{-z^2}\\
&-12\,e^{-2\,z^2}-16\operatorname{erfc}(z))\,z\pi^{-1}+16\,e^{-z^2}\pi^{\frac{-3}{2}}\Big]\,[({A_0}^2-{B_0}^2)\sin(2\,\theta)+2\,A_0\,B_0\\
&\times\cos(2\,\theta)].
\end{aligned}
$$

The corresponding stream function component $\Psi_{0,1}$ is found by integrating $\partial^2\Psi_{0,1}/\partial z^2 = \omega_{0,1}$ subject to $\Psi_{0,1}=0$, $\partial\Psi_{0,1}/\partial z=-\alpha_1$ at $z=0$ and given by

$$\Psi_{0,1}(z,\theta) = \frac{1}{9}\Big\{-3\,z\,\mathrm{erfc}(z)\left((-3+2\,z^2)\,\mathrm{erf}(z)+4\,z^2\right)+\Big[24\sqrt{2}\,\mathrm{erf}(\sqrt{2}\,z)-12\,\mathrm{erf}(z)$$
$$-6+\left((-33+12\,z^2)\,\mathrm{erf}(z)+6+6\,z^2\right)e^{-z^2}\Big]\pi^{\frac{-1}{2}}+8\left[-1+(1+z^2)\,e^{-z^2}\right]\pi^{\frac{-3}{2}}$$
$$+\left[-4\,z\,(3+2\,z^2)\,\mathrm{erfc}(z)+6\,z\,e^{-2\,z^2}\right]\pi^{-1}\Big\}\left[(-{B_0}^2+{A_0}^2)\sin(2\,\theta)+2\,A_0\,B_0\cos(2\,\theta)\right]$$
$$+\frac{1}{9}\Big\{3\,\mathrm{erf}(z)\,z\,(-3+2\,z^2)\,\mathrm{erfc}(z)+\Big[\left((-12\,z^2+33)\,\mathrm{erf}(z)+6\,z^2-12\right)e^{-z^2}+12$$
$$+12\,\mathrm{erf}(z)-24\sqrt{2}\,\mathrm{erf}(\sqrt{2}\,z)\Big]\pi^{\frac{-1}{2}}+\left(4\,z\,(3+2\,z^2)\,\mathrm{erfc}(z)-6\,z\,e^{-2\,z^2}\right)\pi^{-1}$$
$$+8\left(1+(-1-z^2)\,e^{-z^2}\right)\pi^{\frac{-3}{2}}\Big\}\left(\sin(\theta)\,A_0+B_0\cos(\theta)\right)\alpha_0+\frac{1}{3}\left[4\,z^3\mathrm{erfc}(z)-6\mathrm{erf}(z)\,z\right.$$
$$\left.+4\,(1+(-1-z^2)\,e^{-z^2})\pi^{\frac{-1}{2}}\right](A_1\cos(\theta)-B_1\sin(\theta))+\frac{1}{3}\,\alpha_1\left[-z\,(3+2\,z^2)\,\mathrm{erfc}(z)\right.$$
$$\left.+2\,(-1+(1+z^2)\,e^{-z^2})\pi^{\frac{-1}{2}}\right]$$

where

$$A_1 = \sigma_1\sin(\eta), \qquad B_1 = \sigma_1 cos(\eta). \tag{3.3.16}$$

The non-homogenous term $R_{0,2}(z,\theta)$ in (3.3.7) is given by (B.3.1) in Appendix B.3 and the expression for the third term, $\omega_{0,2}(z,\theta)$, in the boundary-layer expansions in terms of Fourier components is obtained from (3.2.1) when $n = 0$ and $m = 2$. It is found that

$$\omega_{0,2}(z,\theta) = G^0_{0,2}(z) + G^1_{0,2}(z)\cos(\theta) + G^2_{0,2}(z)\cos(2\theta) + G^3_{0,2}(z)\cos(3\theta)$$
$$+ g^1_{0,2}(z)\sin(\theta) + g^2_{0,2}(z)\sin(2\theta) + g^3_{0,2}(z)\sin(3\theta). \tag{3.3.17}$$

The exact solutions for $G^0_{0,2}$, $G^1_{0,2}$, $G^2_{0,2}$, $G^3_{0,2}$ and $g^1_{0,2}$, $g^2_{0,2}$, $g^3_{0,2}$ have been determined by solving (B.2.9), (B.2.10), (B.2.11), (B.2.12) and (B.2.13), (B.2.14), (B.2.15) subject to (B.2.9a), (B.2.10a), (B.2.11a), (B.2.12a) and (B.2.13a), (B.2.14a), (B.2.15a) respectively, given in Appendix B.2. However, because of the lengthy expressions

obtained we only present

$$\begin{aligned}
\lim_{z\to 0}\omega_{0,2}(z,\theta) &= \frac{2\,\alpha_0\,\pi^{-5/2}}{135}\,({B_0}^2+{A_0}^2)\,(-1458\,\sqrt{3}\,\pi+2535\,\pi+90\,\pi^2-1024)\\
&+ \frac{\pi^{-5/2}}{135}[3\,\pi\,(-1024+315\,\pi)\,(-B_1\,A_0+A_1\,B_0)+720\,\alpha_2\,\pi^2]\\
&+ \frac{32}{3\,\sqrt{\pi}}\,(\sin(\theta)\,B_2-\cos(\theta)\,A_2)+(\frac{1}{\sqrt{\pi}}-\frac{128\,\pi^{-3/2}}{15})\\
&\times \alpha_0\,(\cos(\theta)\,B_1+\sin(\theta)\,A_1)+({B_0}^2+{A_0}^2)\,(\frac{32}{3\,\sqrt{\pi}}+\frac{244\,\pi^{-3/2}}{15}\\
&- \frac{126\,\pi^{-3/2}}{5}-\frac{2816\,\pi^{-5/2}}{135})\,(\sin(\theta)\,B_0-\cos(\theta)\,A_0)\\
&+ \left(-\frac{16}{3\,\sqrt{\pi}}+\frac{128\,\pi^{-5/2}}{9}\right)\,(A_0\sin(\theta)+\cos(\theta)\,B_0)\,\alpha_1\\
&+ \left(\frac{2}{3\sqrt{\pi}}+\frac{14\,\pi^{-3/2}}{3}-\frac{18\,\sqrt{3}\,\pi^{-3/2}}{5}-\frac{256\,\pi^{-5/2}}{45}\right)\\
&\times {\alpha_0}^2(\sin(\theta)\,B_0-\cos(\theta)\,A_0)+\frac{\alpha_0}{270}\,[({B_0}^2-{A_0}^2)\cos(2\,\theta)\\
&+ 2\,A_0\,B_0\sin(2\,\theta)]\,\left(\frac{-900}{\sqrt{\pi}}+6828\,\pi^{\frac{-3}{2}}-1944\,\sqrt{3}\,\pi^{\frac{-3}{2}}+2048\,\pi^{\frac{-5}{2}}\right)\\
&+ (\frac{31}{3\,\sqrt{\pi}}-\frac{256\,\pi^{-3/2}}{45})\,[(A_1\,B_0+B_1\,A_0)\cos(2\,\theta)+(A_1\,A_0-B_1\,B_0)\\
&\times \sin(2\,\theta)]+\left(\frac{4}{3\,\sqrt{\pi}}+\frac{52\,\pi^{-3/2}}{5}-\frac{54\,\sqrt{3}\,\pi^{-3/2}}{5}+\frac{256\,\pi^{-5/2}}{135}\right)\\
&\times \left[({A_0}^3-3\,A_0\,{B_0}^2)\,\cos(3\,\theta)+({B_0}^3-3\,B_0\,{A_0}^2)\sin(3\,\theta)\right].
\end{aligned}$$

where

$$A_2=\sigma_2\sin(\eta),\qquad B_2=\sigma_2\cos(\eta). \tag{3.3.18}$$

The corresponding stream function component $\Psi_{0,2}$ is determined by integrating $\partial^2\Psi_{0,2}/\partial z^2=\omega_{0,2}$ subject to $\Psi_{0,2}=0$, $\partial\Psi_{0,2}/\partial z=-\alpha_2$ at $z=0$ and has been presented by (B.4.1) in Appendix B.4.

Thus if R is large enough and t is small, the boundary-layer expansion for ζ is given

by the approximate solution

$$\zeta \simeq \frac{R^{1/2}}{2\,(2\,t)^{1/2}}\left(\omega_{0,0} + t\,\omega_{0,1} + t^2\,\omega_{0,2}\right).$$

The corresponding surface vorticity is given by

$$\begin{aligned}
\zeta(0,\theta,t) \;\simeq\; & \frac{R^{1/2}}{2\,(2\,t)^{1/2}}\left\{(2\,\alpha_0 - 4\,A_0\cos(\theta) + 4\,B_0\sin(\theta))\;\pi^{-1/2}\right. \\
& + \; t\{\frac{4\pi^{-3/2}}{3}[\,(-4B_0\alpha_0 - 6A_1\pi)\cos(\theta) + (6A_0B_0\,\pi + 8A_0B_0)\cos(2\theta) + (6B_1\,\pi \\
& - \; 4A_0\,\alpha_0)\sin(\theta) + (-4\,{B_0}^2 + 4\,{A_0}^2 - 3\,{B_0}^2\,\pi + 3\,{A_0}^2\,\pi)\sin(2\,\theta) + 3\pi\alpha_1\,]\} \\
& + \; t^2\{\frac{2\,\alpha_0\,\pi^{-5/2}}{135}\,({B_0}^2 + {A_0}^2)\,(-1458\,\sqrt{3}\,\pi + 2535\,\pi + 90\,\pi^2 - 1024) \\
& + \; \frac{\pi^{-5/2}}{135}[3\,\pi\,(-1024 + 315\,\pi)\,(-B_1\,A_0 + A_1\,B_0) + 720\,\alpha_2\,\pi^2] \\
& + \; \frac{32}{3\,\sqrt{\pi}}\,(\sin(\theta)\,B_2 - \cos(\theta)\,A_2) + (\frac{1}{\sqrt{\pi}} - \frac{128\,\pi^{-3/2}}{15}) \\
& \times \; \alpha_0\,(\cos(\theta)\,B_1 + \sin(\theta)\,A_1) + ({B_0}^2 + {A_0}^2)\,(\frac{32}{3\,\sqrt{\pi}} + \frac{244\,\pi^{-3/2}}{15} \\
& - \; \frac{126\,\pi^{-3/2}}{5} - \frac{2816\,\pi^{-5/2}}{135})\,(\sin(\theta)\,B_0 - \cos(\theta)\,A_0) \\
& + \; \left(-\frac{16}{3\,\sqrt{\pi}} + \frac{128\,\pi^{-5/2}}{9}\right)\,(A_0\sin(\theta) + \cos(\theta)\,B_0)\,\alpha_1 \\
& + \; \left(\frac{2}{3\sqrt{\pi}} + \frac{14\,\pi^{-3/2}}{3} - \frac{18\,\sqrt{3}\,\pi^{-3/2}}{5} - \frac{256\,\pi^{-5/2}}{45}\right) \\
& \times \; {\alpha_0}^2(\sin(\theta)\,B_0 - \cos(\theta)\,A_0) + \frac{\alpha_0}{270}\,[({B_0}^2 - {A_0}^2)\cos(2\,\theta) \\
& + \; 2\,A_0\,B_0\sin(2\,\theta)]\,\left(\frac{-900}{\sqrt{\pi}} + 6828\,\pi^{\frac{-3}{2}} - 1944\,\sqrt{3}\,\pi^{\frac{-3}{2}} + 2048\,\pi^{\frac{-5}{2}}\right) \\
& + \; (\frac{31}{3\,\sqrt{\pi}} - \frac{256\,\pi^{-3/2}}{45})\,[(A_1\,B_0 + B_1\,A_0)\cos(2\,\theta) + (A_1\,A_0 - B_1\,B_0) \\
& \times \; \sin(2\,\theta)] + \left(\frac{4}{3\,\sqrt{\pi}} + \frac{52\,\pi^{-3/2}}{5} - \frac{54\,\sqrt{3}\,\pi^{-3/2}}{5} + \frac{256\,\pi^{-5/2}}{135}\right) \\
& \times \; \left.[({A_0}^3 - 3\,A_0\,{B_0}^2)\;\cos(3\,\theta) + ({B_0}^3 - 3\,B_0\,{A_0}^2)\sin(3\,\theta)]\right\}.
\end{aligned}$$

3.3.2 First and second-order correction terms to the boundary-layer expansion

The first order correction terms of order k are $\Psi_{1,m}$ and $\omega_{1,m}$ in expansions (3.1.1) when $n = 1$. Equations (3.1.2) and (3.1.3) then reduce for n=1 to the equations

$$\frac{\partial^2 \Psi_{1,m}}{\partial z^2} = \omega_{1,m} + 2\,z\,\omega_{0,m} \tag{3.3.19}$$

$$\frac{\partial^2 \omega_{1,m}}{\partial z^2} + 2z\frac{\partial \omega_{1,m}}{\partial z} - 4\,m\,\omega_{1,m} = \mathrm{R}_{1,m}(z,\theta), \tag{3.3.20}$$

where

$$\begin{aligned}\mathrm{R}_{1,m}(z,\theta) \;&= -4\,z^2\frac{\partial \omega_{0,m}}{\partial z} + 4\,z(2m-1)\omega_{0,m} + 4\sum_{j=0}^{m-1}\left(\frac{\partial \Psi_{0,j}}{\partial \theta}\frac{\partial \omega_{1,m-j-1}}{\partial z}\right. \\ &\left. - \frac{\partial \Psi_{0,j}}{\partial z}\frac{\partial \omega_{1,m-j-1}}{\partial \theta}\right) + 4\sum_{j=0}^{m-1}\left(\frac{\partial \Psi_{1,j}}{\partial \theta}\frac{\partial \omega_{0,m-j-1}}{\partial z} - \frac{\partial \Psi_{1,j}}{\partial z}\frac{\partial \omega_{0,m-j-1}}{\partial \theta}\right)\end{aligned} \tag{3.3.21}$$

These equations must be solved subject to the conditions

$$\Psi_{1,m} = \frac{\partial \Psi_{1,m}}{\partial z} = 0 \;\text{ when }\; z = 0; \tag{3.3.22}$$

$$\int_0^\infty \int_0^{2\pi} (\omega_{1,m} + (2-p)z\omega_{0,m})\; d\theta\, dz = 0, \tag{3.3.23a}$$

$$\int_0^\infty \int_0^{2\pi} (\omega_{1,m} + (2-p)z\omega_{0,m})\cos(p\theta)\; d\theta\; dz = 0, \tag{3.3.23b}$$

$$\int_0^\infty \int_0^{2\pi} (\omega_{1,m} + (2-p)z\omega_{0,m})\sin(p\theta)\; d\theta\; dz = 0; \tag{3.3.23c}$$

$$\omega_{1,m} \to 0 \quad \text{as} \quad z \to \infty. \tag{3.3.24}$$

The non-homogenous term $R_{1,m}(z,\theta)$ in equation (3.3.21) for $m = 0$ is given by

$$\begin{aligned} \mathrm{R}_{1,0}(z,\,\theta) &= 8\,z\,e^{-z^2}\,[\alpha_0 - 2\,A_0\cos(\theta) + 2\,B_0\sin(\theta)]\,(2\,z^2-1)\pi^{-\frac{1}{2}} \\ &\times \frac{1}{2}\,[-\mathrm{erfc}(z) + \frac{(-4\,z^3-2\,z)\,e^{-z^2}}{\sqrt{\pi}}]\,\alpha_0 + [-\mathrm{erfc}(z) + (4\,z^3+2\,z)\,e^{-z^2}\pi^{-\frac{1}{2}}] \\ &\times (-B_0\sin(\theta) + A_0\cos(\theta)), \end{aligned}$$

and the first term, $\omega_{1,0}(z,\theta)$, in the first equation of (3.1.1) when $m=0$ and $n=1$, can be written in terms of Fourier components, in a manner described previously, and $n=1$ as follows

$$\omega_{1,0}(z,\theta) = G^0_{1,0}(z) + G^1_{1,0}(z)\cos(\theta) + g^1_{1,0}(z)\sin(\theta). \tag{3.3.25}$$

The exact solutions for $G^0_{1,0}$, $G^1_{1,0}$ and $g^1_{1,0}$ have been determined by solving (B.2.16), (B.2.17) and (B.2.18) subject to (B.2.16a), (B.2.17a) and (B.2.18a), respectively, given in Appendix B.2. Thus, exact expression for $\omega_{1,0}$ is

$$\begin{aligned} \omega_{1,0}(z,\,\theta) &= \frac{1}{2}\,[-\mathrm{erfc}(z) + \frac{(-4\,z^3-2\,z)\,e^{-z^2}}{\sqrt{\pi}}]\,\alpha_0 + [-\mathrm{erfc}(z) + (4\,z^3+2\,z)\,e^{-z^2}\pi^{-\frac{1}{2}}] \\ &\times (-B_0\sin(\theta) + A_0\cos(\theta)). \end{aligned}$$

The corresponding stream function component, $\Psi_{1,0}$, is determined by integrating the equation $\partial^2\Psi_{1,0}/\partial z^2 = \omega_{1,0} + 2\,z\,\omega_{0,0}$ subject to the conditions: $\Psi_{1,0} = \partial\Psi_{1,0}/\partial z = 0$ at $z=0$. It is found that

$$\begin{aligned} \Psi_{1,0}(z,\,\theta) &= \frac{1}{8}\,\alpha_0\,(-2\,z^2\,\mathrm{erfc}(z) + \mathrm{erf}(z) - 2\,z\,e^{-z^2}\pi^{-\frac{1}{2}}) + \frac{1}{4}\,[-\mathrm{erf}(z) + 2\,z^2\,\mathrm{erfc}(z) \\ &+ (-6\,z\,e^{-z^2} + 8\,z)\pi^{-\frac{1}{2}}]\,(B_0\sin(\theta) - A_0\cos(\theta)). \end{aligned}$$

The non-homogenous term $R_{1,1}(z,\theta)$ in (3.3.21) is given by (B.3.2) in Appendix B.3 and the expression for the second term, $\omega_{1,1}(z,\theta)$ in the first equation of (3.1.1) when $m=1$ and $n=1$, in terms of Fourier components are obtained from (3.2.1) and

(3.2.2) when $n = 1$ and $m = 1$. It is found that

$$\omega_{1,1}(z,\theta) = G^0_{1,1}(z) + G^1_{1,1}(z)\cos(\theta) + G^2_{1,1}(z)\cos(2\theta) + g^1_{1,1}(z)\sin(\theta) + g^2_{1,1}(z)\sin(2\theta). \tag{3.3.26}$$

The exact solutions for $G^0_{1,1}$, $G^1_{1,1}$, $G^2_{1,1}$ and $g^1_{1,1}$, $g^2_{1,1}$ have been determined (B.2.19), (B.2.20), (B.2.21) and (B.2.22), (B.2.23) subject to (B.2.19a), (B.2.20a), (B.2.21a) and (B.2.22a), (B.2.23a), respectively, given in Appendix B.2. Thus exact expression for $\omega_{1,1}$ is

$$\begin{aligned}
\omega_{1,1}(z,\theta) = {} & \frac{1}{2}\left[-2\,z\,e^{-z^2}\pi^{\frac{-1}{2}} - (2\,z^2+1)\,\mathrm{erfc}(z)\right]\alpha_1 + \left\{\frac{1}{8}\,\mathrm{erfc}(z)\left[(-16\,\mathrm{erf}(z) - 114\right.\right. \\
& \left.+128\sqrt{2})\,z^2 - 65 + 64\sqrt{2}\right] + \left[-\frac{2}{3}\,(3z + 6\,z^5 + 13\,z^3)\,\mathrm{erf}(z) + \frac{1}{12}\,z\,(-192\sqrt{2}\right. \\
& \left.+189 + 56\,z^2)\right]e^{-z^2}\pi^{-1/2} + \left[-\frac{2}{3}\,(2\,z^2+1)\,\mathrm{erfc}(z) + (\frac{32}{15} + \frac{16}{3}\,z^4 + \frac{32}{5}\,z^2)\,e^{-z^2}\right. \\
& \left.\left.-\frac{4}{3}\,(3\,z^2+2)\,(z^2+1)\,e^{-2z^2}\right]\pi^{-1} + 4\,z\,e^{-z^2}\pi^{(-3/2)}\right\} \times (\sin(\theta)\,A_0 + B_0\cos(\theta))\,\alpha_0 \\
& + \left[(2\,z^2+1)\,\mathrm{erfc}(z) - 6\,z\,e^{-z^2}\pi^{\frac{-1}{2}}\right](B_1\sin(\theta) - A_1\cos(\theta)) + \left\{-\frac{1}{8}\,\mathrm{erfc}(z)\left[(-154\right.\right. \\
& \left.+192\sqrt{2} - 16\,\mathrm{erf}(z))\,z^2 + 96\sqrt{2} - 77\right] + \left[\frac{2}{3}\,(3z + 6\,z^5 + 13\,z^3)\,\mathrm{erf}(z) - \frac{1}{12}\,z\,(249\right. \\
& \left.-288\sqrt{2} + 8\,z^2)\right]e^{-z^2}\pi^{\frac{-1}{2}} + \left[2\,(2\,z^2+1)\,\mathrm{erfc}(z) + (-\frac{32}{5}\,z^2 - \frac{16}{3}\,z^4 - \frac{32}{15})\,e^{-z^2}\right. \\
& \left.\left.+\frac{4}{3}\,(3\,z^2+2)\,(z^2+1)\,e^{-2z^2}\right]\pi^{-1} - \frac{20}{3}\,z\,e^{-z^2}\pi^{\frac{-3}{2}}\right\}\left[({A_0}^2 - {B_0}^2)\sin(2\,\theta) + 2\,A_0\right. \\
& \left.\times B_0\cos(2\,\theta)\right].
\end{aligned}$$

The solution for $\Psi_{1,1}$ is obtained by integrating the equation $\partial^2\Psi_{1,1}/\partial z^2 = \omega_{1,1} + 2\,z\,\omega_{0,1}$ subject to $\Psi_{1,1} = \partial\Psi_{1,1}/\partial z = 0$ at $z = 0$. The expression for $\Psi_{1,1}$ is given by (B.4.2) in Appendix B.4. Equations for $m = 2$ can be obtained from (3.3.19) and (3.3.20). Exact solutions for $\omega_{1,2}(z,\theta)$ and $\Psi_{1,2}(z,\theta)$ have been obtained and consist of $\cos\theta$, $\cos 2\theta$, $\cos 3\theta$, $\sin\theta$, $\sin 2\theta$, $\sin 3\theta$ with coefficients which are functions of z.

Thus, $\omega_{1,2}(z,\theta)$ can be written in terms of Fourier series as follows

$$\omega_{1,2}(z,\theta) = G^0_{1,2}(z) + G^1_{1,2}(z)\cos(\theta) + G^2_{1,2}(z)\cos(2\theta) + G^3_{1,2}(z)\cos(3\theta) + g^1_{1,2}(z)\sin(\theta) + g^2_{1,2}(z)\sin(2\theta) + g^3_{1,2}(z)\sin(3\theta). \quad (3.3.27)$$

where the exact solutions for $G^0_{1,2}$, $G^1_{1,2}$, $G^2_{1,2}$, $G^3_{1,2}$ and $g^1_{1,2}$, $g^2_{1,2}$, $g^3_{1,2}$ have been determined by solving (B.2.24), (B.2.25), (B.2.26), (B.2.27) and (B.2.28), (B.2.29), (B.2.30) subject to (B.2.24a), (B.2.25a), (B.2.26a), (B.2.27a) and (B.2.28a), (B.2.29a), (B.2.30a) respectively, given in Appendix B.2. However, because of their long expression we only present

$$\begin{aligned}
\lim_{z\to 0}\omega_{1,2}(z,\theta) &= \frac{\pi^{-2}}{80640}(A_0{}^2 + B_0{}^2)\,(-196608\sqrt{2}\,\pi + 720896 - 3429216\sqrt{3}\,\pi \\
&- 419265\,\pi^2 + 4224528\,\pi + 705600\sqrt{2}\,\pi^2\Big)\,\alpha_0 + \frac{\pi^{-1}}{1680}\,(A_0\,B_1 - B_0\,A_1) \\
&\times (7035\,\pi - 22528) + \frac{\pi^{-1}}{480}\,(3840\sqrt{2}\,\pi - 4455\,\pi - 1408)\,(A_0\sin(\theta) \\
&+ B_0\cos(\theta))\,\alpha_1 + \frac{\pi^{\frac{-5}{2}}\,\alpha_0{}^2}{40320}\,(62464\sqrt{\pi} + 369495\,\pi^{\frac{-5}{2}} - 584640\sqrt{2}\,\pi^{\frac{-5}{2}} \\
&+ 79872\sqrt{2}\,\pi^{\frac{-3}{2}} - 805104\,\pi^{\frac{-3}{2}} + 585144\sqrt{3}\,\pi^{(3/2)} + 2177280\,\beta\,\pi^2\Big) \\
&\times (-B_0\sin(\theta) + A_0\cos(\theta))\,-\cos(\theta)\,A_2 + \frac{\pi^{-1}}{3360}\,(-25305\,\pi + 26880\sqrt{2}\,\pi \\
&- 7808)\,(A_1\sin(\theta) + B_1\cos(\theta))\,\alpha_0\pi + \sin(\theta)\,B_2 - \frac{\pi^{\frac{-5}{2}}}{26880}\,(1451520\,\beta\,\pi^2 \\
&- 2300144\,\pi^{\frac{-3}{2}} - 776160\sqrt{2}\,\pi^{\frac{-5}{2}} + 610304\sqrt{2}\,\pi^{\frac{-3}{2}} - 362496\sqrt{\pi} \\
&+ 502425\,\pi^{-5/2} + 1533168\sqrt{3}\,\pi^{-3/2})\,(-B_0\sin(\theta) + A_0\cos(\theta)) \\
&\times (-A_0 + B_0\,\beta)\,(A_0 + B_0\,\beta) - \frac{\pi^{-5/2}\,\alpha_0}{80640}\,(-26127360\,\beta\,\pi^2 \\
&- 163296\sqrt{3}\,\pi^{-3/2} - 385024\sqrt{\pi} - 2425815\,\pi^{5/2} - 668688\,\pi^{\frac{3}{2}} \\
&+ 4818240\sqrt{2}\,\pi^{\frac{5}{2}} - 368640\sqrt{2}\,\pi^{\frac{3}{2}})\,(\cos(2\,\theta)\,B_0{}^2 + 2\sin(2\,\theta)\,A_0\,B_0 \\
&- \cos(2\,\theta)\,A_0{}^2) + \frac{\pi^{-1}}{84}(\sin(2\,\theta)\,B_0\,B_1 - A_0\,A_1\sin(2\,\theta) - \cos(2\,\theta)\,B_0\,A_1 \\
&- \cos(2\,\theta)\,A_0\,B_1)(2016\sqrt{2}\,\pi - 352 - 1953\,\pi) + \frac{1}{26880}
\end{aligned}$$

$$\begin{aligned}
&\times \quad \beta\,(\,1239840\,\beta\,\pi^{5/2}\,\sqrt{2} - 798735\,\beta\,\pi^{5/2} + 517104\,\beta\,\pi^{3/2}\,\sqrt{3} \\
&- \quad 927856\,\beta\,\pi^{3/2} + 303104\,\beta\,\pi^{3/2}\,\sqrt{2} - 67584\,\beta\,\sqrt{\pi} + 8709120\,\pi^{2}\Big) \\
&\times \quad (-3\,B_0\,{A_0}^2\sin(3\,\theta) - 3\,{B_0}^2\,A_0\cos(3\,\theta) + {A_0}^3\cos(3\,\theta) \\
&+ \quad {B_0}^3\sin(3\,\theta))\pi^{-5/2} - \frac{1}{2}\,\alpha_2,
\end{aligned}$$

where β is the integral

$$\beta = \int_0^\infty e^{-2\,z^2}\,\mathrm{erf}(z)dz \tag{3.3.28}$$

which can be evaluated as

$$\beta = (2\,\pi)^{-1/2}\arctan(2^{-1/2}). \tag{3.3.29}$$

The solution for $\Psi_{1,2}$ is obtained by integrating the equation $\partial^2\Psi_{1,2}/\partial z^2 = \omega_{1,2} + 2\,z\,\omega_{0,2}$ subject to $\Psi_{1,2} = \partial\Psi_{1,2}/\partial z = 0$ at $z = 0$. The equations for $\omega_{1,m}(z,\theta)$ and $\Psi_{1,m}(z,\theta)$ when $m \geq 3$ and the boundary and integral conditions satisfied by these functions can be found from (3.3.19) and (3.3.20). In theory, exact solutions can be found for all these functions but they rapidly become complicated, and it is virtually impossible to proceed beyond $m = 2$.

The second order correction terms of order k^2 are $\Psi_{2,m}$ and $\omega_{2,m}$ in expansions (3.1.1) when $n = 2$. Equations (3.1.2) and (3.1.3) then reduce for n=2 to the equations

$$\frac{\partial^2\Psi_{2,m}}{\partial z^2} + \frac{\partial^2\Psi_{0,m}}{\partial\theta^2} = \omega_{2,m} + 2z\omega_{1,m} + 2z^2\omega_{0,m} \tag{3.3.30}$$

$$\frac{\partial^2\omega_{2,m}}{\partial z^2} + 2z\frac{\partial\omega_{2,m}}{\partial z} - 2(2m+1)\omega_{2,m} = \mathrm{R}_{2,m}(z,\theta), \tag{3.3.31}$$

where

$$\begin{aligned}
\mathrm{R}_{2,m}(z,\theta) = -\frac{\partial^2\omega_{0,m}}{\partial\theta^2} \quad & -4z^2\left[z\frac{\partial\omega_{0,m}}{\partial z} - (2m-1)\omega_{0,m})\right] - 4z\left[z\frac{\partial\omega_{1,m}}{\partial z} - 2m\omega_{1,m})\right] \\
& + \sum_{q=0}^{2}\left[4\sum_{j=0}^{m-1}\left\{\frac{\partial\Psi_{q,j}}{\partial\theta}\frac{\partial\omega_{2-q,m-j-1}}{\partial z} - \frac{\partial\Psi_{q,j}}{\partial z}\frac{\partial\omega_{2-q,m-j-1}}{\partial\theta}\right\}\right].
\end{aligned} \tag{3.3.32}$$

These equations must be solved subject to the conditions

$$\Psi_{2,m} = \frac{\partial \Psi_{2,m}}{\partial m} = 0 \text{ when } z = 0; \tag{3.3.33}$$

$$\int_0^\infty \int_0^{2\pi} \left(\omega_{2,m} + 2z\omega_{1,m} + 2z^2\omega_{0,m}\right)\, d\theta\, dz = 0, \tag{3.3.34a}$$

$$\int_0^\infty \int_0^{2\pi} \left(\omega_{2,m} + (2-p)z\omega_{1,m} + \frac{1}{2}(2-p)^2 z^2 \omega_{0,m}\right) \cos(p\theta)\, d\theta\, dz = 0, \tag{3.3.34b}$$

$$\int_0^\infty \int_0^{2\pi} \left(\omega_{2,m} + (2-p)z\omega_{1,m} + \frac{1}{2}(2-p)^2 z^2 \omega_{0,m}\right) \sin(p\theta)\, d\theta\, dz = 0; \tag{3.3.23c}$$

$$\omega_{2,m} \to 0 \text{ as } z \to \infty. \tag{3.3.35}$$

The non-homogeneous term $R_{2,m}(z,\theta)$ in equation (3.3.32) for $m = 0$ is given by

$$\begin{aligned} R_{2,0}(z,\theta) &= -4\left[(-8\,z^4 + 4\,z^6 + 2\,z^2)\,\alpha_0 + (8\,z^6 - 16\,z^4 - 1)\,(-A_0\cos(\theta) + B_0\sin(\theta))\right] \\ &\times \quad e^{-z^2}\pi^{-\frac{1}{2}}. \end{aligned}$$

The first terms of the expansions (3.1.1) when $n = 2$ and $m = 0$ are given by

$$\begin{aligned} \omega_{2,0}(z,\,\theta) &= \frac{1}{24}\,(9 + 24\,z^6 - 4\,z^4 + 18\,z^2)\,\alpha_0\,e^{-z^2}\pi^{-\frac{1}{2}} - \frac{1}{12}\,[-12\,z\,\mathrm{erfc}(z) \\ &+ \quad (24\,z^6 - 4\,z^4 - 6\,z^2 - 3)\,e^{-z^2}\pi^{-\frac{1}{2}}]\,(-B_0\sin(\theta) + A_0\cos(\theta)) \end{aligned}$$

$$\begin{aligned} \Psi_{2,0}(z,\,\theta) &= \frac{1}{48}\,\alpha_0\,[-8\,z^3\,\mathrm{erfc}(z) - 3\,\pi^{-\frac{1}{2}} + (12\,z^4 + 12\,z^2 + 3)\,e^{-z^2}\pi^{-\frac{1}{2}}] \\ &+ \quad \frac{1}{24}\,[-6\,z\,\mathrm{erf}(z) + 4\,z^3\,\mathrm{erfc}(z) - 8\,z^3 + 24\,z^2 - 1 + (-12\,z^4 \\ &- \quad 8\,z^2 + 1)\,e^{-z^2}\pi^{-\frac{1}{2}}] \times (-B_0\sin(\theta) + A_0\cos(\theta)). \end{aligned}$$

The non-homogenous term $R_{2,1}(z,\theta)$ in (3.3.32) is given by (B.3.3) in Appendix B.3 and the expression for the second term, $\omega_{2,1}(z,\theta)$, in the first equation of (3.1.1) when

$n = 2$ and $m = 1$, in terms of Fourier components is obtained from (3.2.1) when $n = 2$ and $m = 1$. It is found that

$$\omega_{2,1}(z,\theta) = G^0_{2,1}(z) + G^1_{2,1}(z)\cos(\theta) + G^2_{2,1}(z)\cos(2\theta) + g^1_{2,1}(z)\sin(\theta) + g^2_{2,1}(z)\sin(2\theta). \tag{3.3.36}$$

The exact solutions for $G^0_{2,1}$, $G^1_{2,1}$, $G^2_{2,1}$ and $g^1_{2,1}$, $g^2_{2,1}$ have been determined by solving (B.2.34), (B.2.35), (B.2.36) and (B.2.37), (B.2.38) subject to (B.2.34a), (B.2.35a), (B.2.36a) and (B.2.37a), (B.2.38a), respectively, given in Appendix B.2. Thus exact expression for $\omega_{2,1}$ is

$$\begin{aligned}
\omega_{2,1}(z,\theta) &= \frac{1}{12}\left[-8\,z^3\,\mathrm{erfc}(z) + 3\,(2\,z^2+1)^2\,e^{(-z^2)}\pi^{\frac{-1}{2}}\right]\alpha_1 + \left\{\frac{1}{24}\,z\,\mathrm{erfc}(z)\,[4\,\mathrm{erf}(z)\right. \\
&\times\ (15+16\,z^2) + 2\,(27+64\sqrt{2})\,z^2 + 483 - 192\sqrt{2}] + \frac{1}{12}[(24\,z^8 + 40\,z^6 \\
&+\ 66\,z^4 + 6\,z^2 - 27)\,\mathrm{erf}(z) - 32\,z^6 - 28\,z^4 + (-19 - 64\sqrt{2})\,z^2 - 109 \\
&+\ 32\sqrt{2}]e^{-z^2}\pi^{\frac{-1}{2}} + \left[\frac{2378}{315}\,(2\,z^3+3\,z)\,\mathrm{erfc}(z) - \frac{2}{315}\,(420\,z^7 + 518\,z^5\right. \\
&+\ \left.947\,z^3 + 648\,z)\,e^{-z^2} + \frac{1}{6}\,(12\,z^7 + 14\,z^5 + 32\,z^3 + 19\,z)\,e^{(-2\,z^2)}\right]\pi^{-1} \\
&-\ \left.\frac{1}{105}\,(140\,z^4 + 1632\,z^2 + 1527)\,e^{(-z^2)}\pi^{\frac{-3}{2}}\right\}(\sin(\theta)\,A_0 + B_0\cos(\theta))\,\alpha_0 \\
&+\ \frac{1}{6}\,[(4\,z^3+6\,z)\,\mathrm{erfc}(z) + (-12\,z^4 - 8\,z^2 + 1)\,e^{(-z^2)}\pi^{\frac{-1}{2}}]\,(A_1\cos(\theta) \\
&-\ B_1\sin(\theta)) + \left\{\frac{1}{12}\,z\,\mathrm{erfc}(z)\,[2\,\mathrm{erf}(z)\,(15+28\,z^2) + 380\,z^2 + 711 - 288\sqrt{2}]\right. \\
&+\ \frac{1}{12}[(24\,z^8 + 40\,z^6 + 66\,z^4 - 54\,z^2 - 33)\,\mathrm{erf}(z) - 32\,z^4 - 8\,z^6 - 338\,z^2 \\
&-\ 401 + 144\sqrt{2}]e^{(-z^2)}\pi^{-\frac{1}{2}} + [\frac{8}{63}\,(360\,z + 247\,z^3)\,\mathrm{erfc}(z) - \frac{2}{315}\,(947\,z^3 \\
&+\ 420\,z^7 + 518\,z^5 + 522\,z)\,e^{(-z^2)} + \frac{1}{6}\,(32\,z^3 + 14\,z^5 + z + 12\,z^7)\,e^{(-2\,z^2)}]\pi^{-1} \\
&-\ \left.\frac{1}{21}(28\,z^4 + 668\,z^2 + 591)\,e^{(-z^2)}\pi^{-\frac{3}{2}}\right\}[({B_0}^2 - {A_0}^2)\sin(2\,\theta) - 2\,A_0\,B_0\cos(2\,\theta)]
\end{aligned}$$

The corresponding solution for $\Psi_{2,1}$ is obtained by integrating $\partial^2\Psi_{2,1}/\partial z^2+\partial^2\Psi_{0,1}/\partial\theta^2 = \omega_{2,1}+2z\omega_{1,1}+2z^2\omega_{0,1}$ twice subject to $\Psi_{2,1} = \partial\Psi_{2,1}/\partial z = 0$ at $z = 0$. The expression for $\Psi_{2,1}$ is given by (B.4.3) in Appendix B.4. It becomes too complicated to obtain $\omega_{2,m}(z,\theta)$ and $\Psi_{2,m}(z,\theta)$ for $m \geq 2$ by exact analysis. We thus finally obtain an expression for the vorticity

$$\zeta(\xi,\theta,t) = \frac{1}{k}\left[\omega_{0,0}+\omega_{0,1}t+\omega_{0,2}t^2 + k(\omega_{1,0}+\omega_{1,1}t+\omega_{1,2}t^2) + k^2(\omega_{2,0}+\omega_{2,1}t+O(t^2))\right] \tag{3.3.37}$$

which is valid for small t and large R. In particular, we find for the surface vorticity

$$\begin{aligned}
\zeta(0,\theta,t) &= \frac{1}{8}\alpha_0\left[-4k+(3k^2+16)\pi^{\frac{-1}{2}}\right]+\frac{1}{4}\alpha_1 t\left[-2k+(16+k^2)\pi^{\frac{-1}{2}}\right] \\
&- \frac{1}{241920}t^2\alpha_0\left({A_0}^2+{B_0}^2\right)[(1257795-2116800\sqrt{2})k-322560\pi^{\frac{-1}{2}} \\
&+ (589824\sqrt{2}+10287648\sqrt{3}-12673584)k\pi^{-1}+(5225472\sqrt{3} \\
&- 9085440)\pi^{-3/2}-2162688\times k\pi^{-2}+3670016\pi^{-5/2}]+\frac{1}{241920}t^2\alpha_2 \\
&\times (-120960k+1290240\pi^{\frac{-1}{2}})-\frac{1}{5040}\left(A_1B_0-B_1A_0\right)[(-67584t^2\pi^{-1} \\
&+ 21105t^2)k+114688t^2\pi^{-3/2}-35280t^2\pi^{-1/2}]+\frac{1}{4}(A_0\cos(\theta) \\
&- B_0\sin(\theta))[-4k+(k^2-16)\times\pi^{-1/2}]+\frac{1}{840}(\sin(\theta)A_0+\cos(\theta)B_0)t \\
&+ \alpha_0(-6825+6720\sqrt{2})k+(2240\sqrt{2}-7630)k^2\pi^{-1/2}-1008k\pi^{-1} \\
&+ (-4480-12216k^2)\pi^{-3/2}]-\frac{1}{6}(-\cos(\theta)A_1+\sin(\theta)B_1)t \\
&\times [-6k+(k^2-48)\pi^{-1/2}]+\frac{1}{1440}(\sin(\theta)A_0+\cos(\theta)B_0)t^2\alpha_1[(-13365 \\
&- 4224\pi^{-1}+11520\sqrt{2})k-7680\pi^{-1/2}+20480\pi^{-3/2}]+\{\frac{1}{241920}({A_0}^2 \\
&+ {B_0}^2)(-A_0\cos(\theta)+B_0\sin(\theta))[(6985440\sqrt{2}-4521825)k \\
&+ (-13063680\beta k+2580480)\pi^{-1/2}+(-5492736\sqrt{2}-13798512\sqrt{3}
\end{aligned}$$

$$
\begin{aligned}
&+ \ 20701296)\, k\pi^{-1} + 3262464\, k\pi^{-2} + (-6096384\sqrt{3} + 3935232)\pi^{-3/2} \\
&- \ 5046272\,\pi^{-5/2}] + \frac{1}{3}(32\,\pi^{-1/2} + 3\,k)(\sin(\theta)\,B_2 - \cos(\theta)\,A_2)\,\}t^2 \\
&+ \ \frac{1}{40320}t^2\,{\alpha_0}^2(-A_0\cos(\theta) + B_0\sin(\theta))[584640\,k\sqrt{2} - 369495\,k \\
&+ \ (-2177280\,\beta\,k + 26880)\pi^{-1/2} + (805104\,k - 585144\,k\sqrt{3} - 79872 \\
&\times \ k\sqrt{2})\pi^{-1} + (188160 - 145152\sqrt{3})\pi^{-3/2} - 62464k\pi^{-2} - 229376\pi^{-5/2}] \\
&+ \ \frac{1}{3360}(\cos(\theta)B_1 + \sin(\theta)A_1)t^2\alpha_0(-7808k\pi^{-1} + 26880k\sqrt{2} + 3360\pi^{-1/2} \\
&- \ 25305\,k - 28672\,\pi^{-3/2}) - \frac{1}{420}((-\frac{1}{2}\,{B_0}^2 + \frac{1}{2}\,{A_0}^2)\sin(2\,\theta) \\
&+ \ A_0\,B_0\cos(2\,\theta))t\,[(-8085 + 10080\,\sqrt{2})\,k + (-28070 + 10080\,\sqrt{2})\,k^2 \\
&- \ 3360\pi^{-1/2} - 2128\,k\pi^{-1} + (-23640\,k^2 - 4480)\pi^{-3/2}] + \frac{1}{241920} \\
&\times \ [(-{B_0}^2 + {A_0}^2)\cos(2\,\theta) - 2\,A_0\,B_0\sin(2\,\theta)]\,t^2\,\alpha_0[(14454720\,\sqrt{2} \\
&- \ 7277445)\,k + (806400 - 78382080\,\beta\,k)\pi^{-1/2}(-2006064 \\
&- \ 1105920\,\sqrt{2} - 489888\,\sqrt{3})\,k\pi^{-1} + (-6117888 + 1741824\,\sqrt{3})\pi^{-3/2} \\
&- \ 1155072\,k\pi^{-2} - 1835008\,\pi^{-5/2}] - \frac{1}{1260}t^2[(A_0\,A_1 - B_0\,B_1)\sin(2\,\theta) \\
&+ \ (A_1\,B_0 + B_1\,A_0)\cos(2\,\theta)][(30240\,\sqrt{2} - 29295 - 5280\,\pi^{-1})\,k \\
&- \ 13020\,\pi^{-1/2} + 7168\,\pi^{-3/2}] - \frac{1}{241920}[(3\,A_0\,{B_0}^2 - {A_0}^3)\cos(3\,\theta) \\
&+ \ (-{B_0}^3 + 3\,{A_0}^2\,B_0)\sin(3\,\theta)]\,t^2[(-11158560\,\sqrt{2} + 7188615)\,k \\
&+ \ (322560 + 78382080\,\beta\,k)\pi^{-1/2} + (8350704 - 4653936\,\sqrt{3} - 2727936 \\
&\times \ \sqrt{2})\,k\pi^{-1} + 2515968 - 2612736\,\sqrt{3}\pi^{-3/2} + 608256\,k\pi^{-2} + 458752\,\pi^{-5/2}].
\end{aligned}
$$

It can be seen that ω expansion given in (3.1.1) is uniformly bounded by $M/[(1-t)(1-k)]$ for $0 \leq k, t < 1$ where M is a constant. The constant M can be easily obtained by applying the convergent geometric series on this expansion; it is found

that $M = \max\{\omega_{n,m} : \text{for all } 0 \leq z < \infty \text{ and } 0 \leq \theta < 2\pi]\}$. Thus, the power series used in the expansion (3.1.1) is valid in the range $0 \leq k, t < 1$.

Although this approach has been used by several authors, some of which include Collins and Dennis (1973a), Badr and Dennis (1985), Badr, Dennis and Kocabiyik (1995a), Kocabiyik (1996a,b), there was no attempt to determine the range of convergence of the series (3.1.1). This point was clarified by Dennis, Nguyen and Kocabiyik (2000) for the first time.

3.4 Determination of the initial flow properties

In this section the physical properties of the initial flow are determined by means of analytical expressions. The dimensionless friction and pressure drag and lift coefficients, C_{DF}, C_{DP}; C_{LF}, C_{LP} can be expressed as series in powers of t and k from present results using (2.4.2)-(2.4.5). It is found, as far as the terms calculated, that

$$C_{DF} = \frac{2\pi}{R}\left[\frac{1}{k}\left(g^1_{0,0} + g^1_{0,1}\,t + g^1_{0,2}\,t^2\right) + \left(g^1_{1,0} + g^1_{1,1}\,t + g^1_{1,2}\,t^2\right) + k\,\left(g^1_{2,0} + g^1_{2,1}\,t\right)\right]\Big|_{z=0}, \tag{3.4.1}$$

$$\begin{aligned} C_{DP} &= -\frac{2\pi}{R}\left[\frac{1}{k^2}\left(\frac{\partial g^1_{0,0}}{\partial z} + \frac{\partial g^1_{0,1}}{\partial z}\,t + \frac{\partial g^1_{0,2}}{\partial z}\,t^2\right) + \frac{1}{k}\left(\frac{\partial g^1_{1,0}}{\partial z} + \frac{\partial g^1_{1,1}}{\partial z}\,t + \frac{\partial g^1_{1,2}}{\partial z}\,t^2\right)\right. \\ &+ \left.\left(\frac{\partial g^1_{2,0}}{\partial z} + \frac{\partial g^1_{2,1}}{\partial z}\,t\right)\right]\Big|_{z=0} \end{aligned} \tag{3.4.2}$$

and

$$\begin{aligned} C_{LF} &= -\frac{2\pi}{R}\left[\frac{1}{k}\left(G^1_{0,0} + G^1_{0,1}\,t + G^1_{0,2}\,t^2\right) + \left(G^1_{1,0} + G^1_{1,1}\,t + G^1_{1,2}\,t^2\right)\right. \\ &+ \left. k\,\left(G^1_{2,0} + G^1_{2,1}\,t\right)\right]\Big|_{z=0}, \end{aligned} \tag{3.4.3}$$

$$C_{LP} = \frac{2\pi}{R}\left[\frac{1}{k^2}\left(\frac{\partial G^1_{0,0}}{\partial z}+\frac{\partial G^1_{0,1}}{\partial z}t+\frac{\partial G^1_{0,2}}{\partial z}t^2\right)+\frac{1}{k}\left(\frac{\partial G^1_{1,0}}{\partial z}+\frac{\partial G^1_{1,1}}{\partial z}t+\frac{\partial G^1_{1,2}}{\partial z}t^2\right) + \left(\frac{\partial G^1_{2,0}}{\partial z}+\frac{\partial G^1_{2,1}}{\partial z}t\right)\right]\Bigg|_{z=0}. \tag{3.4.4}$$

The moment coefficient, C_M, can also be expressed as series in powers of t and k by using (2.4.15)

$$C_M = \left[\frac{1}{k}\left(G^0_{0,0}+G^0_{0,1}t+G^0_{0,2}t^2\right)+\left(G^0_{1,0}+G^0_{1,1}t+G^0_{1,2}t^2\right)+k\left(G^0_{2,0}+G^0_{2,1}t\right)\right]\Bigg|_{z=0}. \tag{3.4.5}$$

The analytical expressions for these coefficients are given by

$$\begin{aligned}
C_{DF} &= [2(8\sqrt{2}-\frac{297}{32})\pi-\frac{32\sqrt{\pi}}{3k}-\frac{88}{15}+\frac{256\pi^{-1/2}}{9k}]t^2A_0/R \\
&+ [2(-54\beta+\frac{2}{3k})\pi^{-1/2}+2\pi^{-1/2}(\frac{14}{3}-\frac{18\sqrt{3}}{5})/k \\
&- \frac{1161\sqrt{3}}{40}+\frac{5591}{140}-\frac{416\sqrt{2}}{105}-\frac{976\pi^{-1}}{315}+2(\frac{29\sqrt{2}}{2}-\frac{1173}{128})\pi \\
&- \frac{512\pi^{-3/2}}{45k}]B_0t^2{\alpha_0}^2/R+\{(-\frac{256\pi^{-1/2}}{15k}+2(-\frac{241}{32}+8\sqrt{2})\pi \\
&- \frac{488}{105}+\frac{2\sqrt{\pi}}{k})t^2A_1+[-\frac{12}{5}-\frac{32\pi^{-1/2}}{3k}+2(-\frac{65}{8}+8\sqrt{2})\pi]t \\
&\times A_0\}\alpha_0/R+2t\pi/R(tB_2+B_1)+2[B_0+\frac{33}{256}(-145+224\sqrt{2}) \\
&\times ({B_0}^2+{A_0}^2)B_0t^2]\pi/R+\frac{1}{7560}[(-161280+816480\beta k)\pi^3 \\
&+ (343296\sqrt{2}k+862407\sqrt{3}k-1293831k)\pi^{5/2} \\
&+ (-245952+381024\sqrt{3})\pi^2-203904k\pi^{3/2}+315392\pi](-A_0+B_0\beta) \\
&\times (A_0+B_0\beta)B_0t^2/(Rk\pi^{5/2})+\frac{16}{3}t\sqrt{\pi}(4tB_2+3B_1) \\
&- \frac{1}{2}B_0\sqrt{\pi}[-16+(t+1)k^2],
\end{aligned}$$

$$
\begin{aligned}
C_{DP} &= \frac{1}{R\,k^2}\left[\left(\frac{8\,k}{\sqrt{\pi}}+8\right)t\,B_1+2\,\pi\left(16+\frac{32\,k}{3\,\sqrt{\pi}}\right)t^2\,B_2\right]-\frac{2\,\pi\,A_0\,t^2\,\alpha_1}{k\,R}\left[\left(\frac{176}{3}\right.\right.\\
&- \left.\left.\frac{128\,\sqrt{2}}{3}\right)\pi^{-1/2}-\frac{128\,\pi^{-3/2}}{9}\right]-\frac{2\,\pi\,t^2\,B_0\,{\alpha_0}^2}{k\,R}\left[\left(\frac{94}{3}-\frac{160\,\sqrt{2}}{3}\right)\pi^{-1/2}\right.\\
&+ \left.\frac{288\,\beta}{\pi}+\left(-\frac{256\,\sqrt{2}}{9}+\frac{310}{9}+\frac{18\,\sqrt{3}}{5}\right)\pi^{-3/2}+\frac{256\,\pi^{-5/2}}{45}\right]\\
&- \frac{2\,\pi\,\alpha_0}{R\,k^2}\left\{\left[\left(-32\,\sqrt{2}+32\right)\pi^{-1/2}+\frac{16\,\pi^{-3/2}}{3}\right]A_0\,k\,t\right.\\
&+ \left.\left[\left(\frac{125}{3}-\frac{128\,\sqrt{2}}{3}\right)\pi^{-1/2}+\frac{128\,\pi^{-3/2}}{15}\right]A_1\,k\,t^2\right\}-\frac{2\,\pi B_0}{R\,k^2}\left[-\frac{2\,\pi^{-7/2}}{135}\right.\\
&\times \left.\left(B_0+A_0\,\beta\right)\left(-B_0+A_0\,\beta\right)\left[\left(-4320\,\sqrt{2}+2160\right)\pi^3+19440\,\beta\,\pi^{5/2}\right.\right.\\
&+ \left.\left.\left(-1920\,\sqrt{2}+1542+1701\,\sqrt{3}\right)\pi^2+1408\,\pi\right]k\,t^2-k^2-k^2\,t-\frac{4\,k}{\sqrt{\pi}}\right];
\end{aligned}
$$

$$
\begin{aligned}
C_{LF} &= \frac{-2\,\pi\,t^2}{R\,k}\left\{\left(-k-\frac{32\,\pi^{-1/2}}{3}\right)A_2+\frac{1}{241920}\,\beta\left(A_0-B_0\,\beta\right)\left(A_0+B_0\,\beta\right)A_0\right.\\
&\times \left.\left[\left(-4521825\,k+6985440\,k\,\sqrt{2}+2580480\pi^{-1/2}+\left(-13798512\,k\,\sqrt{3}\right.\right.\right.\right.\\
&- \left.\left.\left.\left.5492736\,k\,\sqrt{2}+20701296\,k\right)\pi^{-1}+\left(-6096384\,\sqrt{3}+3935232\right)\pi^{-3/2}\right.\right.\right.\\
&+ \left.\left.\left.3262464\,k\,\pi^{-2}-5046272\pi^{-5/2}\right)\beta+13063680\,k\pi^{-1/2}\right]\right.\\
&+ \left.\left[\left(-\frac{297}{32}-\frac{44}{15\,\pi}+8\,\sqrt{2}\right)k-\frac{16\,\pi^{-1/2}}{3}+\frac{128\,\pi^{-3/2}}{9}\right]\alpha_1\,B_0\right.\\
&+ \left.\left[\left(-\frac{29\,\sqrt{2}}{2}+\frac{1173}{128}\right)k+\left(\frac{208\,\sqrt{2}}{105}+\frac{1161\,\sqrt{3}}{80}-\frac{5591}{280}\right)k\pi^{-1}\right.\right.\\
&+ \left.\left.\left(-\frac{2}{3}+54\,\beta\,k\right)\pi^{-1/2}+\left(\frac{18\,\sqrt{3}}{5}-\frac{14}{3}\right)\pi^{-3/2}+\frac{488\,k}{315\,\pi^2}\right.\right.\\
&+ \left.\left.\frac{256\,\pi^{-5/2}}{45}\right]A_0\,{\alpha_0}^2+\left[-\frac{128\,\pi^{-3/2}}{15}+\left(-\frac{244}{105\,\pi}+\frac{15}{32}\right)k+\pi^{-1/2}\right]\alpha_0\,B_1\right\}\\
&+ \frac{1}{R}\left[2\,\pi\left(-\frac{k\,t}{2}+\frac{8}{k}-\frac{k}{2}\right)\sqrt{\pi}+\left(\frac{32\,\pi^{-1/2}}{3\,k}-16\,\pi\,\sqrt{2}+\frac{12}{5}+\frac{65\,\pi}{4}\right)\alpha_0\,t\,B_0\right.\\
&+ \left.\left(-\frac{16\,\sqrt{\pi}}{k}-2\,\pi\right)A_1\,t\right],
\end{aligned}
$$

$$
\begin{aligned}
C_{LP} &= \frac{2\pi}{R\,k^2}\left\{t^2\left(\left[\left(-\frac{128\sqrt{2}}{3}+\frac{176}{3}\right)\pi^{-1/2}-\frac{128\,\pi^{-3/2}}{9}\right]B_0\,k\,\alpha_1\left[\left(-\frac{94}{3}\right.\right.\right.\right.\\
&+ \left.\left.\left.\left.\frac{160\sqrt{2}}{3}\right)\pi^{-1/2}-\frac{288\,\beta}{\pi}+\left(-\frac{310}{9}+\frac{256\sqrt{2}}{9}-\frac{18\sqrt{3}}{5}\right)\pi^{-3/2}\right.\right.\right.\\
&- \left.\left.\left.\frac{256\,\pi^{-5/2}}{45}\right]A_0\,k\,{\alpha_0}^2+\left(\frac{128\,\pi^{-3/2}}{15}+\frac{125}{3\sqrt{\pi}}-\frac{128\sqrt{2}}{3\sqrt{\pi}}\right)B_1\,k\,\alpha_0\right.\\
&+ \left(\frac{32\,\pi^{-1/2}}{3}+16\right)A_2+\frac{2}{135}(B_0+A_0\,\beta)(-B_0+A_0\,\beta)\,A_0\\
&\times \left[(2160-4320\sqrt{2})\pi^{-1/2}+\frac{19440\,\beta}{\pi}+(-1920\sqrt{2}+1701\sqrt{3}\right.\\
&+ \left.1542)\pi^{-3/2}+1408\pi^{-5/2}\right](8+8\,k\pi^{-1/2})\,t\,A_1+\left[(t+1)\,k^2\right.\\
&+ \left.4\,k\pi^{-1/2}\right]A_0+\left[(32-32\sqrt{2})\pi^{-1/2}+\frac{16\,\pi^{-3/2}}{3}\right]k\,t\,\alpha_0\,B_0\Bigg\};
\end{aligned}
$$

$$
\begin{aligned}
C_M &= 2\,(\alpha_0+2\,\alpha_1\,t)\pi^{-1/2}+\left[\frac{2\,\pi^{-5/2}\,\alpha_0}{135}\,({A_0}^2+{B_0}^2)\,(90\,\pi^2-1458\sqrt{3}\,\pi\right.\\
&+ \left.2535\,\pi-1024)-\frac{\pi^{-3/2}}{45}\,(-B_0\,A_1+A_0\,B_1)\,(-1024+315\,\pi)+\frac{16}{3}\,\frac{\alpha_2}{\sqrt{\pi}}\right]t^2\\
&+ k\{-\frac{1}{2}\,\alpha_0-\frac{1}{2}\,\alpha_1\,t+[\frac{1}{80640}({A_0}^2+{B_0}^2)(-3429216\sqrt{3}\,\pi+705600\sqrt{2}\,\pi^2\\
&- 196608\sqrt{2}\,\pi-419265\,\pi^2+720896+4224528\,\pi)\alpha_0\,\pi^{-2}+\frac{\pi}{1680}\\
&\times (-B_0\,A_1+A_0\,B_1)\,(-22528+7035\,\pi)-\frac{1}{2}\,\alpha_2]t^2\}+\frac{k^2\,(\frac{3}{8}\,\alpha_0+\frac{1}{4}\,\alpha_1\,t)}{\sqrt{\pi}}.
\end{aligned}
$$

The dimensionless pressure distribution over the cylinder surface, $\tilde{p_0}$, can be written in terms of the series expansion by using (2.3.2) as follows

$$
\begin{aligned}
\tilde{p_0}(\theta) &= \frac{8}{45}\,{\alpha_0}^2t^2\,[(-705+1200\sqrt{2})\pi^{-1/2}-6480\,\beta\pi^{-1/2}+(-775-81\sqrt{3}\\
&+ 640\sqrt{2})\pi^{-3/2}-128\pi^{-5/2}](A_0\sin(\theta)+B_0\cos(\theta))\,/(k\,R)\\
&- \frac{1}{30}\,t\,(960\sqrt{2}\,k-2415\,k+\frac{3840\sqrt{2}-3840}{\sqrt{\pi}}-\frac{2064\,k}{\pi}-\frac{640}{\pi^{3/2}})
\end{aligned}
$$

$$\times \quad (\sin(\theta)\, B_0 - \cos(\theta)\, A_0)/(k\, R\, \alpha_0) - \frac{4}{15}\, t^2\, [-128 + (640\,\sqrt{2} - 625)\,\pi] \quad (3.4.6)$$

$$\times \quad (B_1 \sin(\theta) - A_1 \cos(\theta))\, \alpha_0/(k\, R\, \pi^{3/2}) - \frac{64}{9}\, t^2\, (-33\,\pi + 8 + 24\,\sqrt{2}\,\pi) \quad (3.4.7)$$

$$\times \quad (\sin(\theta)\, B_0 - \cos(\theta)\, A_0)\, \alpha_1/(k\, \pi^{3/2}\, R) + \frac{64}{3}\, t^2\, (\frac{2\,k}{\sqrt{\pi}} + 3)\, (\cos(\theta)\, B_2 \quad (3.4.8)$$

$$+ \quad \sin(\theta)\, A_2)/(k^2\, R) + 4\, t/(k^2\, R)\, (8 + \frac{8\,k}{\sqrt{\pi}} + k^2)\, (\cos(\theta)\, B_1 + \sin(\theta)\, A_1)$$

$$+ \quad \frac{8}{135}\, \frac{\pi^{-7/2}}{kR} (A_0 \sin(\theta) + B_0 \cos(\theta))\, ({B_0}^2 + {A_0}^2) \{[(-4320\,\sqrt{2} + 2160)\,\pi^3$$

$$+ \quad 19440\,\pi^{5/2}\,\beta + (1701\,\sqrt{3} - 1920\,\sqrt{2} + 1542)\,\pi^2 + 1408\,\pi]\, t^2$$

$$- \quad \frac{540}{\sqrt{\pi}} - 135\,k\} + 2[\dot{V}(t) \sin(\theta) + \dot{V}(t) \cos(\eta)(\cos(\theta) - 1)]. \quad (3.4.9)$$

3.5 Symbolic computational program

The exact solutions for $\omega_{0,1}$, $\Psi_{0,1}$, $\omega_{0,2}$, $\Psi_{0,2}$, $\omega_{1,0}$, $\Psi_{1,0}$, $\omega_{1,1}$, $\Psi_{1,1}$, $\omega_{1,2}$, $\Psi_{1,2}$, $\omega_{2,0}$, $\Psi_{2,0}$, $\omega_{2,1}$ and $\Psi_{2,1}$ are obtained and checked with a symbolic computation program written in Maple VII. The computational flowchart is presented in Figure 3.1. The program uses a step-by-step procedure described in Section 3.3 to solve the equations (3.1.2) and (3.1.3) subject to the conditions (3.1.6)-(3.1.8). The solution for the vorticity components, $\omega_{n,m}$, is determined by expanding first equation (3.1.2) into a set of ordinary differential equations in terms of Fourier components. Each ordinary differential equation for the vorticity component is solved by determining the homogenous solution in terms of parabolic cylinder functions and then implementing the method of variation of parameters to obtain the particular solution. The general solution for each vorticity component is completed by determining the unknown coefficients through using the integral conditions and conditions at infinity. The corresponding stream function components, $\Psi_{n,m}$, are determined by integrating equation (3.1.3)

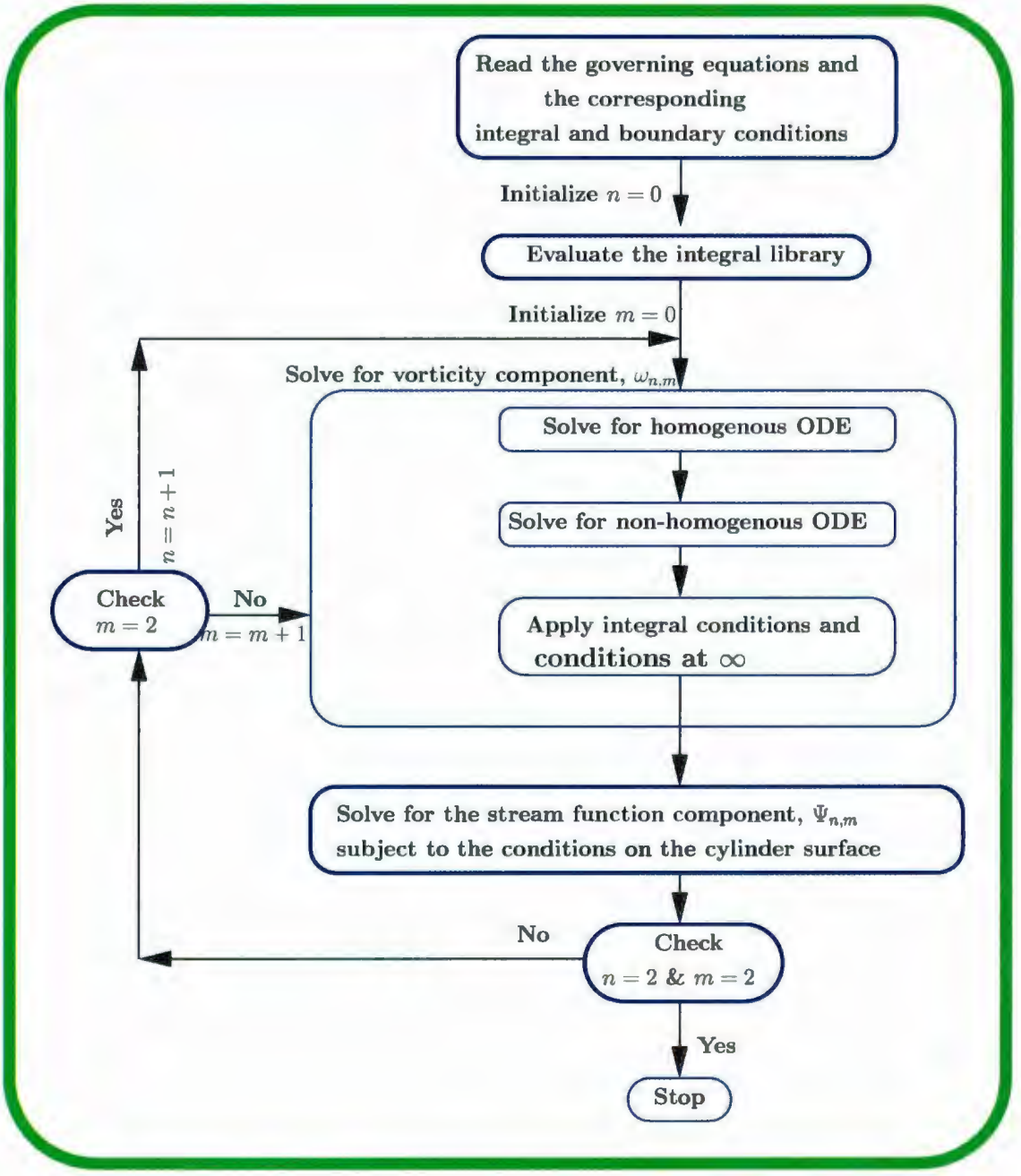

Figure 3.1: Symbolic computation flowchart

twice subject to the conditions on the surface of the cylinder. Finally, the solutions for all the vorticity components are used to calculate the flow properties such as the surface vorticity, drag, lift, moment and surface pressure coefficients. The solution procedure is summarized as

Step 1: Evaluate special integrals from the integral library.

Step 2: Set $n = 0$ and do Steps 3-6

Step 3: Set $m = 0$ and do Steps 4-6

Step 4: Read the equations for the vorticity components given in (3.1.2) and (3.1.3) with the related boundary conditions (3.1.6) -(3.1.8). Then do steps 5 and 6.

Step 5: Use the powerful tools of Maple to combine the equation of each vorticity component term, $\omega_{n,m}$, to be in the Fourier form as in (3.2.3) and then solve the resulted equations. *Thus, $\omega_{n,m}$ has been determined*

Step 6: Determine the solutions for the corresponding stream function component, $\Psi_{n,m}$, by integrating twice equation (3.1.3) with using the required boundary conditions (3.1.6).

Step 7: increment m by 1 and repeat steps 4-6 until the required order.

Step 8: increment n by 1 and repeat steps 3-6 until the required order.

The integral library evaluates over 300 integrals involving error functions, such as

$$\int z^4 \mathrm{erf}(z)^2 e^{-z^2} dz,$$

$$\int z^9 \mathrm{erf}(\sqrt{2}z)\mathrm{erf}(z) dz,$$

$$\int z^8 \mathrm{erf}(z)^2 \mathrm{erf}(\sqrt{3}z) e^{z^2} dz.$$

This integral library used in this program was developed by Karl Lawrence in 2001 and is an extension of the library which was originally produced by Dr. Serpil Kocabiyik in 1995. Furthermore, this library had been used to analyze the solution for the initial motion of circular cylinders and spheres Badr *et al.* (1995a), Kocabiyik (1996a,b) and Lawrence (2002).

Chapter 4

Numerical Method of Solution

The numerical method presented in this chapter aims solving the two-dimensional, unsteady incompressible Navier-Stokes equations in an unbounded domain to model the hydrodynamic environment around a circular cylinder undergoing combined (2-DoF) rotary and translational oscillation. The numerical solution of unbounded problems requires essentially two levels of approximation as reported by Grosch and Orzag (1977). The first one consists in passing from the continuum problem to a discrete set of algebraic equations. The second one requires the proper representation of the boundary conditions after representing the unbounded domain by a finite domain. The problem is described and formulated in modified polar coordinates in Chapter 2 which in turn includes a natural periodic direction θ. The numerical method, in the first stage, is based on the Fourier Galerkin approximation scheme as described in Chapter 2. In the second stage, an implicit Crank-Nicolson method is employed in the time advancement and a second-order central difference scheme is used for spatial derivatives. The discretized nonlinear vorticity equations are solved using a Gauss-Seidel iterative method. Special care has been taken to account for the impulsive start

of the motion. This is done by implementing the special starting procedure, devised by Collins and Dennis (1973a,b) and Badr and Dennis (1985), using similarity coordinates later replaced by physical coordinates. The present method is an extension of the method developed by Collins and Dennis (1973b) and Badr and Dennis (1985) for combined (2-DoF) translational and rotational harmonic cylinder oscillations.

In the following subsections we will describe the numerical method in detail. This method is then used to calculate the unsteady initial flow past a cylinder at a Reynolds number of $R = 855$. Finally, it is tested for uniform flow past a stationary and moving cylinders at five values of the Reynolds number: $R = 100,\ 106,\ ,500,\ 855,\ 10^3$.

4.1 Numerical Solution Procedure

4.1.1 Mesh considerations in computational domains

The cylinder motion starts suddenly from rest at time $t = 0$. Immediately following the start of the cylinder motion, a very thin boundary-layer develops over the cylinder surface and grows with time. Accordingly, we divide the solution time into two distinct zones:

$$(0,\ t_s] \ \text{ and } \ (t_s,\ t_{max}]$$

where, t_s represents the switching time from the spatial boundary-layer coordinate, z, to the spatial physical coordinate, ξ, and t_{max} represents the maximum time used at the end of calculations. First zone begins following the start of fluid motion and continues until the boundary-layer becomes thick enough to use physical coordinates at $t = t_s$. In this zone, we use boundary-layer coordinates to capture the boundary-layer

development of the flow. This is done by the making use of the coordinate stretching given in (2.2.11). In the second zone boundary-layer coordinates are replaced by physical coordinates. This zone starts at $t = t_s^+$ and continues until the termination of calculations when $t = t_{max}$.

The solution domains in both zones, respectively, are given by

$$D_{(z,\theta,t)} = \{(z,\theta,t) : (z,\theta) \in (0,\infty) \times [0,\, 2\pi),\, 0 < t \leq t_s\}, \tag{4.1.1}$$

$$D_{(\xi,\theta,t)} = \{(\xi,\theta,t) : (\xi,\theta) \in (0,\infty) \times [0,\, 2\pi),\, t_s < t \leq t_{max}\}. \tag{4.1.2}$$

Since the computational domains along the spatial, z and ξ, directions are unbounded, we choose artificial outer boundaries for the numerical treatment. Placing the artificial outer boundary, approximating infinity, well outside the growing boundary layer enables us to enforce the free-stream conditions (2.2.16a,b) and (2.2.9a,b) along the line z_∞ and ξ_∞ in the two computational domains, $D_{(z,\theta,t)}$ and $D_{(\xi,\theta,t)}$, respectively. We point out that implementing the boundary-layer coordinate variable z essentially creates a moving mesh in the actual physical domain which grows in time, $\xi = 2(2t/R)^{1/2}z$, to properly accommodate the vortex shedding process until switching to the physical coordinate ξ. Figure 4.1 illustrates how the grid expands for the case of $R = 855$, $z_\infty = 8$ at times $t = 0.4, 0.8$. Shown are 10 equally spaced grid lines for $0 \leq z \leq z_\infty$. If z_∞ is chosen to be large enough then as time increases the outer boundary in the first computational domain will expand and be far enough away that no shed vortices will have reached it. If this is so, then we can correctly apply the condition of zero vorticity along the outer boundary. Although shed vortices propagate faster than the rate of boundary-layer growth, they weaken as they travel

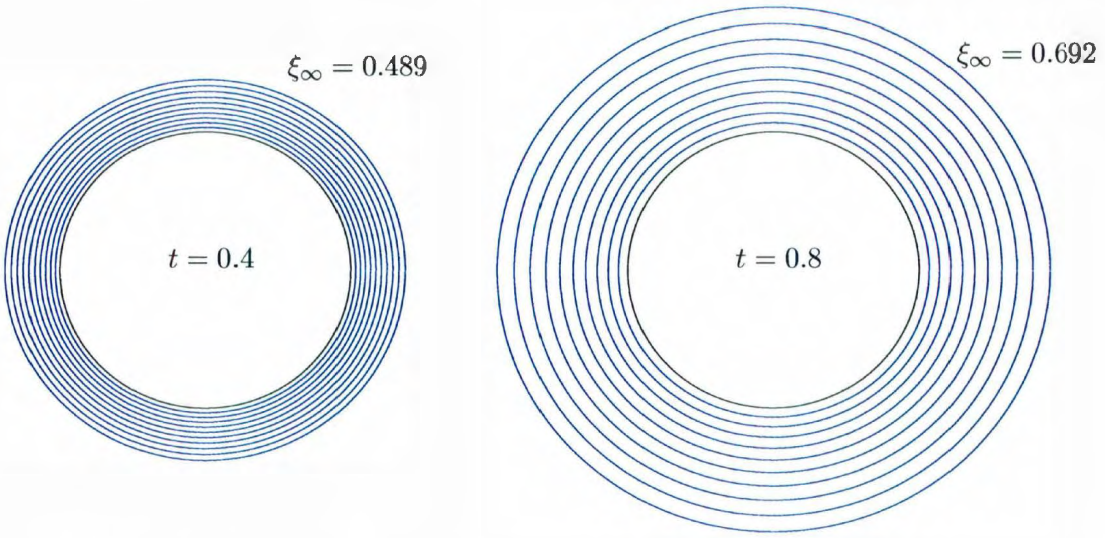

Figure 4.1: An illustration to show how the grid expands with the use of the spatial boundary-layer coordinate z in the first computational domain when viewed in the actual physical space: $R = 855$, $z_\infty = 8$.

downstream in the wake. Clearly, as time increases we may encounter a problem whereby the vorticity reaches the boundary, this is why we replace z by ξ at $t = t_s$ when boundary-layer thickens and it is then more realistic to continue the integration in the physical spatial coordinate ξ so that the grid size in the actual physical space does not become too large. Figure 4.2 illustrates the effect of coordinate stretching property on location of the outer boundaries. The outer boundary, $\xi_\infty = kz_\infty$, is constantly being pushed further away from the cylinder surface at a rate which reflects the growth of the boundary layer when $0 \leq t \leq t_s$. For this reason we are justified in saying that the vorticity, by the mechanism of convection, does not reach the outer boundary, ξ_∞. The location of the outer boundary remains fixed when $t > t_s$ as shown Figure 4.2.

We will now give an outline of the numerical solution procedure in boundary-layer coordinates by assuming that the artificial outer boundary is known.

For simplicity we divide the finite difference solution into two parts where in the first part the solution for the vorticity components G_0, G_n and g_n is discussed and in the second part the solution for the stream function components F_0, F_n and f_n is discussed. In fact these solutions from the two parts are combined together by incorporating the Gauss-Seidel iterative method to obtain a consistent solution for the system given by (2.2.13) and (2.2.14).

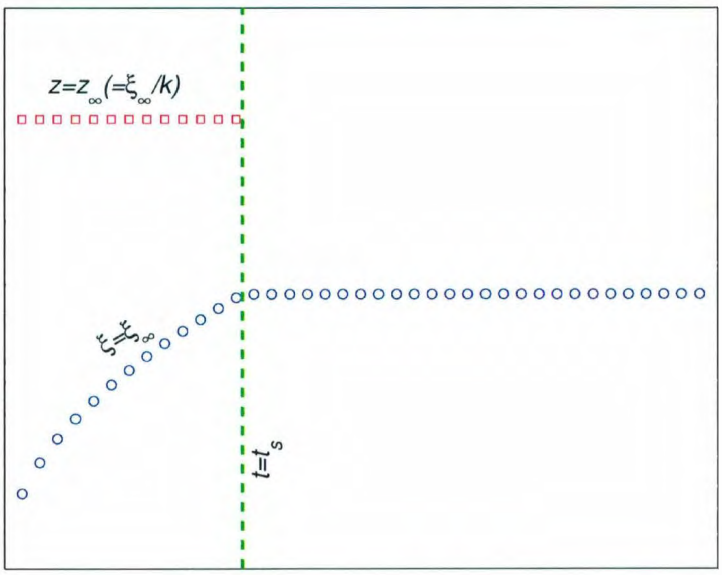

Figure 4.2: An illustration of the implicit relation between z_∞ and ξ_∞ and the stretching property in the first zone, $t \in [0, t_s)$.

The finite difference schemes require dividing the space computational domain $[0, z_\infty]$

into $M+2$ equal subintervals whose endpoints are the mesh points, for $i = 0, 1, ..., M+1$ where $h_z = \frac{z_{M+1}}{M+1}$ represents the uniform grid step. The uniform grids in the computational domain, $[0, z_\infty]$, to a uniform grids in the physical space. However, we set Δt_{j+1} be a non-uniform time increment given by $\Delta t_{j+1} = t_{j+1} - t_j$, where $j = 1, 2, ...$ and $t_1 = 0$. Hence, for each time step t_{j+1} we need to determine the solutions at the mesh points $z_i = i\,h_z$, for $i = 0, 1, ..., M+1$. Furthermore, since we are going to incorporate the Gauss-Seidel iterative method, the solutions at the previous time step t_j is required. The convergence criterion is achieved when the difference between two successive iterations of all the calculated solutions falls below the specified tolerance of $\epsilon = 10^{-6}$ i.e.

$$\begin{aligned} &|G_n^{m+1}(z,t) - G_n^m(z,t)| \leq 10^{-6}, \quad |F_n^{m+1}(z,t) - F_n^m(z,t)| \leq 10^{-6} \\ &|g_n^{m+1}(z,t) - g_n^m(z,t)| \leq 10^{-6}, \quad |f_n^{m+1}(z,t) - f_n^m(z,t)| \leq 10^{-6} \end{aligned} \tag{4.1.3}$$

for all integers $0 \leq n \leq N$. Here m denotes the iteration step and $|.|$ is the infinity norm.

We summarize the numerical solution technique in the boundary layer coordinates by listing the numerical procedure:

Step 1: Assume that $F_0(z,t)$, $F_n(z,t)$, $f_n(z,t)$, $G_0(z,t)$, $G_n(z,t)$ and $g_n(z,t)$ are known at $t = t_j$, for all $0 \leq z \leq z_\infty$. In the following steps we determine the solutions for $F_0(z,t)$, $F_n(z,t)$, $f_n(z,t)$, $G_0(z,t)$, $G_n(z,t)$ and $g_n(z,t)$ at $t = t_{j+1}$ for $0 \leq z \leq z_\infty$.
Step 2: Use equation (2.2.13a) together with the information in Step 1 to determine $G_0(z,t)$, for $0 \leq z \leq z_\infty$.

Step 3: Use equation (2.2.14a) together with the $G_n(z,t)$ obtained in Step 2 to determine $F_0(z,t)$, for $0 \leq z \leq z_\infty$.

$$\text{For} \quad n = 1, 2, \cdots, N; \qquad \text{do Steps 4 and 5.}$$

Step 4: Use the equation (2.2.13b,c) with the most recent information to determine $G_n(z,t)$ and $g_n(z,t)$, for $0 \leq z \leq z_\infty$.

Step 5: Use equations (2.2.14b,c) together with $G_n(z,t)$ and $g_n(z,t)$ obtained in Step 4 to determine $F_n(z,t)$ and $f_n(z,t)$ respectively, for $0 \leq z \leq z_\infty$.

Step 6: Repeat Steps 2 - 5 until the convergence criteria given in (4.1.3) is achieved.

4.1.2 The numerical method of solution for vorticity components

In this section we discuss the solutions of (2.2.13) subject to (2.2.16c) and (2.2.17) for G_n and g_n respectively at time step $t = t_{j+1}$ and fixed n. First of all, assume that $F_0(z_i,t)$, $F_n(z_i,t)$, $f_n(z_i,t)$, $G_0(z_i,t)$, $G_n(z_i,t)$ and $g_n(z_i,t)$ are known at the previous time step $t = t_j$ and for $i = 0, 1, \cdots, M+1$. This assumption is reasonable since the initial condition at $t = 0$ is known and given by (2.2.18). Furthermore, we assume that $F_\nu(z_i,t)$, $f_\nu(z_i,t)$, $G_\nu(z_i,t)$ and $g_\nu(z_i,t)$ are known at $t = t_{j+1}$ for $\nu < n$.

Each equation of (2.2.13) can be rewritten in the form

$$4t\frac{\partial G_n}{\partial t}(z,t) = Q_n(z,t), \tag{4.1.4}$$

$$4t\frac{\partial g_n}{\partial t}(z,t) = q_n(z,t) \tag{4.1.5}$$

where $Q_n(z,t)$ and $q_n(z,t)$ are the right hand sides of equations (2.2.13a,b) and (2.2.13c) respectively.

The Crank-Nicolson scheme was successfully used to advance the solution by integrating equations (4.1.4) and (4.1.5) with respect to t from $t = t_j$ to $t = t_{j+1}$ and then using the trapezoidal rule to obtain

$$Q_n^{j+1}(z) + Q_n^j(z) = \frac{8}{\Delta t_{j+1}}\left[t_{j+1} - \frac{\Delta t_{j+1}}{2}\right]\left[G_n^{j+1}(z) - G_n^j(z)\right], \tag{4.1.6}$$

$$q_n^{j+1}(z) + q_n^j(z) = \frac{8}{\Delta t_{j+1}}\left[t_{j+1} - \frac{\Delta t_{j+1}}{2}\right]\left[g_n^{j+1}(z) - g_n^j(z)\right], \tag{4.1.7}$$

where the symbol $(.)^j$ indicates the value of the function at t_j. Note that each of (4.1.6) and (4.1.7) has a local truncation error of order $O((\Delta t_{j+1})^2)$.

Substituting expressions for $Q_n^{j+1}(z)$ and $q_n^{j+1}(z)$ in equations (4.1.6) and (4.1.7), then arranging the terms we obtain

$$\begin{aligned} e^{-2k_{j+1}z}\frac{d^2G_n^{j+1}}{dz^2}(z) \;+\; & 2z\frac{dG_n^{j+1}}{dz}(z) + [2 - n^2k_{j+1}^2e^{-2k_{j+1}z} - \frac{4}{\Delta t_{j+1}}(2t_{j+1} \\ & - \Delta t_{j+1})]G_n^{j+1}(z) = 2t_{j+1}e^{-2k_{j+1}z}[n\frac{dG_0^{j+1}}{dz}(z)f_n^{j+1}(z) \\ & - S_n^{j+1}(z)] - Q_n^j(z) - \frac{4}{\Delta t_{j+1}}(2t_{j+1} - \Delta t_{j+1})G_n^j(z), \end{aligned} \tag{4.1.8}$$

$$\begin{aligned} e^{-2k_{j+1}z}\frac{d^2g_n^{j+1}}{dz^2}(z) \;+\; & 2z\frac{dg_n^{j+1}}{dz}(z) + [2 - n^2k_{j+1}^2e^{-2k_{j+1}z} - \frac{4}{\Delta t_{j+1}}(2t_{j+1} \\ & - \Delta t_{j+1})]g_n^{j+1}(z) = -2t_{j+1}e^{-2k_{j+1}z}[n\frac{dG_0^{j+1}}{dz}(z)F_n^{j+1}(z) \\ & + T_n^{j+1}(z)] - q_n^j(z) - \frac{4}{\Delta t_{j+1}}(2t_{j+1} - \Delta t_{j+1})g_n^j(z). \end{aligned} \tag{4.1.9}$$

where $k_j = (8t_j/R)^{\frac{1}{2}}$.

Applying the central finite difference approximation with respect to z on all the derivatives for all functions in equations (4.1.8) and (4.1.9) such that

$$\frac{d(.)}{dz}(z_i) = \frac{(.)(z_{i+1}) - (.)(z_{i-1})}{2h_z} - \frac{h_z^2}{6}\frac{d^3(.)}{dz^3}(\epsilon_{i1}),$$

$$\frac{d^2(.)}{dz^2}(z_i) = \frac{(.)(z_{i-1}) - 2(.)(z_i) + (.)(z_{i+1})}{h_z^2} + \frac{h_z^2}{12}\frac{d^4(.)}{dz^4}(\epsilon_{i2}),$$

for some ϵ_{i1}, $\epsilon_{i2} \in (z_{i-1}, z_{i+1})$ gives tri-diagonal systems, which can be rewritten in the following form (after deleting the error terms)

$$A_n^{i,j+1}G_n^{i-1,j+1} + B^{i,j+1}G_n^{i,j+1} + C^{i,j+1}G_n^{i+1,j+1} = D_{G_n}^{i,j+1} + E_{G_n}^{i,1}, \tag{4.1.10}$$

$$A_n^{i,j+1}g_n^{i-1,j+1} + B^{i,j+1}g_n^{i,j+1} + C^{i,j+1}g_n^{i+1,j+1} = D_{g_n}^{i,j+1} + E_{g_n}^{i,1} \tag{4.1.11}$$

where

$$A_n^{i,j+1} = 2e^{-2k_{j+1}z_i} - 2z_i h_z,$$

$$B_n^{i,j+1} = 2h_z^2\left[2 - n^2k_{j+1}^2e^{-2k_{j+1}z_i} - \frac{4}{\Delta t_{j+1}}(2t_{j+1} - \Delta t_{j+1})\right] - 4e^{-2k_{j+1}z_i},$$

$$C_n^{i,j+1} = 2e^{-2k_{j+1}z_i} + 2z_i h_z,$$

$$D_{G_n}^{i,j+1} = 4h_z^2 t_{j+1}e^{-2k_{j+1}z_i}\left[\frac{n}{2h_z}f_n^{i,j+1}\left(G_0^{i+1,j+1} - G_0^{i-1,j+1}\right) - S_n^{i,j+1}\right],$$

$$D_{g_n}^{i,j+1} = -4h_z^2 t_{j+1}e^{-2k_{j+1}z_i}\left[\frac{n}{2h_z}F_n^{i,j+1}\left(G_0^{i+1,j+1} - G_0^{i-1,j+1}\right) + T_n^{i,j+1}\right],$$

$$E_{G_n}^{i,j} = -2h_z^2\left[Q_n^{i,j} + \frac{4}{\Delta t_{j+1}}(2t_{j+1} - \Delta t_{j+1})G_n^{i,j}\right],$$

$$E_{g_n}^{i,j} = -2h_z^2\left[q_n^{i,j} + \frac{4}{\Delta t_{j+1}}(2t_{j+1} - \Delta t_{j+1})g_n^{i,j}\right]$$

where $(.)^i = (.)(z_i)$. It is noted that the local truncation error for (4.1.10) and (4.1.11) is of order $O((\Delta t_{j+1})^2 + h_z^2)$.

The solution of each tri-diagonal system in (4.1.10) and (4.1.11) requires the values for $G_n^{0,j+1}$, $g_n^{0,j+1}$, $G_n^{M+1,j+1}$ and $g_n^{M+1,j+1}$. In fact, these required values correspond to the boundary conditions $G_n(0, t_{j+1})$, $g_n(0, t_{j+1})$, $G_n(z_{M+1}, t_{j+1})$ and $g_n(z_{M+1}, t_{j+1})$. The far field condition (2.2.9c) gives that $G_n^{M+1,j+1} = 0$ and $g_n^{M+1,j+1} = 0$. The values for $G_n^{0,j+1}$ and $g_n^{0,j+1}$ can be determined implicitly from the integral conditions (2.2.10) by writing these integral conditions as a numerical quadrature formula to relate the boundary value with the values of the corresponding function at the internal points, $z_1, z_2, ..., z_M$. Thus, systems (4.1.10) and (4.1.11) can be rewritten as

$$H\mathbf{G}_n^{j+1} = \hat{D}_{G_n}^{j+1} + \hat{E}_{G_n}^{j}, \tag{4.1.12}$$

$$H\mathbf{g}_n^{j+1} = \hat{D}_{g_n}^{j+1} + \hat{E}_{g_n}^{j} \tag{4.1.13}$$

where

$$H = \begin{bmatrix} B_n^{1,j+1} & C_n^{1,j+1} & 0 & \cdots & 0 \\ A_n^{2,j+1} & B_n^{2,j+1} & C_n^{2,j+1} & \vdots & 0 \\ 0 & \ddots & \ddots & \ddots & 0 \\ \vdots & 0 & A_n^{M-1,j+1} & B_n^{M-1,j+1} & C_n^{M-1,j+1} \\ 0 & \cdots & 0 & A_n^{M,j+1} & B_n^{M,j+1} \end{bmatrix},$$

$$\mathbf{G}_n^{j+1} = \begin{bmatrix} G_n^{1,j+1} \\ G_n^{2,j+1} \\ \vdots \\ G_n^{M-1,j+1} \\ G_n^{M,j+1} \end{bmatrix}, \quad \hat{E}_{G_n}^{j} = \begin{bmatrix} E_{G_n}^{1,j} \\ E_{G_n}^{2,j} \\ \vdots \\ E_{G_n}^{M-1,j} \\ E_{G_n}^{M,j} \end{bmatrix}, \quad \hat{D}_{G_n}^{j+1} = \begin{bmatrix} D_{G_n}^{1,j+1} - A_n^{1,j+1} G_n^{0,j+1} \\ D_{G_n}^{2,j+1} \\ \vdots \\ D_{G_n}^{M-1,j+1} \\ D_{G_n}^{M,j+1} \end{bmatrix},$$

$$\mathbf{g}_n^{j+1} = \begin{bmatrix} g_n^{1,j+1} \\ g_n^{2,j+1} \\ \vdots \\ g_n^{M-1,j+1} \\ g_n^{M,j+1} \end{bmatrix}, \quad \hat{E}_{g_n}^{j} = \begin{bmatrix} E_{g_n}^{1,j} \\ E_{g_n}^{2,j} \\ \vdots \\ E_{g_n}^{M-1,j} \\ E_{g_n}^{M,j} \end{bmatrix}, \quad \hat{D}_{g_n}^{j+1} = \begin{bmatrix} D_{g_n}^{1,j+1} - A_n^{1,j+1} g_n^{0,j+1} \\ D_{g_n}^{2,j+1} \\ \vdots \\ D_{g_n}^{M-1,j+1} \\ D_{g_n}^{M,j+1} \end{bmatrix}.$$

It is noted that $\hat{D}_{G_n}^{j+1}$ and $\hat{D}_{g_n}^{j+1}$ appear in the right hand side of (4.1.10) depend on the solution $\mathbf{G}_n^{j+1}$ or $\mathbf{G}_n^{j+1}$ at time $t = t_{j+1}$, so the Gauss-Siedel iterative technique is used with the recent information for the dependent variables. In fact, we need to solve $2N + 1$ equations of the forms (4.1.12) and (4.1.13). However, it is noted that the matrix H is strictly diagonally dominant under the condition

$$\Delta t_{j+1} < \frac{4h_z^2 t_{j+1}}{3h_z^2 + z_i h_z - e^{-2k_{j+1} z_i}}, \qquad \text{when} \qquad A_n^{i,j+1} < 0 \tag{4.1.14}$$

and thus it is non-singular. Consequently, each of the non-homogenous systems (4.1.12) and (4.1.13) has a unique solution and can be solved by a direct method which is stable with respect to the growth of roundoff error [see for example Ascher *et al.* (1995)].

4.1.3 The numerical method of solution for stream function components

The calculated vorticity components $\mathbf{G}_n^{j+1}$ and $\mathbf{g}_n^{j+1}$ will be used to calculate the corresponding stream function components $\mathbf{F}_n^{j+1}$ and $\mathbf{f}_n^{j+1}$ by solving equations (2.2.5) at $t = t_{j+1}$. The integration of (2.2.5a) subject to the (2.2.8) is quite simple and thus, it will not be considered here. Furthermore, since the equations for $\mathbf{F}_n^{j+1}$ and $\mathbf{f}_n^{j+1}$ are similar for $n \neq 0$ we only present the details of the solution for $\mathbf{F}_n^{j+1}$. (2.2.5b) can be rewritten in an ordinary differential equations form as

$$\frac{d^2F_n^{j+1}}{dz^2}(z) - \beta^2 F_n^{j+1}(z) = r_n^{j+1}(z), \tag{4.1.15}$$

subject to

$$F_n^{j+1}(0) = 0 \quad \frac{\partial F_n^{j+1}}{\partial z}(0) = 0 \tag{4.1.16}$$

where $\beta = nk_{j+1}$ and $r_n^{j+1}(z) = e^{2k_{j+1}z}G_n(z, t_{j+1})$. It is noted by Dennis and Chang (1969) that most step-by-step procedures applied to solve (4.1.16) for large β are unsatisfactory. Thus, the stable integration procedure given by Dennis and Chang (1969) is used to obtain the numerical solution. The procedure is to factorize equation (4.1.15) as follows

$$\left(\frac{d}{dz} - \beta\right)\left(\frac{d}{dz} + \beta\right) F_n^{j+1}(z) = r_n^{j+1}(z). \tag{4.1.17}$$

For simplicity define the functions $P_n^{j+1}(z)$ and $Q_n^{j+1}(z)$ by

$$P_n^{j+1}(z) = \frac{dF_n^{j+1}}{dz}(z) + \beta F_n^{j+1}(z), \tag{4.1.18a}$$

and

$$Q_n^{j+1}(z) = \frac{dF_n^{j+1}}{dz}(z) - \beta F_n^{j+1}(z). \tag{4.1.18b}$$

P_n^{j+1} and Q_n^{j+1} satisfy the following equations

$$\frac{dP_n^{j+1}}{dz}(z) - \beta P_n^{j+1}(z) = r_n^{j+1}(z), \tag{4.1.19a}$$

$$\frac{dQ_n^{j+1}}{dz}(z) + \beta Q_n^{j+1}(z) = r_n^{j+1}(z). \tag{4.1.19b}$$

According to the boundary conditions of (4.1.16), the initial conditions for the equations (4.1.19) are given by

$$P_n^{j+1}(0) = 0 \qquad \text{and} \qquad Q_n^{j+1}(0) = 0.$$

Thus, equation (4.1.15) is equivalent to a set of coupled equations and initial conditions given by

$$\begin{cases} \dfrac{dQ_n^{j+1}}{dz}(z) + \beta Q_n^{j+1}(z) = r_n^{j+1}(z), \\ \\ Q_n^{j+1}(0) = 0; \end{cases} \tag{4.1.20a}$$

and

$$\begin{cases} \dfrac{dP_n^{j+1}}{dz}(z) - \beta P_n^{j+1}(z) = r_n^{j+1}(z), \\ \\ P_n^{j+1}(0) = 0. \end{cases} \tag{4.1.20b}$$

To solve equation (4.1.20a) for $Q_n^{j+1}(z)$, we multiply both sides of it by $e^{\beta z}$ and then integrating with respect to z from $z = z_{i-1}$ to $z = z_{i+1}$, one obtains

$$Q_n^{i+1,j+1} = \gamma^2 Q_n^{i-1,j+1} + \gamma e^{-\beta z_i} \int_{z_{i-1}}^{z_{i+1}} e^{\beta z} r_n^{j+1}(z) dz \tag{4.1.21}$$

where $\gamma = e^{-\beta h_z}$ and $Q_n^{i,j+1} = Q_n^{j+1}(z_i)$. We assume that $r_n^{j+1}(z)$ represents a polynomial of degree two over the three grid points z_{i-1}, z_i, z_{i+1} on the interval $[z_{i-1}, z_{i+1}]$

and obtain

$$\begin{aligned} Q_n^{i+1,j+1} &= \gamma^2 Q_n^{i-1,j+1} + \frac{1}{\beta}\left(r_n^{i+1,j+1} - \gamma^2 r_n^{i-1,j+1}\right) - \frac{1}{2h_z\beta^2}\left[\left(3r_n^{i+1,j+1} - 4r_n^{i,j+1}\right.\right. \\ &\quad \left. + r_n^{i-1,j+1}\right) - \gamma^2\left(4r_n^{i,j+1} - 3r_n^{i-1,j+1} - r_n^{i+1,j+1}\right)\Big] + \frac{1}{h_z^2\beta^3}\left[\left(r_n^{i+1,j+1}\right.\right. \\ &\quad \left.\left. -2\, r_n^{i,j+1} + r_n^{i-1,j+1}\right)(1-\gamma^2)\right], \end{aligned} \tag{4.1.22}$$

$i = 1, 2, \cdots, M$, where $Q_n^{1,j+1}$ is given by

$$\begin{aligned} Q_n^{1,j+1} &= \gamma Q_n^{0,j+1} + \frac{1}{\beta}\left(r_n^{1,j+1} - \gamma r_n^{0,j+1}\right) - \frac{1}{2h_z\beta^2}\left[r_n^{2,j+1} - r_n^{0,j+1} - \gamma\left(4r_n^{1,j+1}\right.\right. \\ &\quad \left.\left. -3r_n^{0,j+1} - r_n^{2,j+1}\right)\right] + \frac{1}{h_z^2\beta^3}\left[\left(r_n^{0,j+1} - 2r_n^{1,j+1} + r_n^{2,j+1}\right)(1-\gamma)\right]. \end{aligned} \tag{4.1.23}$$

Thus, (4.1.22) and (4.1.23) with the initial value $Q_n^{j+1}(0)$ are all used to determine the solution for $Q_n^{j+1}(z)$ at the grid points $z_1, \cdots, z_{M+1}$.

It is noted that following the same procedure to solve (4.1.20b) for $P_n^{j+1}(z)$ gives unstable method with an exponential error growth [see Dennis and Chang (1969), Collins and Dennis (1973b), and Badr *et al.* (1989)]. Thus to overcome this problem we follow closely the methodology of Dennis and Chang (1969) by implementing a transformation of the type

$$\hat{x} = z_{M+1} - z.$$

Thus (4.1.20b) can be rewritten with respect to the new variable $\hat{x}$ as follow

$$\frac{d\hat{P}_n^{j+1}}{d\hat{x}}(\hat{x}) + \beta\hat{P}_n^{j+1}(\hat{x}) = \hat{r}_n^{j+1}(\hat{x}) \tag{4.1.24}$$

where $\hat{P}_n^{j+1}(\hat{x}) = P_n^{j+1}(z_{M+1} - \hat{x})$ and $\hat{r}_n^{j+1}(\hat{x}) = -r_n^{j+1}(z_{M+1} - \hat{x})$. The initial condition $\hat{P}_n^{j+1}(\hat{x} = 0)$, is determined by multiplying both sides of (4.1.19a) by $e^{-\beta z}$ and then integrating from $z = 0$ to $z = z_{M+1}$

$$\hat{P}_n^{j+1}(\hat{x} = 0) = -2e^{\beta z_{M+1}} V(t_{j+1}) \sin(\eta)\delta_{n,1}. \tag{4.1.25}$$

It is obvious that the integral condition (2.2.17b) has been employed to determine the right-hand side of (4.1.25). It can been seen that the solution of (4.1.24) is similar to the solution of (4.1.20a) so it can be solved by using (4.1.22) and (4.1.23) with Q and r replaced with $\hat{Q}$ and $\hat{r}$.

Thus, the solution for $P_n^{j+1}(z)$ at the grid points $z_0, z_1, \cdots, z_M, z_{M+1}$ is determined and finally the values of $\mathbf{F}_n^{j+1}$ at the grid points can be determined easily by the formula

$$F_n^{j+1}(z) = \frac{P_n^{j+1}(z) - Q_n^{j+1}(z)}{2\beta}.$$

As we mentioned earlier, the solution process in this computational domain is continued until the switching time t_s when the solution process switches to the physical computational domain. Furthermore, the physical computational domain should be related to the computational domain in which boundary-layer coordinate z is used, by $k_s = (8\,t_s/R)^{1/2}$. Thus, the physical computational domain is $[0, \xi_{M+1}]$ where $\xi_{M+1} = k_s\, z_{M+1}$ and the grid points are $\xi_i = i\, h_\xi$ with grid step size $h_\xi = k_s\, h_z$. The solution for both the vorticity and stream function components in the physical coordinate system is similar to the ones in the boundary-layer coordinate system, thus the procedure will not be repeated again. Furthermore, the numerical solution technique in the physical coordinate is similar to the one presented for the boundary-layer coordinates in Section 4.1.1. It is noted that the initial condition at $t = t_s$ is implicity known from the boundary-layer solution and given by

$$G_0(\xi, t_s) = \frac{G_0(z, t_s)}{k_s}, \qquad G_n(\xi, t_s) = \frac{G_n(z, t_s)}{k_s}, \qquad g_n(\xi, t_s) = \frac{g_n(z, t_s)}{k_s};$$

$$F_0(\xi, t_s) = k_s\, F_0(z, t_s), \qquad F_n(\xi, t_s) = k_s\, F_n(z, t_s), \qquad f_n(\xi, t_s) = k_s\, f_n(z, t_s).$$

The flowchart which summarizes the numerical procedure to advance the solution at $t = t_{j+1}$ is presented in Figure 4.3. Assuming first that all the functions, $F_0^{i,j}$, $F_n^{i,j}$, $f_n^{i,j}$, $G_0^{i,j}$, $G_n^{i,j}$ and $g_n^{i,j}$ are known at the previous time step $t = t_j$ and at all the grid points. Solve for the functions in a sequence manner corresponds to the Fourier index by using the most recent information. Since the solutions for $F_0^{i,j+1}$, $F_n^{i,j+1}$ and $f_n^{i,j+1}$ depend only on the quantities $G_0^{i,j+1}$, $G_n^{i,j+1}$ and $g_n^{i,j+1}$ respectively, we prefer to solve first the n-th component of the vorticity and then the corresponding n-th component of the stream function. In this manner, we ensure that the most recent information is used in each iteration. The required solutions at $t = t_{j+1}$ are obtained once the convergence criteria given in (4.1.3) are satisfied. Note that the switching time, t_s, should be checked at every time step in order to replace h_z and z by h_ξ and ξ where $h_\xi = (8\,t_s/R)^{1/2} h_z$ and $\xi = (8\,t_s/R)^{1/2} z$.

The numerical program is written in the C^{++} language. The numerical simulations were carried out on both a 64-processor Beowulf cluster located at the Department of Mathematics and Statistics of Memorial University of Newfoundland and a Silicon Graphics (SGI) Onyx 3400 computer, which has 28 400MHz IP35 MIPS R12000 processors located at the Advanced Computation and Visualization Centre of Memorial University of Newfoundland. The data analysis are done by using the tools of Matlab 6, Maple 8, Golden Software Surfer 7 and Golden Software Grapher 3.

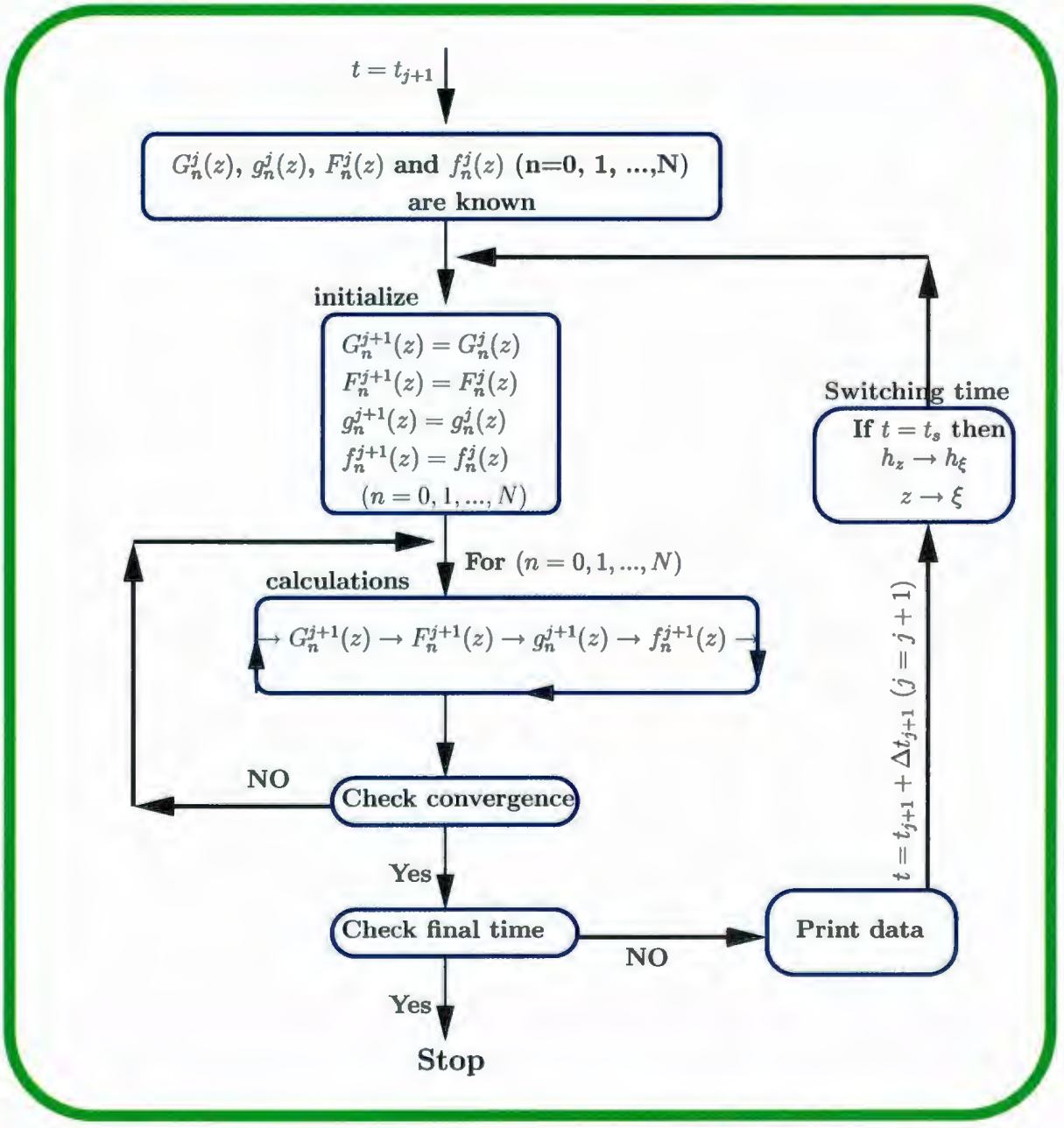

Figure 4.3: The numerical flowchart.

4.1.4 The parameter considerations in numerical procedure

It is well-known in the subject of Fourier series approximation that the order truncation of the Fourier series N plays a crucial rule in the accuracy of the results. Moreover, the accuracy of finite difference schemes absolutely depends on the uniform grid steps, h_z, h_ξ and $\Delta\tau_{j+1}$. Thus, in order to implement this numerical scheme correctly from the mathematical point of view we need to pay attention to the values of the parameters N, h_z, h_ξ and $\Delta\tau_{j+1}$. The uniform grids h_z and h_ξ should be chosen consistently with z_∞ and ξ_∞ respectively. Furthermore, since ξ_∞ depends on both k_s and z_∞ we find that choosing the switching time t_s value between 0.6 and 1 does not show any notable effect on the results. In fact, the best "optimal" values for these parameters are determined by using experimental simulations for each choice of flow parameters. Here we present some simulation samples for calculating the drag coefficient C_D for the case of uniform flow around a fixed cylinder at relatively low and high Reynolds numbers , $R = 100$ and 10^3, in order to determine the optimal choices for $\Delta\tau_{j+1}$, z_∞, h_z and N.

It is noted that the rapid variation of vorticity near $t = 0$ requires the use of a small time step initially. This can be understood from Figure 4.4 in which the drag coefficient, C_D, has been plotted by using two different sets of time steps. The first set consists $\Delta_{j+1} = 10^{-4}$ for the first 10 steps, then was increased to $\Delta_{j+1} = 10^{-3}$ for the next 10 steps and finally $\Delta_{j+1} = 10^{-2}$ was taken for the rest of the solution, however, the second set consists $\Delta_{j+1} = 10^{-3}$ for the first 10 steps and finally $\Delta_{j+1} = 10^{-2}$ was taken for the rest of the solution. It can be seen that the first set of time steps (solid line) controlling the variation of vorticity near $t = 0$ is better than the second

set. Thus, it is evident that small time steps are required to capture correctly the development of the flow at small time. In this study we used the first set of time steps regardless of the flow parameters.

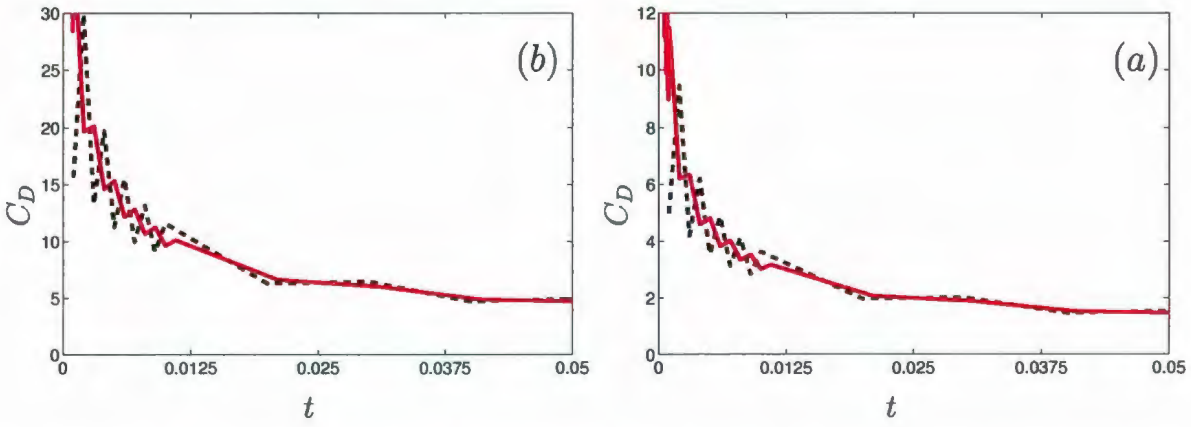

Figure 4.4: Time variation of drag coefficient C_D for the cases flow around a fixed cylinder at $R =$ (a) 100 (b) 10^3; by using set one of time steps (—) and the second set of time steps (- - -): $z_\infty = 8$, $h_z = 0.025$ and $N = 60$.

Figure 4.5 shows three simulation cases on different artificial outer boundaries $z_\infty =$ 6, 8 and 10 to calculate the the drag coefficient, C_D. It is noted that the effect of the artificial outer boundary is more reliable on the case of high Reynolds number, $R = 10^3$, than that of Reynolds number $R = 100$. Moreover, using the outer boundary $z_\infty \geq 8$ for the case of relatively high Reynolds number is reasonable; otherwise it causes inaccurate results. This conclusion is confirmed by Table 4.1 in which the calculated values of the drag coefficient at the instants $t = 10$ and 20 for the considered outer boundaries, $z_\infty = 6$, 8 and 10, are displayed.

Figure 4.6 shows three simulation cases on different grid size $h_z = 0.05$, 0.025 and 0.01 to calculate the drag coefficient, C_D. Furthermore, Table 4.2 shows the calculated values of the C_D at the instants $t = 10$ and 20 for $h_z = 0.05$, 0.025 and 0.01. It is noted that using $h_z = 0.05$ for low or high Reynolds number causes inaccurate

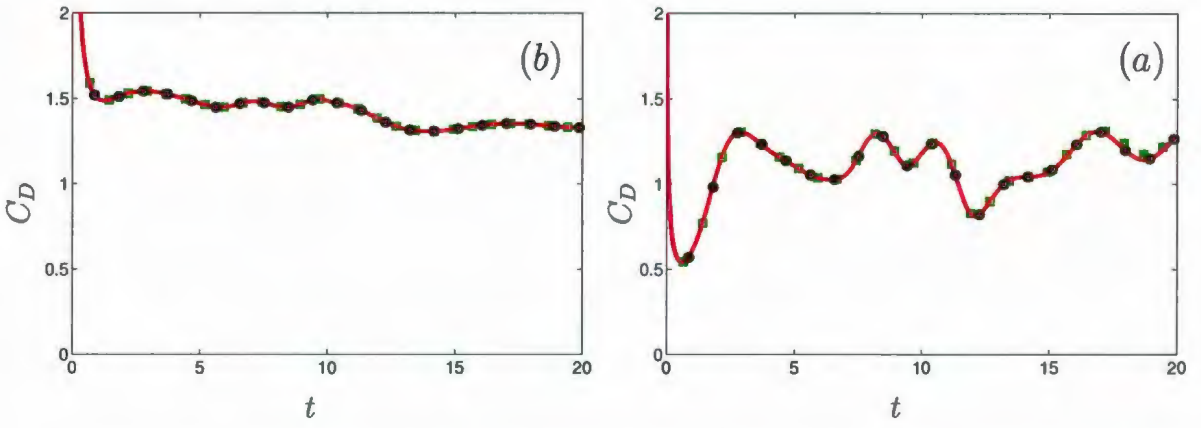

Figure 4.5: Time variation of drag coefficient, C_D, for the case flow around fixed cylinder at (a)$R = 100$, (b)$R = 10^3$; by using the artificial outer boundaries $z_\infty = 6$ (□), $z_\infty = 8$ (—) and $z_\infty = 10$ (•): $h_z = 0.025$ and $N = 60$.

	$t = 10$			$t = 20$		
R \ z_∞	6	8	10	6	8	10
100	1.48810	1.48810	1.48810	1.33080	1.33080	1.33080
10^3	1.18143	1.18145	1.18141	1.30408	1.28568	1.28591

Table 4.1: Calculated values of drag coefficient, C_D, for the case flow around fixed cylinder at$R = 100$ and 10^3; by using the artificial outer boundaries $z_\infty = 6$, 8 and 10 at the instants $t = 10$ and 20: $h_z = 0.025$ and $N = 60$.

results. Moreover, the accuracy of the results is not affected by using h either 0.025 or 0.01 but only using $h = 0.025$ reduces the simulations time.

In Figure 4.7, the drag coefficient C_D is presented by using three simulation cases on three different order truncation of the Fourier series $N = 50$, 60 and 70. It is noted that using $N \geq 60$ is reasonable to obtain accurate results especially for the case of high Reynolds number. The calculated values of C_D at the instants $t = 10$ and 20 are displayed in Table 4.3.

In fact, the number of terms in the Fourier expansion has been arranged automatically. Initially we take two terms and then one more term is added when the last term

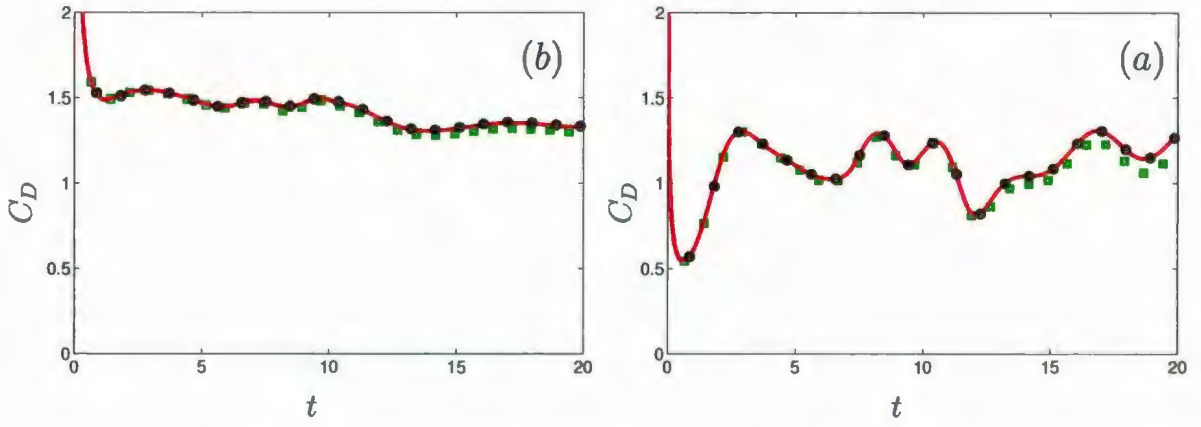

Figure 4.6: Time variation of drag coefficient, C_D, for the case flow around fixed cylinder at (a)$R = 100$, (b)$R = 10^3$; by using grid size $h_z = 0.05$ (□), $h_z = 0.025$ (—) and $h_z = 0.01$ (•): $z_\infty = 8$ and $N = 60$.

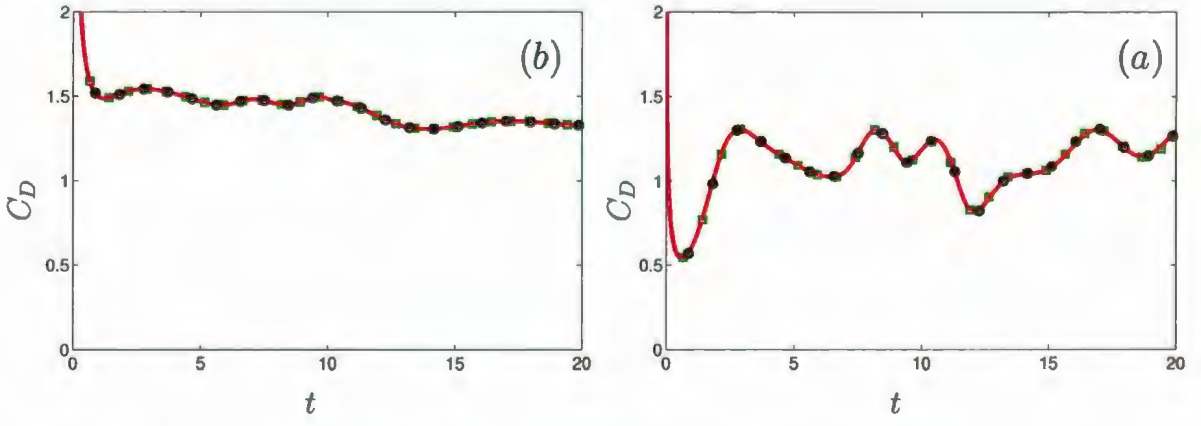

Figure 4.7: Time variation of drag coefficient, C_D, for the case flow around fixed cylinder at (a)$R = 100$, (b)$R = 10^3$; by using order truncation of the Fourier series $N = 50$ (□), $N = 60$ (—) and $N = 70$ (•): $h_z = 0.025$ and $z_\infty = 8$.

R \ h_z	$t = 10$			$t = 20$		
	0.05	0.025	0.01	0.05	0.025	0.01
100	1.47392	1.48810	1.48825	1.29896	1.33080	1.33277
10^3	1.17700	1.18145	1.18142	1.19937	1.28568	1.28505

Table 4.2: Calculated values of drag coefficient, C_D, for the case flow around fixed cylinder at$R = 100$ and 10^3; by using grid size $h_z = 0.05$, 0.025 and 0.01 at the instants $t = 10$ and 20: $z_\infty = 8$ and $N = 60$.

R \ N	$t = 10$			$t = 20$		
	50	60	70	50	60	70
100	1.48811	1.48810	1.48811	1.33087	1.33080	1.33079
10^3	1.17751	1.18145	1.18145	1.28454	1.28568	1.29036

Table 4.3: Calculated values of drag coefficient, C_D, for the case flow around fixed cylinder at$R = 100$ and 10^3; by using order truncation of the Fourier series $N = 50$, 60 and 70 at the instants $t = 10$ and 20: $h_z = 0.025$ and $z_\infty = 8$.

exceeds 10^{-3} where the maximum number of terms N should not exceed 60. In fact it is found that N depends proportionally on both the time and Reynolds number R.

In summary, the majority of the computations are carried out using the numerical scheme parameters: $h_z = 0.025$, $z_\infty = 8$, $N = 60$ and $t_s = 40$. On the other hand, we use different parameters at some flow parameters to get better accuracy. These cases will be reported in the subsequent chapters. In fact, the accuracy of these parameters are checked through the infinity norm of the residual, $|R_1(\zeta_N, \psi_N)|$, given in (2.2.2) verses the time t for the cases $R = 100$ and $R = 10^3$ as seen in Figure 4.8 Thus, this is an evidence that using the convergence criteria (4.1.3) to check the convergence in the numerical scheme is more reliable than using the residual method.

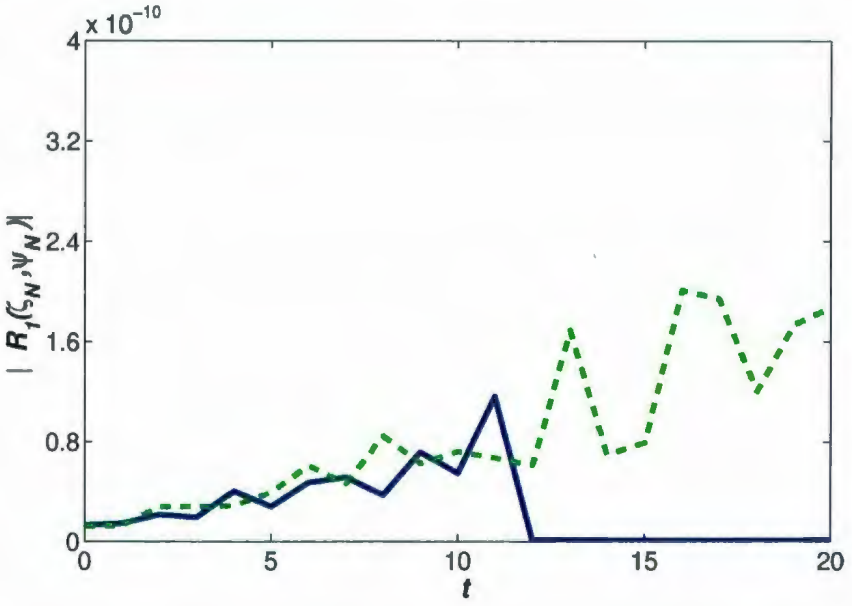

Figure 4.8: The residual, $|R_1(\zeta_N, \psi_N)|$ verses time for the cases flow around a fixed cylinder at $R = 100$ (—) and $R = 10^3$ (- - -) by using $z_\infty = 8$, $h_z = 0.025$ and $N = 60$.

4.2 Validation of the numerical scheme

In this section the validation of the numerical scheme is presented for uniform flow past a (i) stationary cylinder (no forced oscillations); (ii) steadily rotating cylinder (no forced oscillations); (iii) cylinder undergoing 1-DoF forced recti-linear oscillations at angles $\eta = 0^o$, 60^o and 90^o, with respect to the uniform free-stream direction; (iv) cylinder undergoing 2-DoF motion produced by combined forced recti-linear and rotational oscillations. The dimensionless recti-linear and rotational oscillatory velocities are

$$V(t) = -2\pi f A \sin(2\pi f t) \quad \text{and} \quad \Omega(t) = 2\pi f_\theta \Theta_m \sin(2\pi f_\theta t),$$

respectively. The streamline patterns presented in the subsequent sections are plotted in the same frame of reference which is fixed with respect to the translational and

oscillatory motions except for section 4.2.3 in which we used a moving frame of reference with respect to both the translational and oscillation motions of the cylinder (see Appendix C.3.1).

4.2.1 Simulations for the case of a stationary cylinder

The accuracy of the numerical scheme is tested by comparing the present results with previous theoretical and experimental results for the case of uniform flow past a stationary circular cylinder. The numerical simulations are carried out at $R = 100$, 106 and 10^3 by setting oscillatory velocities $V(t)$ and $\Omega(t)$ to zero.

It is well-known that vortex shedding for the case of uniform flow past a stationary cylinder absolutely depends on the Reynolds number R so that the asymmetrical eddy pattern is observed behind the circular cylinder at $R \geq 40$. This asymmetrical eddy pattern is due to the instability of the flow effects. These instabilities naturally occur in physical experiments of uniform flow past a fixed circular cylinder but it is absent in the numerical solutions. This is due to the influence of the symmetrical behavior of both the geometry of the flow and the boundary conditions on the solutions of Navier-Stokes equations [see Braza *et al.* (1986)]. In order to obtain these asymmetrical eddy patterns from the numerical solution we need to establish a similar perturbation to that in the physical experiment caused by the running conditions such as vibrations. Thus, in our numerical simulations we establish artificial perturbation by forcing the cylinder to perform rotational oscillations about its axis for one period. The use of this artificial perturbation is similar to the most common approach

reported in previous studies (Martinez and Hinh (1978), Braza *et al.* (1986), Justesen (1991)) in which a clockwise rotation of the circular cylinder was followed after a short period of time by a counterclockwise rotation. Following the work of Braza *et al.* (1986), we implemented vortex shedding by using the dimensionless angular displacement given by

$$\Theta(t) = -\frac{\pi}{4}\cos(\frac{2\pi}{5}t), \tag{4.2.1}$$

for the time $t = t_0$ to $t = t_0 + T$, where $T(= 5)$ represents the period of vortex shedding. We note that using different rates of rotations of the circular cylinder in (4.2.1) leads to different perturbations which cause different transition period to steady state.

Essentially, one of the most important concepts in the flow past a stationary bluff body is the measurement of dimensionless natural vortex shedding frequency, f_0, of the body wake which is related to the Strouhal frequency, S_0, by $S_0 = 2f_0$. This measurement can be computed from the time variation of the induced oscillating lift force by calculating the Power Spectral Density through Fourier analysis explained in Appendix C.1. In fact, checking the dependence of the Strouhal frequency and the Reynolds number is one of the standard methods of validating computer code for numerical simulation of a flow around a stationary cylinder. Figures 4.9(a,b), show the Power Spectral Density for the lift record and the time variation of drag coefficient C_D, and lift coefficient C_L, respectively, for the case of a stationary cylinder at $R = 100$. The predicted value of the Strouhal frequency together with experimental values (Roshko (1954), Williamson (1989), Hammache and Gharib (1991), Wen and Lin (2001)) and computational ones of other methods (Braza *et al.* (1986), Meneghini (1993), Herfjord (1995), Barkley and Henderson (1996), Kravchenko *et al.* (1999),

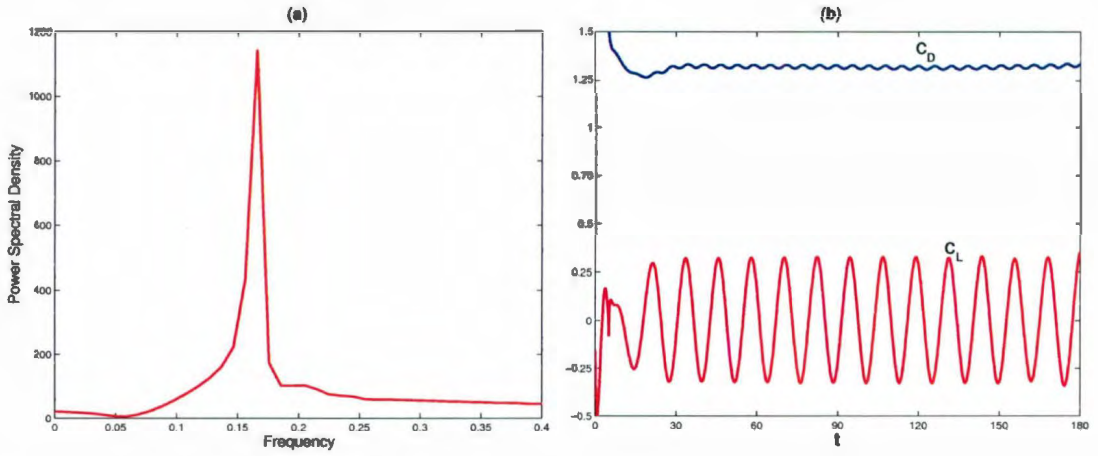

Figure 4.9: (a) Fourier analysis of lift records; and (b) the time variation of drag coefficient C_D, and lift coefficient C_L for the case of a stationary cylinder at $R = 100$.

Ayyalasomayajula *et al.* (2003)) for the case of a stationary cylinder at $R = 100$ are displayed in Tables 4.4 and 4.5. It can be seen that the experimental and numerical results of the calculated Strouhal frequency have the range from $0.164 - 0.167$ and $0.16 - 0.168$ respectively, which shows excellent agreement with the present calculated value. Moreover, some computational results of the predicted maximum value of the drag coefficient $C_{D,max}$, maximum value of the lift coefficient $C_{L,max}$ and time-average drag coefficient $\overline{C_D}$ at $R = 100$ obtained by the present study and previous investigators are presented in Table 4.5. The value for $C_{D,max}$, $\overline{C_D}$ and $C_{L,max}$ are reported as being in the ranges $1.31 - 1.52$, $1.253 - 1.32$ and $0.195 - 0.353$ respectively, again showing excellent agreement between the present and other computational methods.

It is noted that the computational results were obtained in previous studies using the following methods. Braza *et al.* (1986): the finite volume method; Meneghini

No.	Reference	S_0
2	Roshko (1954)	0.167
3	Williamson (1989)	0.164
4	Hammache and Gharib (1991)	0.166-0.167
5	Wen and Lin (2001)	0.165-0.167
6	Present study	0.164

Table 4.4: The predicted Strouhal frequency, S_0, and comparisons with experimental investigations for the case of a stationary cylinder at $R = 100$.

No.	Reference	S_0	$C_{D,max}$	$\overline{C_D}$	$C_{L,max}$
1	Braza *et al.* (1986)	0.16	-	1.253	-
2	Meneghini (1993)	0.162	1.52	-	0.353
3	Herfjord (1995)	0.168	1.36	-	0.34
4	Barkley and Henderson (1996)	0.166-0.167	-	-	-
6	Kravchenko *et al.* (1999)	0.164	1.314	-	0.314
8	Ayyalasomayajula *et al.* (2003)	0.164	1.31	-	0.313
9	Present study	0.164	1.33	1.32	0.33

Table 4.5: The predicted Strouhal frequency, S_0, maximum value of drag coefficient $C_{D,max}$, maximum value of lift coefficient $C_{L,max}$ and time-averaged drag coefficient $\overline{C_D}$ at $R = 100$ and comparisons with previous numerical studies for the case of a stationary cylinder.

(1993): a discrete vortex method; Herfjord (1995): the finite element method; Barkley and Henderson (1996): the spectral element method; Kravchenko *et al.* (1999): the B-spline method and zonal grids; Ayyalasomayajula *et al.* (2003): a higher order compact differencing scheme with 10^{th} order filtering.

Figures 4.10-4.13 show the fluid velocities, equivorticity lines, streamline patterns and pressure distribution during one half of the shedding period for the case of a stationary cylinder at $R = 106$. Figure 4.10 shows the comparison of velocity traces in the

stream direction, u, at different locations, $(x, y) = (5.4, 0.64)$, $(5.4, 0.86)$, $(9.8, 0.34)$, $(9.8, 0.66)$, $(15, 1)$, $(15, 1.5)$, between the present computational method and the computational and experimental methods of Anagnostopoulos (1997) where he utilized a finite element method in his numerical solution. It is noted that the discrepancy which appears in the wake is smaller than that close to the cylinder. Moreover, the frequency of the velocity traces curves is exactly the same as the natural vortex shedding frequency f_0. We note that in these comparisons of the velocity traces in the free stream directions between the computed and the experimental results slightly different Reynolds number were used ($R = 115$ experimentally and $R = 106$ numerically). Anagnostopoulos (1997) reported that this difference in R can be ignored because of the following two reasons: firstly the proximity of the solid boundaries which makes the experimental free stream velocity higher than the theoretical one, and secondly the numerical model is two dimensional while the experimental one is three dimensional since the vortices were shedding at an angle. In fact this shedding at an angle has an effect on the Strouhal frequency or, obviously, the shedding period $T_0 = 1/f_0$.

Figure 4.11 shows a good agreement between the equivorticity lines with the previous computational study by Anagnostopoulos (1997) for the case of a stationary cylinder at $R = 106$, and at the instant $t/T_0 = 0$ which corresponds to the instant at which $C_L = 0$ and once C_L turns from positive to negative. The development of a Kármán vortex street with alternately shedding vortices from the upper and lower surfaces of the cylinder is observed in this figure. However, it can be seen that Anagnostopoulos figure shows disturbed lines especially as the vortices are moving away

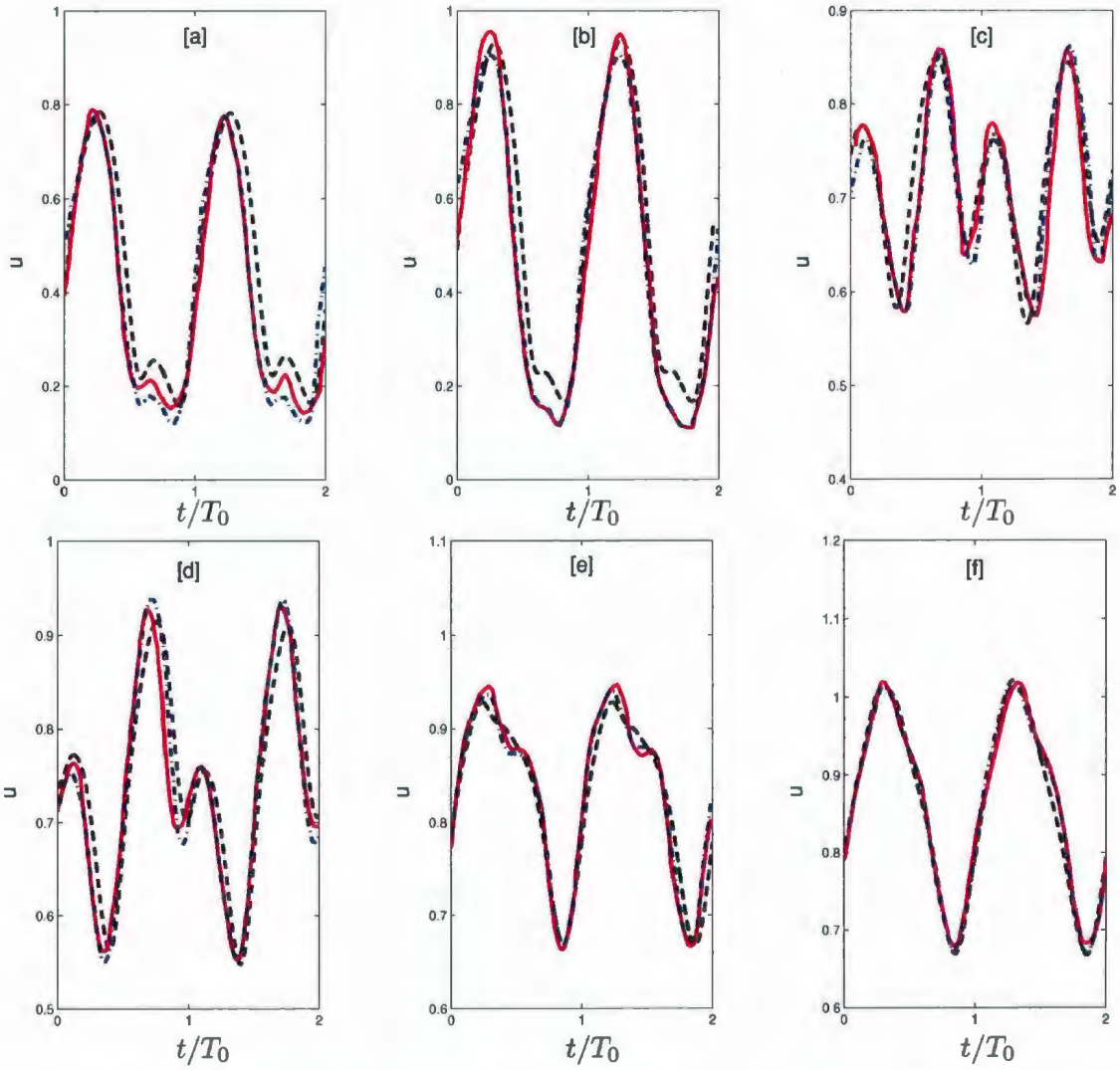

Figure 4.10: Comparison of streamwise velocities of the fluid as a function of time between the present results (- - -), experimental results (—) and computational results (- . -) of Anagnostopoulos (1997) at the locations [a] (x, y)=(5.4,0.64), [b] (x, y)=(5.4,0.86), [c] (x, y)=(9.8,0.34), [d] (x, y)=(9.8,0.66), [e] (x, y)=(15,1), [f] (x, y)=(15,1.5), for the case of a stationary cylinder at $R = 106$.

downstream. This disturbance might be reflected from the accuracy or interpolation problem.

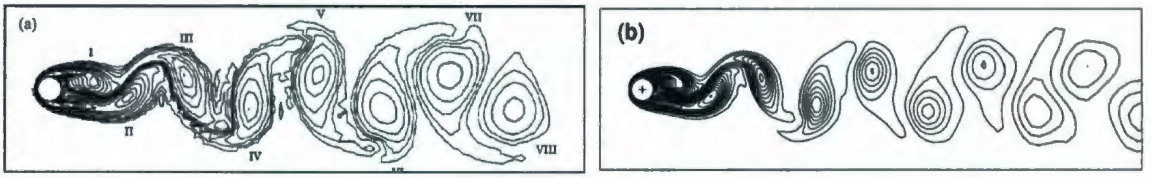

Figure 4.11: Equivorticity lines comparison with (a) numerical study by Anagnostopoulos (1997) and (b) present study, for the case of a stationary cylinder at R=106: at the instant $t/T_0 = 0$, $T_0 = 12.2$.

Figure 4.12 shows the superimposed equivorticity lines on streamlines with respect to the frame of reference fixed on the cylinder surface over half shedding period in the near wake region for the case of a stationary cylinder at $R = 106$. These snapshots show part of the vortex shedding process where two vortices are alternatively shed from the bottom and the top of the cylinder per one shedding cycle with equal sizes forming the classical Kármán vortex street. To be more specific, Figure 4.12(a) shows, according to the streamlines, a small counterclockwise circulation located at the bottom of the cylinder and another clockwise large scale vortex located in the near wake-region which is originally shed from the top part of the cylinder. However, Figures 4.12(b)-4.12(d) show the growth of the small circulation with time which help the large-scale vortex to move downstream until it vanishes. Moreover, it can be clearly seen that the equivorticity lines are very extensive and very close near the cylinder which indicates large vorticity near the surface of the cylinder.

The pressure distributions throughout the flow field are determined from the solution of Poisson equation for the pressure where the boundary conditions for pressure at

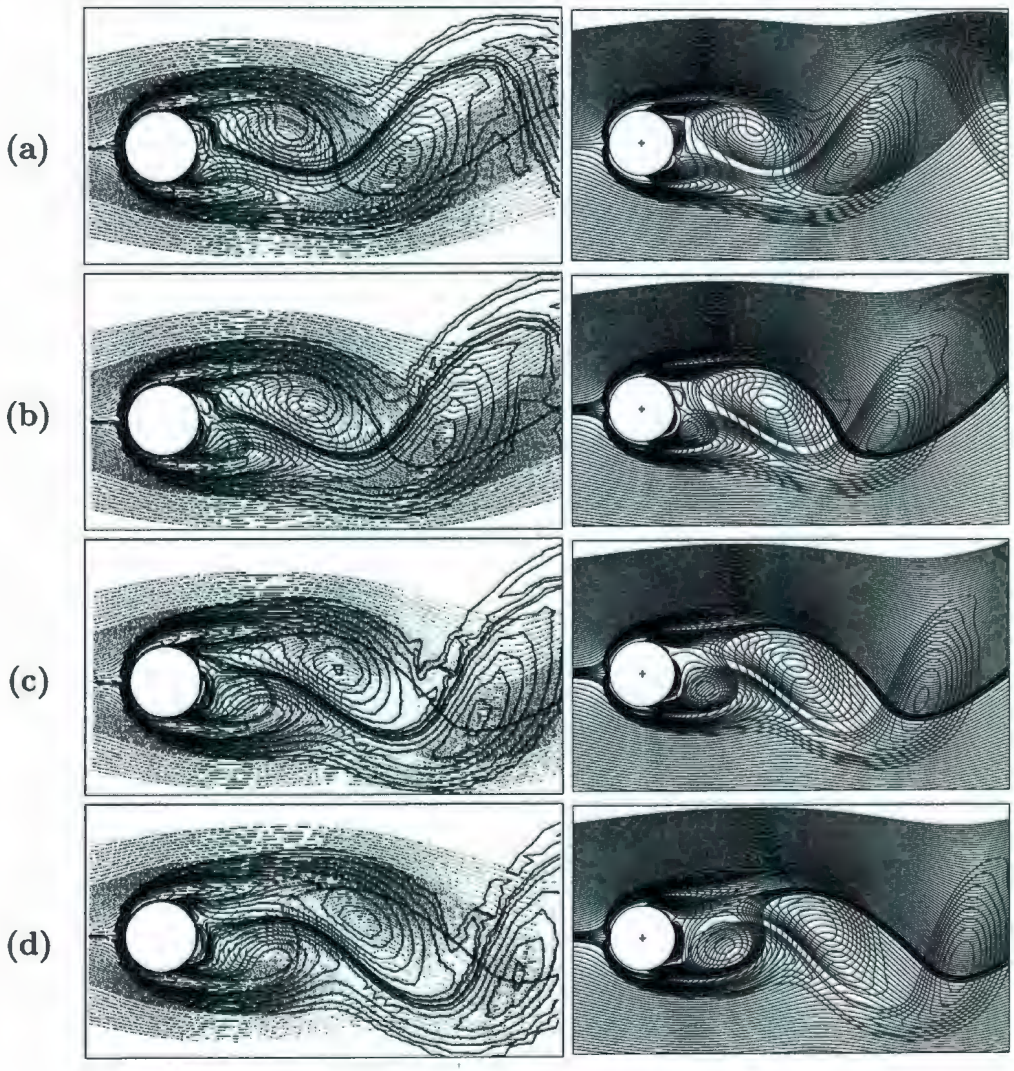

Figure 4.12: Superimposed equivorticity lines and streamline patterns in the near wake region for the case of a stationary cylinder at R=106: at the instances (a)$t/T_0 = 0$, (b)$t/T_0 = 1/8$, (c)$t/T_0 = 1/4$, (d)$t/T_0 = 3/8$ ($T_0 = 12.2$). Comparison between numerical method used by Anagnostopoulos (1997) (left) and present study (right).

the outer boundaries and the surface of the cylinder are determined from the angular and radial momentum equations given in (2.1.30) and (2.1.31) after making use of the boundary conditions (2.1.34)-(2.1.36) (see Appendix C.2). The pressure is the most sensitive quantity among all the flow variables because of its relatively small values. The pressure distribution in the near wake region of the cylinder at three different instances during three eighths of the shedding period are presented in Figure 4.13. The results compare well with the numerical results of Anagnostopoulos (1997).

Figure 4.14 shows an excellent comparison between our results and the experimental ones obtained by Coutanceau and Pineau (1997) at $R = 10^3$. It is noted that an artificial perturbation is implemented in the numerical scheme by forcing the cylinder to perform rotational oscillation about its axis with the non-dimensional angular displacement given by

$$\Omega(t) = \frac{\pi}{4} \sin(\frac{2\pi}{5} t),$$

for the time $t = 3.33$ to 3.51. It can be seen from Figure 4.14 that two symmetrical vortices grow first behind the cylinder and then become asymmetrical at the time $t \geq 4$ with the detachment from the cylinder.

4.2.2 Simulations for the case of a steadily rotating cylinder

The numerical simulations are carried out at $R = 500$ and 10^3 for the case of a steadily rotating cylinder by setting recti-linear and rotational oscillatory velocities to $V(t) = 0$ and $\Omega(t) = 1$, 3, respectively. Figure 4.15 shows the present predictions of the early development of the flow behind a steadily rotating cylinder immersed in

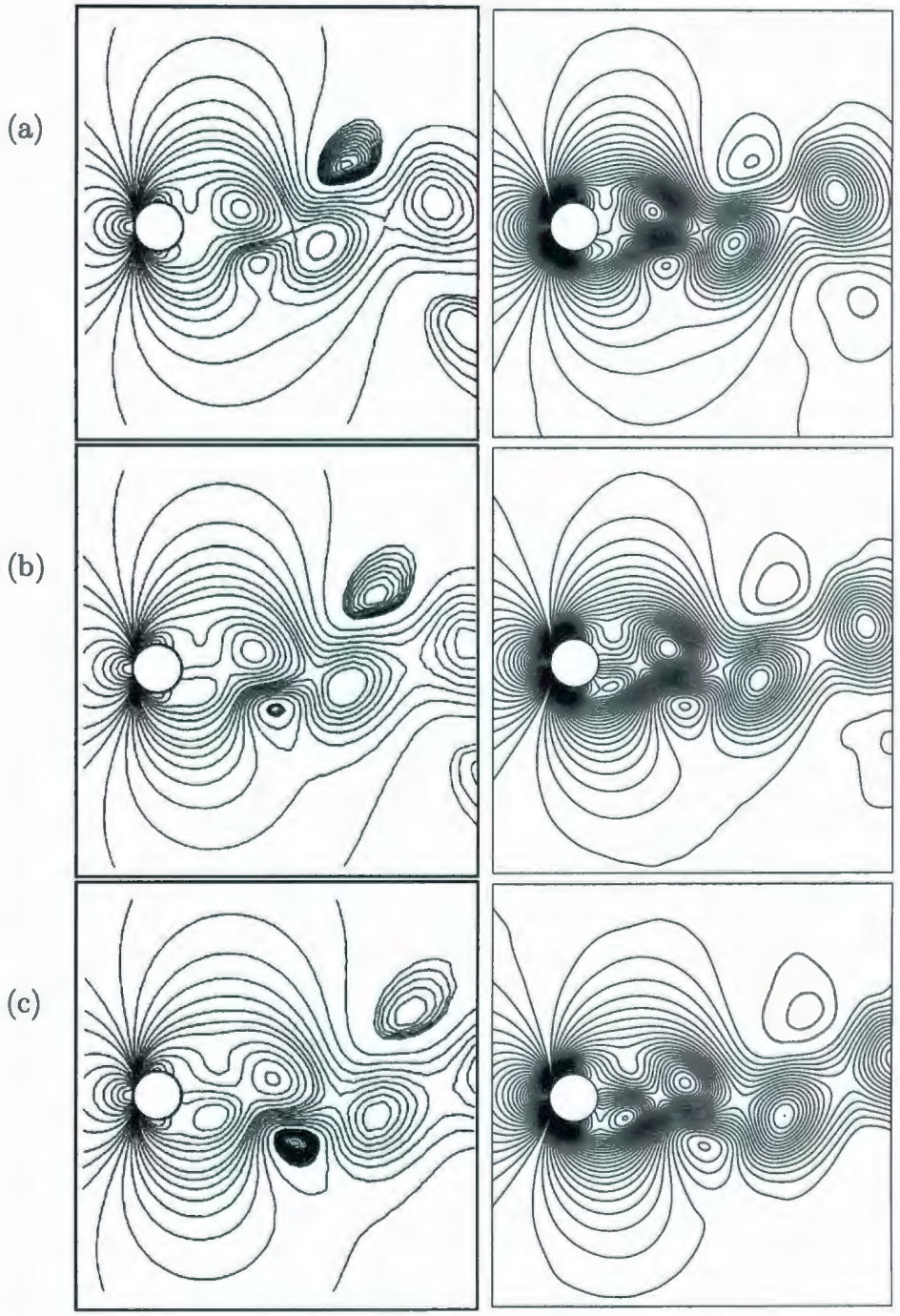

Figure 4.13: Pressure distribution in the near wake region for the the case of a stationary cylinder at R=106: at the instances (a)$t/T_0 = 0$, (b)$t/T_0 = 1/8$, (c)$t/T_0 = 2/8$ ($T_0 = 12.2$). Comparison between numerical method used by Anagnostopoulos (1997) (left) and present study (right).

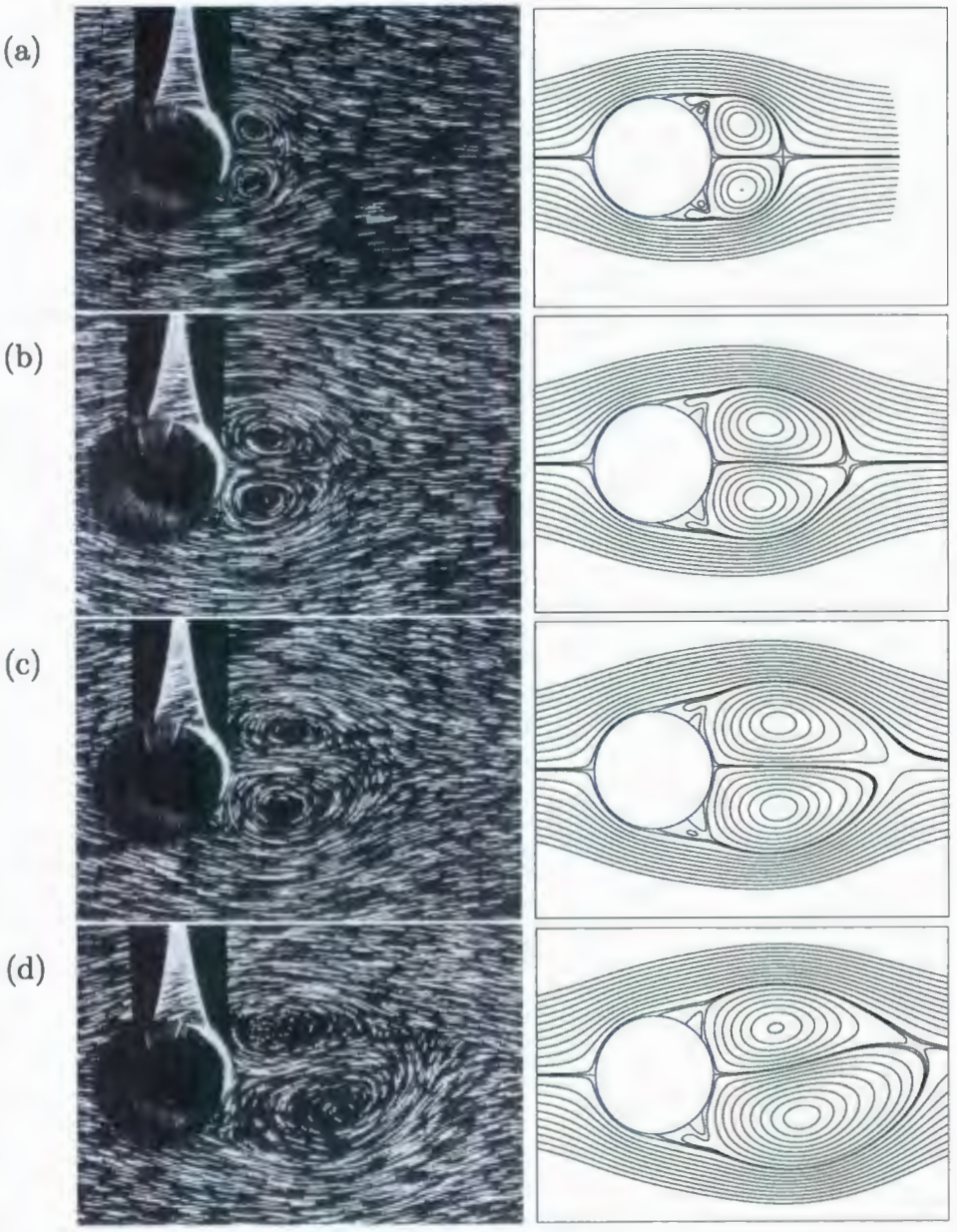

Figure 4.14: Streamline patterns in the near wake region for the impulsively started flow over a stationary cylinder for $R = 10^3$ at the instances: (a) $t = 4$, (b) $t = 8$, (c) $t = 12$, (d) $t = 16$. Comparison between experimental results of Coutanceau and Pineau (1997) (left) and present computational results (right).

a uniform flow are compared with that obtained from the numerical study of Chou (2000) and the available experimental results by Badr *et al.* (1990) at $R = 10^3$ and $\Omega(t) \equiv 3$. It can be seen that these comparisons are in good agreement. On the other hand, Figure 4.16 show comparisons of the time evolution of the drag and moment coefficients for the case of $R = 500$ and $\Omega(t) \equiv 1$ with the computations of Badr *et al.* (1985). The comparisons between these results shows a discrepancy of less than 0.05.

4.2.3 Simulations for the case of 1-DoF forced cylinder oscillations

The numerical simulations are carried out at $R = 855$ for the case of uniform flow past a cylinder undergoing 1-DoF forced recti-linear oscillations at angles $\eta = 0^o$, 60^o and 90^o with respect to the free-stream direction by setting rotational oscillatory velocity to $\Omega(t) = 0$. Figures 4.17-4.19 show comparisons between the near-wake structures obtained in the present study for the 1-DoF forced recti-linear oscillation case when $A = 0.26$ and $f/f_0 = 0.5$, 1, 2, 3, 4 and those obtained experimentally by Ongoren and Rockwell (1988b). In all these figures, the present simulations are presented by the equivorticity lines and streamline patterns. Present computations are carried out over five, nine and twenty cycles for the cases of $f/f_0 = 0.5$, 1, 2, respectively, and about thirty cycles for the cases of $f/f_0 = 3$, 4. Bearing in mind that the number of oscillation cycles for the experimental runs by Ongoren and Rockwell (1988b) is considerably higher than that of the present case, it may be noted that, even so there is very good qualitative agreement between computed near-wake structures and those

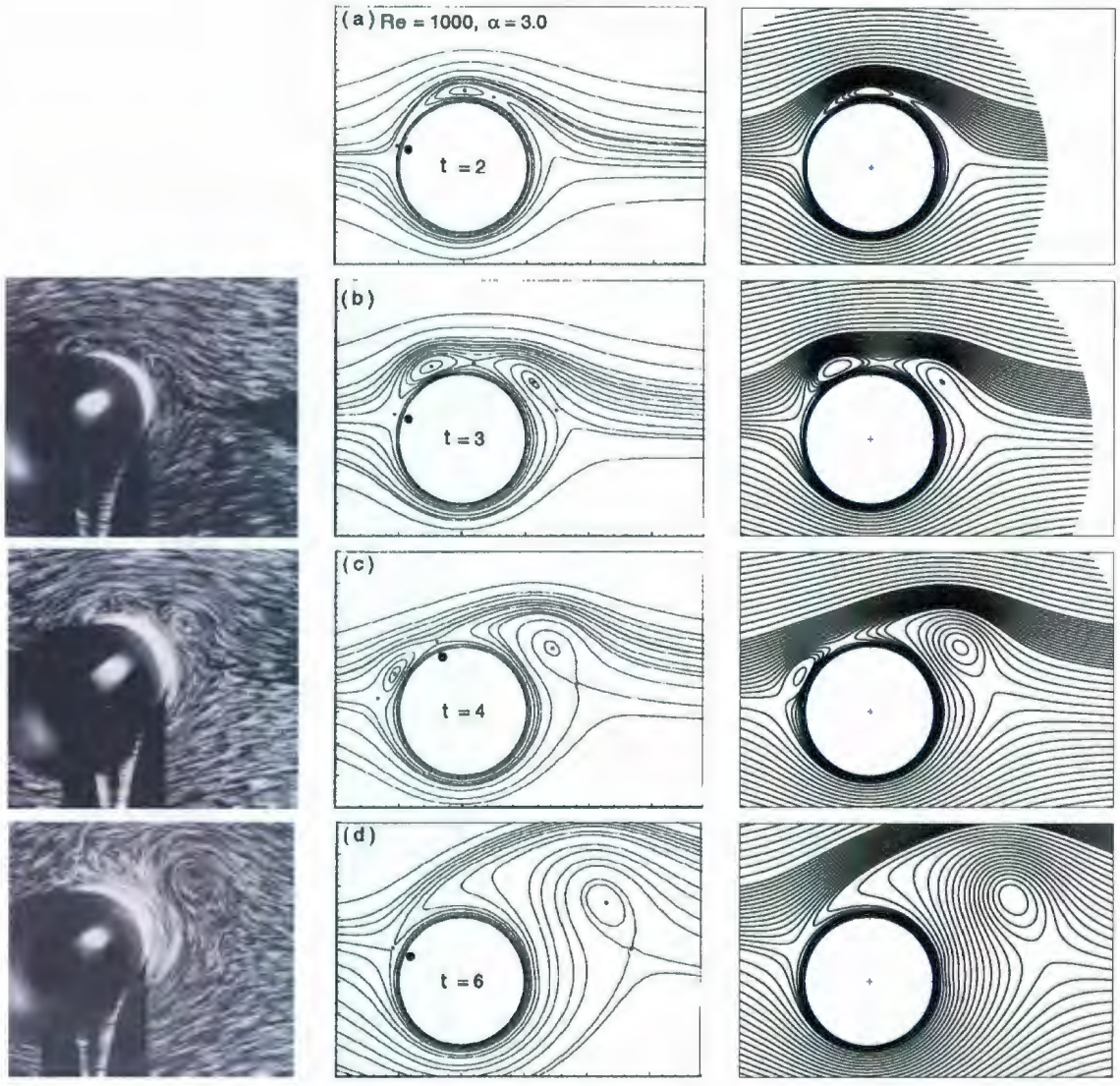

Figure 4.15: Streamline patterns in the near wake region for $R = 10^3$, $\Omega(t) = 3$ at the instances: (a) $t = 2$, (b) $t = 3$, (c) $t = 4$, (d) $t = 6$. Comparison between experimental results of Badr *et al.* (1990)(left), computational results of Chou (2000) (middle) and present numerical results (right).

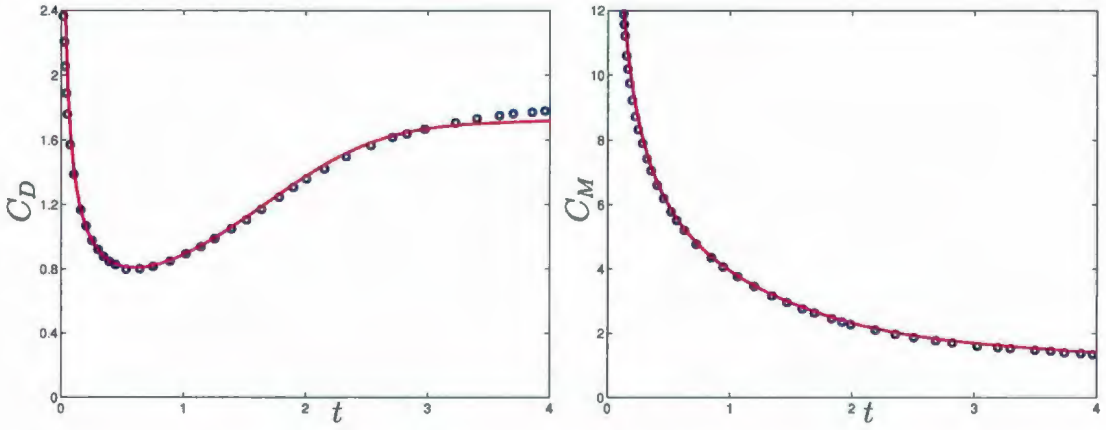

Figure 4.16: Comparisons of C_D (left) and C_M (right) between the present numerical results (—) and numerical results of Badr *et al.* (1990) (o) for the case of uniform flow past a steadily rotating circular cylinder at $R = 500$ and $\Omega(t) \equiv 1$.

shown in experimental diagrams.

4.2.4 Simulations for the case of 2-DoF forced cylinder oscillations

In this section we verify the accuracy of the present method for the case of an initial uniform flow past a circular cylinder undergoing combined (2-DoF) forced recti-linear and rotational oscillations. To do this we first compare the numerical results with those obtained by the analytical solutions of Chapter 3 at small times. We then carry out further tests to check the periodicity of the surface pressure for large values of the time. Two types of 2-DoF forced oscillation simulations are performed when the cylinder is forced to move by combined (i) in-line (streamwise), $\eta = 0^o$, and rotational oscillation; (ii) transverse (cross-stream), $\eta = 90^o$, and rotational oscillation. The frequency of the recti-linear oscillation is the same as for the rotational oscillation i.e., $f = f_\theta$. The results are obtained for $R = 855$, $A = 0.26$, $f/f_0 = 1.0$ and $\Theta_m = 30^o$. In figures 4.20 and 4.21 the numerical results for the surface vorticity and pressure

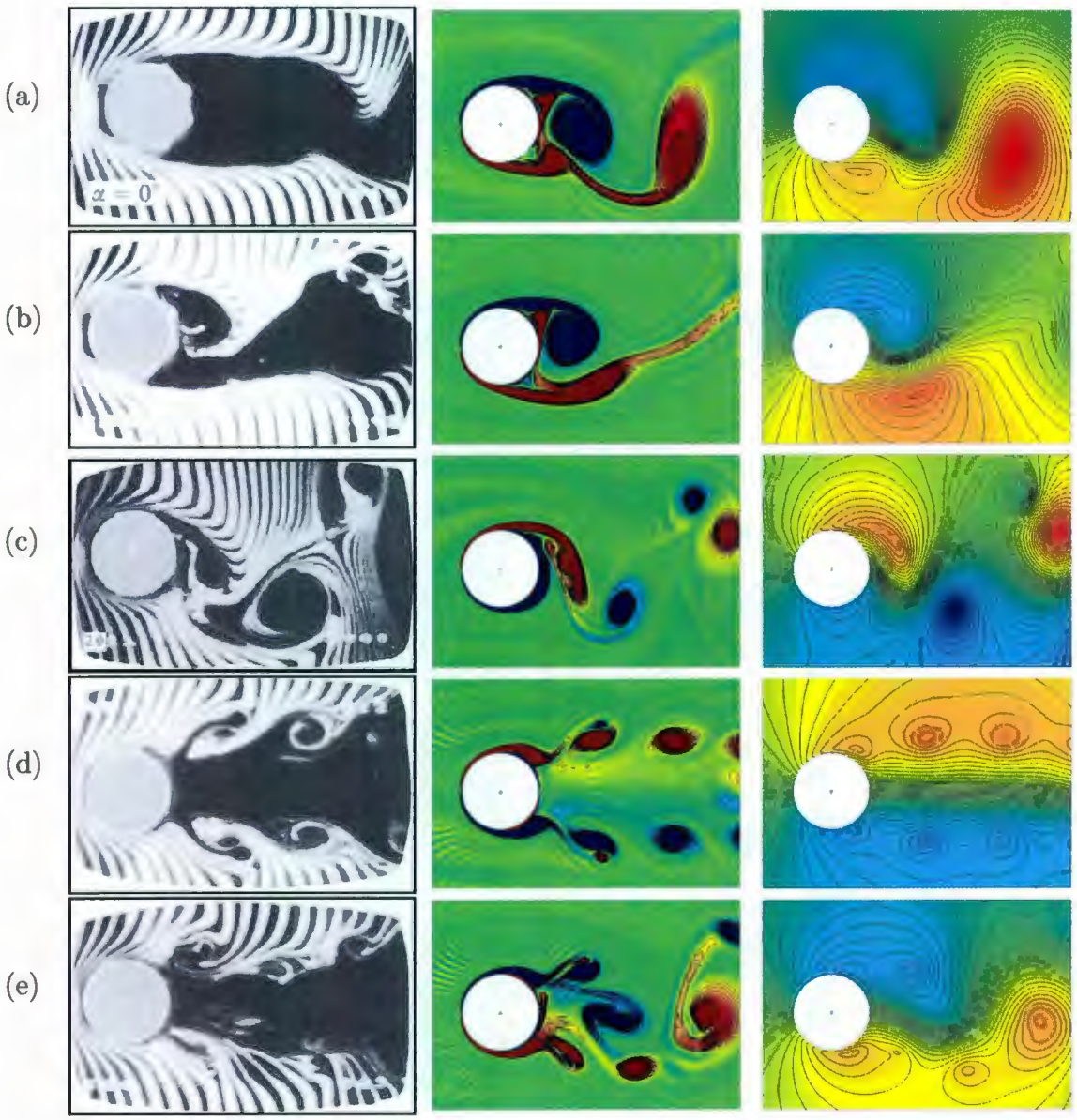

Figure 4.17: Comparison of flow visualization of Ongoren and Rockwell (1988b) (left) and computed present equivorticity lines (middle) and streamline patterns (right) for the case of $R = 855$, $A = 0.26$ and $\eta = 0^o$ at the frequency ratios: (a) $f/f_0 = 0.5$; (b) $f/f_0 = 1$; (c) $f/f_0 = 2$; (d) $f/f_0 = 3$; (e) $f/f_0 = 4$. All snapshots are taken at the instant corresponding to the maximum negative displacement.

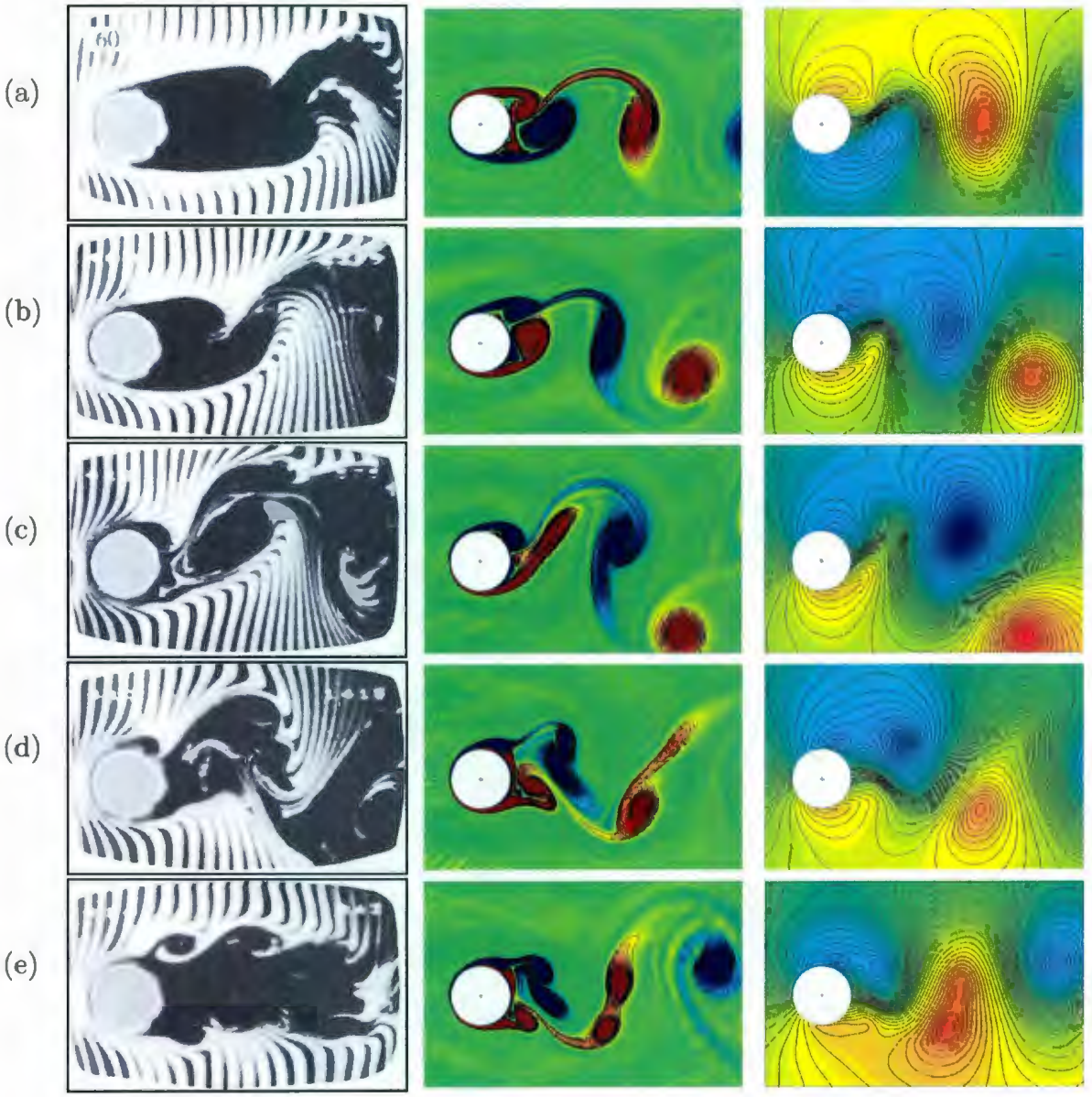

Figure 4.18: Comparison of flow visualization of Ongoren and Rockwell (1988b) (left) and computed present equivorticity lines (middle) and streamline patterns (right) for the case of $R = 855$, $A = 0.26$ and $\eta = 60^o$ at the frequency ratios: (a) $f/f_0 = 0.5$; (b) $f/f_0 = 1$; (c) $f/f_0 = 2$; (d) $f/f_0 = 3$; (e) $f/f_0 = 4$. All snapshots are taken at the instant corresponding to the maximum negative displacement.

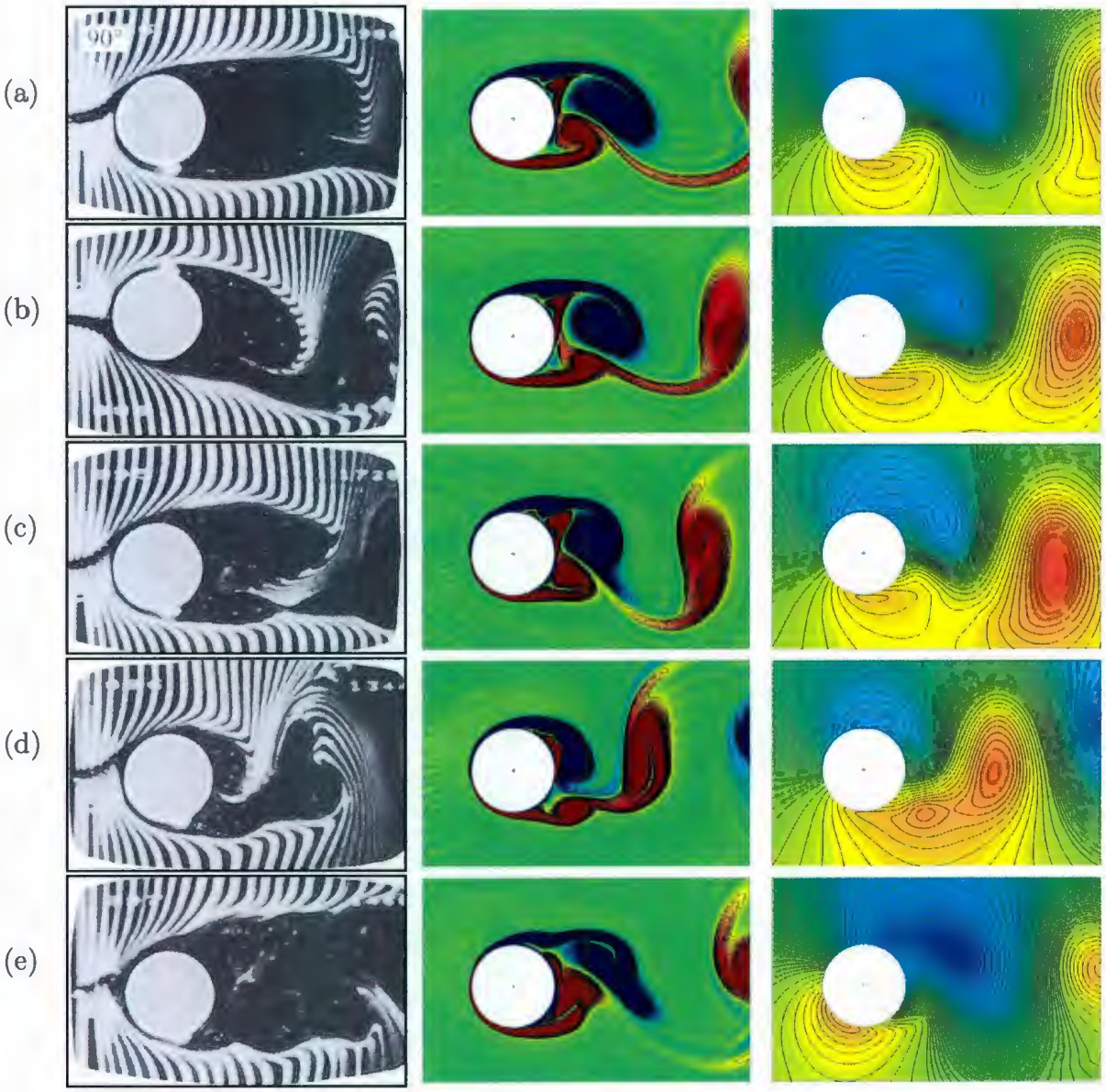

Figure 4.19: Comparison of flow visualization of Ongoren and Rockwell (1988b) (left) and computed present equivorticity lines (middle) and streamline patterns (right) for the case of $R = 855$, $A = 0.26$ and $\eta = 90^o$ at the frequency ratios: (a) $f/f_0 = 0.5$; (b) $f/f_0 = 1$; (c) $f/f_0 = 2$; (d) $f/f_0 = 3$; (e) $f/f_0 = 4$. All snapshots are taken at the instant corresponding to the maximum negative displacement.

distributions, defined in (2.2.1a) and (2.3.2), are compared with the results of the analytical solutions using (3.3.37) and (3.4.6) at $t = 0.1$, 0.5 and 1.0. The comparison is extremely good at small times ($t \leq 0.5$). The frictional, pressure, total drag and lift coefficients defined in (2.4.2)-(2.4.5); (2.4.7) and (2.4.8) have been determined using (3.4.1)-(3.4.4) analytically and figures 4.22 and 4.23 show these results together with ones obtained from the numerical solution for the small values of time ($0 \leq t \leq 1$). The analytical results exhibited in these figures compare satisfactory with results derived from the numerical results for $t < 0.5$. As a further check on the verification of the numerical scheme, the moment coefficient defined by (3.4.5) is compared for both numerical and analytical methods. The comparison seems to be satisfactory at small times ($0 \leq t \leq 0.4$).

The calculated surface pressure, $\tilde{p_0}$, defined in (2.3.2) is plotted in Figure 4.25 for the combined (2-DoF) recti-linear and rotational oscillation cases when $\Theta_m = 30^o$: $\eta = 0^o$ and $\eta = 90^o$. This figure shows the surface pressure distribution during one period of oscillation and confirms that the periodicity condition is satisfied ($\tilde{p_0}(0) = \tilde{p_0}(2\pi)$). For the case of combined (2-DoF) in-line and rotational oscillation, the maximum value of $\tilde{p_0}$ is steadily decreasing as t increases as shown in Figure 4.25a unlike the combined (2-DoF) transverse and rotational case (see Figure 4.25b).

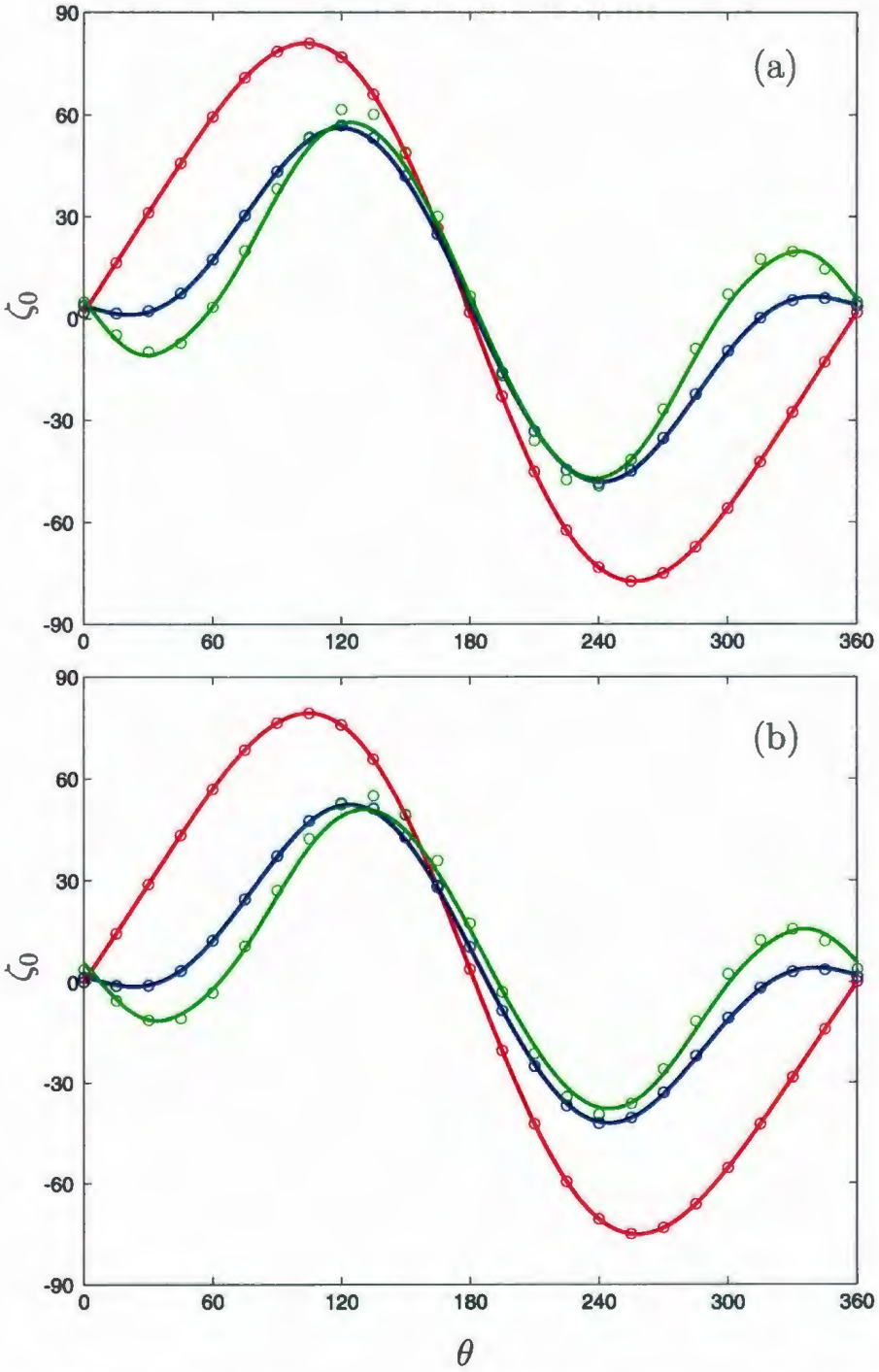

Figure 4.20: Comparison of the surface vorticity distribution at $R = 855$, $A = 0.26$, $\Theta_m = 30^o$ and $f/f_0 = 1$: (a) $\eta = 0^o$ and (b) $\eta = 90^o$; —, **numerical solution,** ∘, **analytical solution at the instants** $t = 0.1$ **(red),** $t = 0.5$ **(blue) and** $t = 1.0$ **(green).**

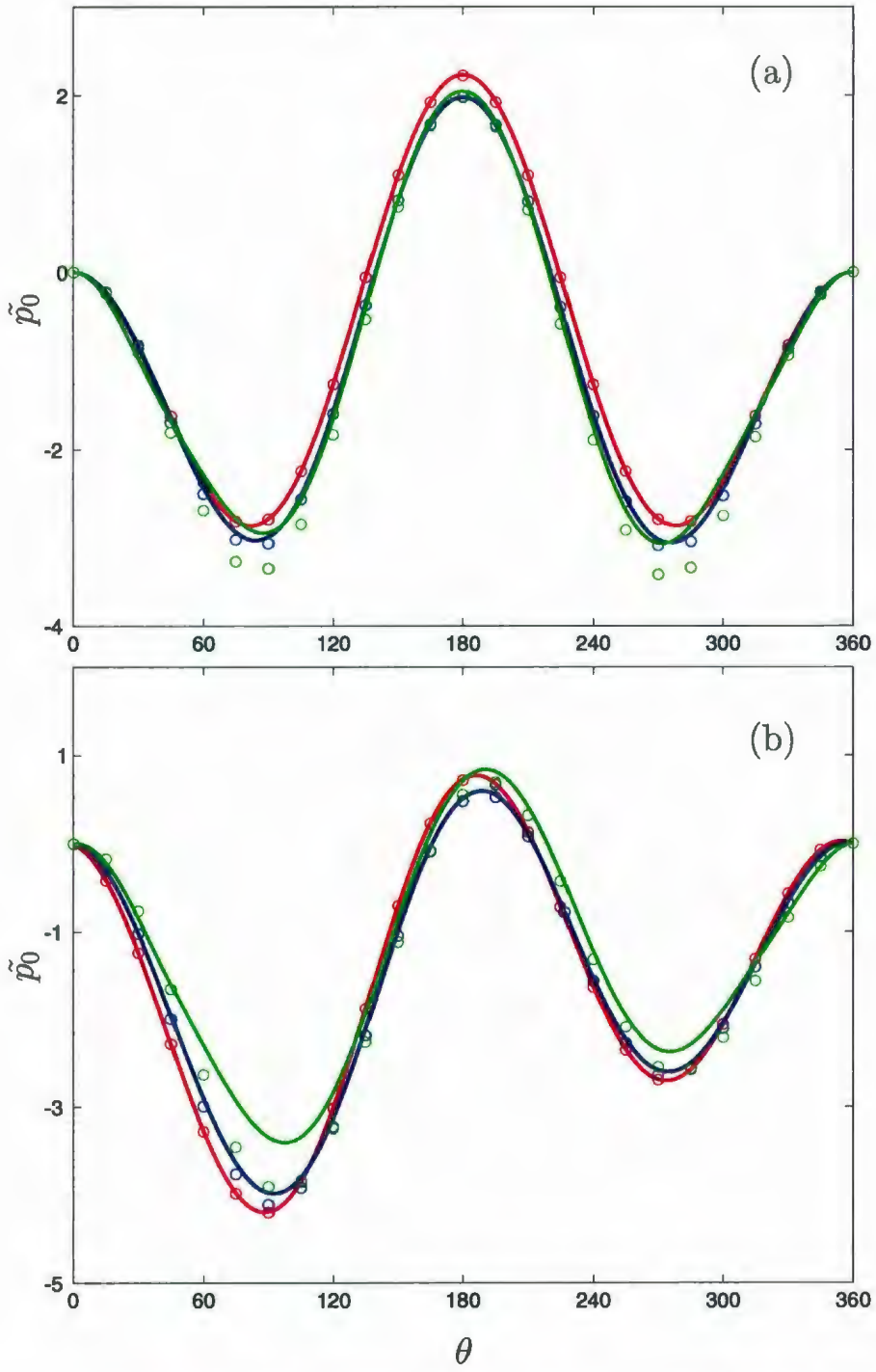

Figure 4.21: Comparison of the surface pressure distribution at $R = 855$, $A = 0.26$, $\Theta_m = 30^o$ and $f/f_0 = 1$: (a) $\eta = 0^o$ and (b) $\eta = 90^o$; —, **numerical solution,** ∘, **analytical solution at the instants** $t = 0.1$ **(red),** $t = 0.5$ **(blue) and** $t = 1.0$ **(green).**

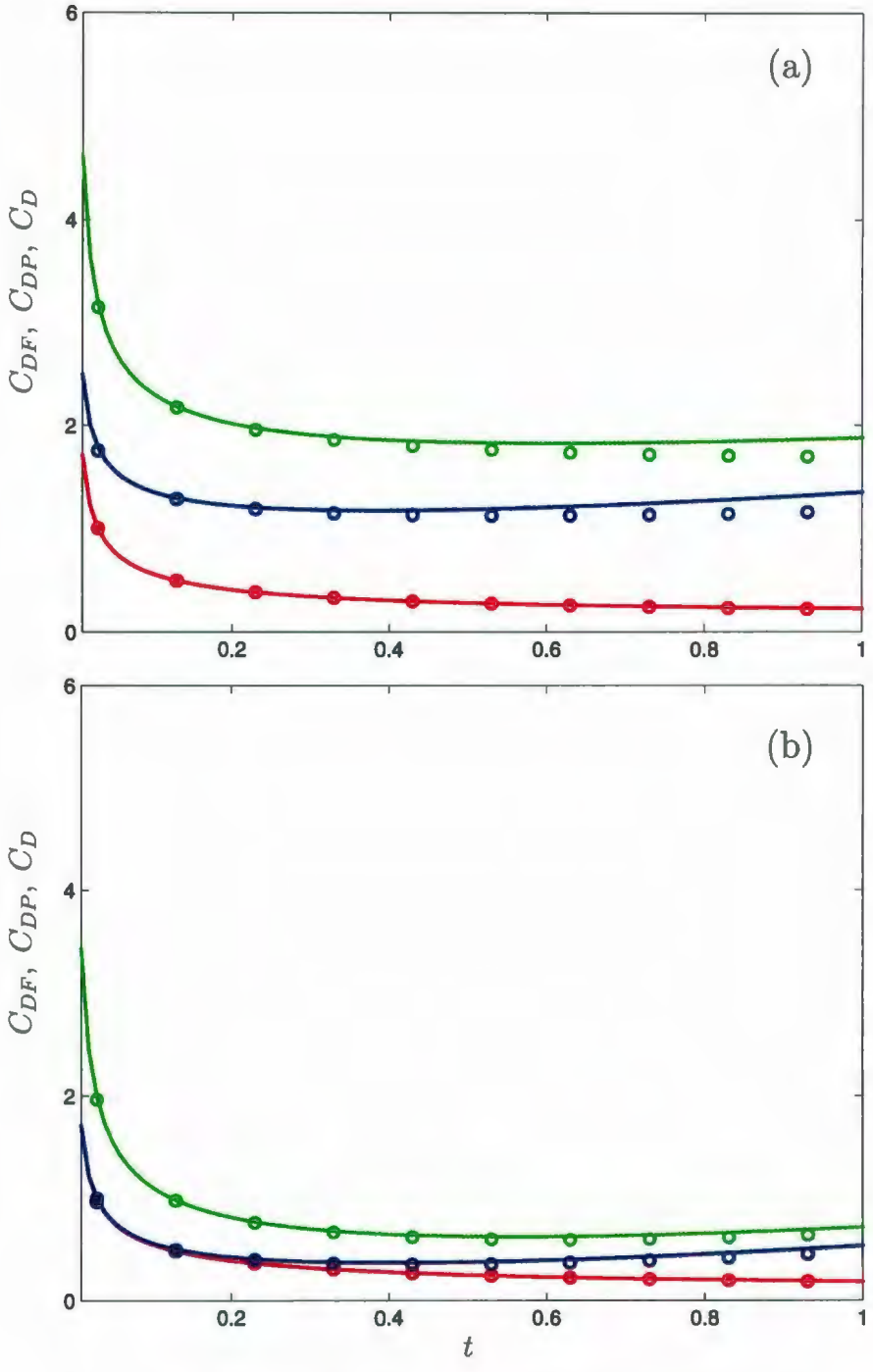

Figure 4.22: Variation of C_{DF} (red), C_{DP} (blue) and C_D (green) at $R = 855$, $A = 0.26$, $\Theta_m = 30^o$ and $f/f_0 = 1$: (a) $\eta = 0^o$ and (b) $\eta = 90^o$; —, **numerical solution,** ∘, **analytical solution.**

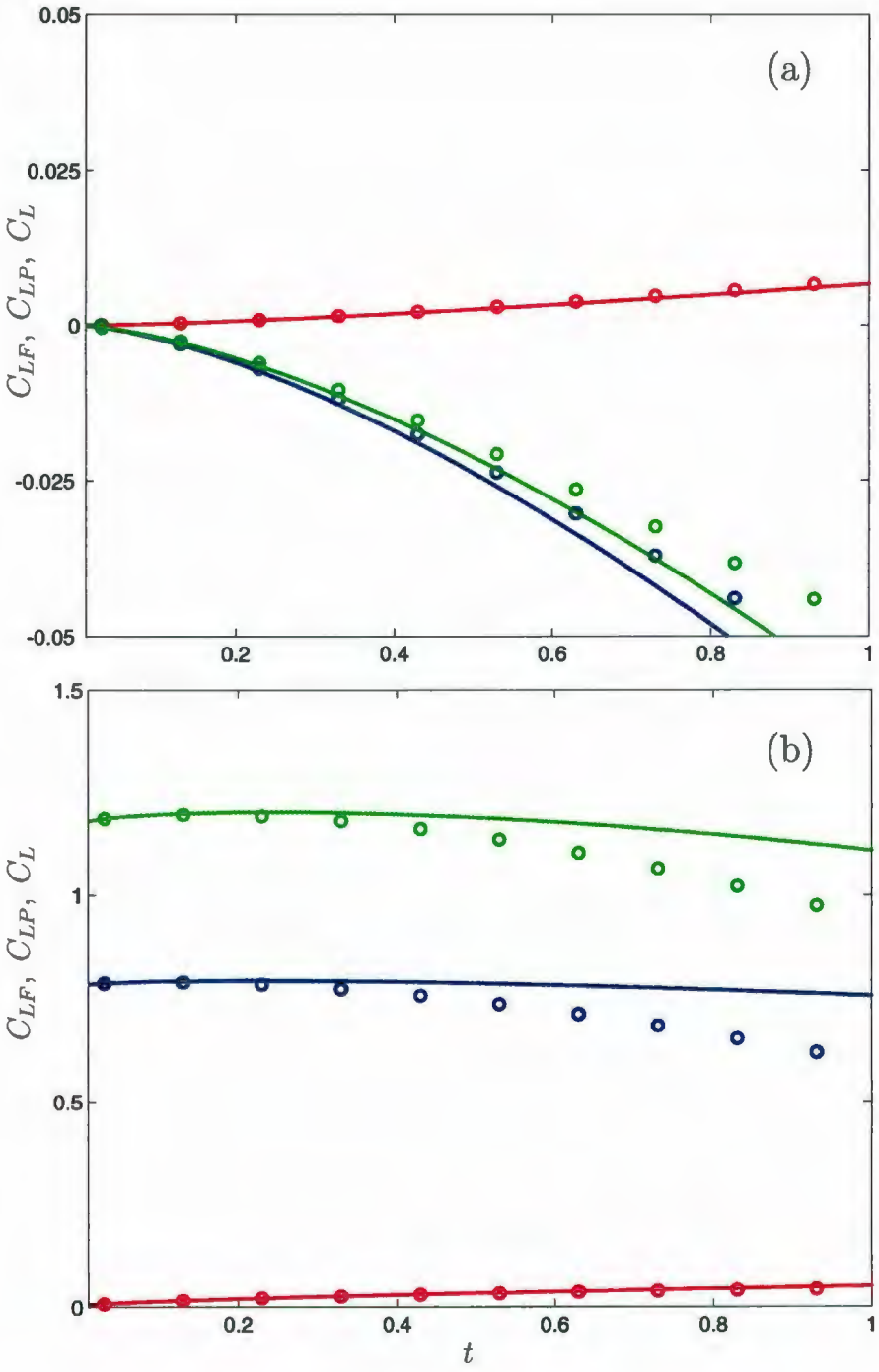

Figure 4.23: Variation of C_{LF} (red), C_{LP} (blue) and C_L (green) at $R = 855$, $A = 0.26$, $\Theta_m = 30^o$ and $f/f_0 = 1$: (a) $\eta = 0^o$ and (b) $\eta = 90^o$; —, **numerical solution,** ∘, **analytical solution.**

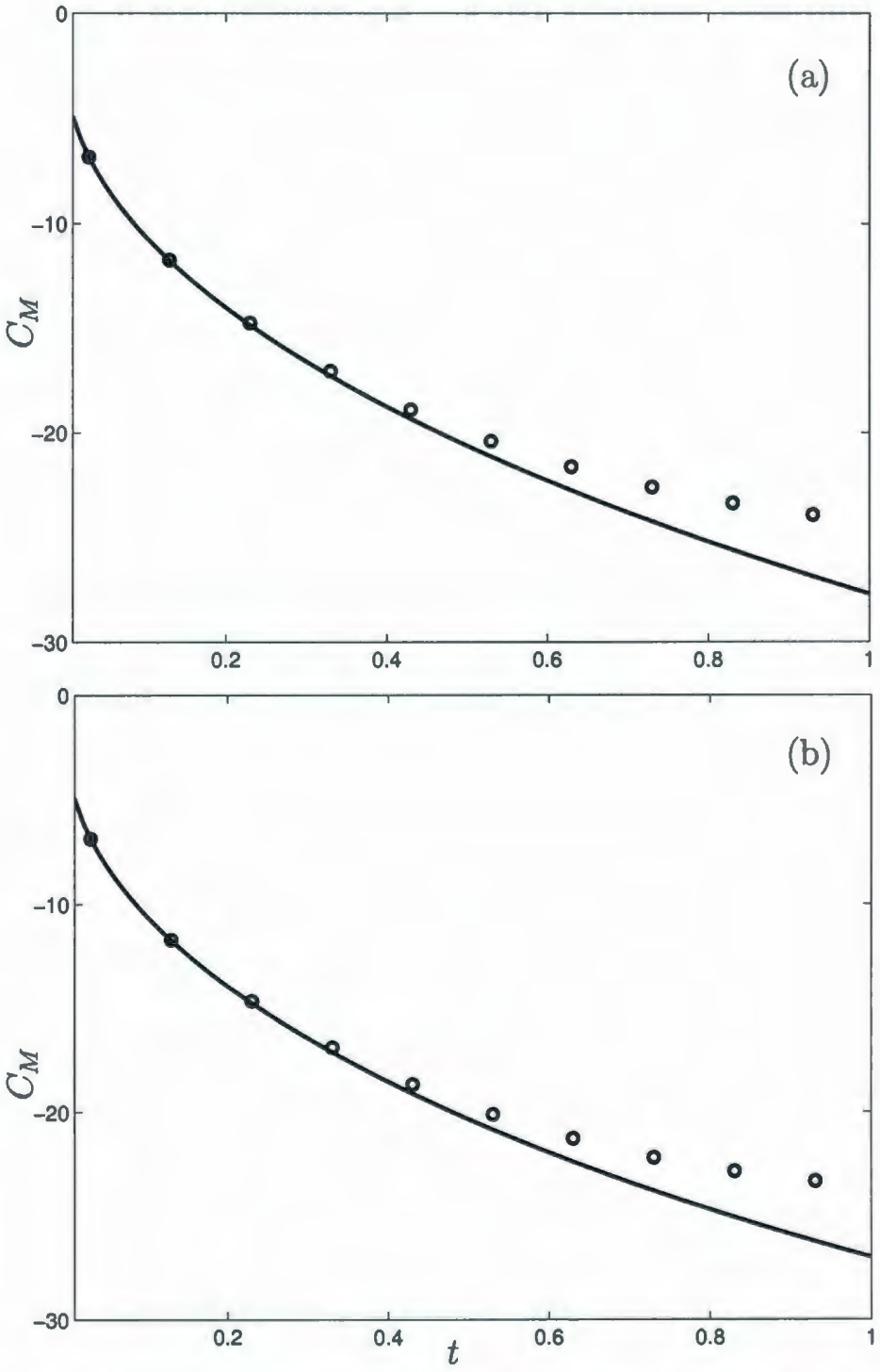

Figure 4.24: Variation of C_M at $R = 855$, $A = 0.26$, $\Theta_m = 30^o$ and $f/f_0 = 1$: (a) $\eta = 0^o$ and (b) $\eta = 90^o$; —, **numerical solution,** ∘, **analytical solution.**

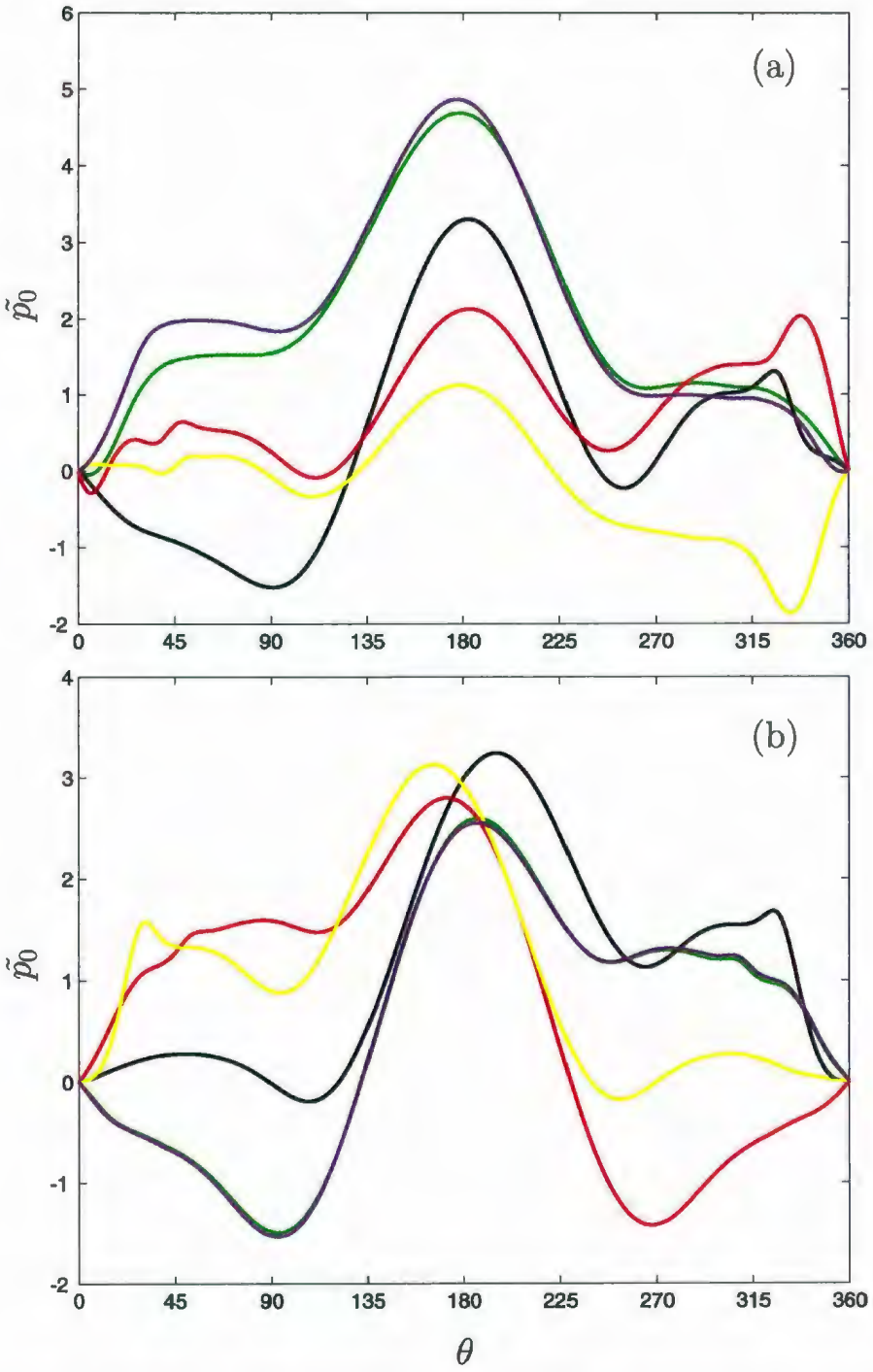

Figure 4.25: Surface pressure distribution during one period of oscillation, T, for $R = 855$, $A = 0.26$, $\Theta_m = 30^o$ and $f/f_0 = 1$: (a) $\eta = 0^o$ and (b) $\eta = 90^o$; at $t = 0T$ (—), $t = T/4$ (—), $t = T/2$ (—), $t = 3T/4$ (—) **and** $t = T$ (—) ($T = 9.09$, $81.82 \leq t \leq 90.91$).

Chapter 5

The wake flow generated by combined (2-DoF) transverse and rotational cylinder oscillation

In this chapter, we focus on the numerical investigation of the wake flow created in a steady free-stream by combined transverse (cross-stream) and rotational oscillation of a circular cylinder. The dimensionless transverse and rotational oscillatory velocities are

$$V(t) = -2\pi f A \sin(2\pi f t) \quad \text{and} \quad \Omega(t) = 2\pi f_\theta \Theta_m \sin(2\pi f_\theta t),$$

respectively. The frequency of the transverse oscillation is the same as for the rotational oscillation i.e., $f = f_\theta$. The near-wake structure as well as the fluid forces acting on the cylinder are then determined for five sets of the four dimensionless groups: $R = 855$, $A = 0.26$, $15^o \leq \Theta_m \leq 75^o$ when $f/f_0 = 0.5,\ 1,\ 2,\ 3,\ 4$ by setting the angle of inclination to $\eta = 90^o$. The connection between lift coefficient and vortex lock-on regimes is also investigated using Power Spectrum Density of the lift coefficient through Fourier analysis.

The simulations are carried out by using the time step $\Delta t_{j+1} = 10^{-4}$, for the first 10 steps. This is then increased to $\Delta t_{j+1} = 10^{-3}$ for the next 10 steps. Finally $\Delta t_{j+1} = 10^{-2}$ is taken for the rest of the solution. In the first computational domain $[0, t_s]$, the number of points in the z direction is taken as 319 with a grid size of $\Delta z = 0.025$. In the the second computational domain $[t_s, t_{max}]$ where $t_s = 40$, the number of points in the ξ direction is taken as 319 with a grid size of $\Delta\xi = 0.01529$. With these choices we set the outer boundary of computational domain at a physical distance of at least 133 times the radius of the cylinder for $R = 855$ and $40 \leq t \leq 120$. The maximum number of terms in the Fourier series is taken as $N = 65$ for all cases considered in this chapter.

5.1 Wake modes and synchronization (lock-on) phenomena in the near-wake region

Figure 5.1 shows the equivorticity lines over one period, T, for the combined transverse and rotational oscillation case when $f/f_0 = 0.5$ and $15^o \leq \Theta_m \leq 75^o$. We note that relatively large-scale vortex formations occur in the asymmetrical **2S** mode, per $T/2$, for $\Theta_m = 15^o$, 30^o in which two vortices are alternatively shed from the upper and lower surfaces of the cylinder per half cycle. In addition, we observe the asymmetrical **4S** mode, per T, for $\Theta_m = 60^o$, 75^o in which four vortices are alternatively shed from the upper and lower surfaces of the cylinder per one cycle. The near-wake structure is almost periodic at $\Theta_m = 15^o$, 30^o per half period of cylinder oscillation, $T/2$ (or T_0). Increasing Θ_m beyond 30^o seems to destroy this periodic behavior in the near-wake region. On the other hand, the near-wake structure shows almost periodic

behavior over one period of oscillation, T, when $\Theta_m = 60^o$, 75^o i.e., vortex lock-on occurs in **4S** mode, per T, at $f/f_0 = 0.5$ and $\Theta_m = 60^o$, 75^o.

For the frequency ratio when $f/f_0 = 1$, the equivorticity lines are plotted in Figure 5.2 for $15^o \leq \Theta_m \leq 75^o$. The vortex shedding mode at this frequency is the synchronized asymmetrical **2S** mode over one oscillation cycle, T, for all values of Θ_m. By tracking the snapshots in the first row of Figure 5.2, which are taken at the instants corresponding to maximum negative angular displacement $-\Theta_m$, we observe a substantial decrease in vortex formation length as Θ_m increases. The vortex formation length is defined in this study as the dimensionless length of the developing vortex on the bottom of the cylinder measured in radii along the wake centerline from the rearmost portion of the cylinder surface to the end of the re-circulating region at the instant corresponding to $-\Theta_m$. In addition, the inclination angle of the base region is also increasing with Θ_m except at $\Theta_m = 15^o$. It is noted that the near-wake structure is inversely repeatable every half period, $T/2$, of oscillation in the range $30^o \leq \Theta_m \leq 75^o$ which is characterized by vortices of equal magnitude shedding from each side of the cylinder.

In the range of the frequency ratios when $f/f_0 \geq 2$, the vortex shedding becomes more complicated due to the strong interaction between the body of the cylinder and the shed vortices. Coalescence of vortices appears in the region very close to the cylinder surface. Consequently, tracking the vortices shedding from the cylinder is difficult especially for cases in which recti-linear amplitude of oscillation is small. At $f/f_0 = 2$, the increase of Θ_m produces different vortex shedding modes as seen in

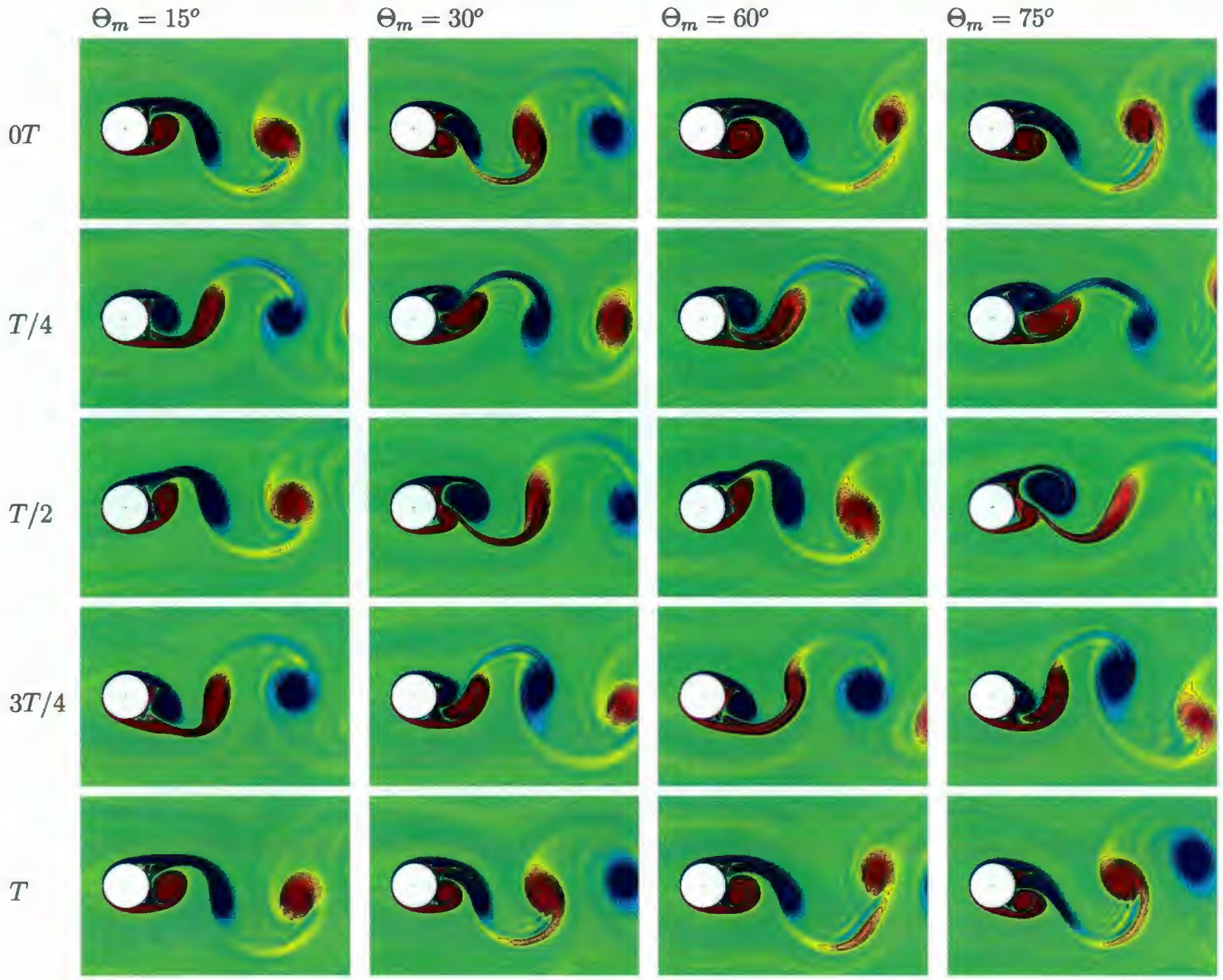

Figure 5.1: Equivorticity lines over one period of oscillation, T, for the combined (2-DoF) transverse and rotational oscillation case ($\eta = 90^o$, $15^o \leq \Theta_m \leq 75^o$) when $R = 855$, $A = 0.26$: $f/f_0 = 0.5$ ($T = 18.18$, $90.9 \leq t \leq 109.08$).

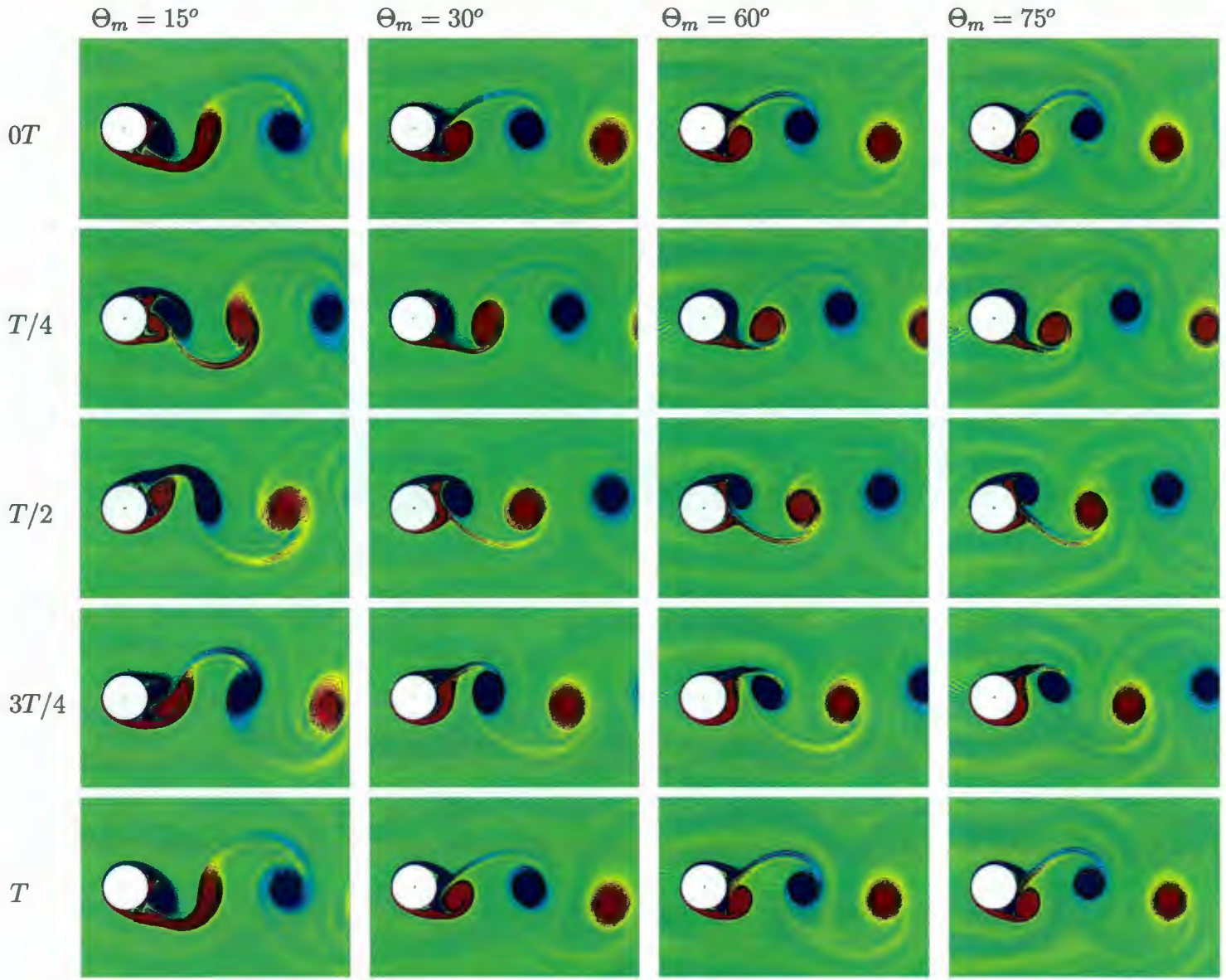

Figure 5.2: Equivorticity lines over one period of oscillation, T, for the combined (2-DoF) transverse and rotational oscillation case ($\eta = 90^o$, $15^o \leq \Theta_m \leq 75^o$) when $R = 855$, $A = 0.26$: $f/f_0 = 1$ ($T = 9.09$, $81.82 \leq t \leq 90.91$).

Figure 5.3. Tracking the snapshots in the first row we observe a reduction in the size of shedding vortices as Θ_m increases. Furthermore, the inclination angle of the top region increases as Θ_m increases whereas inclination angle of the bottom region decreases. For $\Theta_m = 15^o$, we observe the synchronized asymmetrical **S+P** mode, per $2T$, where two positive vortices are shed from the bottom of the cylinder and a large counter-rotating vortex is shed from the top of the cylinder over two periods of oscillation. It is noted that the shedding layer of the upper vortex remains attached to the vortex for a relatively long time as the vortex moves away from the cylinder. As a result another weak vortex breaks away from this shedding layer and accompany the larger vortex downstream. For $\Theta_m = 30^o$, the synchronized asymmetrical mode is **2P** mode, per $2T$, in which two vortices are shed from each side of the cylinder over two periods of cylinder oscillation. It is noted that the two vortices which are shed from the top side of the cylinder coalesce in the near-wake region to form a single vortex during the second period. For $\Theta_m = 60^o$, 75^o, the vortex shedding is characterized by the synchronized asymmetrical **2S** mode, per T, in which a dominant or large vortex is alternatively shed from each side of the cylinder over one period of cylinder oscillation. In this mode, each large vortex is accompanied by another weak counter-rotating vortex. Typical equivorticity and streamline plots for $f/f_0 = 2$ with $\Theta_m = 60^o$, 75^o are plotted in Figure 5.4. The weake vortices decay at a distance of approximately twice the diameter of the cylinder. It is also evident that the near-wake structure is inversely repeatable every $T/2$ for $\Theta_m = 60^o$, 75^o. Thus, it is evident that the near-wake structure is controlled by the rotational oscillation as Θ_m increases.

The equivorticity lines over three periods of oscillations, $3T$, for the frequency ratio

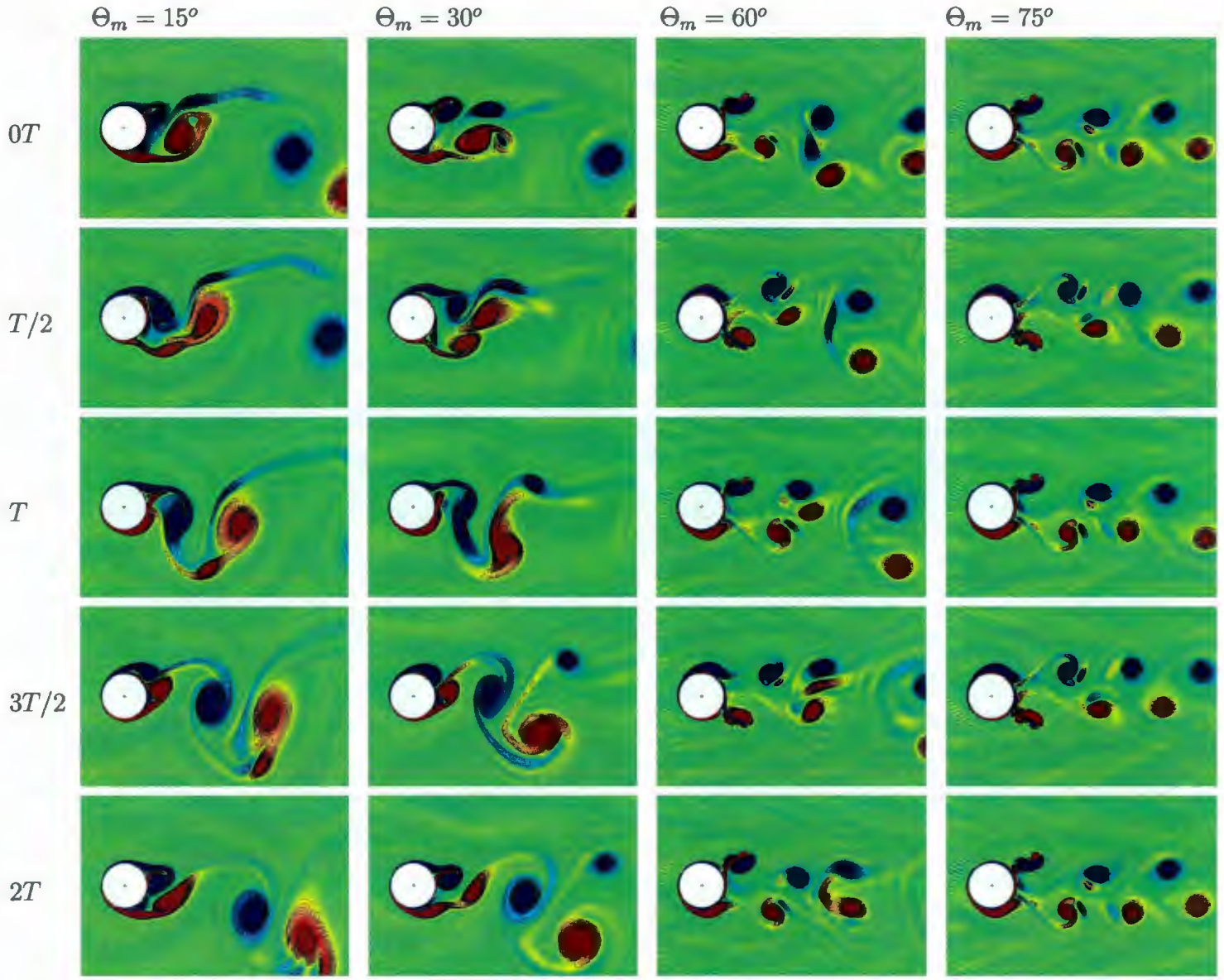

Figure 5.3: Equivorticity lines over two periods of oscillation, $2T$, for the combined (2-DoF) transverse and rotational oscillation case ($\eta = 90^o$, $15^o \leq \Theta_m \leq 75^o$) when $R = 855$, $A = 0.26$: $f/f_0 = 2$ ($T = 4.55$, $90.9 \leq t \leq 99.99$).

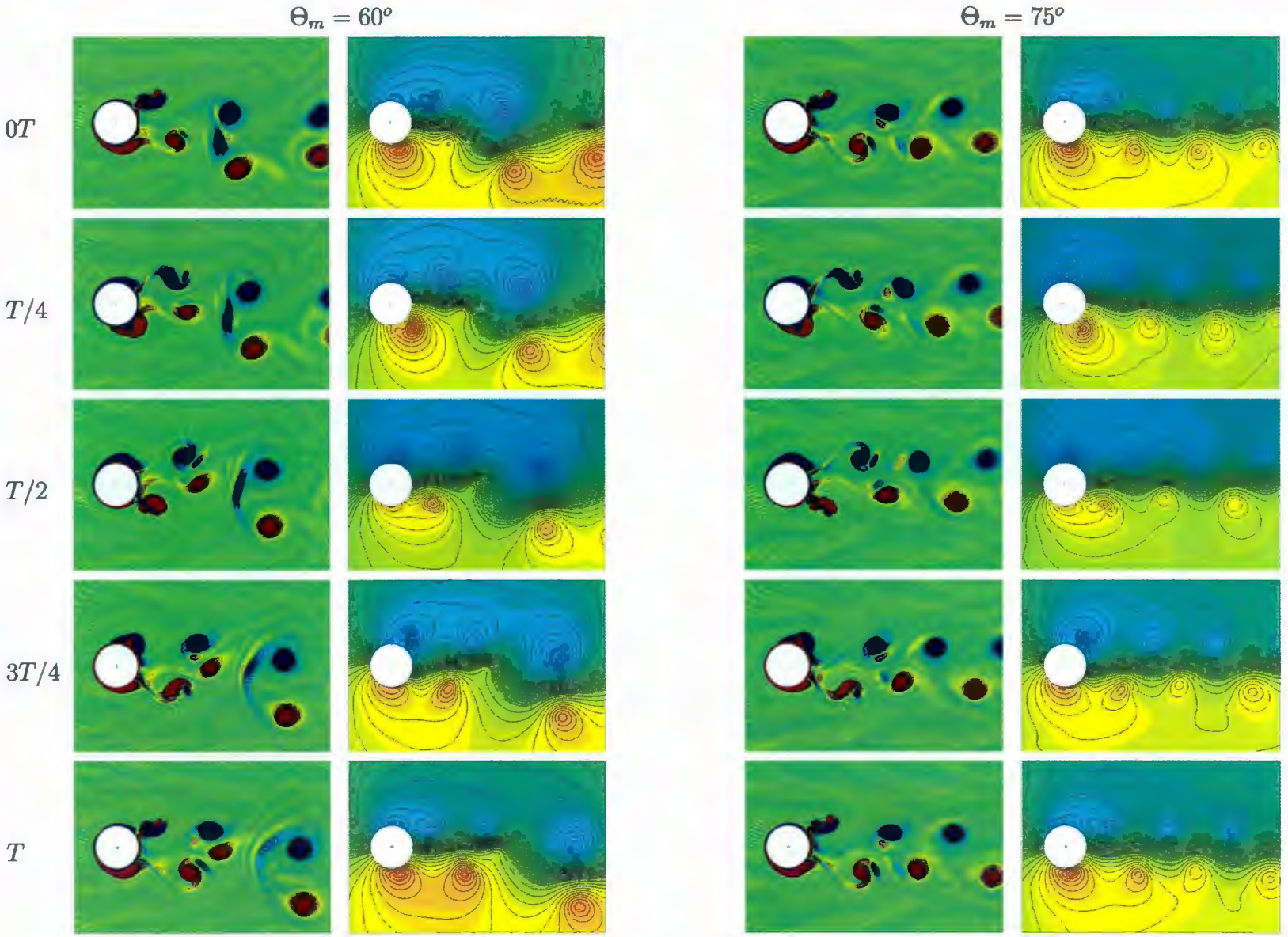

Figure 5.4: Equivorticity lines and streamline patterns over one period of oscillation, T, for the combined (2-DoF) transverse and rotational oscillation case ($\eta = 90^o$: $\Theta_m = 60^o$ (left) and $\Theta_m = 75^o$ (right)) when $R = 855$, $A = 0.26$: $f/f_0 = 2$ ($T = 4.55$, $90.9 \leq t \leq 95.45$).

$f/f_0 = 3.0$ when $15^o \leq \Theta_m \leq 75^o$ are displayed in Figure 5.5. Comparing the snapshots in the first row of Figure 5.5, we observe a reduction in the strength of shedding vortices. At the same time, the vertical distance between the shedding vortices is decreasing as Θ_m increases. It seems that the increase in Θ_m draws irrotational fluid along the wake centerline towards the cylinder base. Moreover, the vortex shedding for $\Theta_m = 15^o$ exhibits a synchronized asymmetrical **2P** mode, per $3T$, in which two vortices are shed from each side of the cylinder over two periods of oscillations. Increasing Θ_m to 30^o produces an interesting synchronized asymmetrical **6S** mode, per $3T$, in which three vortices alternately develop from each side of the cylinder. In addition, the first two vortices which develop from each side coalesce to form one single vortex followed by a third vortex shed from each side in the third period. Increasing Θ_m to 60^o and 75^o, the vortex shedding mode switches to the synchronized asymmetrical **2S** mode, per T, which is similar to that observed for the previous case when $f/f_0 = 3$ and $\Theta_m = 60^o$, 75^o. It is noted that each large vortex is accompanied by another weak counter-rotating vortex. Typical equivorticity and streamline plots for $f/f_0 = 3$ and $\Theta_m = 60^o$, 75^o are plotted in Figure 5.6. It is noted that at $\Theta_m = 60^o$ all the weak vortices disappear at a distance which is less than one diameter of the cylinder while at $\Theta_m = 75^o$ they disappear at a distance of more than twice the cylinder diameter.

Equivorticity lines at $f/f_0 = 4.0$ when $15^o \leq \Theta_m \leq 75^o$ are displayed in Figure 5.7. The snapshots in the first row which are taken at the instant corresponding to the maximum negative displacement, $-\Theta_m$, show that there is a reduction in the vortex formation length and the size of the vortices as Θ_m increases. Furthermore, it is noted

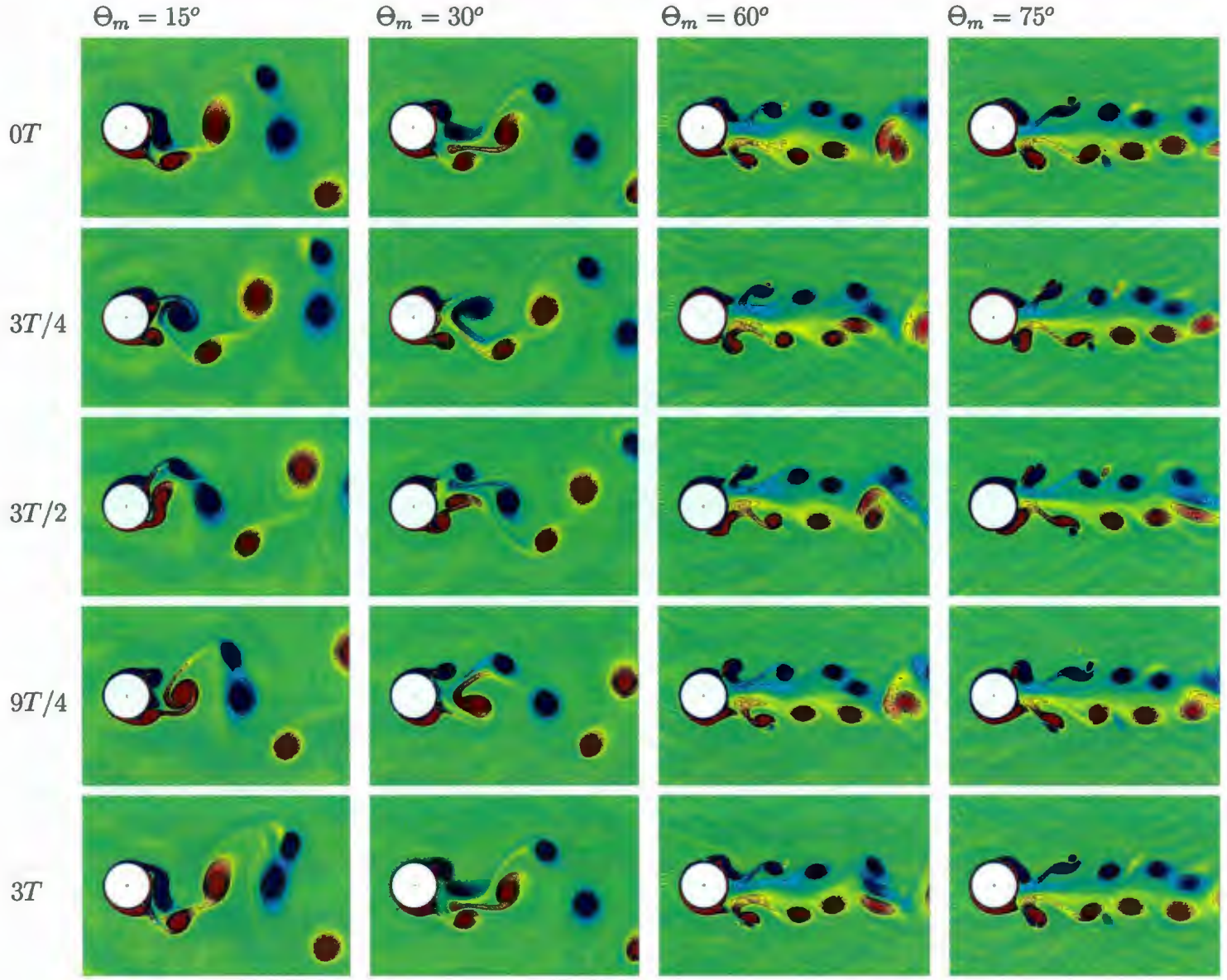

Figure 5.5: Equivorticity lines over three periods of oscillation, $3T$, for the combined (2-DoF) transverse and rotational oscillation case ($\eta = 90^o$, $15^o \leq \Theta_m \leq 75^o$) when $R = 855$, $A = 0.26$: $f/f_0 = 3$ ($T = 3.03$, $90.9 \leq t \leq 99.99$).

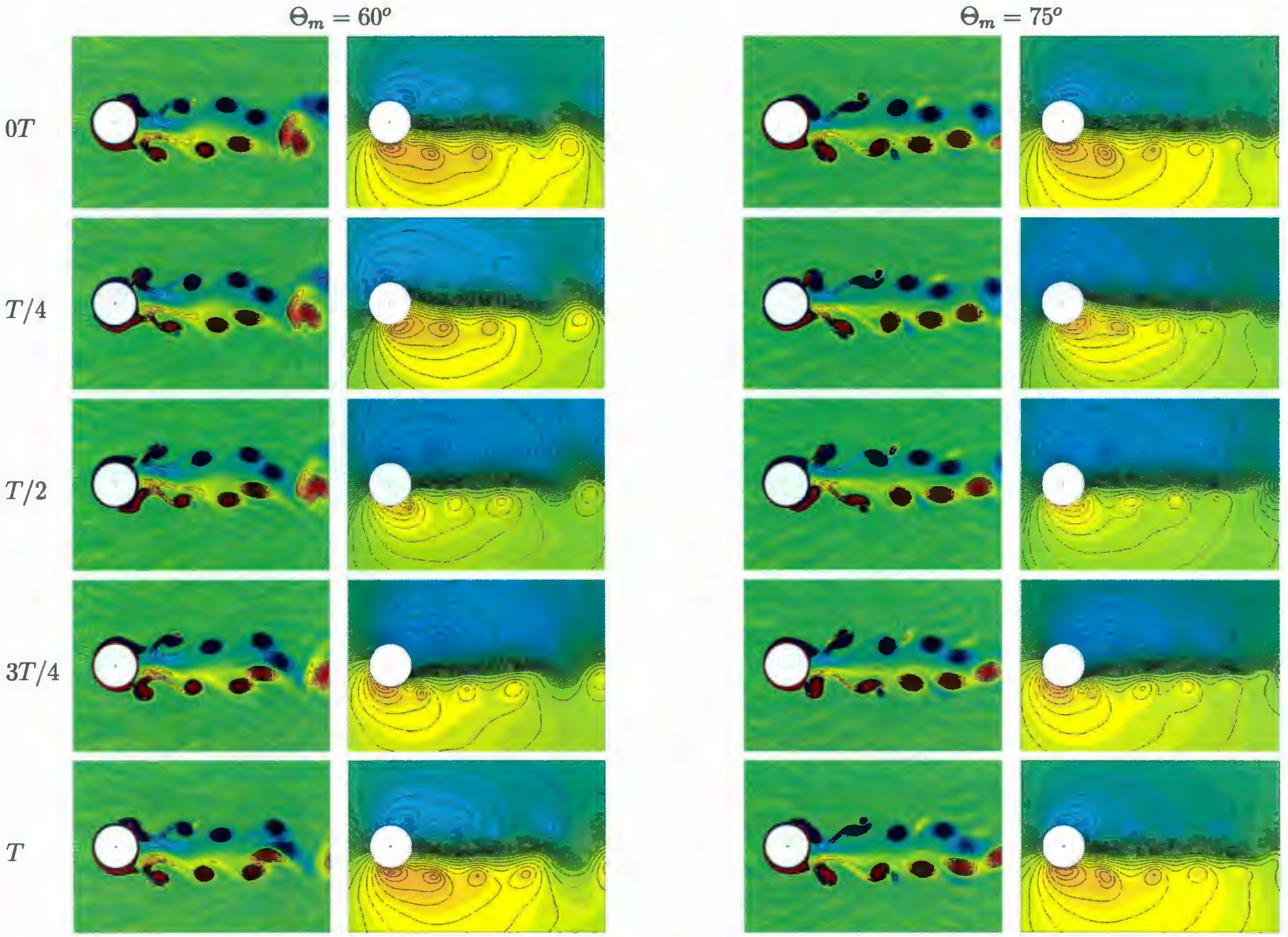

Figure 5.6: Equivorticity lines and streamline patterns over one period of oscillation, T, for the combined (2-DoF) transverse and rotational oscillation case ($\eta = 90^o$: $\Theta_m = 60^o$ (left) and $\Theta_m = 75^o$ (right)) when $R = 855$, $A = 0.26$: $f/f_0 = 3$ ($T = 3.03$, $90.9 \leq t \leq 93.93$).

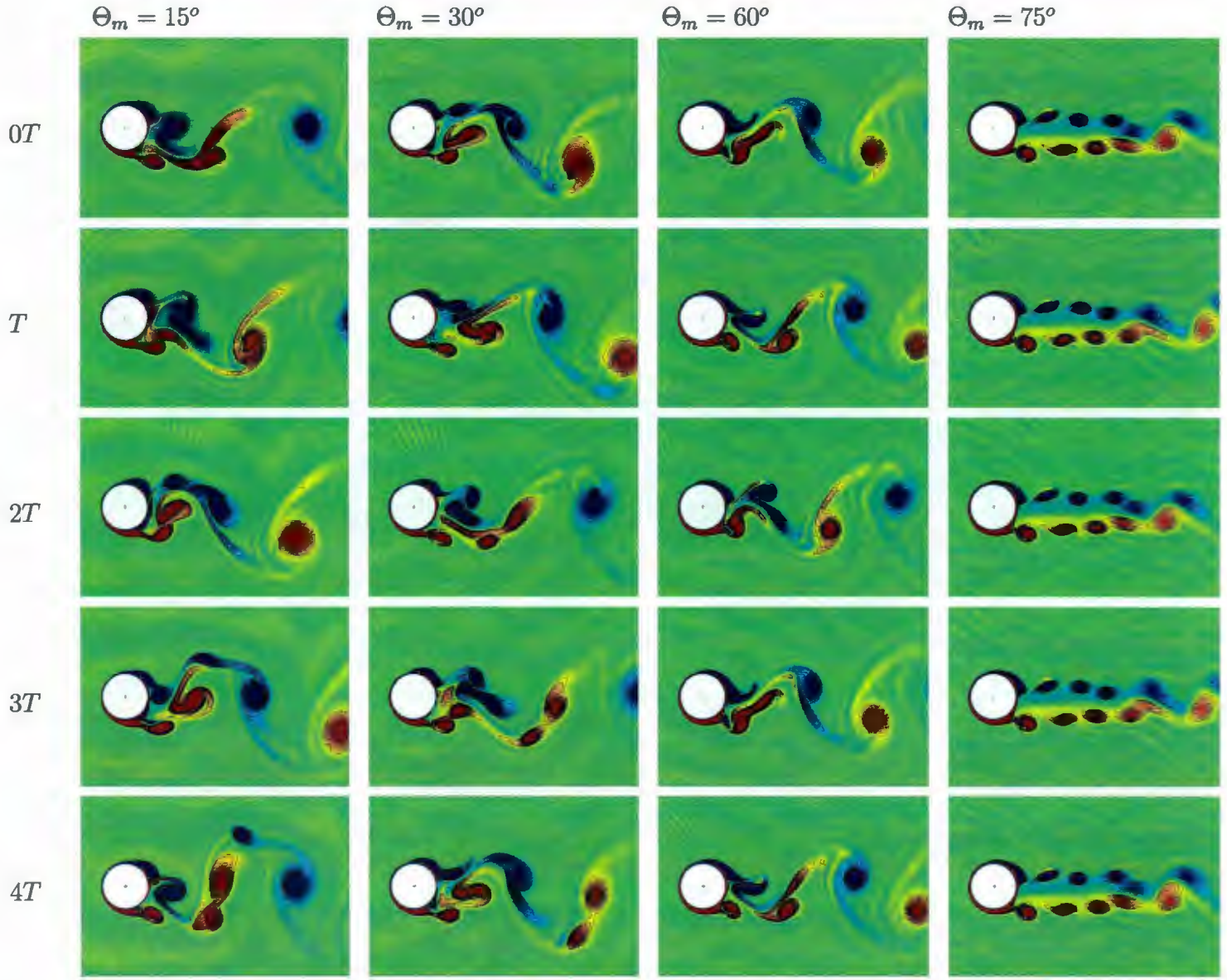

Figure 5.7: Equivorticity lines over four periods of oscillation, $4T$, for the combined (2-DoF) transverse and rotational oscillation case ($\eta = 90^o$, $15^o \leq \Theta_m \leq 75^o$) when $R = 855$, $A = 0.26$: $f/f_0 = 4$ ($T = 2.27$, $84.09 \leq t \leq 93.18$).

that the vertical distance between the shedding vortices is reduced as Θ_m increases. For $\Theta_m = 15^o$ we observe the synchronized asymmetrical **8S** mode, per $4T$, as shown in Figure 5.8. In this mode, four vortices develop on each side of the cylinder. It is noted that the first three vortices which develop from each side coalesce to form a single large vortex which is then followed by a fourth vortex. In addition the coalescence of the three vortices appears in the near-wake region very close to the cylinder surface. Increasing Θ_m to 30^o we obtain the synchronized asymmetrical **8S** mode, per $4T$, in which four alternately vortices are shed from each side of the cylinder as shown in Figure 5.9. Furthermore, four vortices which are shed from the upper side coalesce immediately after the shedding of the second vortex so that they appear as one, two or three positive vortices in the near-wake region. The first three vortices which are shed from the bottom side coalesce to form a single large vortex which is then followed by a fourth vortex which gives two negative vortices in the near-wake region. Increasing Θ_m to 60^o, the vortex shedding pattern changes to the synchronized asymmetrical **6S** mode, per $3T$, as shown in Figure 5.10. In this mode, three alternately shed vortices develop from each side of the cylinder. The first two vortices shed from each side coalesce to form a single vortex which is followed by the third vortex from each side. Therefore, it appears as if two vortices are shed from each side of the cylinder over three periods of oscillation. At $\Theta_m = 75^o$, the dominant vortex shedding mode is the asymmetric **2S** mode, per T, as shown in Figure 5.11. Thus, it is evident that increasing Θ_m has a significant effect on vortex shedding modes and their periods.

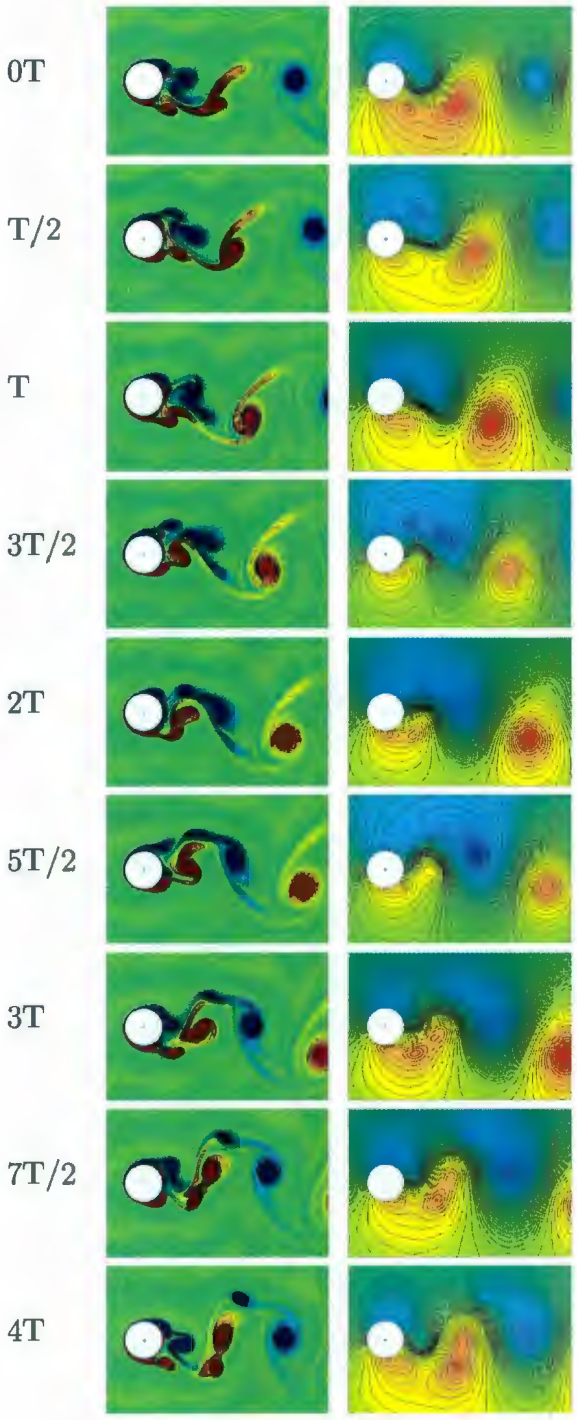

Figure 5.8: Equivorticity lines (left) and streamline patterns (right) over four periods, $4T$, for the combined (2-DoF) transverse and rotational oscillation case ($\eta = 90^o$, $\Theta_m \neq 0$) when $R = 855$, $A = 0.26$: $\Theta_m = 15^o$ and $f/f_0 = 4.0$ ($T = 2.27$, $84.09 \leq t \leq 93.18$).

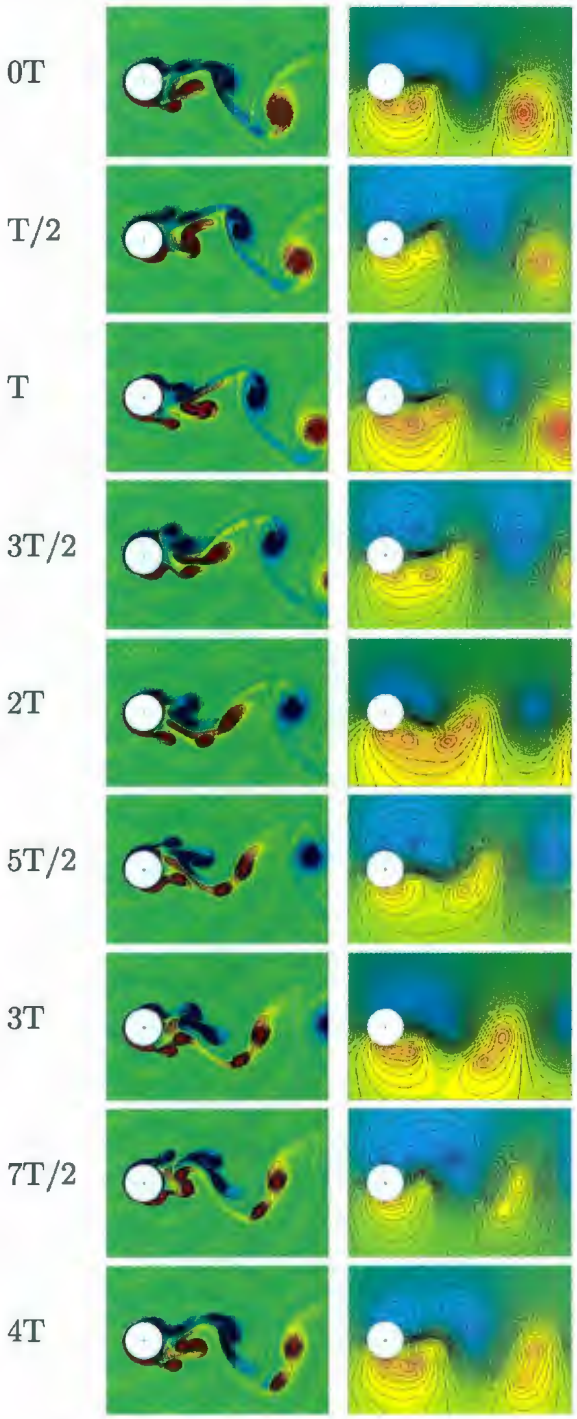

Figure 5.9: Equivorticity lines (left) and streamline patterns (right) over four periods, $4T$, for the combined (2-DoF) transverse and rotational oscillation case ($\eta = 90^o$, $\Theta_m \neq 0$) when $R = 855$, $A = 0.26$: $\Theta_m = 30^o$ and $f/f_0 = 4.0$ ($T = 2.27$, $84.09 \leq t \leq 93.18$).

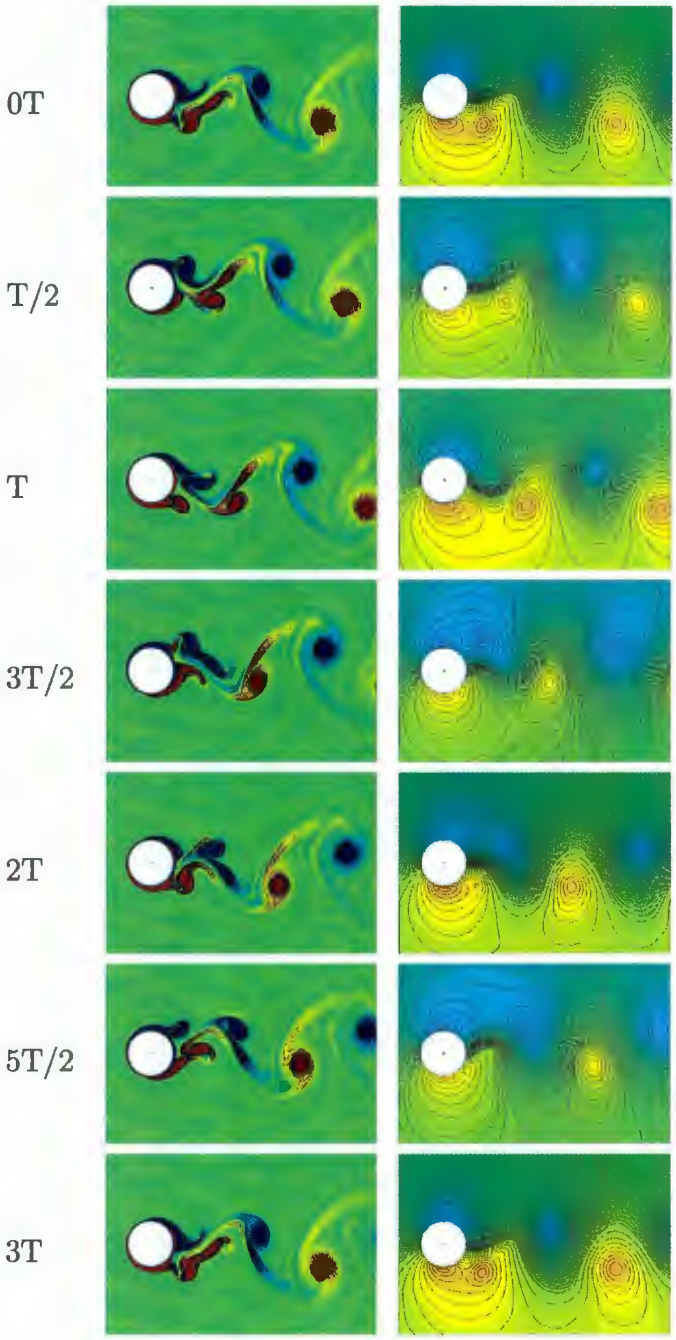

Figure 5.10: Equivorticity lines (left) and streamline patterns (right) over three periods, $3T$, for the combined (2-DoF) transverse and rotational oscillation case ($\eta = 90^o$, $\Theta_m \neq 0$) when $R = 855$, $A = 0.26$: $\Theta_m = 60^o$ and $f/f_0 = 4.0$ ($T = 2.57$, $84.09 \leq t \leq 90.91$).

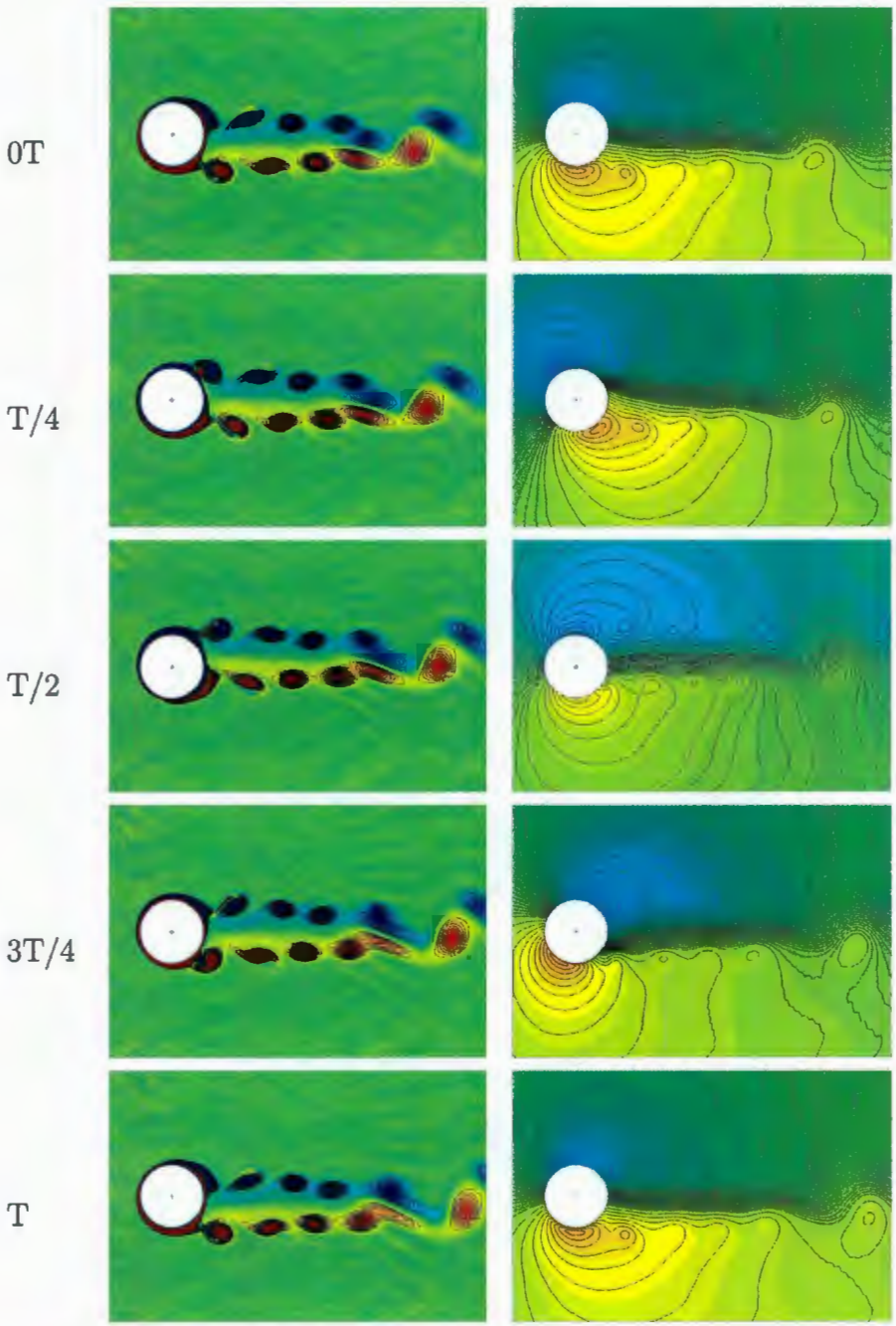

Figure 5.11: Equivorticity lines (left) and streamline patterns (right) over one period, T, for the combined (2-DoF) transverse and rotational oscillation case ($\eta = 90^o$, $\Theta_m \neq 0$) when $R = 855$, $A = 0.26$: $\Theta_m = 75^o$ and $f/f_0 = 4.0$ ($T = 2.27$, $84.09 \leq t \leq 86.36$).

The effect of flow parameters on the near-wake structure can be summarized as follows. Increasing the maximum angular displacement , Θ_m, or the excitation frequency, f/f_0, leads to the breaking up of the near-wake vorticity and thus we obtain different modes of vortex shedding. Tables 5.1, 5.2 show the effect of both Θ_m and f/f_0 on the vortex shedding modes and their periods. It can be seen that as Θ_m increases the vortex shedding mode tends to, in general, the **2S** mode, per T, except for $f/f_0 = 0.5$. The classical **2S** mode is the dominant mode for low values of the excitation frequency, $f/f_0 \leq 1$ since the maximum oscillatory speeds of both motions are less than the uniform flow speed. Further, period reduction is observed at high value of f/f_0 as Θ_m increases. In addition, the lock-on regimes are observed for $f/f_0 \geq 1$ when $15^o \leq \Theta_m \leq 75^o$. Inversely repeatable phenomenon every half of the vortex shedding period is reported in all lock-on cases for combined transverse and rotational oscillation. The coalescence between the shed vortices in the near-wake region appears at high frequency ratios (i.e. $f/f_0 \geq 2$).

f/f_0 \ Θ_m	15^o	30^o	60^o	75^o
0.5	**2S** •	**2S** •	**4S** •	**4S** •
1	**2S** •	**2S** •	**2S** •	**2S** •
2	**S+P** •	**2P** •	**2S** •	**2S** •
3	**2P** •	**6S** •	**2S** •	**2S** •
4	**8S** •	**8S** •	**6S** •	**2S** •

Table 5.1: The effect of f/f_0 and Θ_m on the vortex shedding modes for the combined (2-DoF) transverse and rotational oscillation case ($\eta = 90^o$, $\Theta_m \neq 0$) when $R = 855$, $A = 0.26$: • lock-on mode; • non-lock mode.

f/f_0 \ Θ_m	15^o	30^o	60^o	75^o
0.5	T/2	T/2	T	T
1	T	T	T	T
2	2T	2T	T	T
3	3T	3T	T	T
4	4T	4T	3T	T

Table 5.2: The effect of f/f_0 and Θ_m on the vortex shedding periods for the combined (2-DoF) transverse and rotational oscillation case ($\eta = 90^o$, $\Theta_m \neq 0$) when $R = 855$, $A = 0.26$.

5.2 Time histories of fluctuating fluid forces

Figure 5.12 shows the time evolution of the lift coefficient, C_L, plotted with the cylinder displacement and the Power Spectral Density (PSD) of the lift coefficient at $f/f_0 = 0.5$ and $15^o \leq \Theta_m \leq 75^o$. The lift coefficient for each has two dominant frequencies. These frequencies are the forcing and natural frequencies as suggested by the corresponding PSD of each lift record. However, it can be seen that the effect of the oscillating frequency becomes stronger with the increase of Θ_m. This behavior of the lift coefficient confirms that the near-wake structure is almost periodic per $T/2$ when $\Theta_m = 15^o$, 30^o or per T when $\Theta_m = 60^o$, 75^o (see Figure 5.1). Further, the amplitude of the lift coefficient, $C_{L,amp}$, is increasing for $\Theta_m \geq 30^o$. Figures 5.13 and 5.14 show the time evolution of the drag and moment coefficients plotted with the cylinder displacement for $f/f_0 = 0.5$. It can be seen that the amplitude of both the drag coefficient, $C_{D,amp}$, and moment coefficients are increasing proportionally with Θ_m. Further, the minimum value of the drag coefficient, $C_{D,min}$, is deceasing with the increase of Θ_m. The moment coefficient shows oscillatory behavior at the forcing

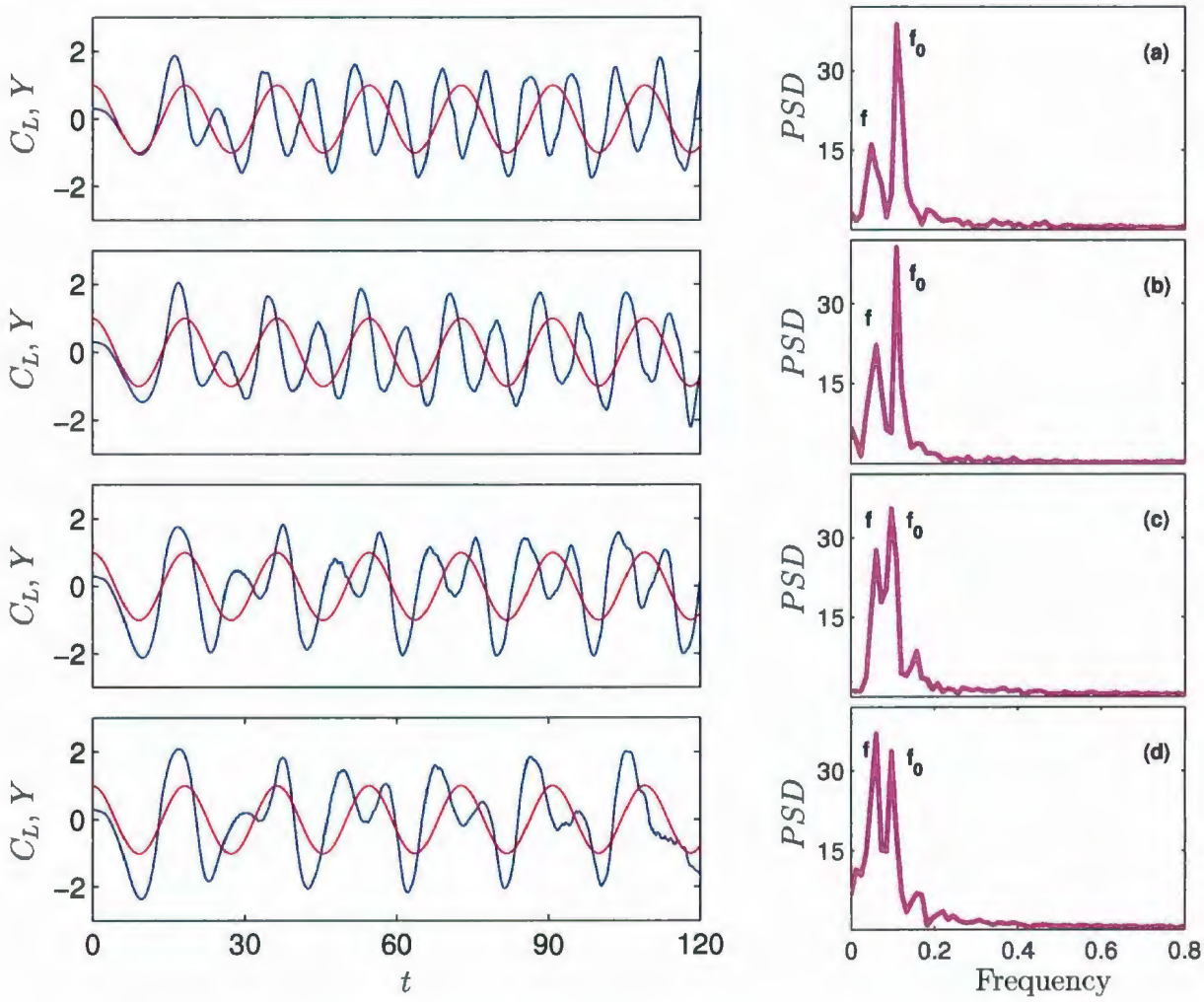

Figure 5.12: The time variation of C_L (—) with respect to cylinder displacement, Y (—) and the Fourier analysis of the lift coefficient PSD (----) for the combined (2-DoF) transverse and rotational oscillation case ($\eta = 90^o$, $\Theta_m \neq 0$) when $R = 855$, $A = 0.26$ and $f/f_0 = 0.5$: (a) $\Theta_m = 15^o$; (b) $\Theta_m = 30^o$; (c) $\Theta_m = 60^o$ and (d) $\Theta_m = 75^o$.

frequency f and is out of phase with Y. Also, C_M shows beating wave forms which indicates the competition between the forcing and natural shedding frequencies.

For the case of $f/f_0 = 1$, the lift coefficient for each case exhibits a periodic behavior which suggests that it only has one dominant frequency. The superimposed lift coefficient, C_L, and cylinder displacement, Y, are plotted for $15^o \leq \Theta_m \leq 75^o$ in Figure 5.15. This dominant frequency in the lift record has been calculated using the PSD and found to be exactly the forcing frequency as shown in Figure 5.15. This confirms our finding that vortex lock-on occurs at $f/f_0 = 1$ (see Figure 5.2). We also noted that C_L oscillates in phase with Y. Moreover, the lift records show a reduction in their maximum and amplitude values, $C_{L,max}$ and $C_{L,amp}$ respectively, as Θ_m increases. The time evolution of the drag and moment coefficients at $f/f_0 = 1$ are plotted in Figures 5.16 and 5.17, respectively. It is noted that C_D oscillates at twice the forcing frequency, $2f$, and shows very little phase shift with respect to the cylinder motion. It can be seen that $C_{D,min}$ is decreasing while $C_{D,amp}$ is increasing as Θ_m increases in the range $\Theta_m \geq 30^o$. On the other hand, the moment coefficient C_M oscillates at the forcing frequency, f, and C_M and Y are out of phase with each other as shown in Figure 5.17. The amplitude of the moment coefficient is increasing as Θ_m increases.

At $f/f_0 = 2$, the time variation of C_L, Y and the PSD are plotted in Figure 5.18 for $15^o \leq \Theta_m \leq 75^o$. C_L oscillates at f and is in phase with the cylinder motion. It is noted that one dominant peak develops in the PSD of the lift coefficient as Θ_m increases. The effect of the natural frequency (small peak) becomes relatively

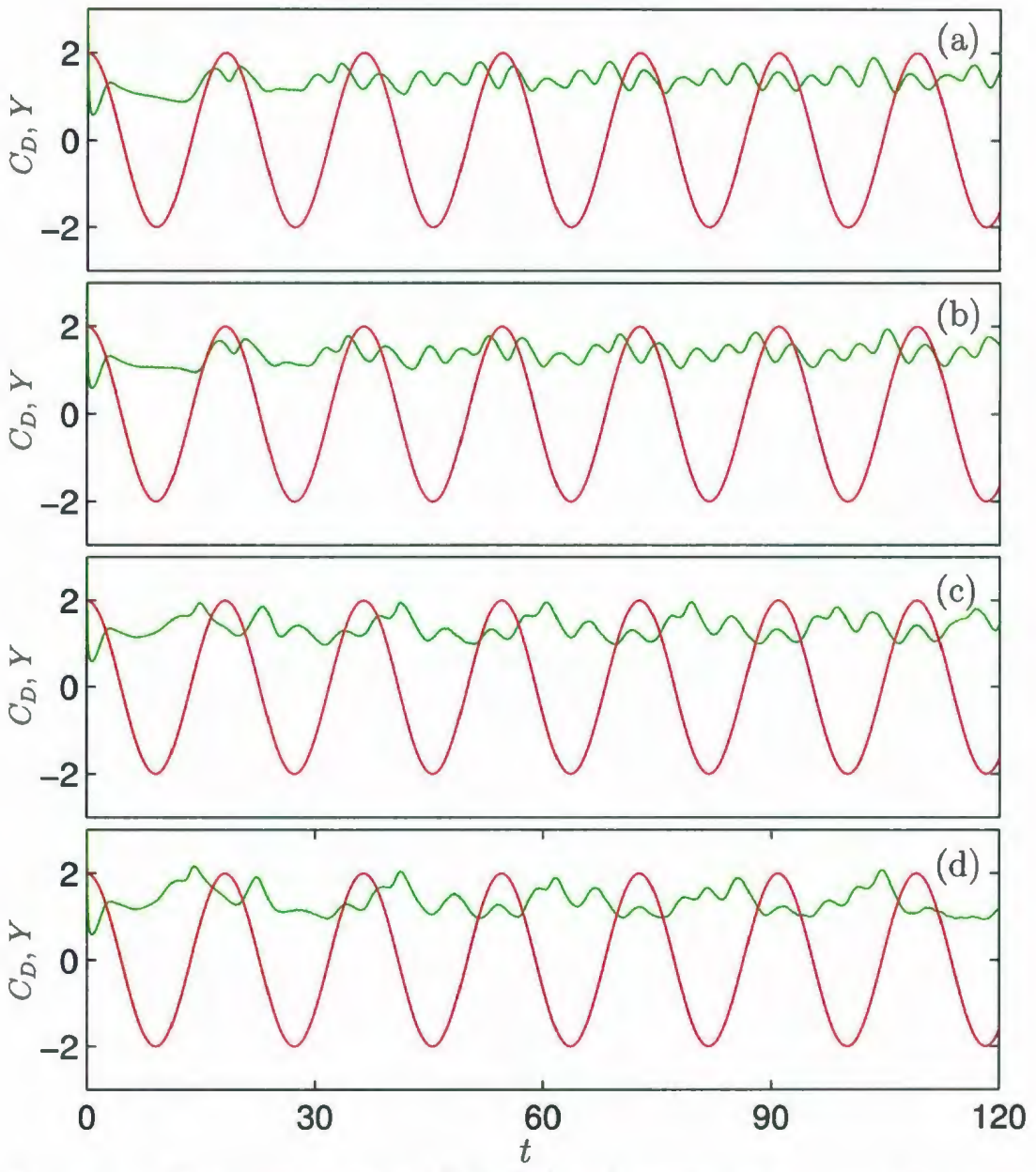

Figure 5.13: The time variation of C_D (—) with respect to cylinder displacement, Y (—) for the combined (2-DoF) transverse and rotational oscillation case ($\eta = 90^o$, $\Theta_m \neq 0$) when $R = 855$, $A = 0.26$ and $f/f_0 = 0.5$: (a) $\Theta_m = 15^o$; (b) $\Theta_m = 30^o$; (c) $\Theta_m = 60^o$ and (d) $\Theta_m = 75^o$.

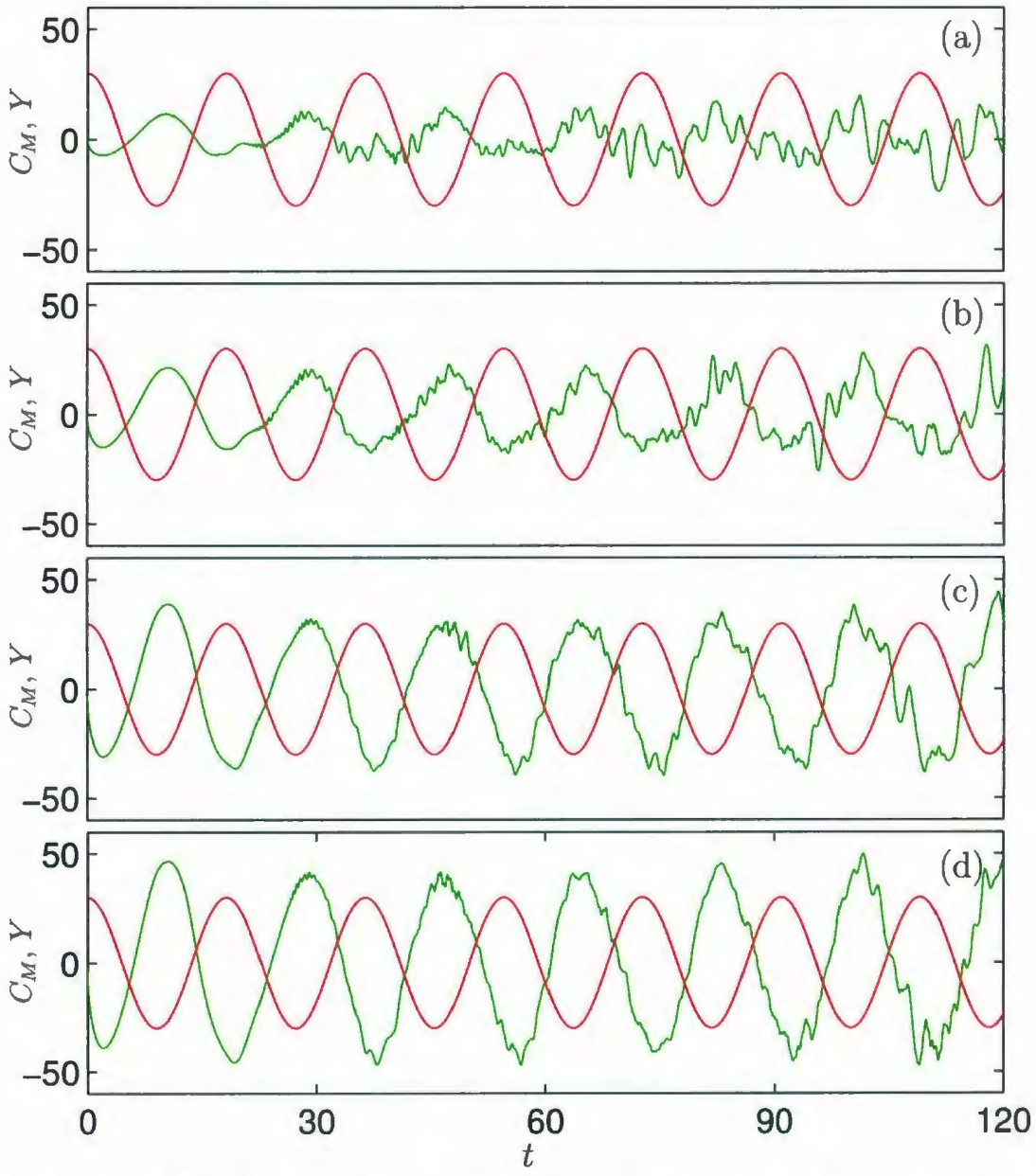

Figure 5.14: The time variation of C_M (—) with respect to cylinder displacement, Y (—) for the combined (2-DoF) transverse and rotational oscillation case ($\eta = 90^o$, $\Theta_m \neq 0$) when $R = 855$, $A = 0.26$ and $f/f_0 = 0.5$: (a) $\Theta_m = 15^o$; (b) $\Theta_m = 30^o$; (c) $\Theta_m = 60^o$ and (d) $\Theta_m = 75^o$.

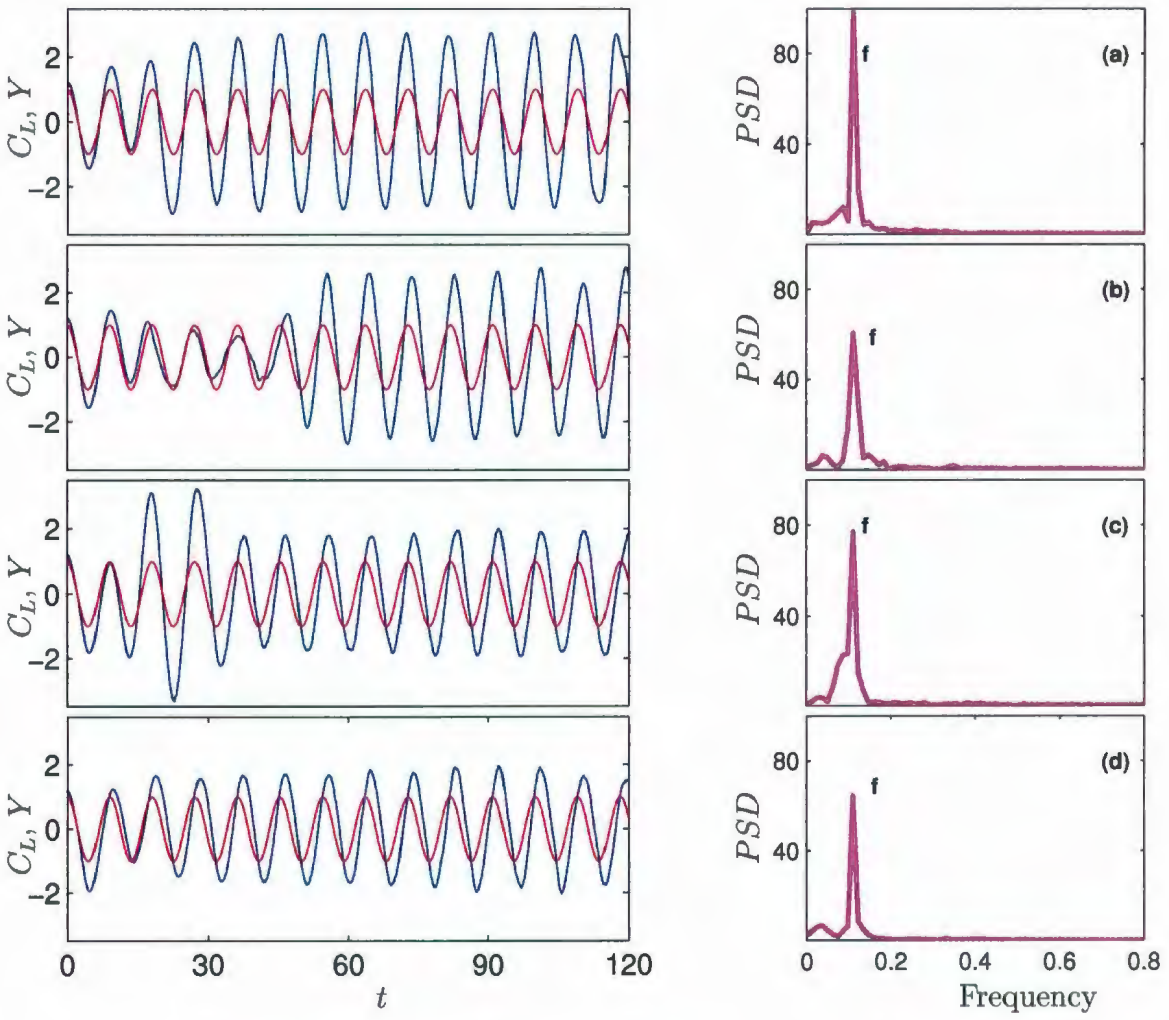

Figure 5.15: The time variation of C_L (—) with respect to cylinder displacement, Y (—) and the Fourier analysis of the lift coefficient PSD (----) for the combined (2-DoF) transverse and rotational oscillation case ($\eta = 90^o$, $\Theta_m \neq 0$) when $R = 855$, $A = 0.26$ and $f/f_0 = 1.0$: (a) $\Theta_m = 15^o$; (b) $\Theta_m = 30^o$; (c) $\Theta_m = 60^o$ and (d) $\Theta_m = 75^o$.

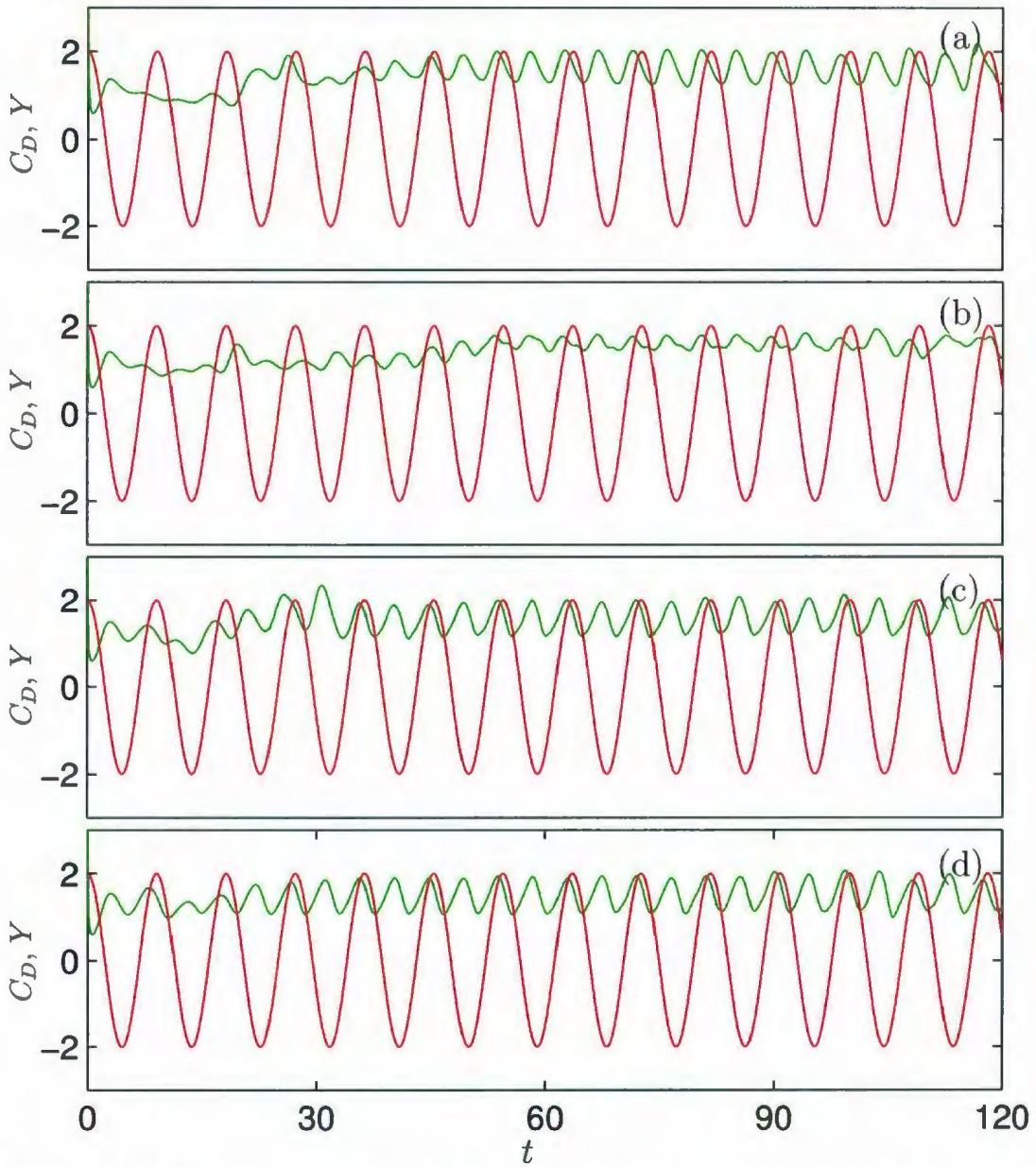

Figure 5.16: The time variation of C_D (—) with respect to cylinder displacement, Y (—) for the combined (2-DoF) transverse and rotational oscillation case ($\eta = 90^o$, $\Theta_m \neq 0$) when $R = 855$, $A = 0.26$ and $f/f_0 = 1.0$: (a) $\Theta_m = 15^o$; (b) $\Theta_m = 30^o$; (c) $\Theta_m = 60^o$ and (d) $\Theta_m = 75^o$.

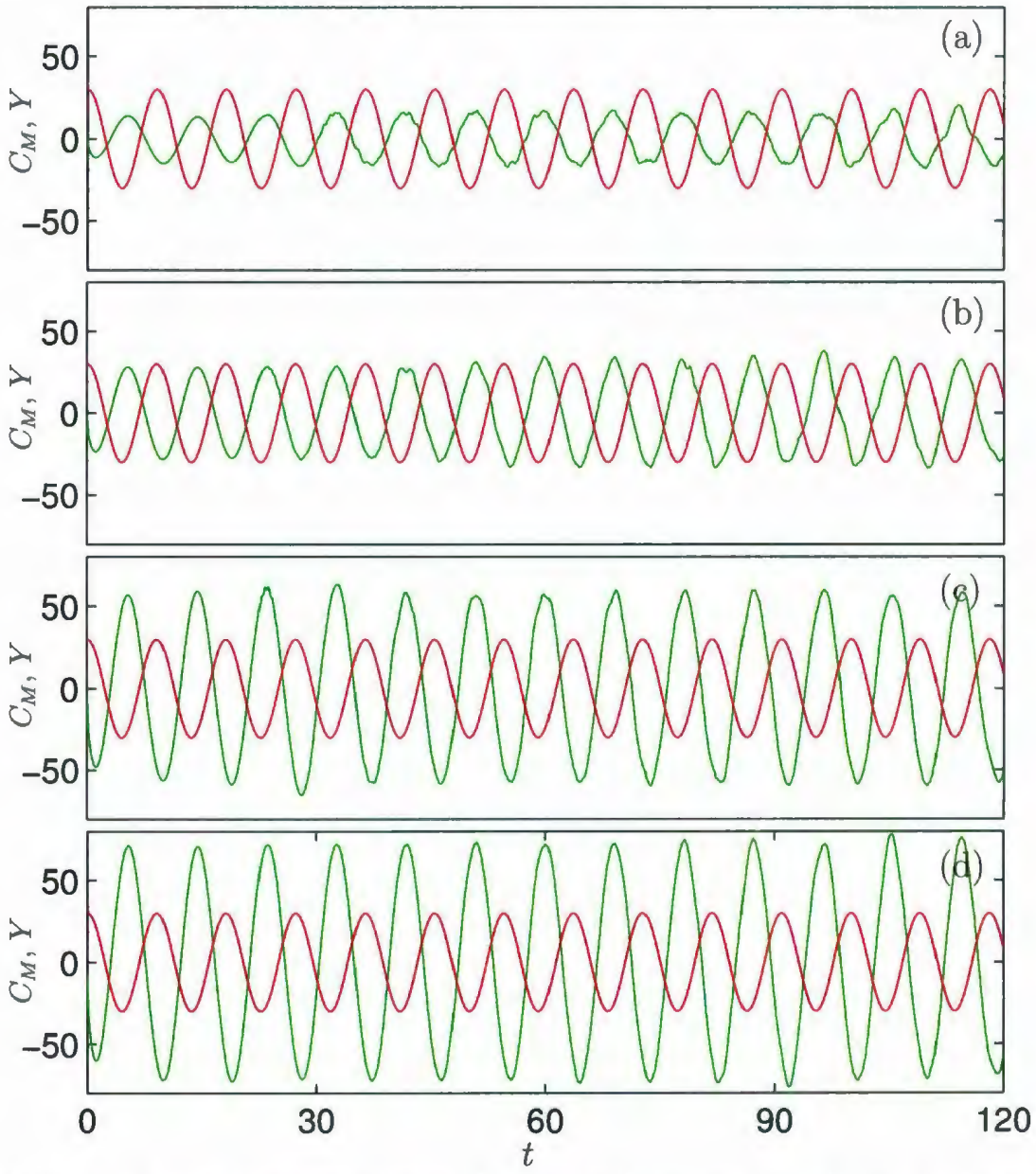

Figure 5.17: The time variation of C_M (—) with respect to cylinder displacement, Y (—) for the combined (2-DoF) transverse and rotational oscillation case ($\eta = 90^o$, $\Theta_m \neq 0$) when $R = 855$, $A = 0.26$ and $f/f_0 = 1.0$: (a) $\Theta_m = 15^o$; (b) $\Theta_m = 30^o$; (c) $\Theta_m = 60^o$ and (d) $\Theta_m = 75^o$.

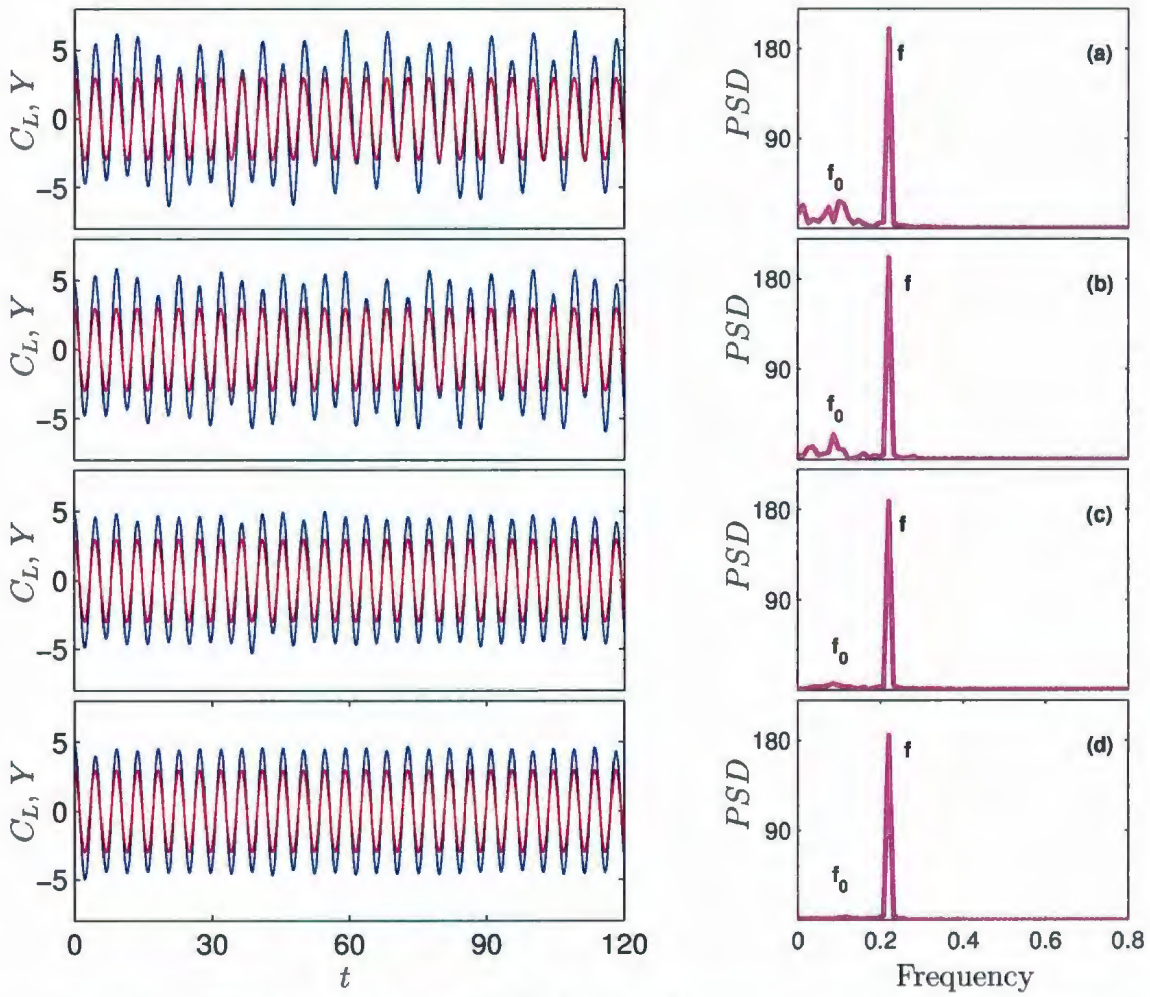

Figure 5.18: The time variation of C_L (—) with respect to cylinder displacement, Y (—) and the Fourier analysis of the lift coefficient PSD (---) for the combined (2-DoF) transverse and rotational oscillation case ($\eta = 90^o$, $\Theta_m \neq 0$) when $R = 855$, $A = 0.26$ and $f/f_0 = 2.0$: (a) $\Theta_m = 15^o$; (b) $\Theta_m = 30^o$; (c) $\Theta_m = 60^o$ and (d) $\Theta_m = 75^o$.

weak with respect to the oscillating frequency (large peak) as Θ_m increases. Thus, synchronization observed at $f/f_0 = 2$ for all values of Θ_m is confirmed (see Figure 5.3). The values of $C_{L,max}$ and $C_{L,amp}$ are decreasing while $C_{L,min}$ is increasing as Θ_m increases. The drag coefficient presented in Figure 5.19 shows that the maximum, minimum and amplitude values of the drag coefficient, $C_{D,max}$, $C_{D,min}$ and $C_{D,amp}$ respectively, are all decreasing as Θ_m increases. The moment coefficient oscillates at the forcing frequency, f, and C_M and Y are out of phase with each other as shown in Figure 5.20.

By investigating the lift records for the case of $f/f_0 = 3$, plotted in Figure 5.21, we observe a tendency to fully periodic behavior with one dominant peak as Θ_m increases. This behavior suggests that the effect of the natural shedding frequency disappears gradually and so the dominant frequency is the forcing frequency with the increase of Θ_m as confirmed by the PSD. It can be seen that C_L oscillates at f and is in phase with the cylinder motion. However, the lift record for $\Theta_m = 15^o$ shows a repeatable behavior every three periods of oscillation, $3T$, where we observe three peaks with different amplitudes. This behavior confirms the lock-on regime observed, per $3T$, at $f/f_0 = 3$ and $\Theta_m = 15^o$ (see Figure 5.5). Furthermore, the difference in the amplitude of these peaks gradually decreases as Θ_m increases. For $\Theta_m \geq 60^o$ we note that the lift coefficient oscillates solely with the forcing frequency, f, which explains the reduction of the vortex lock-on period from $3T$ to T observed at these values of Θ_m in Figure 5.6. As a result of increasing Θ_m, the values of $C_{L,max}$ and $C_{L,amp}$ are decreasing while the minimum value of the lift coefficient, $C_{L,min}$, is increasing. The drag and moment coefficients at $f/f_0 = 3$ are plotted in Figures 5.22 and 5.23. The

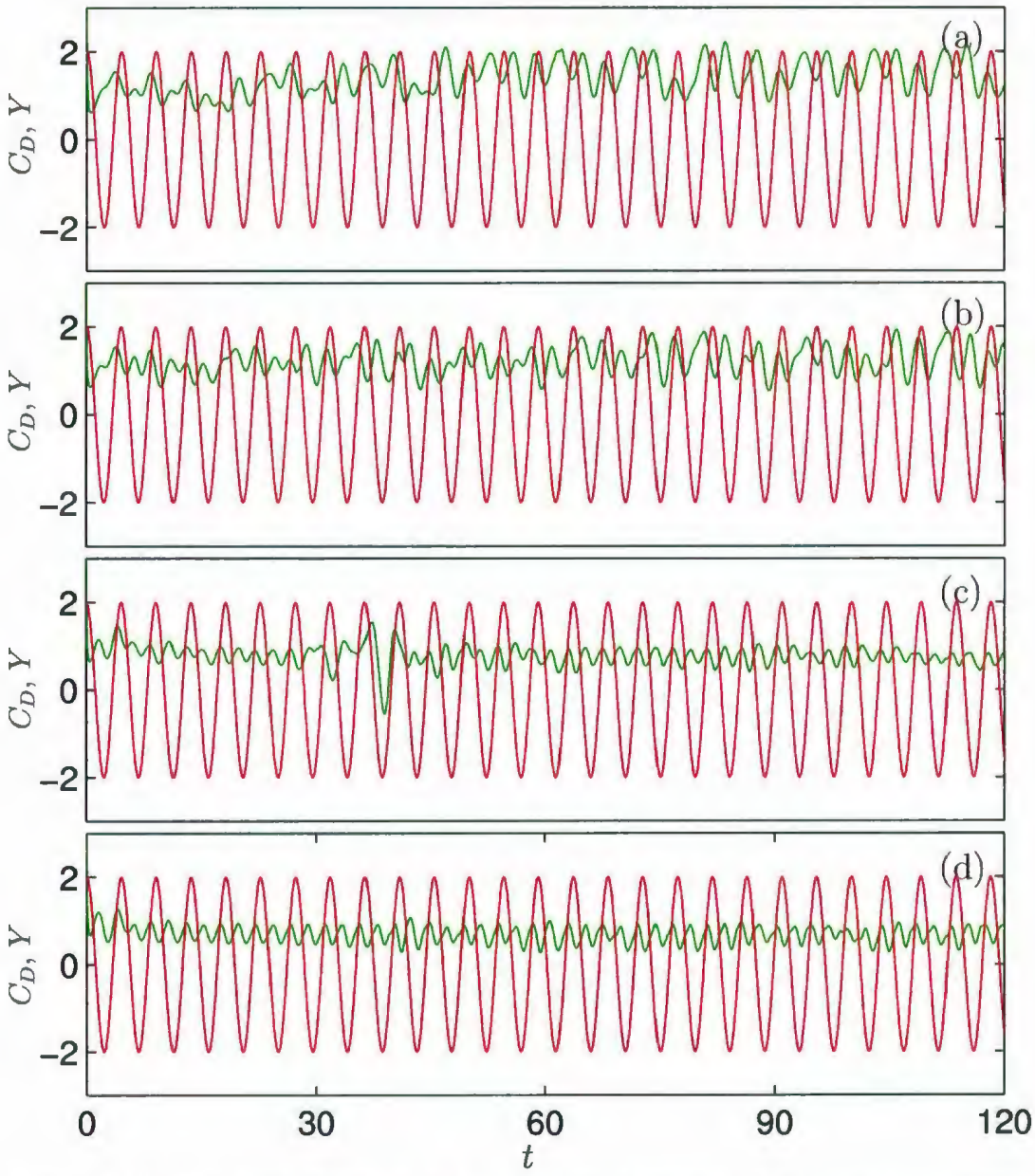

Figure 5.19: The time variation of C_D (—) with respect to cylinder displacement, Y (—) for the combined (2-DoF) transverse and rotational oscillation case ($\eta = 90^o$, $\Theta_m \neq 0$) when $R = 855$, $A = 0.26$ and $f/f_0 = 2.0$: (a) $\Theta_m = 15^o$; (b) $\Theta_m = 30^o$; (c) $\Theta_m = 60^o$ and (d) $\Theta_m = 75^o$.

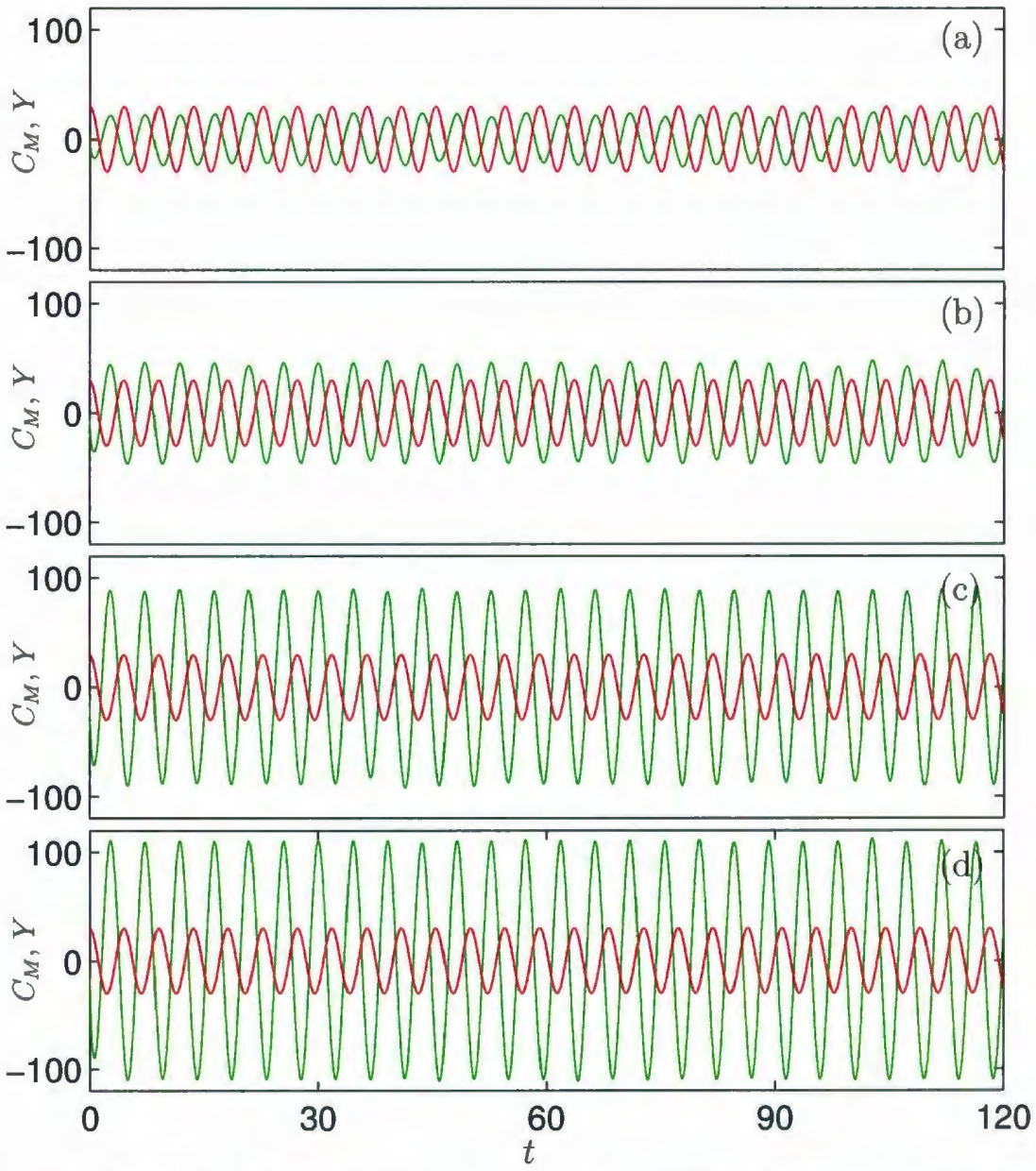

Figure 5.20: The time variation of C_M (—) with respect to cylinder displacement, Y (—) for the combined (2-DoF) transverse and rotational oscillation case ($\eta = 90^o$, $\Theta_m \neq 0$) when $R = 855$, $A = 0.26$ and $f/f_0 = 2.0$: (a) $\Theta_m = 15^o$; (b) $\Theta_m = 30^o$; (c) $\Theta_m = 60^o$ and (d) $\Theta_m = 75^o$.

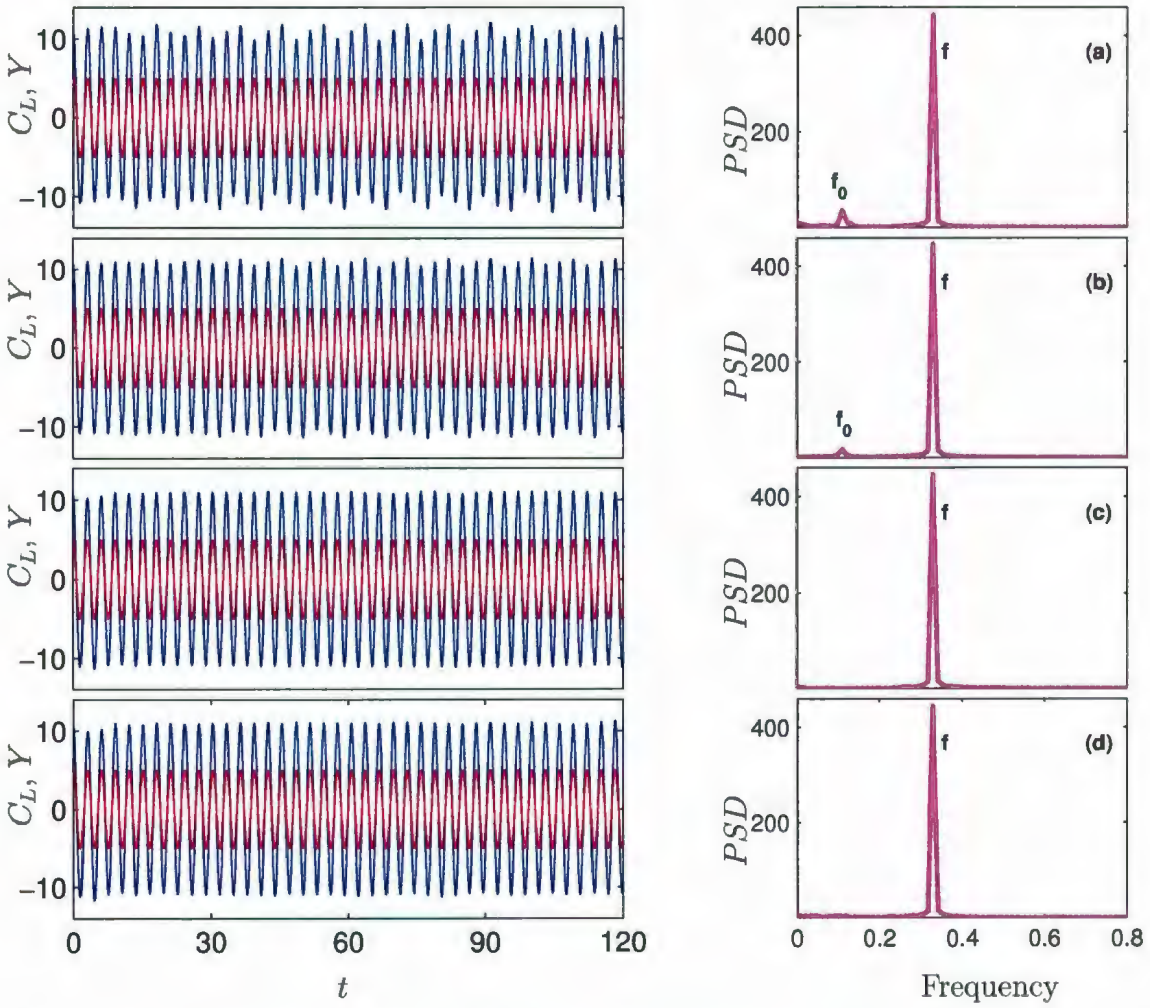

Figure 5.21: The time variation of C_L (—) with respect to cylinder displacement, Y (—) and the Fourier analysis of the lift coefficient PSD (····) for the combined (2-DoF) transverse and rotational oscillation case ($\eta = 90^o$, $\Theta_m \neq 0$) when $R = 855$, $A = 0.26$ and $f/f_0 = 3.0$: (a) $\Theta_m = 15^o$; (b) $\Theta_m = 30^o$; (c) $\Theta_m = 60^o$ and (d) $\Theta_m = 75^o$.

drag coefficient oscillates at f for $\Theta_m \geq 60^o$. The values of $C_{D,max}$ and $C_{D,min}$ are decreasing as Θ_m increases. However, $C_{D,amp}$ is increasing as Θ_m increases in the range $\Theta_m \geq 30^o$. The amplitude of the C_M is increasing as Θ_m increases. Figure 5.23 shows that C_M oscillates with f and shows a phase difference between C_M and Y at all vales of Θ_m.

At $f/f_0 = 4$, the lift coefficient tends to have a fully periodic behavior per $4T$, $3T$ or T as Θ_m increases as shown in Figure 5.24. By investigating the lift behavior for $\Theta_m = 15^o$, 30^o, it is found that the lift coefficient is repeatable every four periods of oscillation whereas, for $\Theta_m = 60^o$, it is repeatable every three periods of oscillations and for $\Theta_m = 75^o$, it is repeatable only over one period of oscillation. These cycles are consistent with the vortex shedding periods presented in Table 5.2 and vortex lock-on observed, in Figures 5.8-5.11, at $f/f_0 = 4$ and $15^o \leq \Theta_m \leq 75^o$ is then confirmed. We can also conclude that the effect of the cylinder rotation is to eliminate the effect of the natural shedding frequency with the increase of Θ_m. It is noted that $C_{L,max}$ and $C_{L,amp}$ are decreasing while $C_{L,min}$ is increasing as Θ_m increases. The drag coefficient presented in Figure 5.25 shows that $C_{D,min}$ is decreasing whereas $C_{D,amp}$ is increasing as Θ_m increases. Moreover, C_D oscillates at f for all values of Θ_m. On the other hand, the moment coefficient amplitude is increasing with the increase of Θ_m as shown in Figure 5.26. This figure also shows a phase difference between C_M and Y at all values of Θ_m.

In summary, the effect of increasing the maximum angular displacement, Θ_m, is to eliminate the effect of the natural shedding frequency as expected. Tables 5.3-5.9

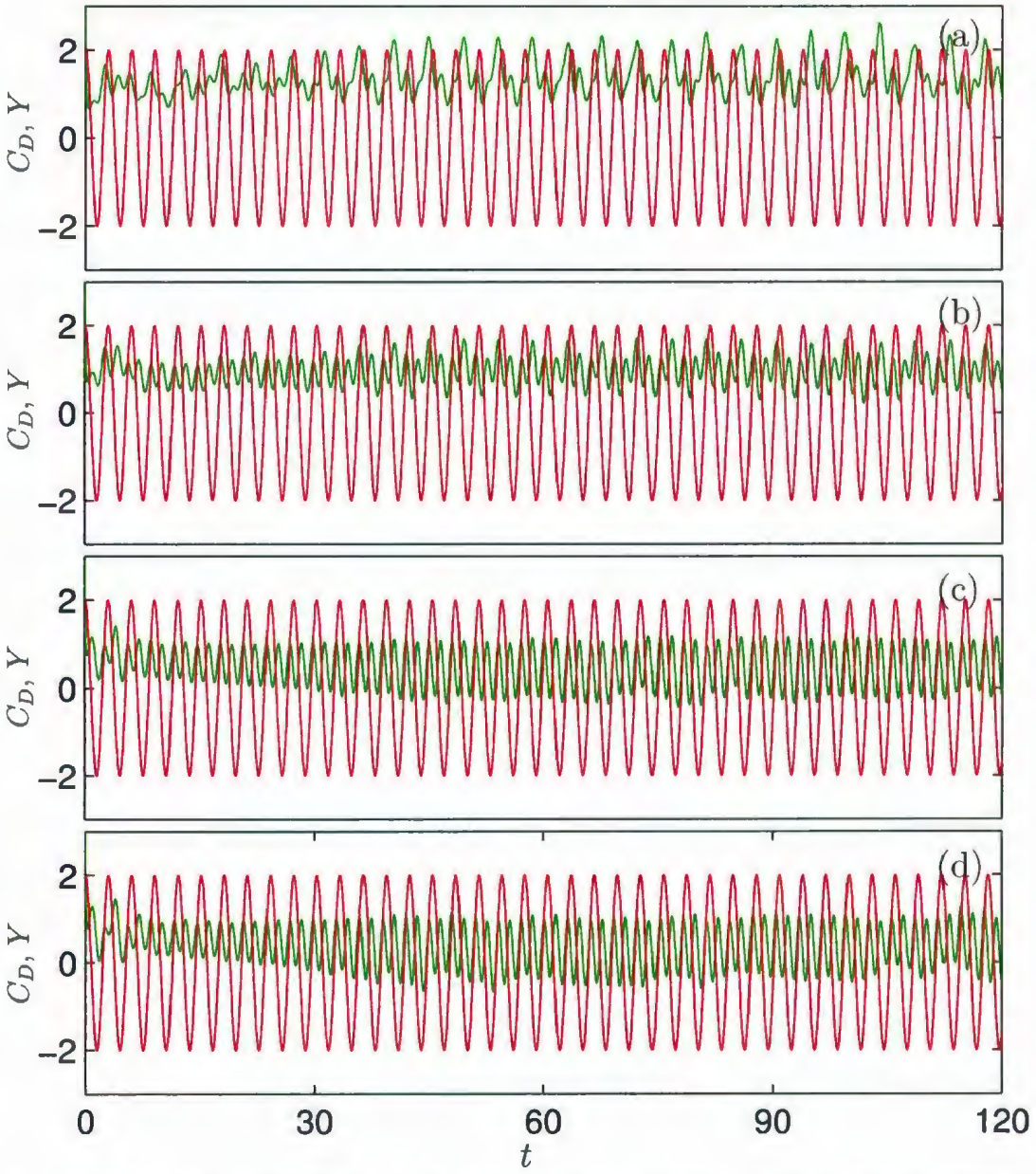

Figure 5.22: The time variation of C_D (—) with respect to cylinder displacement, Y (—) for the combined (2-DoF) transverse and rotational oscillation case ($\eta = 90^o$, $\Theta_m \neq 0$) when $R = 855$, $A = 0.26$ and $f/f_0 = 3.0$: (a) $\Theta_m = 15^o$; (b) $\Theta_m = 30^o$; (c) $\Theta_m = 60^o$ and (d) $\Theta_m = 75^o$.

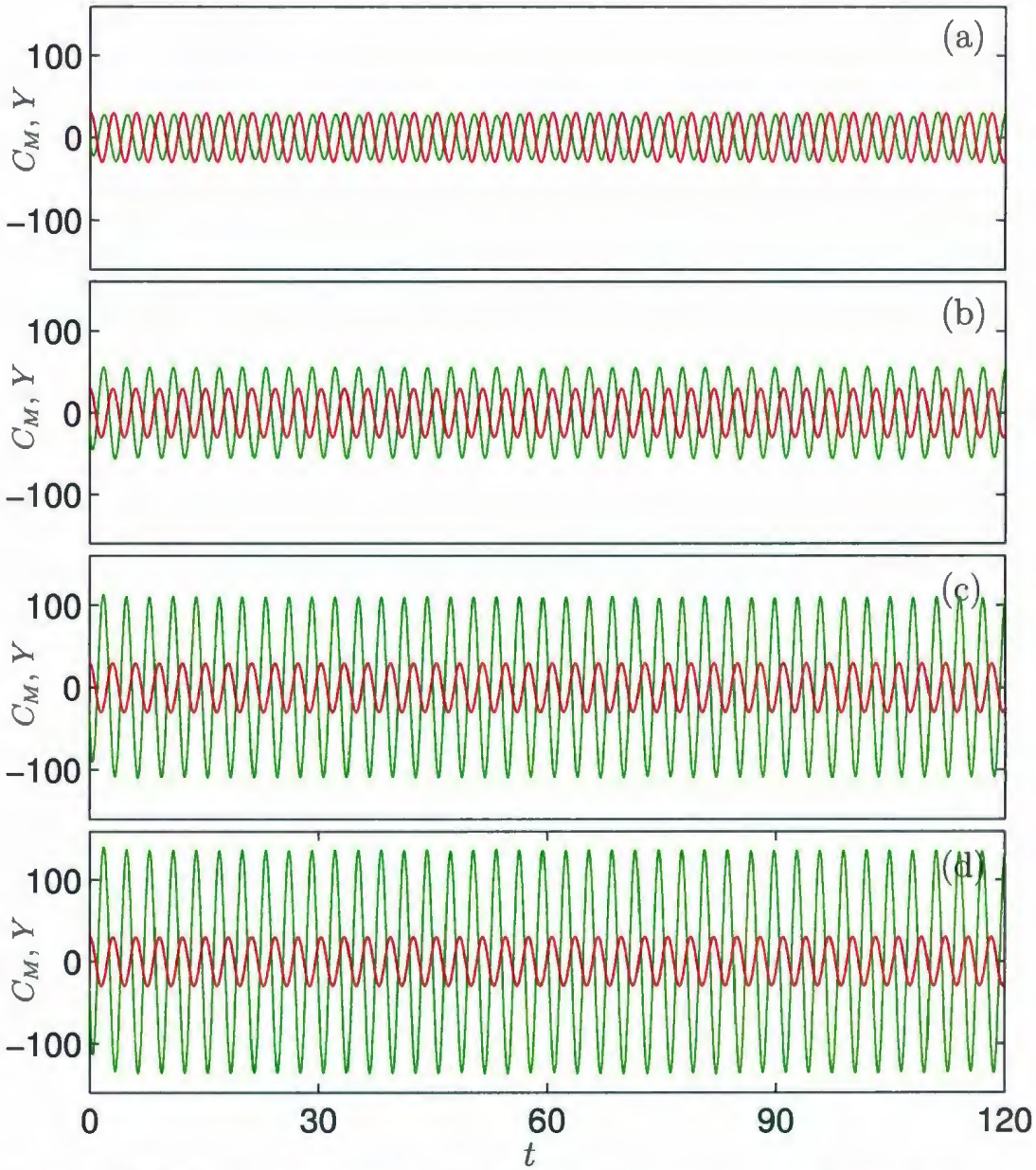

Figure 5.23: The time variation of C_M (—) with respect to cylinder displacement, Y (—) for the combined (2-DoF) transverse and rotational oscillation case ($\eta = 90^o$, $\Theta_m \neq 0$) when $R = 855$, $A = 0.26$ and $f/f_0 = 3.0$: (a) $\Theta_m = 15^o$; (b) $\Theta_m = 30^o$; (c) $\Theta_m = 60^o$ and (d) $\Theta_m = 75^o$.

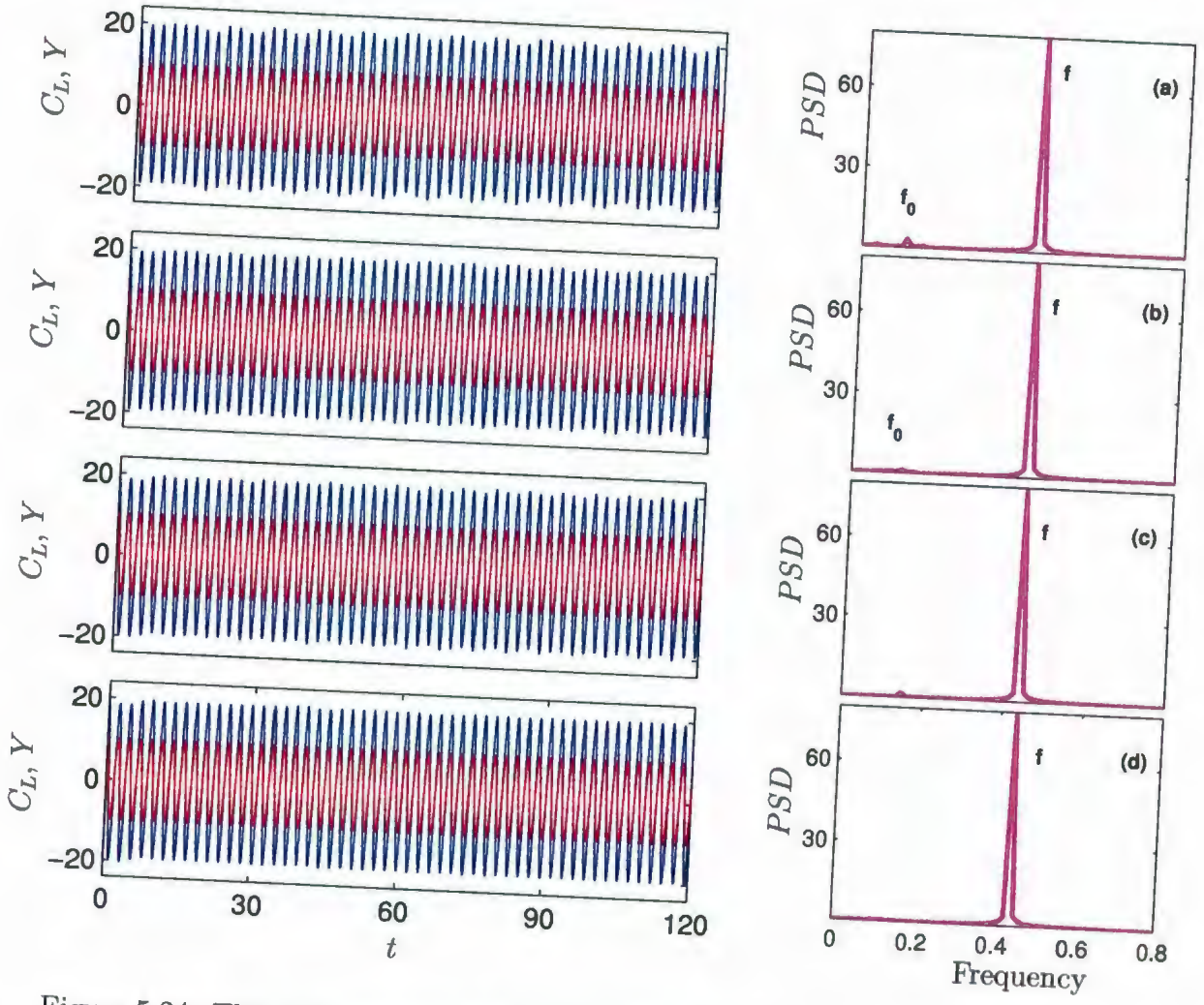

Figure 5.24: The time variation of C_L (—) with respect to cylinder displacement, Y (—) and the Fourier analysis of the lift coefficient PSD (---) for the combined (2-DoF) transverse and rotational oscillation case ($\eta = 90^o$, $\Theta_m \neq 0$) when $R = 855$, $A = 0.26$ and $f/f_0 = 4.0$: (a) $\Theta_m = 15^o$; (b) $\Theta_m = 30^o$; (c) $\Theta_m = 60^o$ and (d) $\Theta_m = 75^o$.

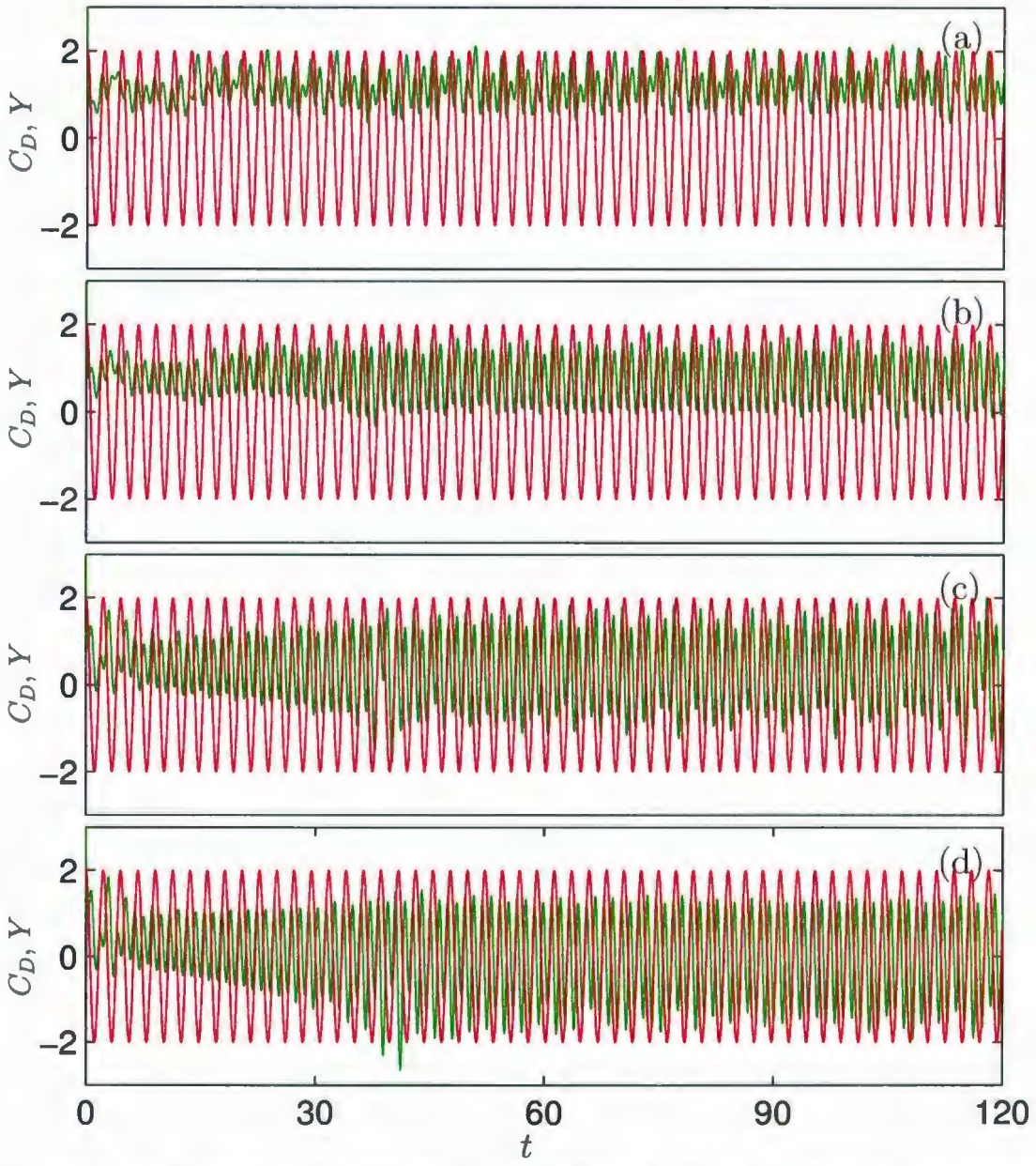

Figure 5.25: The time variation of C_D (—) with respect to cylinder displacement, Y (—) for the combined (2-DoF) transverse and rotational oscillation case ($\eta = 90^o$, $\Theta_m \neq 0$) when $R = 855$, $A = 0.26$ and $f/f_0 = 4.0$: (a) $\Theta_m = 15^o$; (b) $\Theta_m = 30^o$; (c) $\Theta_m = 60^o$ and (d) $\Theta_m = 75^o$.

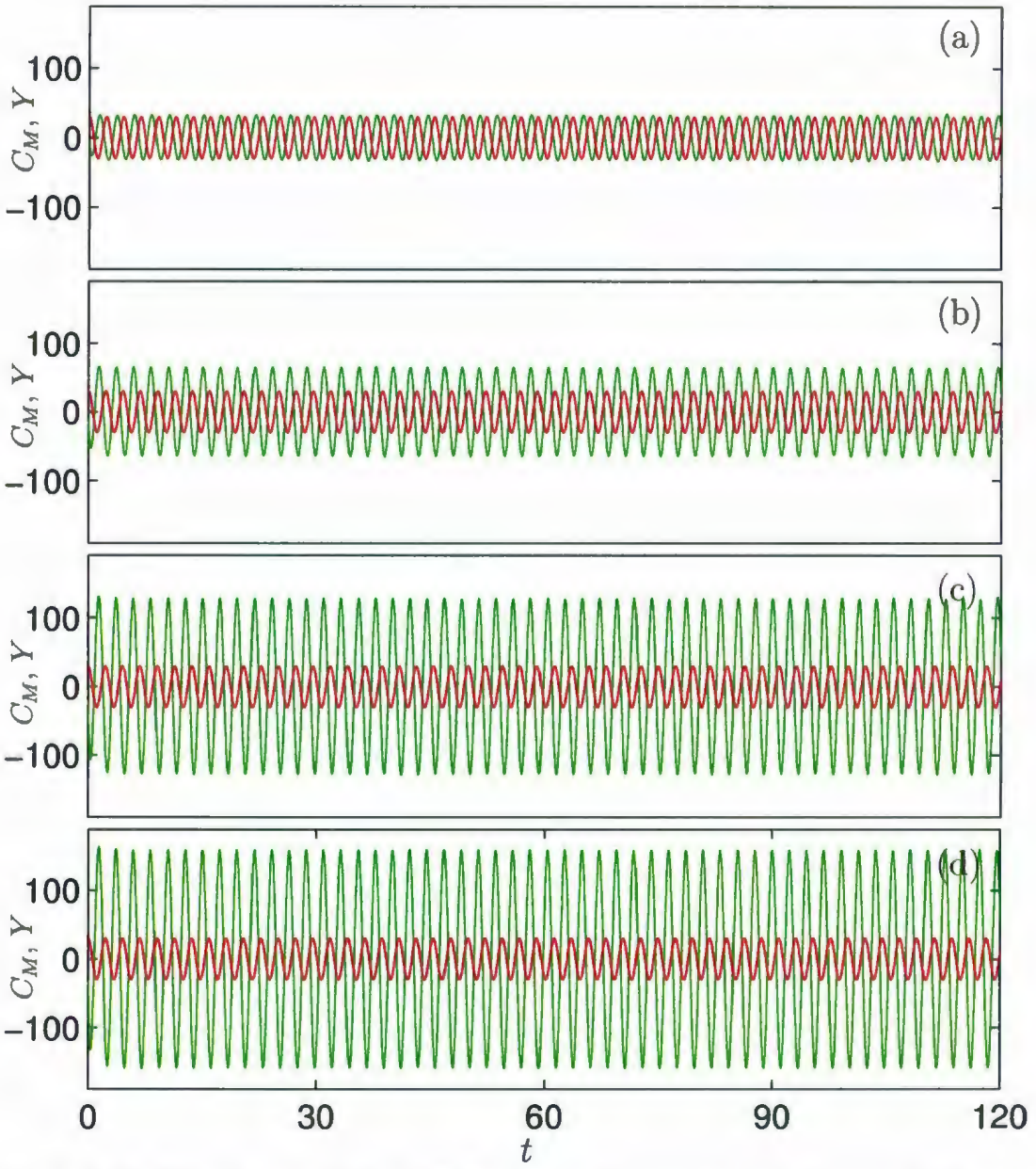

Figure 5.26: The time variation of C_M (—) with respect to cylinder displacement, Y (—) for the combined (2-DoF) transverse and rotational oscillation case ($\eta = 90^o$, $\Theta_m \neq 0$) when $R = 855$, $A = 0.26$ and $f/f_0 = 4.0$: (a) $\Theta_m = 15^o$; (b) $\Theta_m = 30^o$; (c) $\Theta_m = 60^o$ and (d) $\Theta_m = 75^o$.

show the values of $C_{L,max}$, $C_{L,min}$, $C_{L,amp}$, $C_{D,max}$, $C_{D,min}$, $C_{D,amp}$ and the time-averaged drag coefficient, $\bar{C}_D$. These quantities are calculated over two periods of cylinder oscillation for $f/f_0 = 0.5$ and over four periods for $f/f_0 = 1$, 2, 3 and 4. The maximum lift coefficient, $C_{L,max}$, decreases as Θ_m increases in the range $1 \leq f/f_0 \leq 4$. However, at high values of the oscillation frequency ratio, $f/f_0 \geq 1$, the minimum value of the lift coefficient increases as Θ_m increases. In the contrary, the value of $C_{L,amp}$ decreases as Θ_m increases at high values of the excitation frequency, $f/f_0 \geq 2$. A reduction in $C_{D,max}$ value is observed, in general, as Θ_m increases at high values of f/f_0, $f/f_0 \geq 2$. Furthermore, as a result of increasing Θ_m beyond 30^o, $C_{D,min}$ is decreasing at all values of f/f_0. However, $\bar{C}_D$ is decreasing at all values of f/f_0 as Θ_m increases.

f/f_0 \ Θ_m	15^o	30^o	60^o	75^o
0.5	1.8117	1.7660	1.6039	2.0132
1.0	2.7490	2.6703	1.9945	1.9616
2.0	6.0354	5.4568	4.7273	4.5592
3.0	12.0587	11.3770	11.0585	11.0227
4.0	20.2919	20.0046	20.0016	19.6554

Table 5.3: The effect of f/f_0 and Θ_m on $C_{L_{max}}$ for the combined (2-DoF) transverse and rotational oscillation case ($\eta = 90^o$, $\Theta_m \neq 0$) when $R = 855$, $A = 0.26$.

f/f_0 \ Θ_m	15^o	30^o	60^o	75^o
0.5	-1.7412	-1.6981	-2.0639	-2.0380
1.0	-2.7092	-2.5450	-1.9551	-1.9836
2.0	-5.9030	-5.7538	-4.8081	-4.5513
3.0	-11.8475	-11.3979	-11.1959	-11.1940
4.0	-20.2558	-19.9763	-19.9759	-19.7055

Table 5.4: The effect of f/f_0 and Θ_m on $C_{L,min}$ for the combined (2-DoF) transverse and rotational oscillation case ($\eta = 90^o$, $\Theta_m \neq 0$) when $R = 855$, $A = 0.26$.

f/f_0 \ Θ_m	15^o	30^o	60^o	75^o
0.5	3.5529	3.4641	3.6678	4.0512
1.0	5.4581	5.2153	3.9496	3.9452
2.0	11.9384	11.2106	9.5354	9.1105
3.0	23.9062	22.7749	22.2544	22.2167
4.0	40.5477	39.9809	39.9775	39.3609

Table 5.5: The effect of f/f_0 and Θ_m on $C_{L,amp}$ for the combined (2-DoF) transverse and rotational oscillation case ($\eta = 90^o$, $\Theta_m \neq 0$) when $R = 855$, $A = 0.26$.

5.3 Combined (2-DoF) transverse and rotational oscillation versus a transverse-only or rotational-only (1-DoF) cylinder oscillation: wake modes

In this section a series of 1-DoF forced transverse or rotational cylinder oscillations in a steady uniform flow is analyzed under the same oscillation conditions of Sections 5.1 and 5.2 to better understand what differences result from the addition of the two 1-DoF oscillatory motions. The simulations for the (1-DoF) oscillatory motion cases

f/f_0 \ Θ_m	15^o	30^o	60^o	75^o
0.5	1.8870	1.9345	1.8496	2.0761
1.0	2.0329	1.8281	2.0720	2.0355
2.0	2.2124	1.8909	1.0429	0.9318
3.0	2.4308	1.6783	1.1770	1.1127
4.0	2.0546	1.7258	1.8182	1.3024

Table 5.6: The effect of f/f_0 and Θ_m on $C_{D,max}$ for the combined (2-DoF) transverse and rotational oscillation case ($\eta = 90^o$, $\Theta_m \neq 0$) when $R = 855$, $A = 0.26$.

f/f_0 \ Θ_m	15^o	30^o	60^o	75^o
0.5	1.0999	1.0679	0.9891	0.9608
1.0	1.2490	1.4138	1.1713	1.0928
2.0	0.8456	0.5264	0.4084	0.3059
3.0	0.6894	0.2997	-0.3955	-0.5957
4.0	0.5185	-0.1068	-1.1797	-1.7001

Table 5.7: The effect of f/f_0 and Θ_m on $C_{D,min}$ for the combined (2-DoF) transverse and rotational oscillation case ($\eta = 90^o$, $\Theta_m \neq 0$) when $R = 855$, $A = 0.26$.

are carried out by using the same set of numerical parameters used for the combined (2-DoF) transverse and rotational oscillation case. The results for transverse-only simulations are obtained by setting maximum angular displacement and angle of inclination to $\Theta_m = 0$ and $\eta = 90^o$, respectively. The results for rotational-only simulations are obtained by setting recti-linear oscillatory velocity to $V(t) = 0$. Tables 5.10 and 5.11 summarize the effect of the 1-DoF rotational oscillation on the vortex shedding modes and their periods in terms of the parameters Θ_m and f/f_0. In addition, a summary of the vortex shedding modes and their periods for the case of the 1-DoF forced transverse oscillation is displayed in Table 5.12.

f/f_0 \ Θ_m	15^o	30^o	60^o	75^o
0.5	0.7871	0.8666	0.8605	1.1154
1.0	0.7838	0.4143	0.9007	0.9427
2.0	1.3668	1.3645	0.6345	0.6260
3.0	1.7414	1.3786	1.5725	1.7084
4.0	1.5360	1.8326	2.9979	3.0025

Table 5.8: The effect of f/f_0 and Θ_m on $C_{D,amp}$ for the combined (2-DoF) transverse and rotational oscillation case ($\eta = 90^o$, $\Theta_m \neq 0$) when $R = 855$, $A = 0.26$.

f/f_0 \ Θ_m	15^o	30^o	60^o	75^o
0.5	1.4408	1.4308	1.3677	1.3404
1.0	1.6133	1.6011	1.5940	1.5335
2.0	1.5343	1.2660	0.7486	0.6670
3.0	1.4042	0.9788	0.4358	0.3258
4.0	1.2024	0.7985	0.3846	-0.0526

Table 5.9: The effect of f/f_0 and Θ_m on $\bar{C}_D$ for the combined (2-DoF) transverse and rotational oscillation case ($\eta = 90^o$, $\Theta_m \neq 0$) when $R = 855$, $A = 0.26$.

Overview of equivorticity lines for 1-DoF and 2-DoF motions under consideration is presented in Figures 5.27-5.31 at $f/f_0 = 0.5$, 1, 2, 3 and 4. In each figure, the top row of snapshots corresponds to the 1-DoF rotational oscillation case, taken at the maximum negative angular displacement, $-\Theta_m$, with amplitudes $\Theta_m = 15^o$, 30^o, 60^o and 75^o. In the middle row we display a series of the same snapshot for the 1-DoF transverse oscillation case taken at the maximum positive displacement, A. The bottom row exhibits snapshots of the combined (2-DoF) transverse and rotational oscillations at the instant corresponding to $-\Theta_m$. The instantaneous rotational and transverse

f/f_0 \ Θ_m	15^o	30^o	60^o	75^o
0.5	**2S** •	**2S** •	**4S** •	**4S** •
1	**2S** •	**2S** •	**2S** •	**2S** •
2	**S+P** •	**2P** •	**2S** •	**2S** •
3	**2P** •	**6S** •	**2S** •	**2S** •
4	**6S** •	**2S** •	**2S** •	**2S** •

Table 5.10: The effect of f/f_0 and Θ_m on the vortex shedding modes for the rotational-only oscillation case ($V(t) = 0$, $\Theta_m \neq 0$) when $R = 855$, $A = 0.26$: • lock-on mode; • non-lock mode.

f/f_0 \ Θ_m	15^o	30^o	60^o	75^o
0.5	T/2	T/2	T	T
1	T	T	T	T
2	2T	2T	T	T
3	3T	3T	T	T
4	4T	T	T	T

Table 5.11: The effect of f/f_0 and Θ_m on the vortex shedding periods for the rotational-only oscillation case ($V(t) = 0$, $\Theta_m \neq 0$) when $R = 855$, $A = 0.26$.

speeds of the cylinder are zero at these positions.

It is notable for the combined (2-DoF) transverse and rotational oscillation case that increasing the maximum angular displacement, Θ_m, or the oscillation frequency, f/f_0, leads to breaking a part of the near-wake vortices and thus we may obtain different modes. In fact, as Θ_m increases beyond 15^o at all values of f/f_0 the effect of the rotational oscillation increases because the maximum rotational speed $\Omega = 2\pi f\theta_m$ is at least twice the maximum transverse speed $V = 2\pi fA$. However, even if the

f/f_0	Mode	Period
0.5	**2S** •	T/2
1	**2S** •	T
2	**2S** •	2T
3	**S+P** •	3T
4	**2P** •	4T

Table 5.12: The effect of f/f_0 and Θ_m on the vortex shedding modes and their periods for the transverse-only (1-DoF) oscillation case ($\eta = 90^o$, $\Theta_m = 0^o$) when $R = 855$, $A = 0.26$: • lock-on mode; • non-lock mode.

near-wake structures for rotational-only (1-DoF) oscillation and combined (2-DoF) transverse and rotational oscillation cases are similar, they may exhibit different vortex shedding modes as seen at high frequencies. In fact, the movement of the cylinder in the negative and positive directions of the y-axis causes the coalescence of the shedding vortices in the near-wake region at $f/f_0 \geq 3$ which causes the development of different vortex shedding modes.

The vortex shedding modes and their periods for $f/f_0 = 0.5$ and $f/f_0 = 1$ for the combine (2-DoF) transverse and rotational oscillation case are similar to that for the transverse-only or rotational-only (1-DoF) oscillation case as shown in Tables 5.10-5.12. However, the bottom row of Figure 5.27 shows that the transverse-only (1-DoF) oscillation is the dominant motion at $\Theta_m = 15^o$. On the other hand, a high competition between the transverse-only and rotational-only (1-DoF) oscillation is observed at $\Theta_m = 30^o$. On the other hand, the vortex shedding is controlled by the rotational-only (1-DoF) oscillations for all values of Θ_m at $f/f_0 = 1$ as shown in Figure 5.28. It is remarkable to see the reduction of the vertical distance between the shed vortices in the near-wake region at $f/f_0 = 1$ as a result of the effect of the

transverse-only (1-DoF) oscillation.

At $f/f_0 = 2.0$, the vortex shedding is controlled, in general, by the rotational-only (1-DoF) oscillation as shown in Figure 5.29. For $\Theta_m = 15^o$, the development of the flow at the top side of the cylinder is similar to the rotational-only (1-DoF) oscillation case. On the other hand, the flow structure at the bottom side of the cylinder is similar to the transverse-only (1-DoF) oscillation case. In addition, the vortex shedding modes and their periods are similar to that for the rotational-only (1-DoF) oscillation case. On the other hand, for $\Theta_m = 30^o$, the vortex shedding is controlled by the rotational-only (1-DoF) oscillation. Further, Tables 5.10-5.12 show that the vortex shedding modes and periods for $\Theta_m = 60^o$ and 75^o are controlled by rotational-only (1-DoF) oscillation. The effect of the transverse-only (1-DoF) oscillation is evident in reducing the vertical distance between the shedding vortices in the near-wake region for $30^o \leq \Theta_m \leq 75^o$.

For $f/f_0 = 3.0$, it is observed that the vortex shedding modes for transverse-only and rotational-only (1-DoF) oscillations at $\Theta_m = 15^o$ are the asymmetrical **S+P** and **2P** modes, respectively, with $3T$ whereas the combined (2-DoF) transverse and rotational oscillation exhibits asymmetrical **2P** mode, with $3T$. In addition, the vortex patterns presented in Figure 5.30 show different structure in the near-wake for all cases at $\Theta_m = 15^o$ which reflects the competition between these oscillatory motions. For $\Theta_m = 30^o$, the vortex shedding process produces asymmetric modes **S+P** and **6S** respectively, per $3T$. By combining the two oscillations at $\Theta_m = 30^o$, the wake exhibits a different mode labelled **6S** per $3T$. Typical equivorticity lines for 1-DoF

and 2-DoF motions under consideration are presented in Figure 5.32 at $f/f_0 = 3$ over three periods of cylinder oscillations, $3T$. It is evident that the transverse-only (1-DoF) oscillation causes the coalescence phenomena even if the rotational-only (1-DoF) oscillation is the dominant motion. As Θ_m increases to 60^o and 75^o, the vortex shedding modes are characterized by synchronized asymmetric **2S** modes, per T, which is similar to that observed for the rotational-only (1-DoF) oscillation case.

For $f/f_0 = 4.0$, it can been seen that the transverse-only (1-DoF) oscillation has a larger influence on the near-wake structure than the frequency ratio cases when $f/f_0 < 4$. For instance, the **2S** mode which appeared in the rotational-only (1-DoF) oscillation case at $f/f_0 = 4$ when $30^o \leq \Theta_m \leq 60^o$ is almost eliminated in the combined (2-DoF) oscillation case. Furthermore, the transverse-only (1-DoF) oscillation plays an important role in activating the coalesce phenomenon in the combined (2-DoF) transverse and rotational oscillation case as shown in Figure 5.32. In addition, equivorticity lines for 1-DoF and 2-DoF motions under consideration are presented in Figure 5.33 and 5.34 at $f/f_0 = 4$ over $4T$ when $\Theta_m = 30^o$ and 60^o. It can be easily observed that transverse-only (1-DoF) oscillation has a great influence in obtaining different vortex shedding modes.

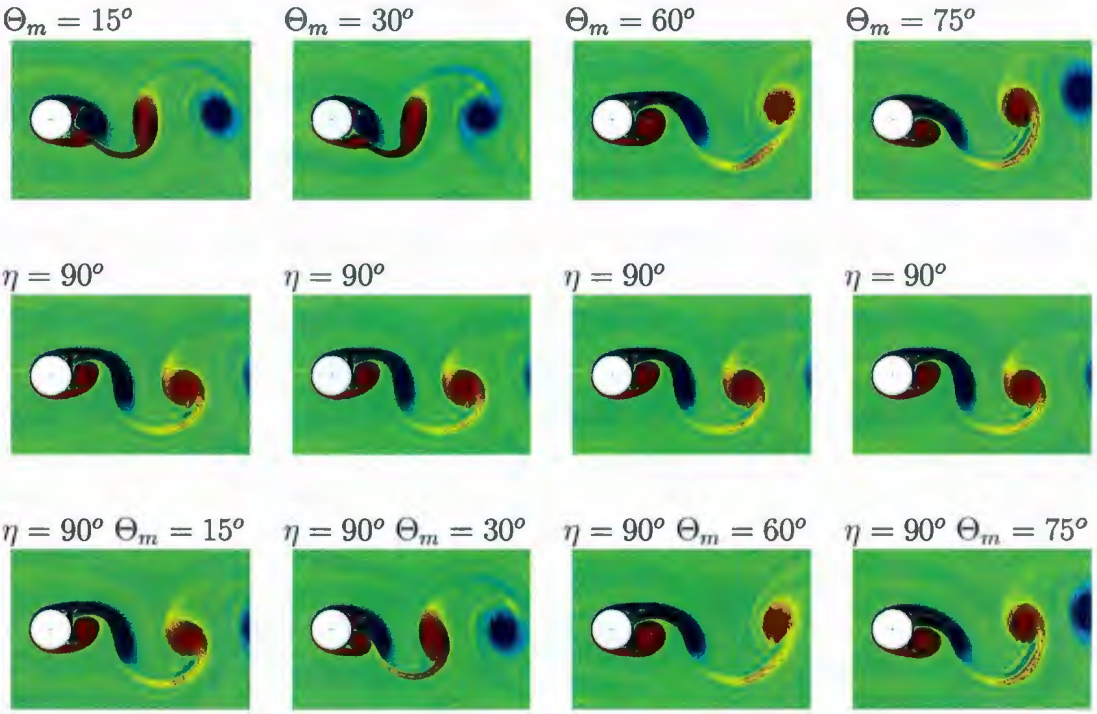

Figure 5.27: A rotational-only or transverse-only (1-DoF) cylinder oscillation (top or middle) versus combined (2-DoF) transverse and rotational oscillation (bottom): overview of near-wake structure for $R = 855$, $A = 0.26$ and $f/f_0 = 0.5$ when $\Theta_m = 15^o$, $\Theta_m = 30^o$, $\Theta_m = 60^o$ and $\Theta_m = 75^o$. All snapshots in the top and bottom rows are taken at the instant corresponding to maximum negative angular displacement, $-\Theta_m$, while the middle row corresponds to maximum positive cylinder displacement, A.

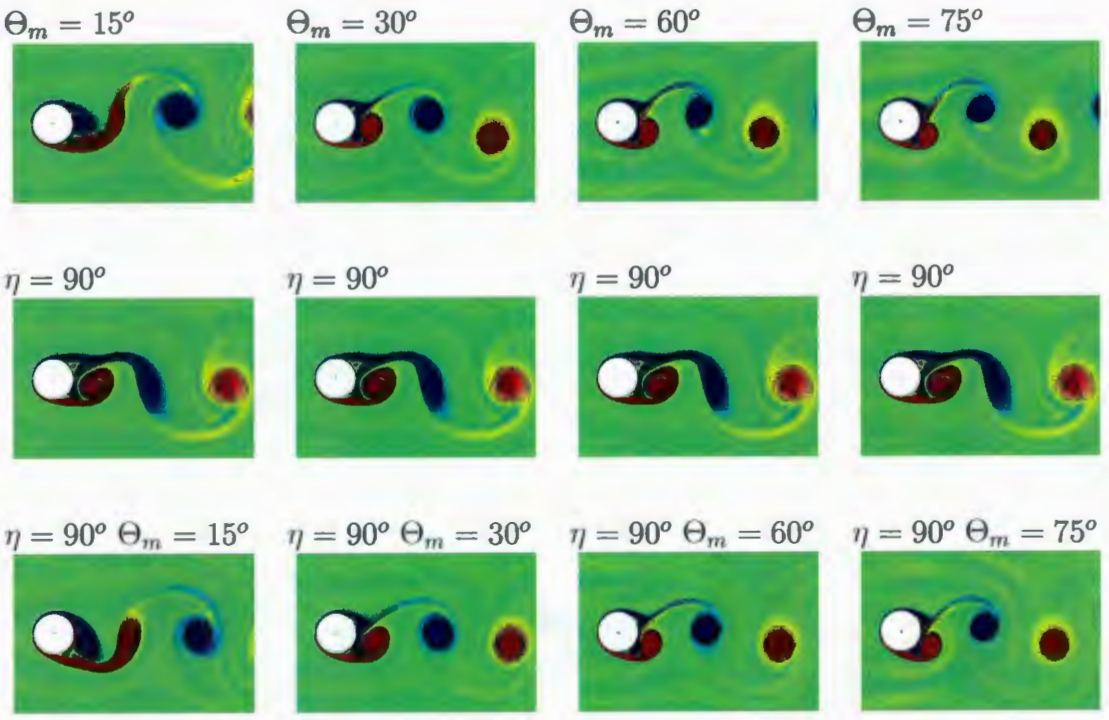

Figure 5.28: A rotational-only or transverse-only (1-DoF) cylinder oscillation (top or middle) versus combined (2-DoF) transverse and rotational oscillation (bottom): overview of near-wake structure for $R = 855$, $A = 0.26$ and $f/f_0 = 1$ when $\Theta_m = 15^o$, $\Theta_m = 30^o$, $\Theta_m = 60^o$ and $\Theta_m = 75^o$. All snapshots in the top and bottom rows are taken at the instant corresponding to maximum negative angular displacement, $-\Theta_m$, while the middle row corresponds to maximum positive cylinder displacement, A.

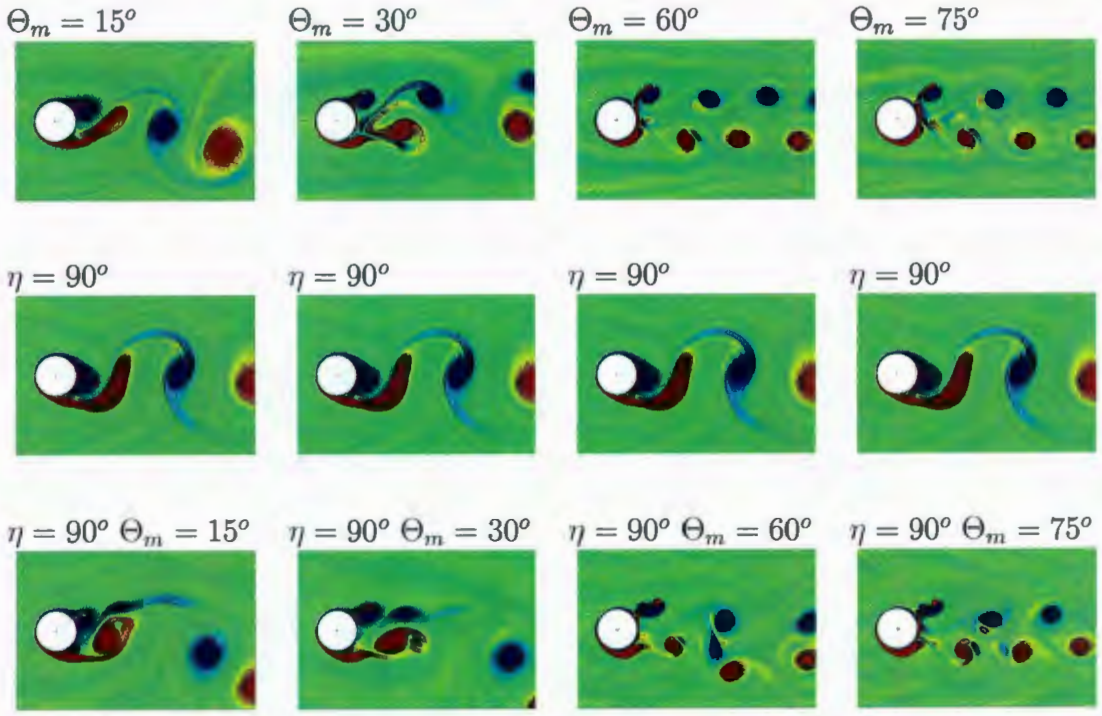

Figure 5.29: A rotational-only or transverse-only (1-DoF) cylinder oscillation (top or middle) versus combined (2-DoF) transverse and rotational oscillation (bottom): overview of near-wake structure for $R = 855$, $A = 0.26$ and $f/f_0 = 2$ when $\Theta_m = 15^o$, $\Theta_m = 30^o$, $\Theta_m = 60^o$ and $\Theta_m = 75^o$. All snapshots in the top and bottom rows are taken at the instant corresponding to maximum negative angular displacement, $-\Theta_m$, while the middle row corresponds to maximum positive cylinder displacement, A.

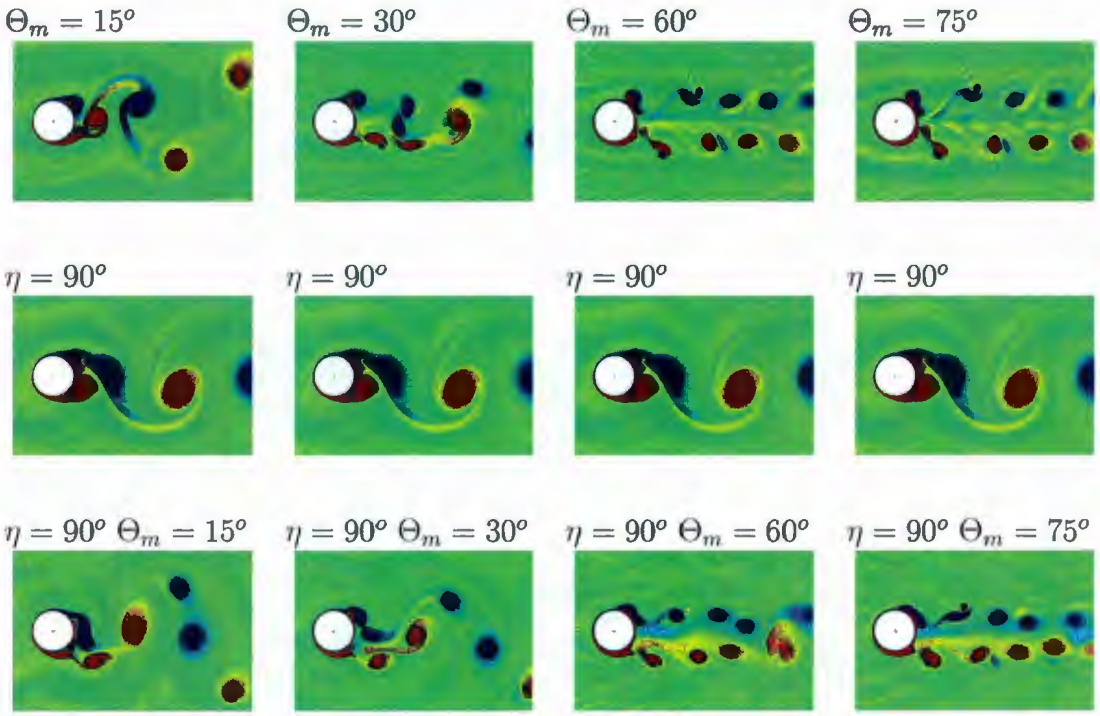

Figure 5.30: A rotational-only or transverse-only (1-DoF) cylinder oscillation (top or middle) versus combined (2-DoF) transverse and rotational oscillation (bottom): overview of near-wake structure for $R = 855$, $A = 0.26$ and $f/f_0 = 3$ when $\Theta_m = 15^o$, $\Theta_m = 30^o$, $\Theta_m = 60^o$ and $\Theta_m = 75^o$. All snapshots in the top and bottom rows are taken at the instant corresponding to maximum negative angular displacement, $-\Theta_m$, while the middle row corresponds to maximum positive cylinder displacement, A.

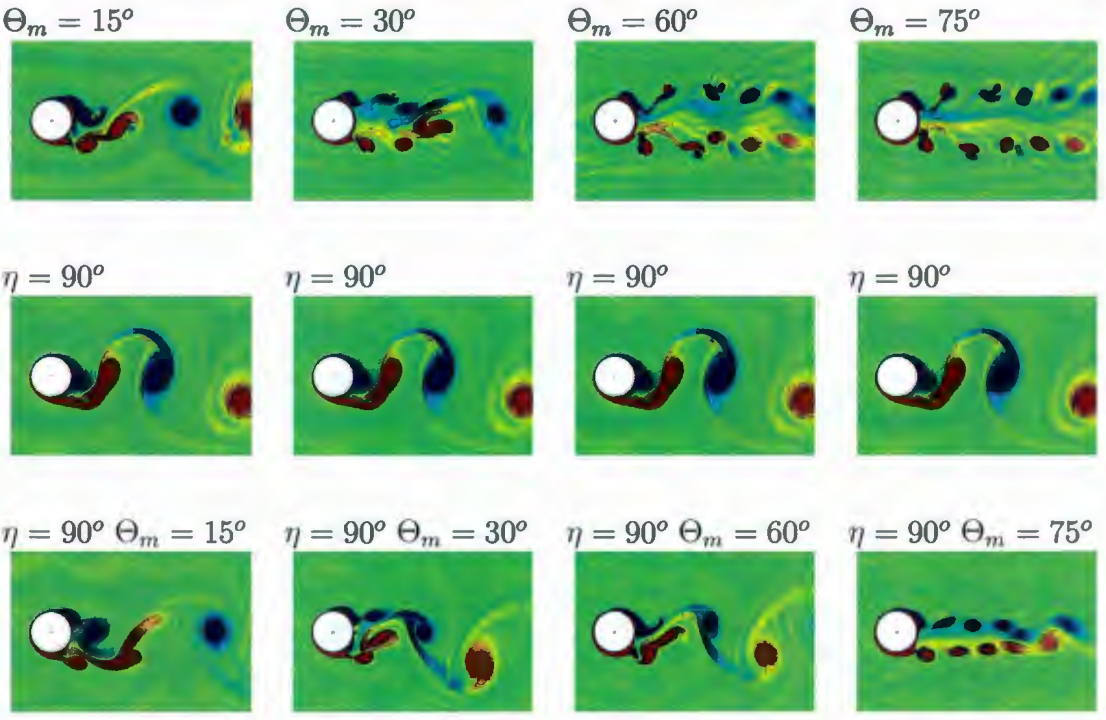

Figure 5.31: A rotational-only or transverse-only (1-DoF) cylinder oscillation (top or middle) versus combined (2-DoF) transverse and rotational oscillation (bottom): overview of near-wake structure for $R = 855$, $A = 0.26$ and $f/f_0 = 4$ when $\Theta_m = 15^o$, $\Theta_m = 30^o$, $\Theta_m = 60^o$ and $\Theta_m = 75^o$. All snapshots in the top and bottom rows are taken at the instant corresponding to maximum negative angular displacement, $-\Theta_m$, while the middle row corresponds to maximum positive cylinder displacement, A.

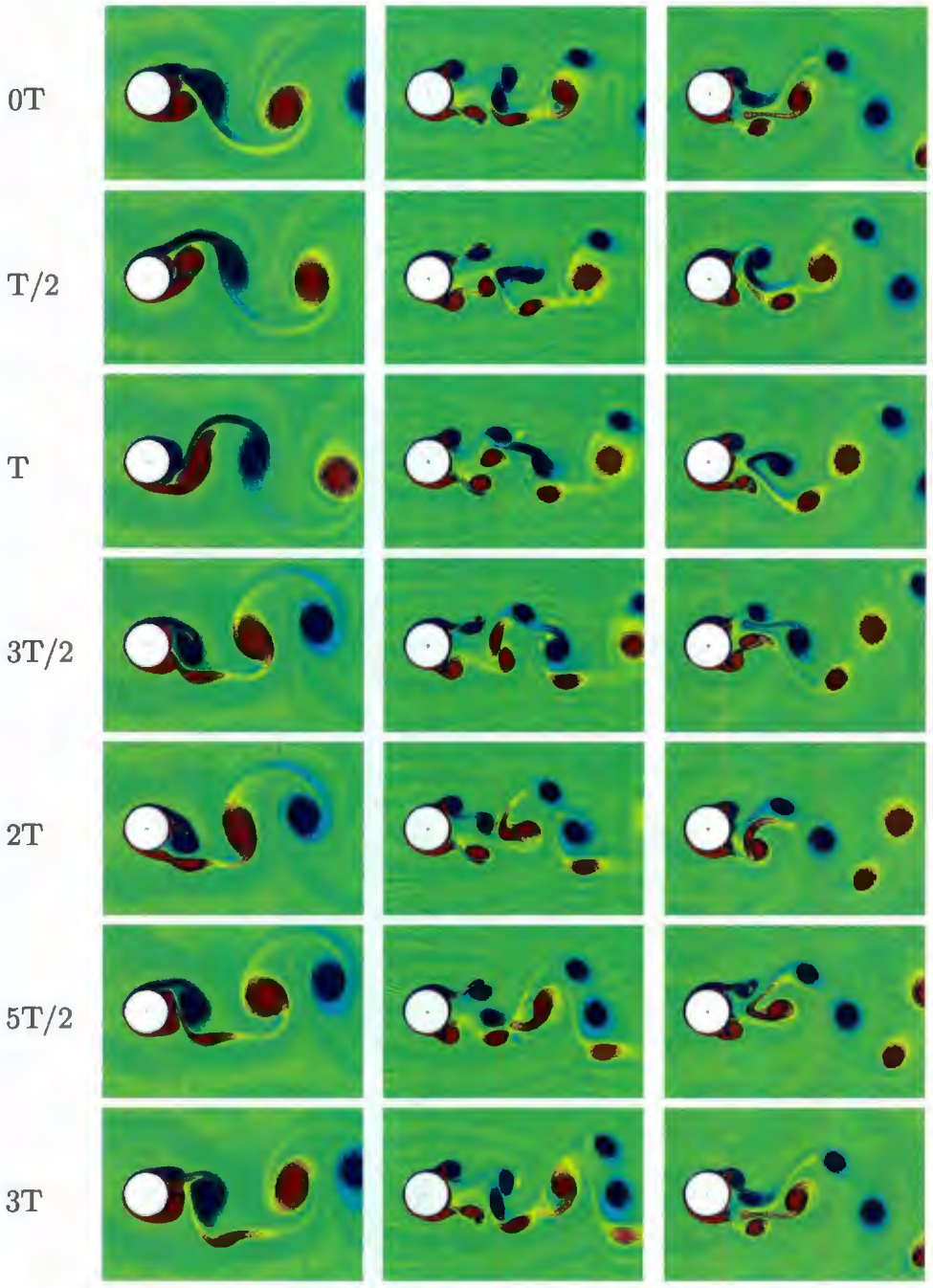

Figure 5.32: Equivorticity lines over three periods of oscillation, $3T$, for transverse-only (1-DoF) oscillation (left); rotational-only (1-DoF) oscillation (middle); combined (2-DoF) transverse and rotational oscillation case (right) when $R = 855$, $A = 0.26$: $\Theta_m = 30^o$ and $f/f_0 = 3$ ($T = 3.03$, $90.9 \leq t \leq 99.99$).

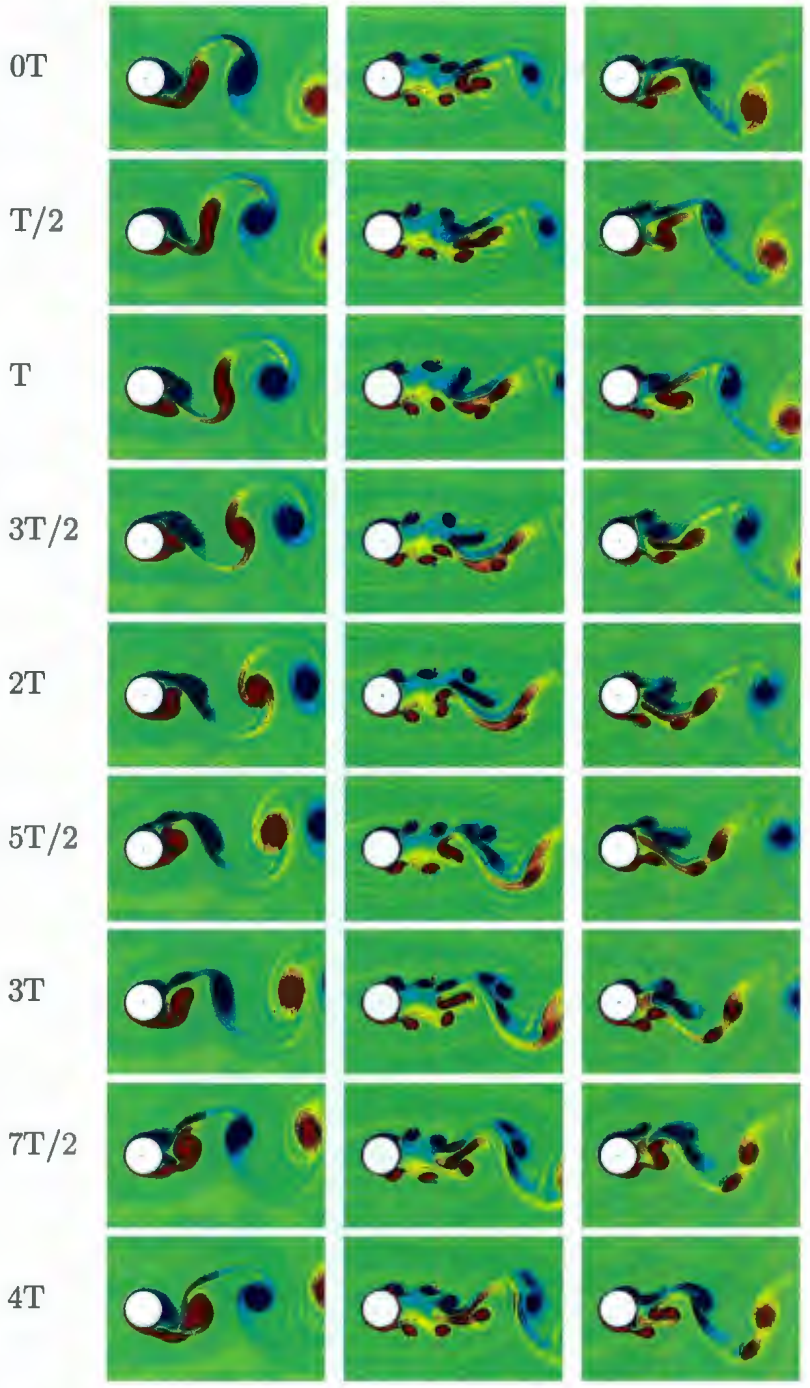

Figure 5.33: Equivorticity lines over four periods of oscillation, $4T$, for transverse-only (1-DoF) oscillation (left); rotational-only (1-DoF) oscillation (middle); combined (2-DoF) transverse and rotational oscillation case (right) when $R = 855$, $A = 0.26$: $\Theta_m = 30^o$ and $f/f_0 = 3$ ($T = 2.27$, $84.09 \leq t \leq 93.18$).

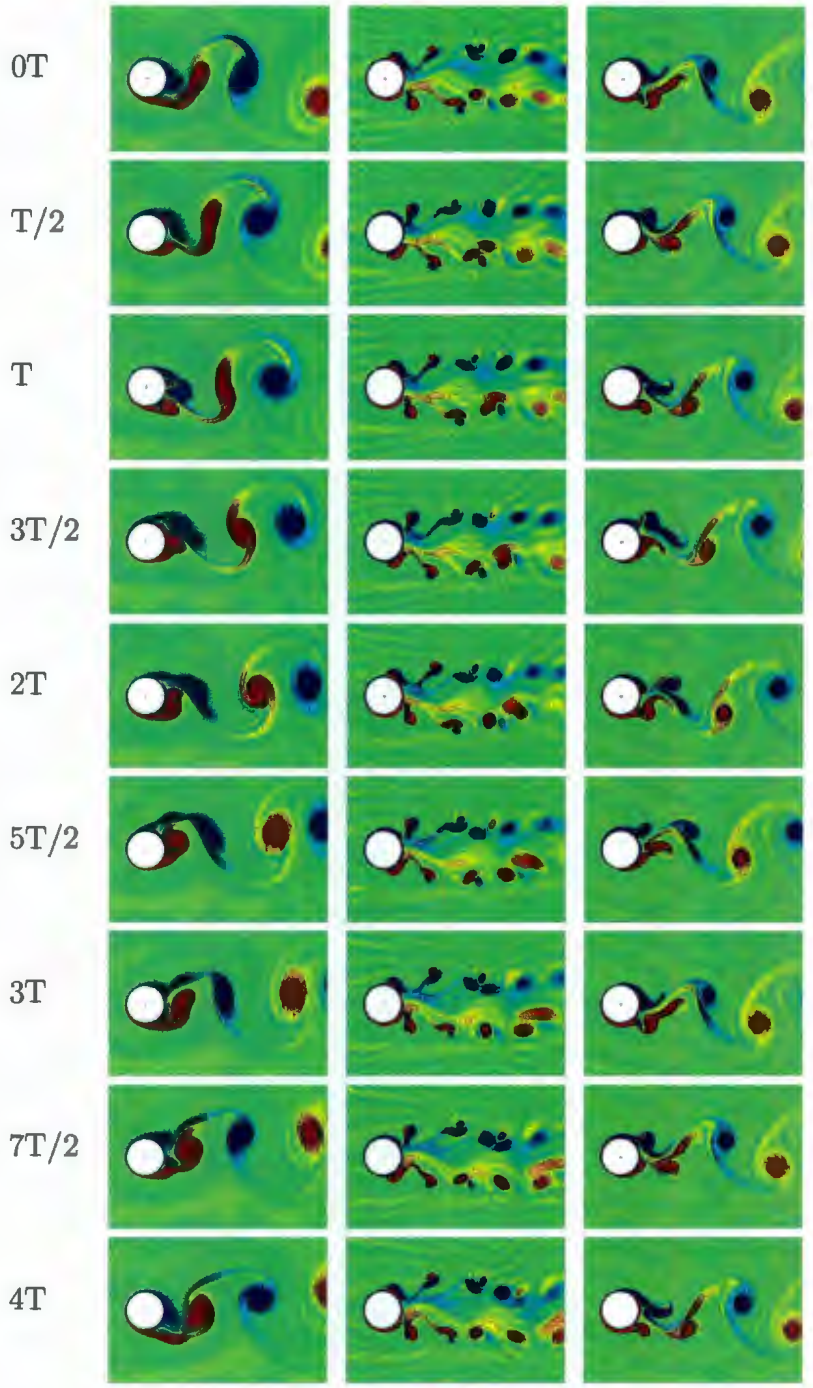

Figure 5.34: Equivorticity lines over four periods of oscillation, $4T$, for transverse-only (1-DoF) oscillation (left); rotational-only (1-DoF) oscillation (middle); combined (2-DoF) transverse and rotational oscillation case (right) when $R = 855$, $A = 0.26$: $\Theta_m = 60^o$ and $f/f_0 = 4$ ($T = 2.27$, $84.09 \leq t \leq 93.18$).

Chapter 6

The wake flow generated by combined (2-DoF) in-line and rotational cylinder oscillation

In this chapter, we focus on the numerical investigation of the wake flow created in a steady free-stream by combined in-line (streamwise) and rotational oscillation of a circular cylinder. The dimensionless in-line and rotational oscillatory velocities are

$$V(t) = -2\pi f A \sin(2\pi f t) \quad \text{and} \quad \Omega(t) = 2\pi f_\theta \Theta_m \sin(2\pi f_\theta t),$$

respectively. The frequency of the in-line oscillation is the same as for the rotational oscillation i.e., $f = f_\theta$. The near-wake structure as well as the fluid forces acting on the cylinder are then determined for five sets of the four dimensionless groups: $R = 855$, $A = 0.26$, $15^o \leq \Theta_m \leq 75^o$ when $f/f_0 = 0.5,\ 1,\ 2,\ 3,\ 4$ by setting the angle of inclination to $\eta = 0^o$. The connection between lift coefficient and vortex lock-on regimes is also investigated using Power Spectrum Density of the lift coefficient through Fourier analysis.

The simulations are carried out by using the time step $\Delta t_{j+1} = 10^{-4}$, for the first 10 steps. This is increased to $\Delta t_{j+1} = 10^{-3}$ for the next 10 steps. Finally $\Delta t_{j+1} = 10^{-2}$ is taken for the rest of the calculations. In the first computational domain $[0, t_s]$, the number of points in the z direction is taken as

1. 799 with a grid size of $\Delta z = 0.01$ when $f/f_0 = 0.5$
2. 319 with a grid size of $\Delta z = 0.025$ when $1 \leq f/f_0 \leq 4$.

In the second computational domain $[t_s, t_{max}]$ where $t_s = 40$, the number of points in the ξ direction is taken as

1. 799 with a grid size of $\Delta \xi = 0.00612$ when $f/f_0 = 0.5$
2. 319 with a grid size of $\Delta \xi = 0.01529$ when $1 \leq f/f_0 \leq 4$.

With these choices we set the outer boundary of computational domain at a physical distance of at least 133 times the radius of the cylinder for $R = 855$ and $40 \leq t \leq 120$. The maximum number of terms in the Fourier series is taken as $N = 65$ for all cases considered in this chapter.

6.1 Wake modes and synchronization (lock-on) phenomena in the near-wake region

Figure 6.1 shows the equivorticity lines over one period, T, for the combined in-line and rotational oscillation case when $f/f_0 = 0.5$ and $15^o \leq \Theta_m \leq 75^o$. The vortex formations occur in the non-synchronized asymmetrical **2S** mode, per $T/2$, for all values of Θ_m. In addition, it is obvious that the vortex shedding length decreases with the increase of Θ_m at $f/f_0 = 0.5$.

For the frequency ratio, $f/f_0 = 1$, the equivorticity lines are plotted in Figure 6.2 for

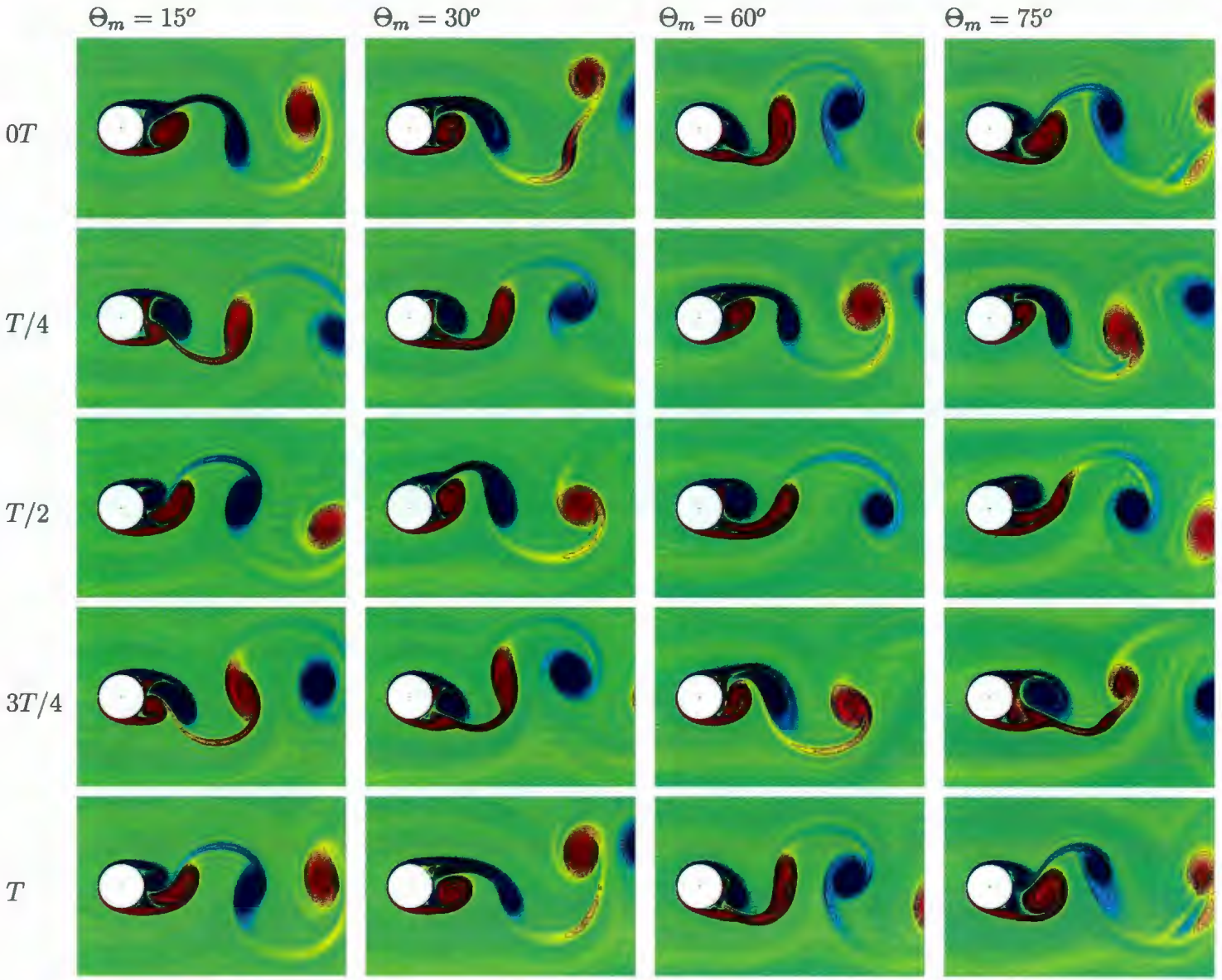

Figure 6.1: Equivorticity lines over one period of oscillation, T, for combined in-line and rotational (2-DoF) oscillation case ($\eta = 0^o$, $15^o \leq \Theta_m \leq 75^o$) when $R = 855$, $A = 0.26$: $f/f_0 = 0.5$ ($T = 18.18$, $90.9 \leq t \leq 109.08$).

$15^o \leq \Theta_m \leq 75^o$. The vortex shedding mode at this frequency is the synchronized asymmetrical **2S** mode, per T, for all values of Θ_m. Furthermore, the first row of Figure 6.2 shows that the inclination angle of the top region and the vertical distance between the shedding vortices are increasing with the increase of Θ_m. However, we observe a reduction in the size of shedding vortices as Θ_m increases. It is noted that, for $\Theta_m = 15^o$, the amount of positive base and negative top vorticity generated is reaching the maximum at the instants $T/2$ and T, respectively. For $30^o \leq \Theta_m \leq 75^o$, the maximum amount of positive base and negative top vorticity generated at the instants corresponding to $T/4$ and $3T/2$, respectively. Moreover, the shed vortices from the upper side of the cylinder are moving to a higher distance than the shedding vortices from the lower side for all values of Θ_m.

At $f/f_0 = 2$, the vortex shedding process produces different vortex shedding modes with the increase of Θ_m in the range $15^o \leq \Theta_m \leq 75^o$ as shown in Figure 6.3. For instance, for $\Theta_m = 15^o$, we observe a synchronized asymmetrical **S+P** mode, per $2T$, where two negative vortices are shed from the top of the cylinder and a large counter-rotating vortex is shed from the bottom of the cylinder over two periods of oscillation. It is noted that the second large vortex which is shed from the top of the cylinder is accompanied by another weak counter-rotating vortex. For $\Theta_m = 30^o$, the vortex shedding is characterized by a synchronized asymmetrical **S+P** mode over two periods, $2T$. It is noted that two negative vortices with smaller companion vortices are shed from the top side of the cylinder followed by the shedding of a positive vortex from the bottom side. Also, the shedding layer of the lower vortex remains attached to the vortex for a relatively long time as the vortex moves away from the

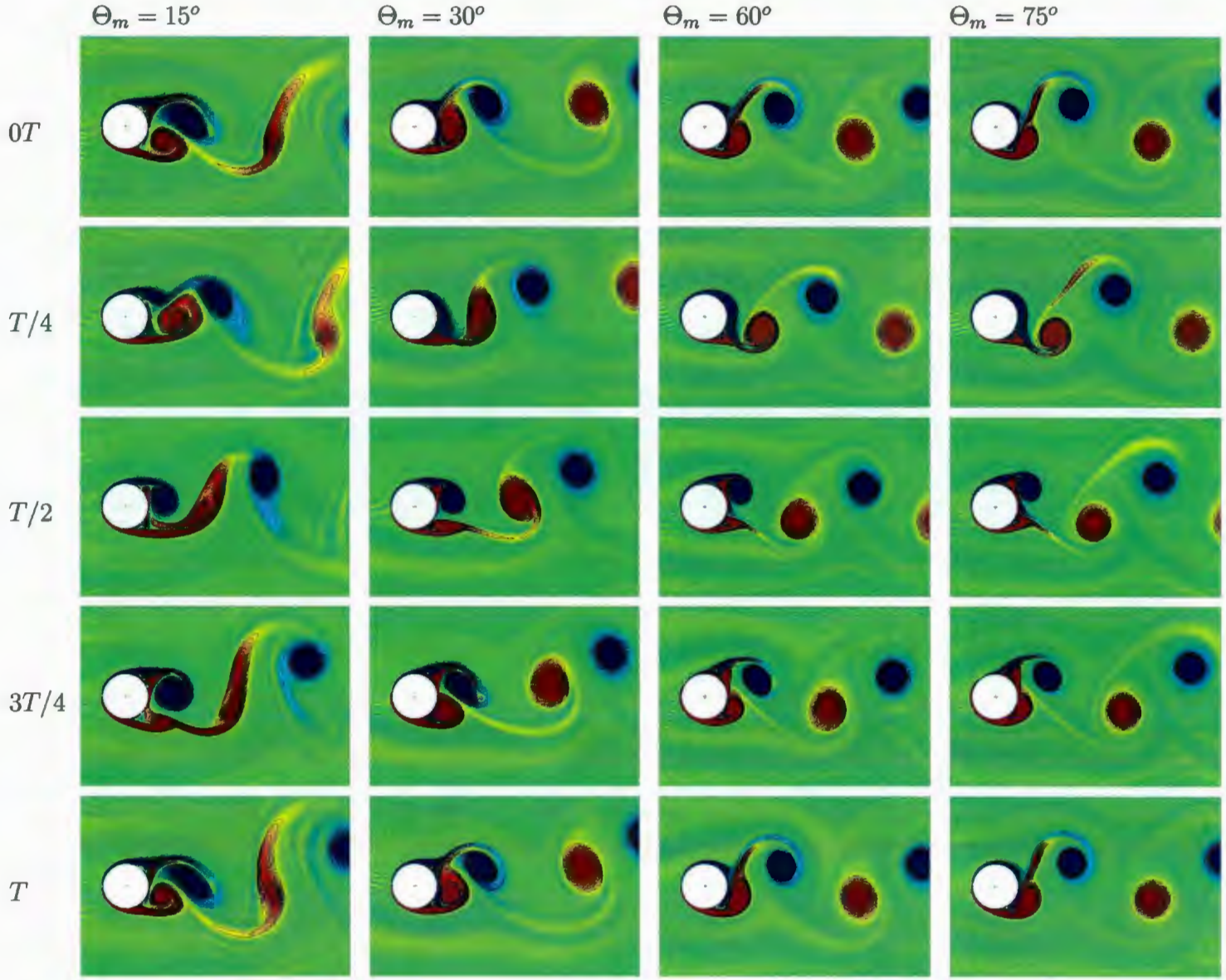

Figure 6.2: Equivorticity lines over one period of oscillation, T, for combined in-line and rotational (2-DoF) oscillation case ($\eta = 0^o$, $15^o \leq \Theta_m \leq 75^o$) when $R = 855$, $A = 0.26$: $f/f_0 = 1$ ($T = 9.09$, $81.82 \leq t \leq 90.91$).

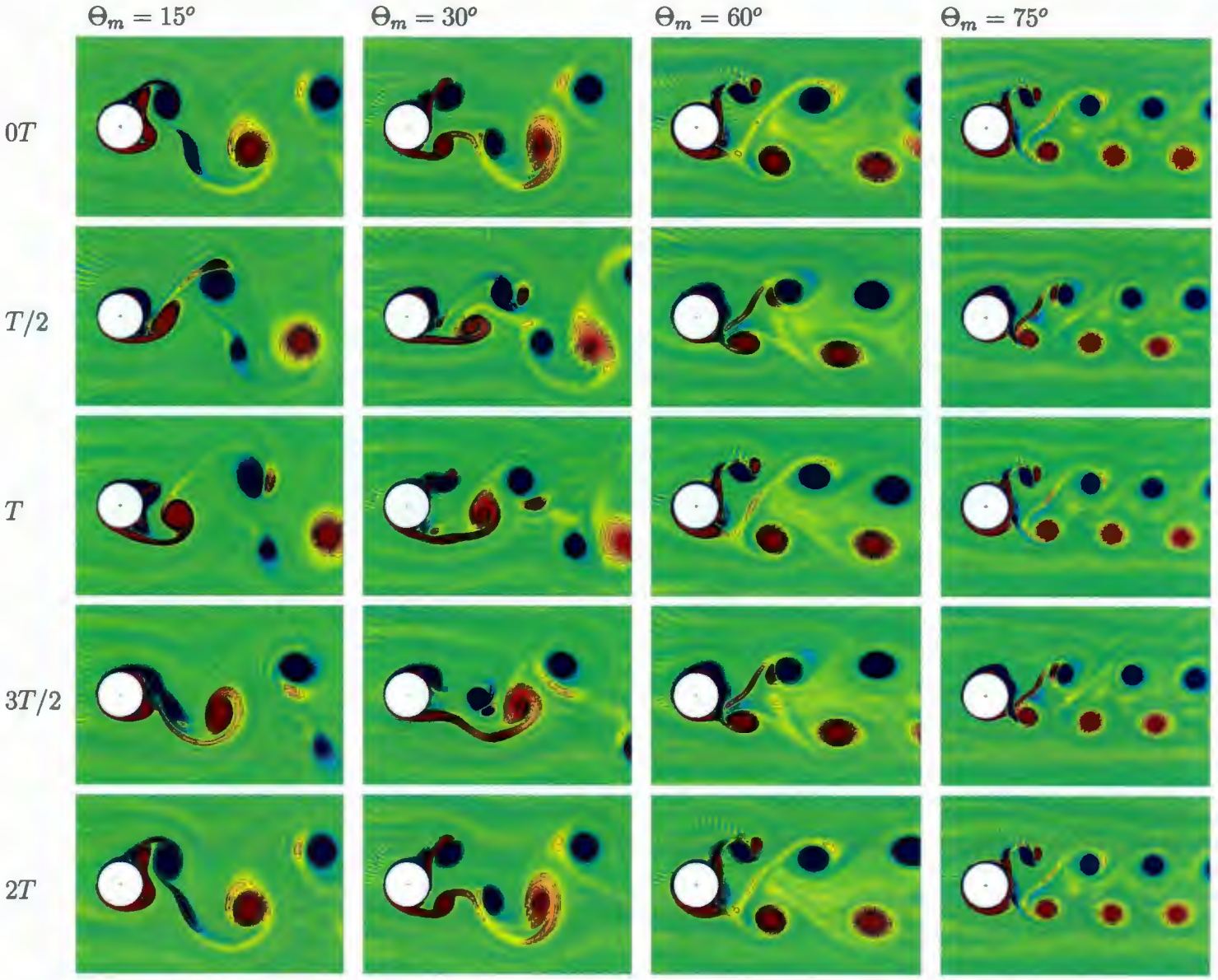

Figure 6.3: Equivorticity lines over two periods of oscillation, $2T$, for combined in-line and rotational (2-DoF) oscillation case ($\eta = 0^o$, $15^o \leq \Theta_m \leq 75^o$) when $R = 855$, $A = 0.26$: $f/f_0 = 2$ ($T = 4.55$, $90.9 \leq t \leq 99.99$).

cylinder. For $\Theta_m = 60^o$, 75^o, we observe the synchronized asymmetrical **2S** mode, per T, in which two vortices are alternatively shed from both sides of the cylinder over one period of cylinder oscillation. The upper shed vortex is accompanied by another weak vortex. Typical equivorticity and streamline plots for $f/f_0 = 2$ when $\Theta_m = 60^o$, 75^o are plotted in Figure 6.4. This figure shows a complex asymmetric pattern which consists of two rows of vortices: one row consists of a line of single vortices, whereas the other row consists a line of counter-rotating vortex pairs and single vortices. Further, the weaker vortices decay at a distance of approximately twice the diameter of the cylinder. Thus, it is evident that the effect of rotational oscillation at $f/f_0 = 2$ and $\Theta_m \geq 60^o$ is to reduce the vortex shedding period from $2T$ to T.

The equivorticity lines over one period of oscillation, T, for combined in-line and rotational oscillations for $f/f_0 = 3$ when Θ_m 15^o, 30^o, 60^o and 75^o are displayed in Figure 6.5. Comparing the snapshots in the first row of Figure 6.5, we observe a reduction in the strength of the shed vortices. At the same time, the vertical distance between the shed vortices and the inclination angle of the top region are increasing as Θ_m increases. It seems that the effect of increase in Θ_m draws irrotational fluid along the wake centerline towards the cylinder base resulting in a complex asymmetric pattern: one row consists of a line of single vortices, whereas the other row consists a line of counter-rotating vortex pairs; or co-rotating and counter-rotating vortex triplets; and single vortices. For all Θ_m, the vortex shedding produces the synchronized asymmetrical **2S** mode over one period of cylinder oscillation. It is noted that the dominant or larger vortex shed from the top of the cylinder is accompanied by another weak

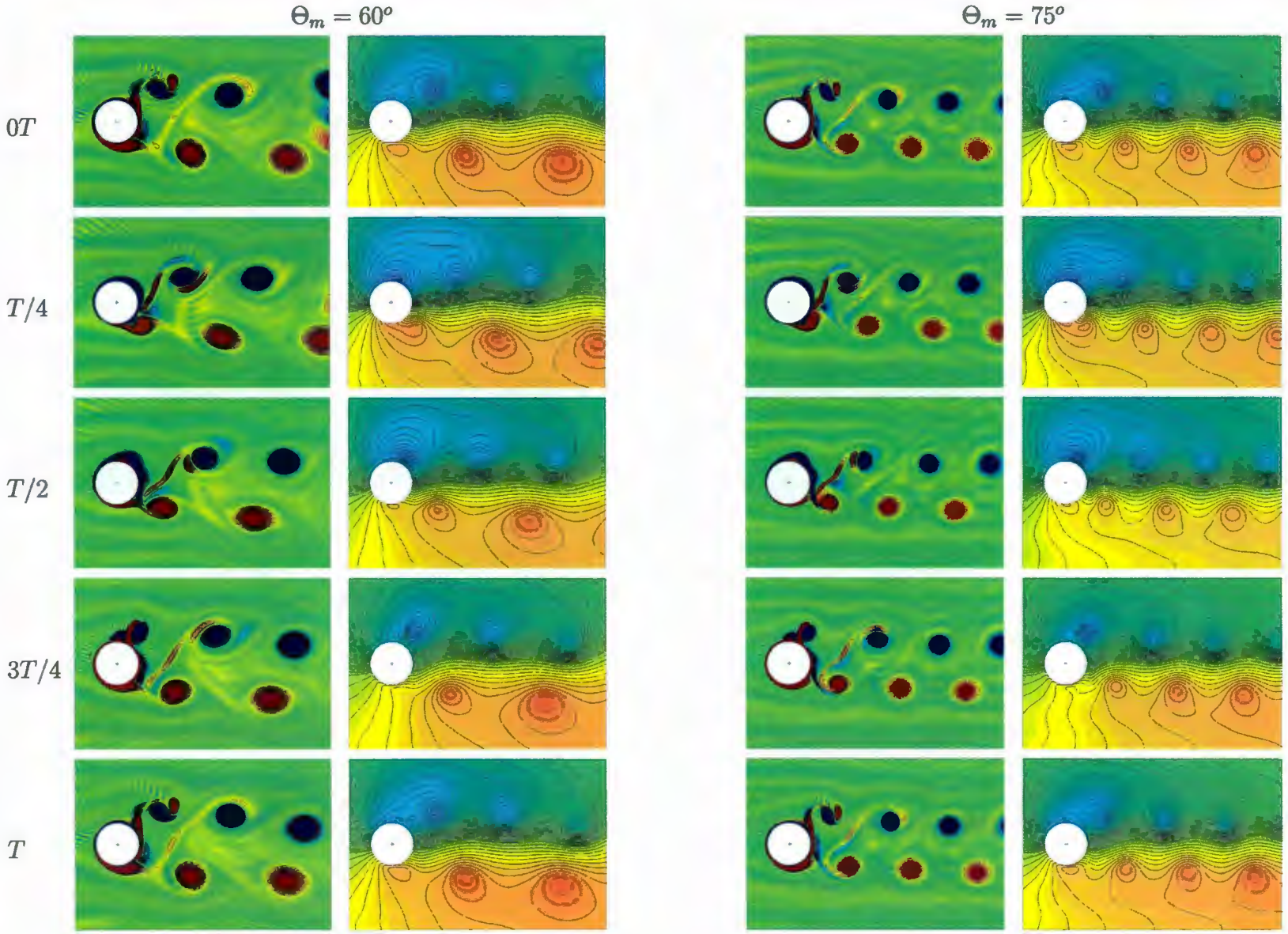

Figure 6.4: Equivorticity lines and streamline patterns over one period of oscillation, T, for combined in-line and rotational (2-DoF) oscillation case ($\eta = 0^o$, $\Theta_m = 60^o$ (left) and $\Theta_m = 75^o$ (right)) when $R = 855$, $A = 0.26$: $f/f_0 = 2$ ($T = 4.55$, $90.9 \leq t \leq 95.45$).

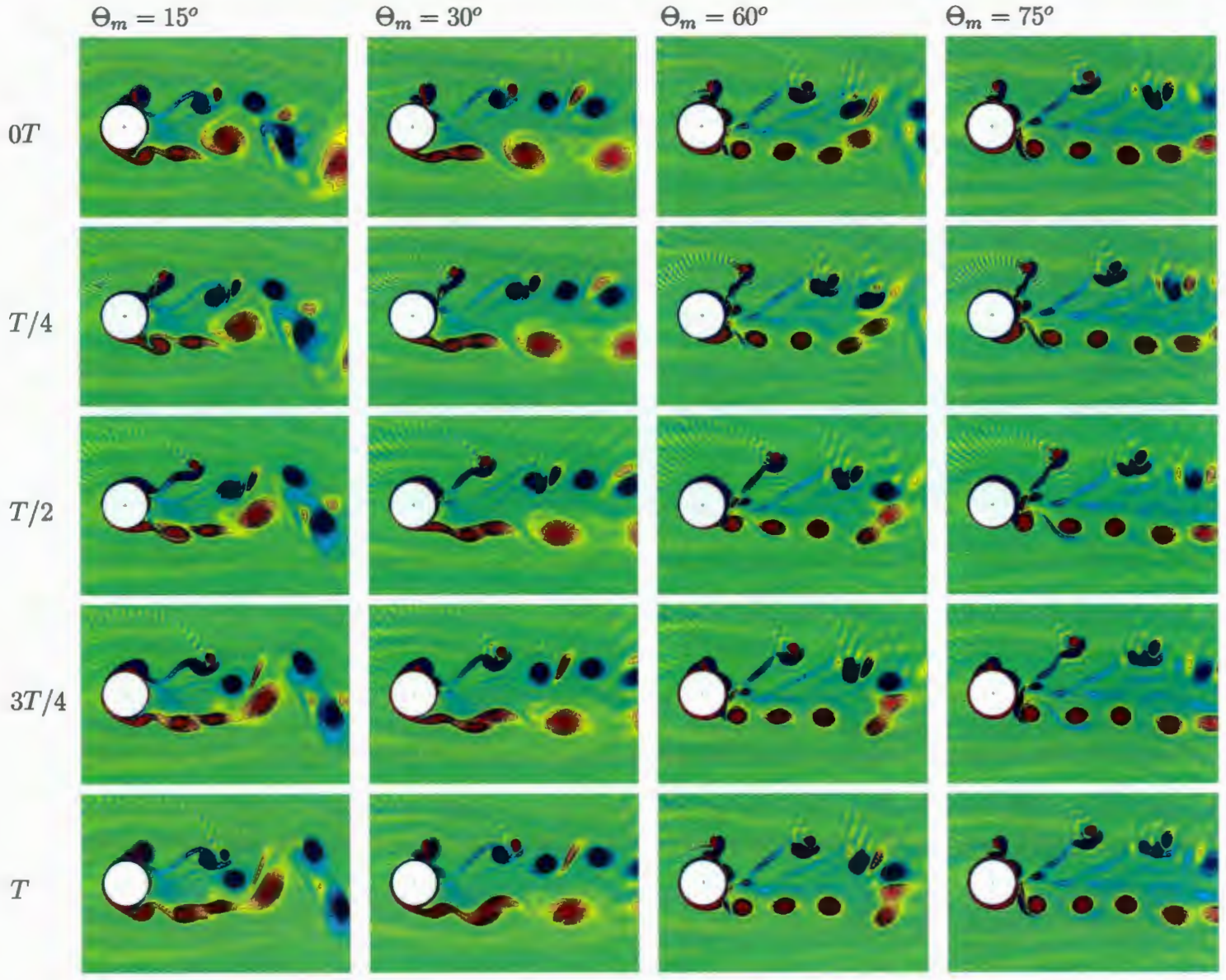

Figure 6.5: Equivorticity lines over one period of oscillation, T, for combined in-line and rotational (2-DoF) oscillation case ($\eta = 0^o$, $15^o \leq \Theta_m \leq 75^o$) when $R = 855$, $A = 0.26$: $f/f_0 = 3$ ($T = 3.03$, $90.9 \leq t \leq 93.94$).

vortex. For $\Theta_m = 30^o$, the vortex shedding produces an interesting repeatable phenomena during two periods of cylinder oscillation in which the two shed vortices from the bottom of the cylinder are coalesce to form one large vortex at a distance, $4a$. However, increasing Θ_m beyond 30^o eliminates the coalescence between the vortices in the near-wake region.

The equivorticity lines over one period of oscillation, T, for the frequency ratio, $f/f_0 = 4.0$, when $15^o \leq \Theta_m \leq 75^o$ are displayed in Figure 6.6. The snapshots in the first row show that there is a reduction in the vortex formation length and the size of the vortices as Θ_m increases. Furthermore, it is noted that the vertical distance between the shed vortices is increasing as Θ_m increases below 30^o while it is decreasing as Θ_m increases beyond this value. The vortex shedding produces the synchronized asymmetrical **2S** mode, per T, for all Θ_m. It is noted, for $\Theta_m = 15^o$, 30^o, that the dominant or large vortex shed from the top of the cylinder is accompanied by another counter-rotating vortex whereas, for $\Theta_m = 75^o$, this counter-rotating vortex is accompanied by the shed vortex from the bottom of the cylinder. On the other hand, for $\Theta_m = 60^o$, each shed vortex is accompanied with another counter-rotating vortex. In fact, the vortex shedding mode at $f/f_0 = 4$ and $\Theta_m = 60^o$ is quite similar to symmetrical mode. The vortex shedding for $\Theta_m = 15^o$, 30^o produces an interesting repeatable phenomena, similar to that reported at $f/f_0 = 3$ and $\Theta_m = 30^o$, every $3T$, in which the three shed vortices from the bottom of the cylinder are coalesce to form one large vortex at a distance, $4a$, as shown in Figures 6.7 and 6.8. Note that the vortex formation from each side of the cylinder draws a parallel street of vortices to the wake centerline. Thus, the effect of increase in Θ_m at $f/f_0 = 4$ is to suppress

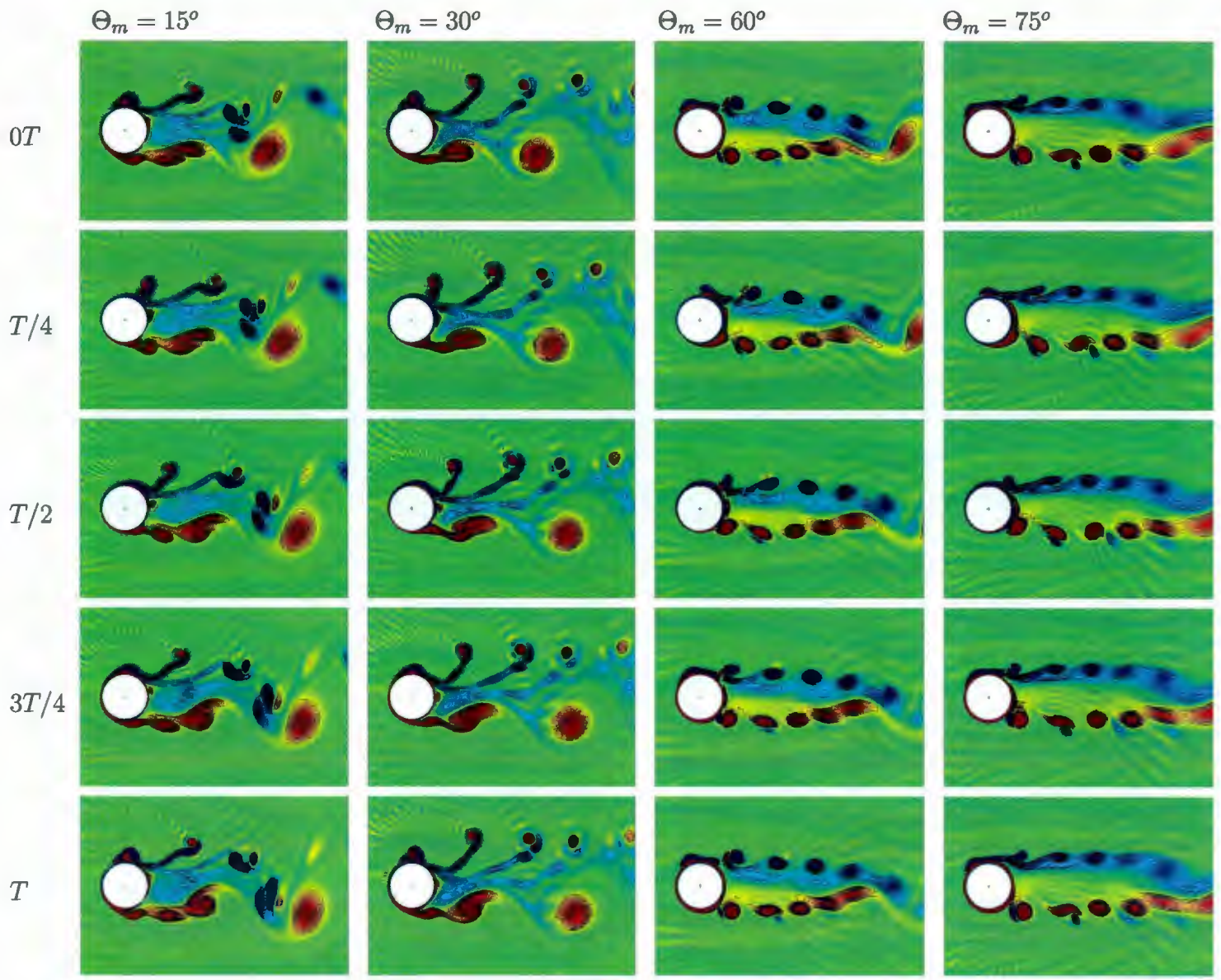

Figure 6.6: Equivorticity lines over one period of oscillation, T, for combined in-line and rotational (2-DoF) oscillation case ($\eta = 0^o$, $15^o \leq \Theta_m \leq 75^o$) when $R = 855$, $A = 0.26$: $f/f_0 = 4$ ($T = 2.27$, $84.09 \leq t \leq 86.36$).

the vortex shedding process.

The effect of Θ_m and f/f_0 on the periodic vortex shedding modes and their periods for the combined (2-DoF) in-line and rotational oscillations case is summarized in Tables 6.1 and 6.2. As a result of increasing either Θ_m or f/f_0 the near-wake vorticity breaks up to produce different modes of vortex shedding. Also, the inversely repeatable near-wake structure every half of the vortex shedding period is not captured in the combined (2-DoF) in-line and rotational oscillation cases. It can be seen that as Θ_m or f/f_0 increases the vortex shedding mode tends to, in general, the **2S** mode, per T. The classical **2S** mode occurs for low values of the frequency ratio, $f/f_0 \leq 1$, since the oscillatory speeds considered in this chapter are less than the uniform flow speed. The common vortex shedding period is T at hight values of Θ_m or f/f_0. Furthermore, the existence of lock-on regimes at $f/f_0 = 2$, 3 and 4 is confirmed in this study.

f/f_0 \ Θ_m	15^o	30^o	60^o	75^o
0.5	**2S** •	**2S** •	**2S** •	**2S** •
1	**2S** •	**2S** •	**2S** •	**2S** •
2	**S+P** •	**S+P** •	**2S** •	**2S** •
3	**2S** •	**2S** •	**2S** •	**2S** •
4	**2S** •	**2S** •	**2S** •	**2S** •

Table 6.1: The effect of f/f_0 and Θ_m on the vortex shedding modes for the combined (2-DoF) in-line and rotational oscillation case ($\eta = 0^o$, $\Theta_m \neq 0$) when $R = 855$, $A = 0.26$: • lock-on mode; • non-lock mode.

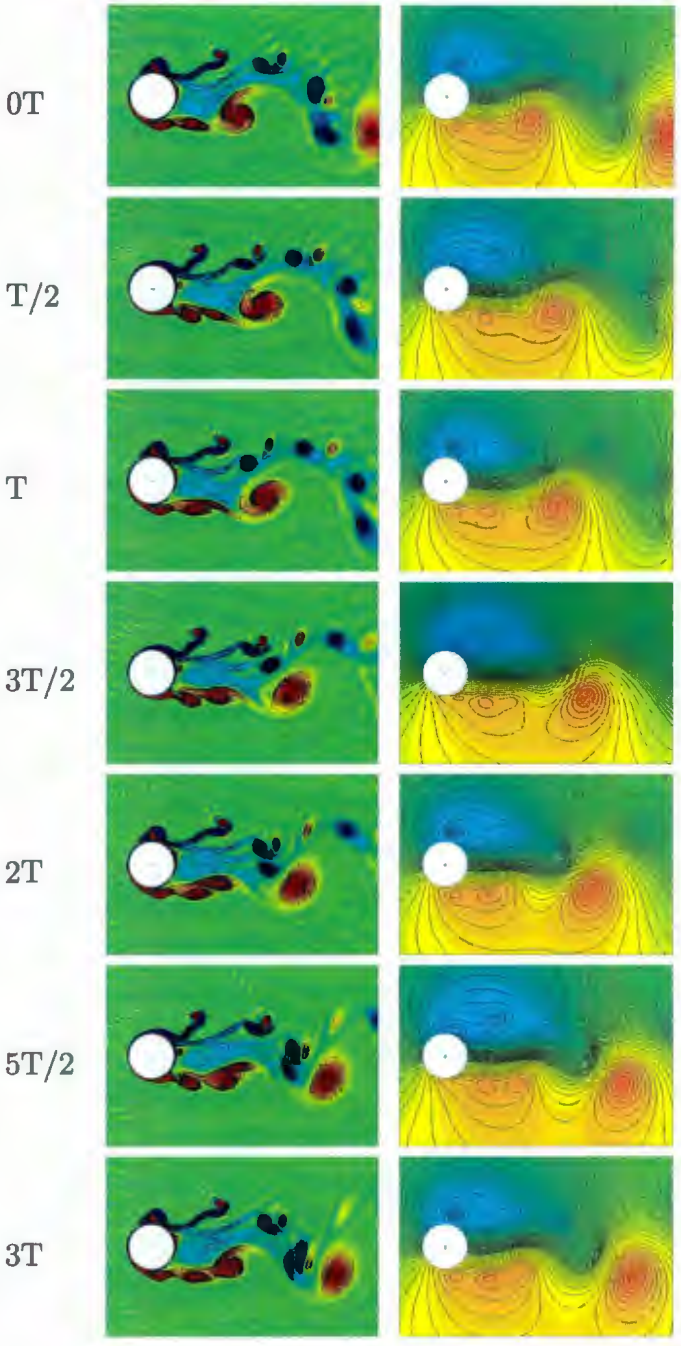

Figure 6.7: Equivorticity lines (left) and streamline patterns (right) over three periods, $3T$, for the combined (2-DoF) in-line and rotational oscillation case ($\eta = 0^o$, $\Theta_m \neq 0$) when $R = 855$, $A = 0.26$: $\Theta_m = 15^o$ and $f/f_0 = 4.0$ ($T = 2.57$, $84.09 \leq t \leq 90.91$).

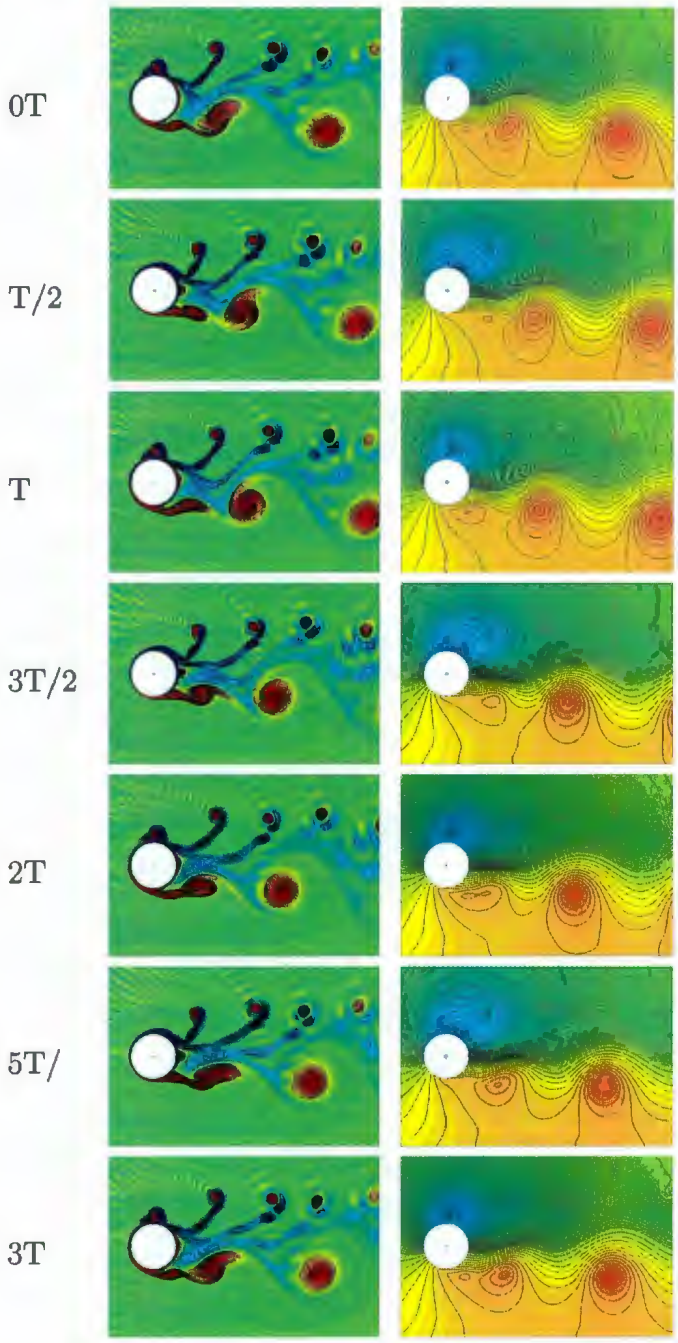

Figure 6.8: Equivorticity lines (left) and streamline patterns (right) over three periods, $3T$, for the combined (2-DoF) in-line and rotational oscillation case ($\eta = 0^o$, $\Theta_m \neq 0$) when $R = 855$, $A = 0.26$: $\Theta_m = 15^o$ and $f/f_0 = 4.0$ ($T = 2.57$, $84.09 \leq t \leq 90.91$).

f/f_0 \ Θ_m	15^o	30^o	60^o	75^o
0.5	T/2	T/2	T/2	T/2
1	T	T	T	T
2	2T	2T	T	T
3	T	T	T	T
4	T	T	T	T

Table 6.2: The effect of f/f_0 and Θ_m on the vortex shedding periods for the combined (2-DoF) in-line and rotational oscillation case ($\eta = 0^o$, $\Theta_m \neq 0$) when $R = 855$, $A = 0.26$.

6.2 Time histories of fluctuating fluid forces

The interaction between the vortex shedding process and the cylinder oscillations result in an oscillating lift coefficient with a complex behavior for the combined (2-DoF) in-line and rotational oscillation case. This complexity, in general, creates a difficulty in calculating the PSD of the lift records as we will see in this section.

Figure 6.9 shows the time evolution of the lift coefficient, C_L, plotted with the displacement and the Power Spectral Density of the lift coefficient, PSD, at $f/f_0 = 0.5$ when $15^o \leq \Theta_m \leq 75^o$. The lift coefficients show a repeatable pattern with two different amplitudes and thus with two different frequencies. These frequencies are the forcing and natural frequencies, f and f_0 respectively, as suggested by the corresponding PSD of each lift record. However, the PSD shows that the effect of f in the lift records increases with the increase of Θ_m. Further, the minimum value of the lift coefficient, $C_{L,min}$, is decreasing while its amplitude , $C_{L,amp}$, is increasing as Θ_m increases. The history of drag and moment coefficients are presented in Figures

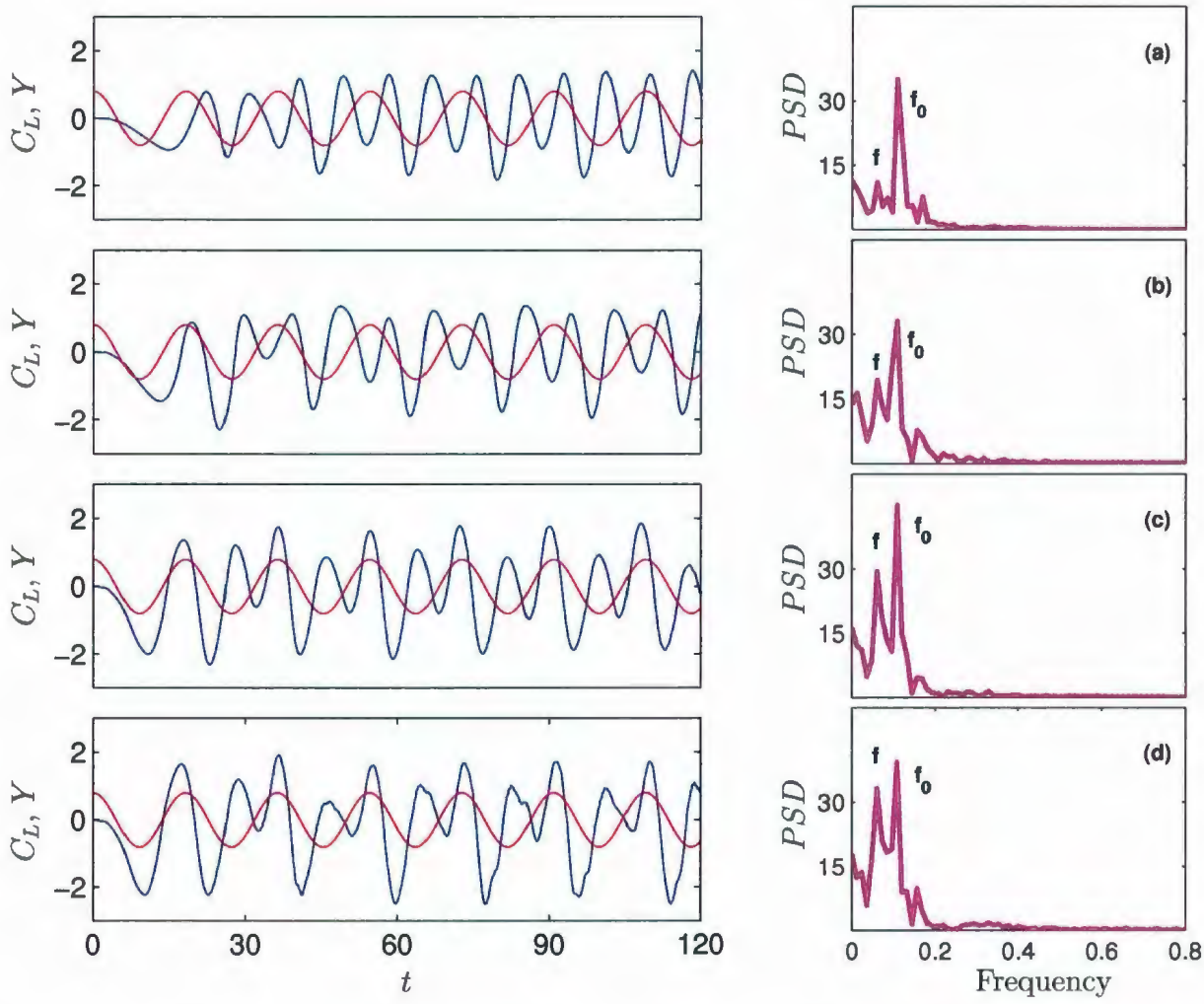

Figure 6.9: The time variation of C_L (—) with respect to cylinder displacement, Y (—) and the Fourier analysis of the lift coefficient PSD (---) for the combined (2-DoF) in-line and rotational oscillation case ($\eta = 0^o$, $\Theta_m \neq 0$) when $R = 855$, $A = 0.26$ and $f/f_0 = 0.5$: (a) $\Theta_m = 15^o$; (b) $\Theta_m = 30^o$; (c) $\Theta_m = 60^o$ and (d) $\Theta_m = 75^o$.

6.10-6.11. It can be seen that the values for $C_{D,max}$ and $C_{D,amp}$ are increasing while $C_{D,min}$ is decreasing as Θ_m increases in the range $\Theta_m \geq 30^o$. The amplitude of C_M is increasing proportionally with Θ_m. Furthermore, the moment coefficient oscillates at the forcing frequency, f, and C_M and Y are out of phase with each other. Also, C_M shows beating wave forms which indicates the competition between the forcing and natural shedding frequencies.

Figure 6.12 shows the time variation of C_D, C_L, Y and the PSD at $f/f_0 = 1$ when $15^o \leq \Theta_m \leq 75^o$. Each lift coefficient shows a repeatable periodic behavior with peak-to-peak distance equal $1/f$ which confirms our finding that the vortex lock-on occurs in these cases (see Figure 6.2). The corresponding PSD of each C_L confirms that the dominant frequency is the forcing frequency, f, for all Θ_m. It can be seen that C_L and Y are out of phase with each other. Furthermore, the minimum value of the lift coefficient, $C_{L,min}$, is increasing while its amplitude, $C_{L,amp}$, is decreasing as Θ_m increases beyond $\Theta_m = 30^o$. The time evolution of the drag and moment coefficients at $f/f_0 = 1$ are plotted in Figures 6.13-6.14, respectively. It is noted that both C_M and C_D oscillate at the forcing frequency, f. In addition, C_D is in phase with Y whereas C_M and Y are out of phase with each other. Moreover, the amplitude of C_M is increasing proportionally. The minimum value of the drag coefficient, $C_{D,min}$, is increasing as Θ_m increases. It is noted that, C_D behavior shows a competition between two frequencies.

It is noted from Figure 6.15, for the case of $f/f_0 = 2$, that the lift coefficient has a

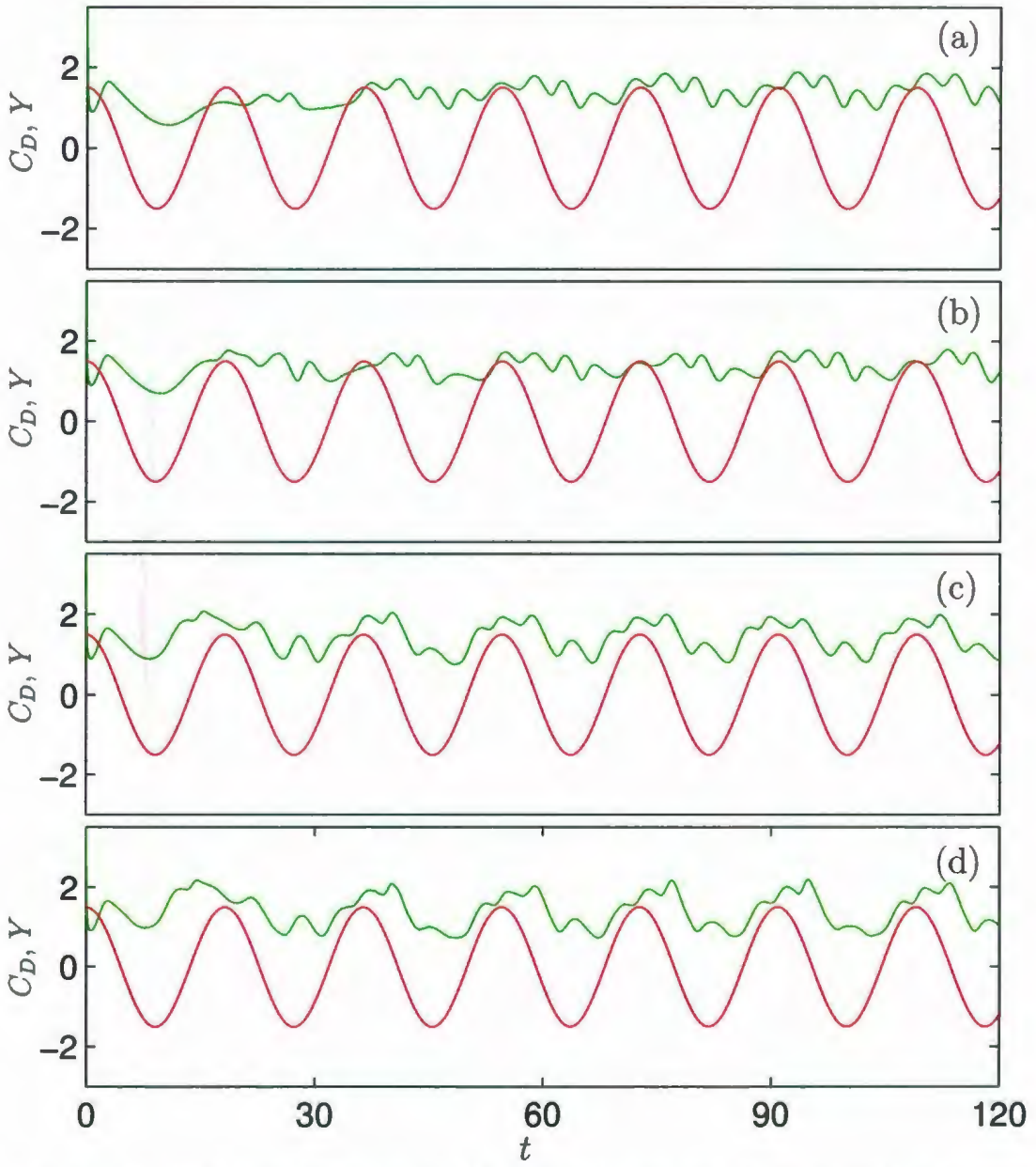

Figure 6.10: The time variation of C_D (—) with respect to cylinder displacement, Y (—) for the combined (2-DoF) in-line and rotational oscillation case ($\eta = 0^o$, $\Theta_m \neq 0$) when $R = 855$, $A = 0.26$ and $f/f_0 = 0.5$: (a) $\Theta_m = 15^o$; (b) $\Theta_m = 30^o$; (c) $\Theta_m = 60^o$ and (d) $\Theta_m = 75^o$.

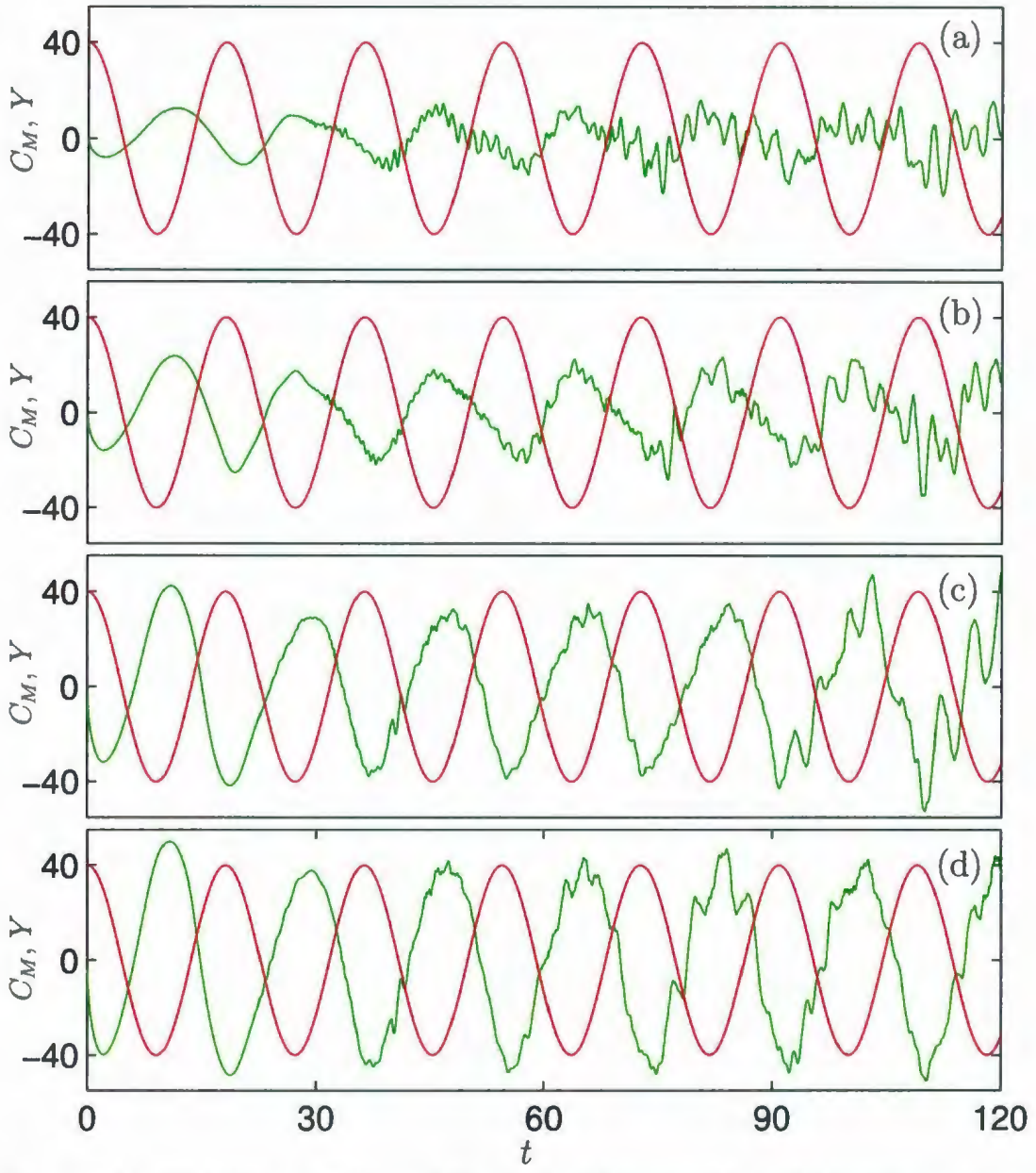

Figure 6.11: The time variation of C_M (—) with respect to cylinder displacement, Y (—) for the combined (2-DoF) in-line and rotational oscillation case ($\eta = 0^o$, $\Theta_m \neq 0$) when $R = 855$, $A = 0.26$ and $f/f_0 = 0.5$: (a) $\Theta_m = 15^o$; (b) $\Theta_m = 30^o$; (c) $\Theta_m = 60^o$ and (d) $\Theta_m = 75^o$.

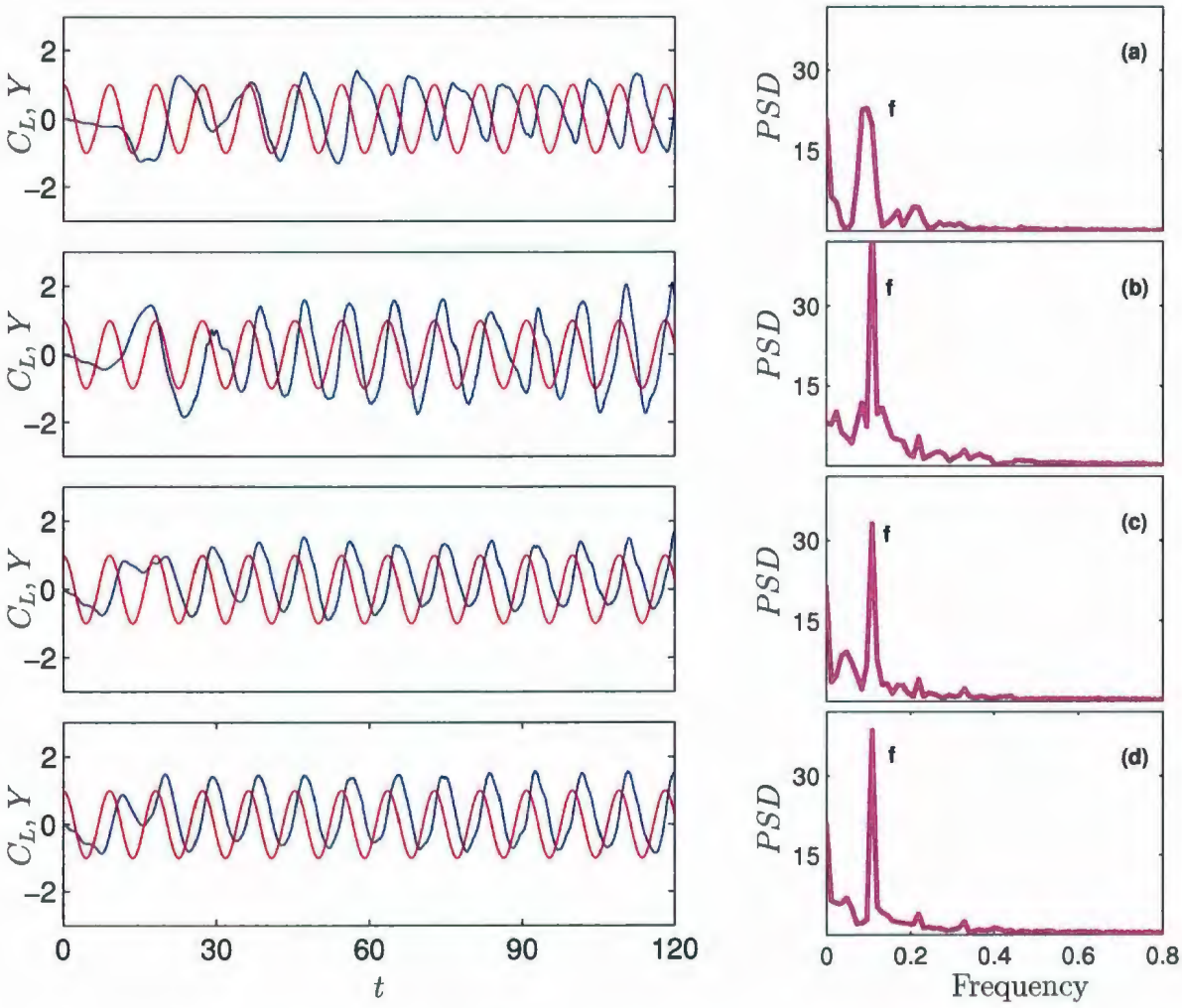

Figure 6.12: The time variation of C_L (—) with respect to cylinder displacement, Y (—) and the Fourier analysis of the lift coefficient PSD (·····) for the combined (2-DoF) in-line and rotational oscillation case ($\eta = 0^o$, $\Theta_m \neq 0$) when $R = 855$, $A = 0.26$ and $f/f_0 = 1.0$: (a) $\Theta_m = 15^o$; (b) $\Theta_m = 30^o$; (c) $\Theta_m = 60^o$ and (d) $\Theta_m = 75^o$.

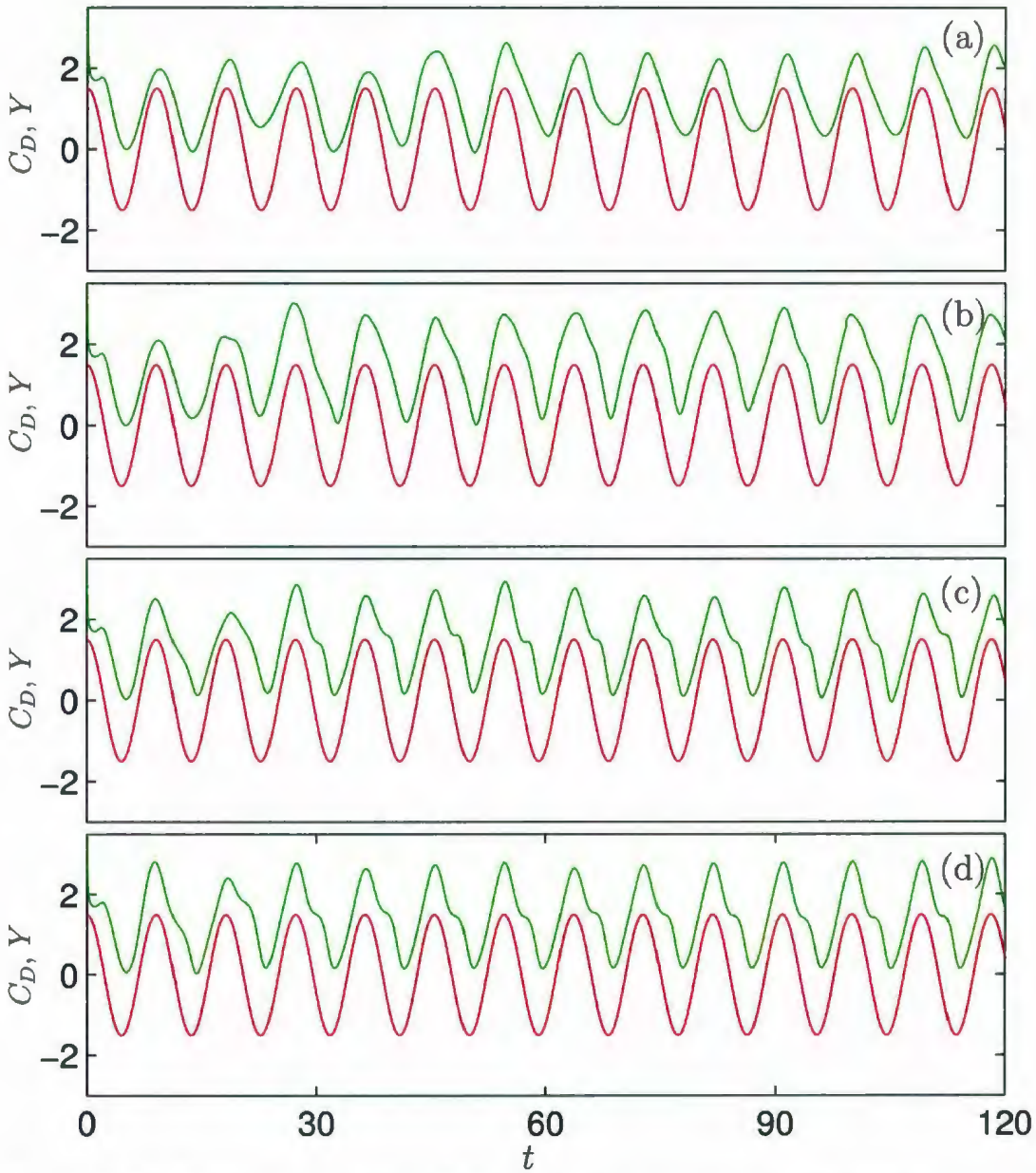

Figure 6.13: The time variation of C_D (—) with respect to cylinder displacement, Y (—) for the combined (2-DoF) in-line and rotational oscillation case ($\eta = 0^o$, $\Theta_m \neq 0$) when $R = 855$, $A = 0.26$ and $f/f_0 = 1.0$: (a) $\Theta_m = 15^o$; (b) $\Theta_m = 30^o$; (c) $\Theta_m = 60^o$ and (d) $\Theta_m = 75^o$.

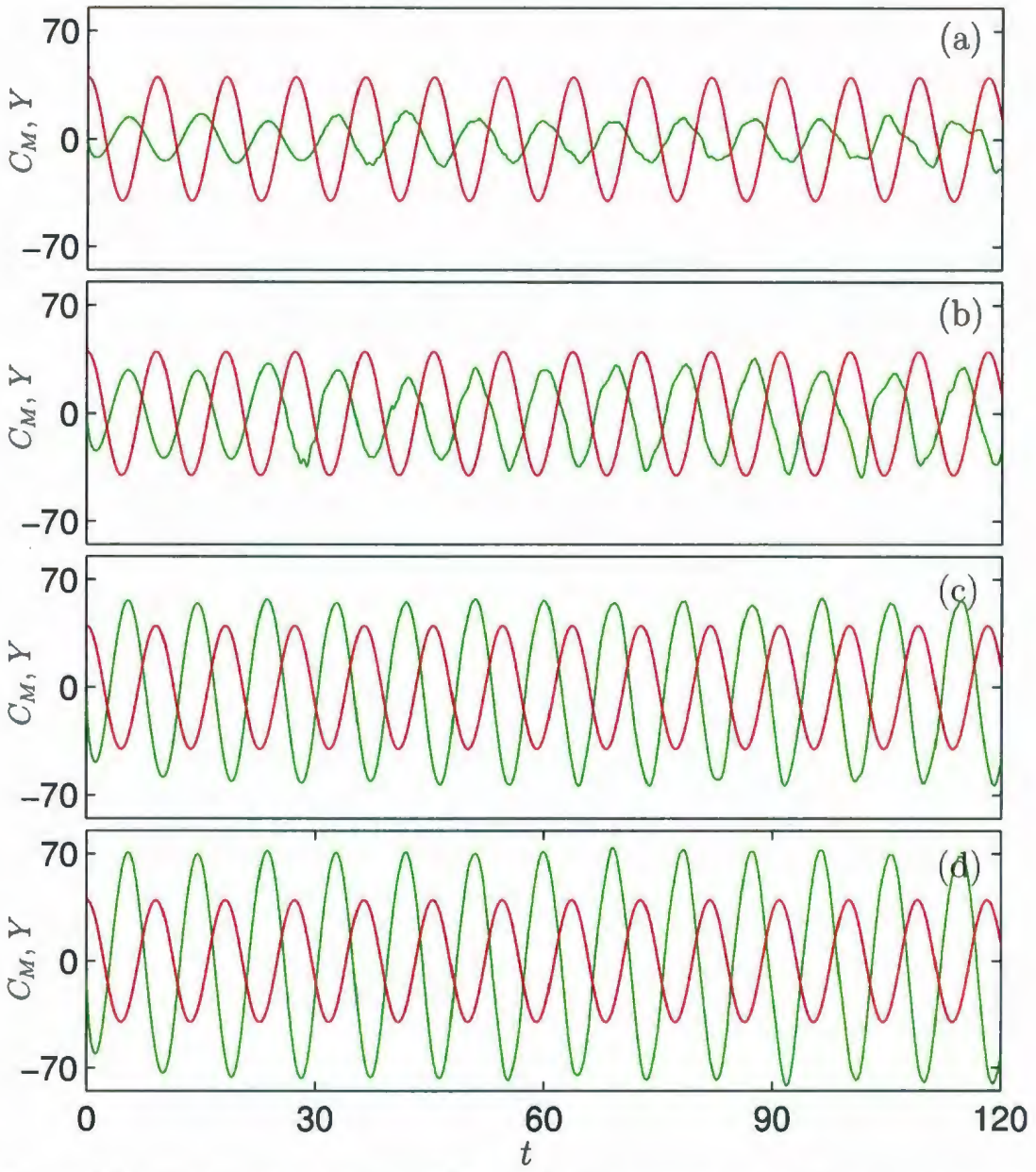

Figure 6.14: The time variation of C_M (···) with respect to cylinder displacement, Y (—) for the combined (2-DoF) in-line and rotational oscillation case ($\eta = 0^o$, $\Theta_m \neq 0$) when $R = 855$, $A = 0.26$ and $f/f_0 = 1.0$: (a) $\Theta_m = 15^o$; (b) $\Theta_m = 30^o$; (c) $\Theta_m = 60^o$ and (d) $\Theta_m = 75^o$.

repeatable periodic pattern for all Θ_m. In addition, the behavior of C_L varies according to the values of Θ_m. For instance, at $\Theta_m = 15^o$ and $\Theta_m = 30^o$, C_L is repeatable every two periods of oscillations with two different amplitudes whereas it is repeatable every one period of oscillation with a single amplitude for $\Theta_m = 60^o$ and $\Theta_m = 75^o$. These results confirm our finding that the vortex shedding period at $\Theta_m = 15^o,\ 30^o$ is $2T$ whereas it is T for $\Theta_m = 60^o,\ 75^o$ (see Figure 6.3). Fourier analysis of C_L shows that the effect of natural shedding frequency, f_0, decreases with the increase of Θ_m. In contrast, the forcing frequency, f, is increasing with the increase of Θ_m. An interesting result shown in the PSD of Figure 6.15 is the increasing of the effect of the frequency $f + 2f_0$ as Θ_m increases. Similar phenomena has been reported by Kim (2000) and Karanth *et al.* (1995) for the in-line-only (1-DoF) oscillation case. Furthermore, the value of $C_{L,min}$ is increasing as Θ_m increases except at 75^o. The value of $C_{L,amp}$ is decreasing as Θ_m increases below $\Theta_m = 30^o$ whereas it is increasing beyond $\Theta_m = 60^o$. The drag and momentum coefficients presented in Figure 6.16-6.17 respectively are oscillating at the same frequency of the forcing frequency, f. We also noted that, C_D is in phase with Y whereas C_M and Y are out of phase with each other. In addition, C_D and C_M have a repeatable periodic behavior with two different amplitudes. The difference between these amplitudes is decreasing as Θ_m increases. The amplitude of C_M increases as Θ_m increases. However, the values for $C_{D,max}$ and $C_{D,min}$ are decreasing while its amplitude, $C_{D,amp}$, is increasing as Θ_m increases.

By investigating the lift records for the case of $f/f_0 = 3$ when $15^o \leq \Theta_m \leq 75^o$ we observe a repeatable periodic behavior every one period of cylinder oscillation as shown in Figure 6.18. In addition, the corresponding PSD of each C_L confirms our

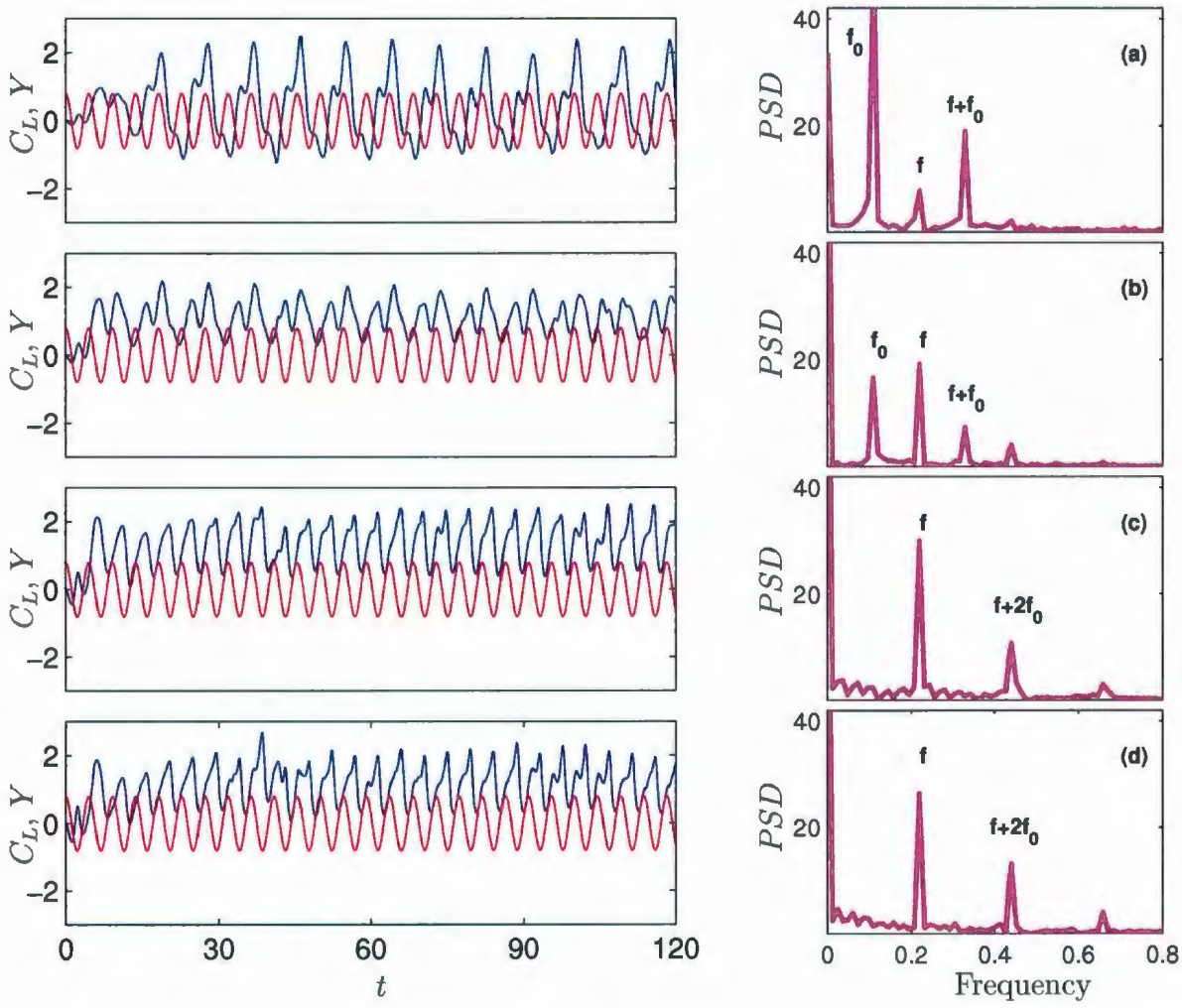

Figure 6.15: The time variation of C_L (—) with respect to cylinder displacement, Y (—) and the Fourier analysis of the lift coefficient PSD (···) for the combined (2-DoF) in-line and rotational oscillation case ($\eta = 0^o$, $\Theta_m \neq 0$) when $R = 855$, $A = 0.26$ and $f/f_0 = 2.0$: (a) $\Theta_m = 15^o$; (b) $\Theta_m = 30^o$; (c) $\Theta_m = 60^o$ and (d) $\Theta_m = 75^o$.

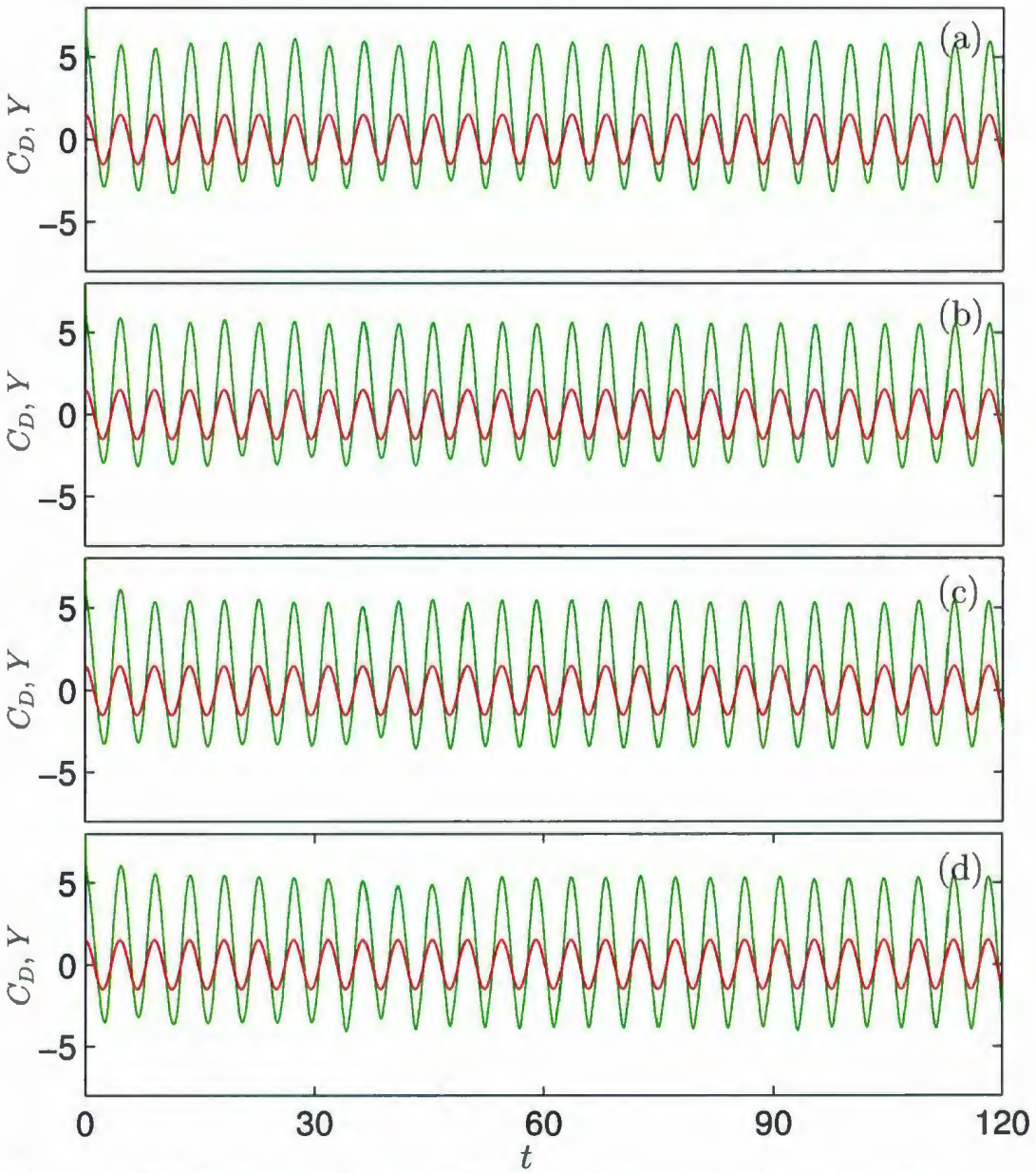

Figure 6.16: The time variation of C_D (—) with respect to cylinder displacement, Y (—) for the combined (2-DoF) in-line and rotational oscillation case ($\eta = 0^o$, $\Theta_m \neq 0$) when $R = 855$, $A = 0.26$ and $f/f_0 = 2.0$: (a) $\Theta_m = 15^o$; (b) $\Theta_m = 30^o$; (c) $\Theta_m = 60^o$ and (d) $\Theta_m = 75^o$.

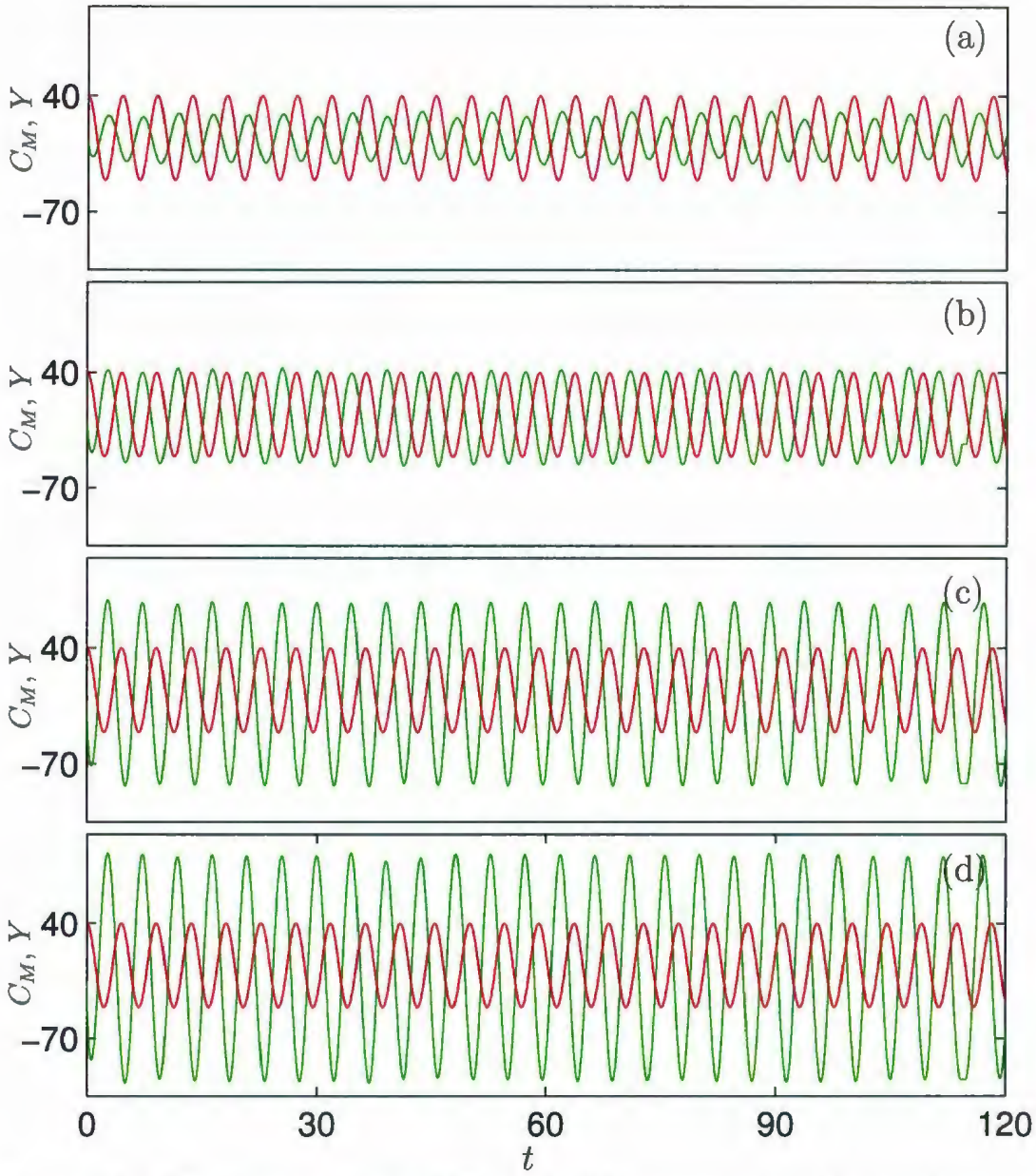

Figure 6.17: The time variation of C_M (—) with respect to cylinder displacement, Y (—) for the combined (2-DoF) in-line and rotational oscillation case ($\eta = 0^o$, $\Theta_m \neq 0$) when $R = 855$, $A = 0.26$ and $f/f_0 = 2.0$: (a) $\Theta_m = 15^o$; (b) $\Theta_m = 30^o$; (c) $\Theta_m = 60^o$ and (d) $\Theta_m = 75^o$.

results that the dominant frequency is exactly the forcing frequency for all Θ_m. Thus, the lift coefficient is successfully used to predict both vortex lock-on modes and their periods at these values which are presented in Figure 6.5. In addition, the PSD of each C_L predicts the existence of another frequency at $f + 3f_0$ which gradually becomes stronger as Θ_m increases. As a result of increasing Θ_m, the values of $C_{L,max}$ and $C_{L,amp}$ are increasing while $C_{L,min}$ is decreasing. The drag coefficient oscillates at the forcing frequency, f, and in phase with Y as shown in Figure 6.19 whereas the moment coefficient displayed in Figure 6.20 oscillates at f and C_M and Y are out of phase with each other. The amplitude of C_M is increasing as Θ_m increases.

At $f/f_0 = 4$, it is noted that the lift coefficients has a repeatable periodic behavior every period of cylinder oscillation as shown in Figure 6.21. By investigating the PSD of each C_L we see that the dominant frequency is the forcing frequency, f, which confirms our previous observation that the vortex lock-on occurs, per T, for all Θ_m (see Figure 6.6). We also note that the amplitude of C_L is increasing as Θ_m increases whereas the values of $C_{L,max}$ and $C_{L,min}$ are decreasing as Θ_m increases in the range $\Theta_m \geq 30^o$. The drag and moment coefficients presented in Figures 6.22-6.23 show that they are oscillating at the same forcing frequency, f. Moreover, C_D is in phase with Y whereas C_M and Y are out of phase with each other. On the other hand, the moment coefficient amplitude is increasing with the increase of Θ_m. By investigating the drag coefficient, C_D, we note that the values of $C_{D,max}$ and $C_{D,amp}$ are increasing while $C_{D,min}$ is decreasing as Θ_m increases beyond 30^o.

Tables 6.3-6.9 summarize the effect of f/f_0 and Θ_m on the maximum lift coefficient

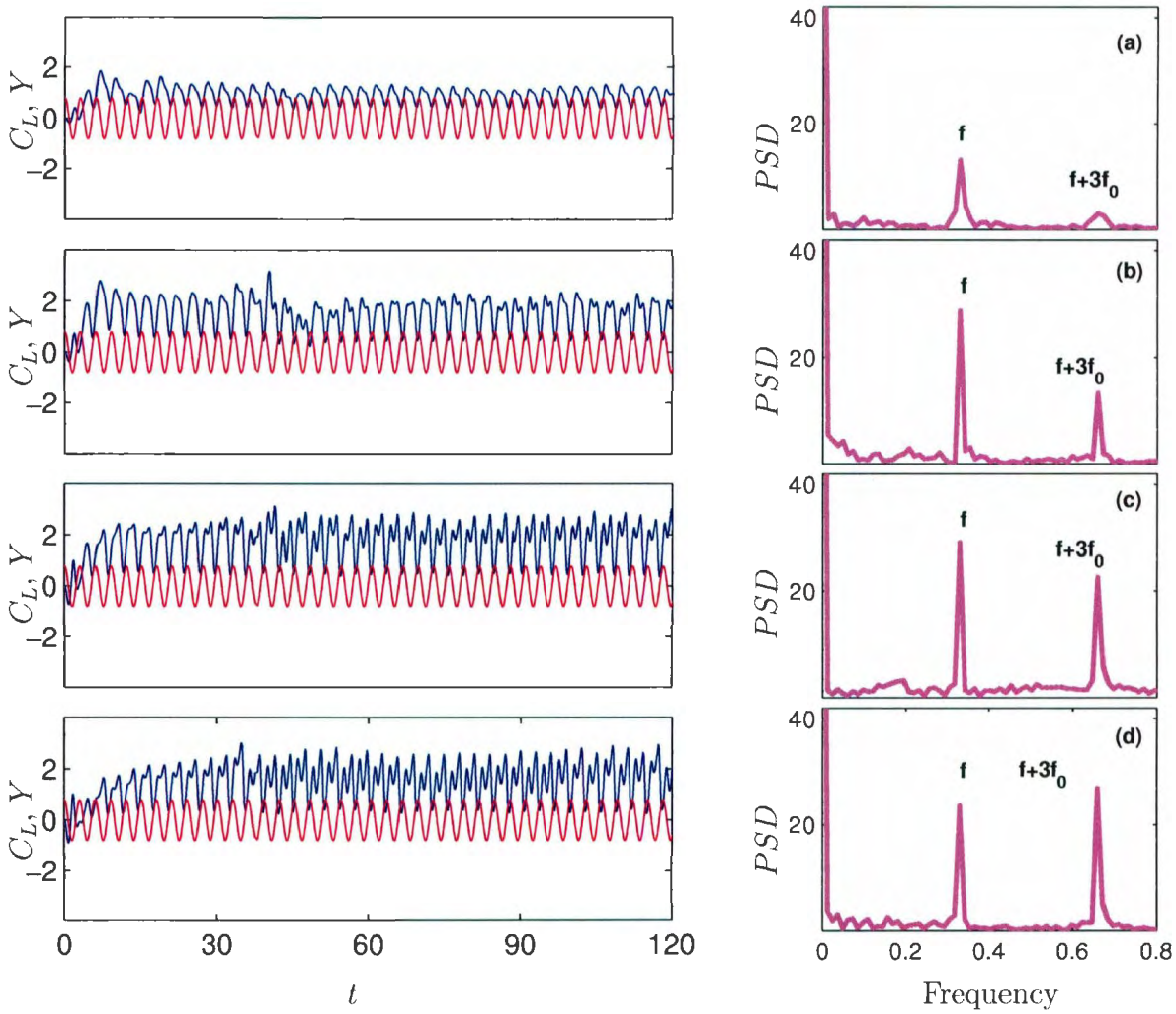

Figure 6.18: The time variation of C_L (—) with respect to cylinder displacement, Y (—) and the Fourier analysis of the lift coefficient PSD ( ) for the combined (2-DoF) in-line and rotational oscillation case ($\eta = 0^o$, $\Theta_m \neq 0$) when $R = 855$, $A = 0.26$ and $f/f_0 = 3.0$: (a) $\Theta_m = 15^o$; (b) $\Theta_m = 30^o$; (c) $\Theta_m = 60^o$ and (d) $\Theta_m = 75^o$.

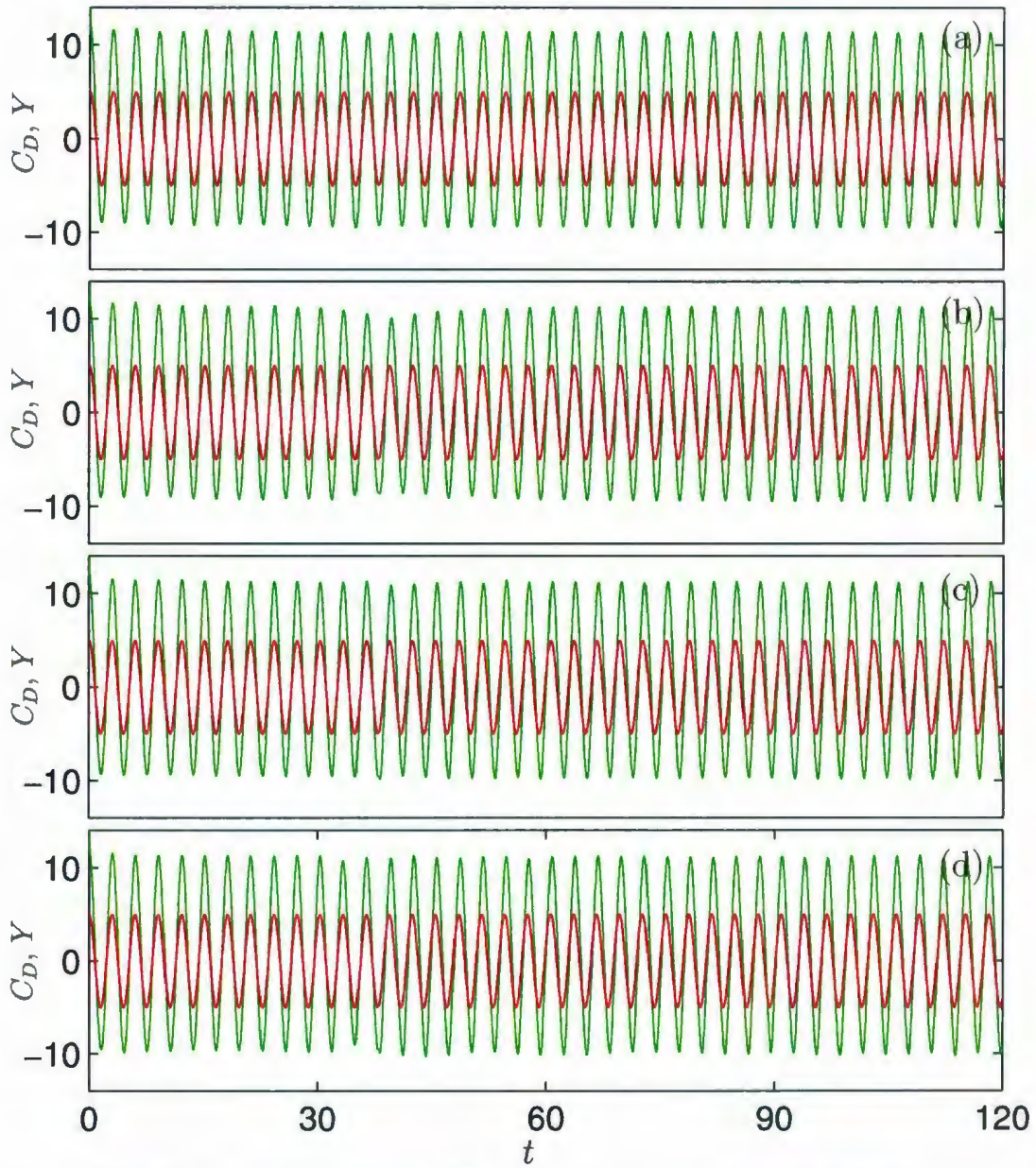

Figure 6.19: The time variation of C_D (—) with respect to cylinder displacement, Y (—) for the combined (2-DoF) in-line and rotational oscillation case ($\eta = 0^o$, $\Theta_m \neq 0$) when $R = 855$, $A = 0.26$ and $f/f_0 = 3.0$: (a) $\Theta_m = 15^o$; (b) $\Theta_m = 30^o$; (c) $\Theta_m = 60^o$ and (d) $\Theta_m = 75^o$.

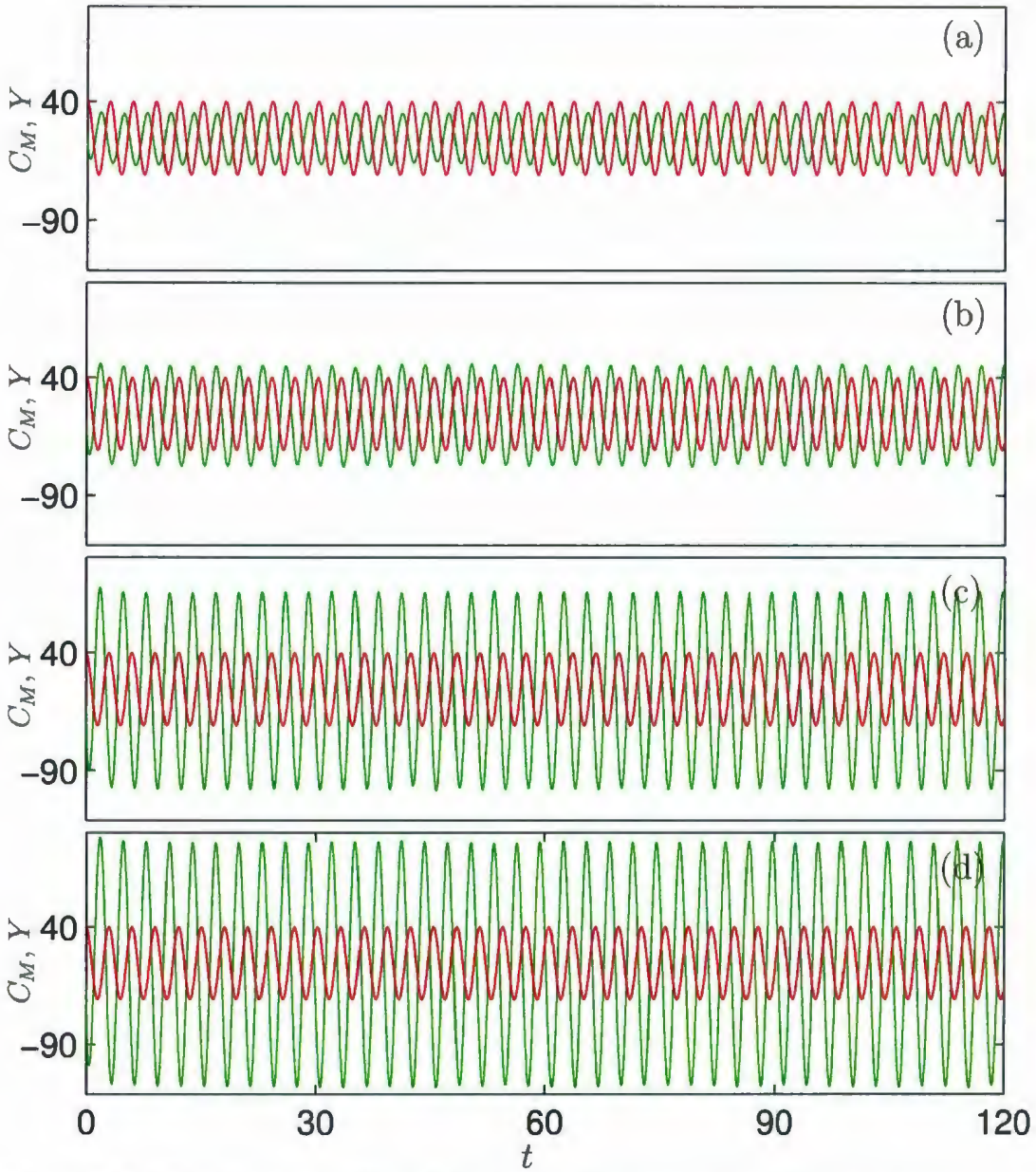

Figure 6.20: The time variation of C_M (—) with respect to cylinder displacement, Y (—) for the combined (2-DoF) in-line and rotational oscillation case ($\eta = 0^o$, $\Theta_m \neq 0$) when $R = 855$, $A = 0.26$ and $f/f_0 = 3.0$: (a) $\Theta_m = 15^o$; (b) $\Theta_m = 30^o$; (c) $\Theta_m = 60^o$ and (d) $\Theta_m = 75^o$.

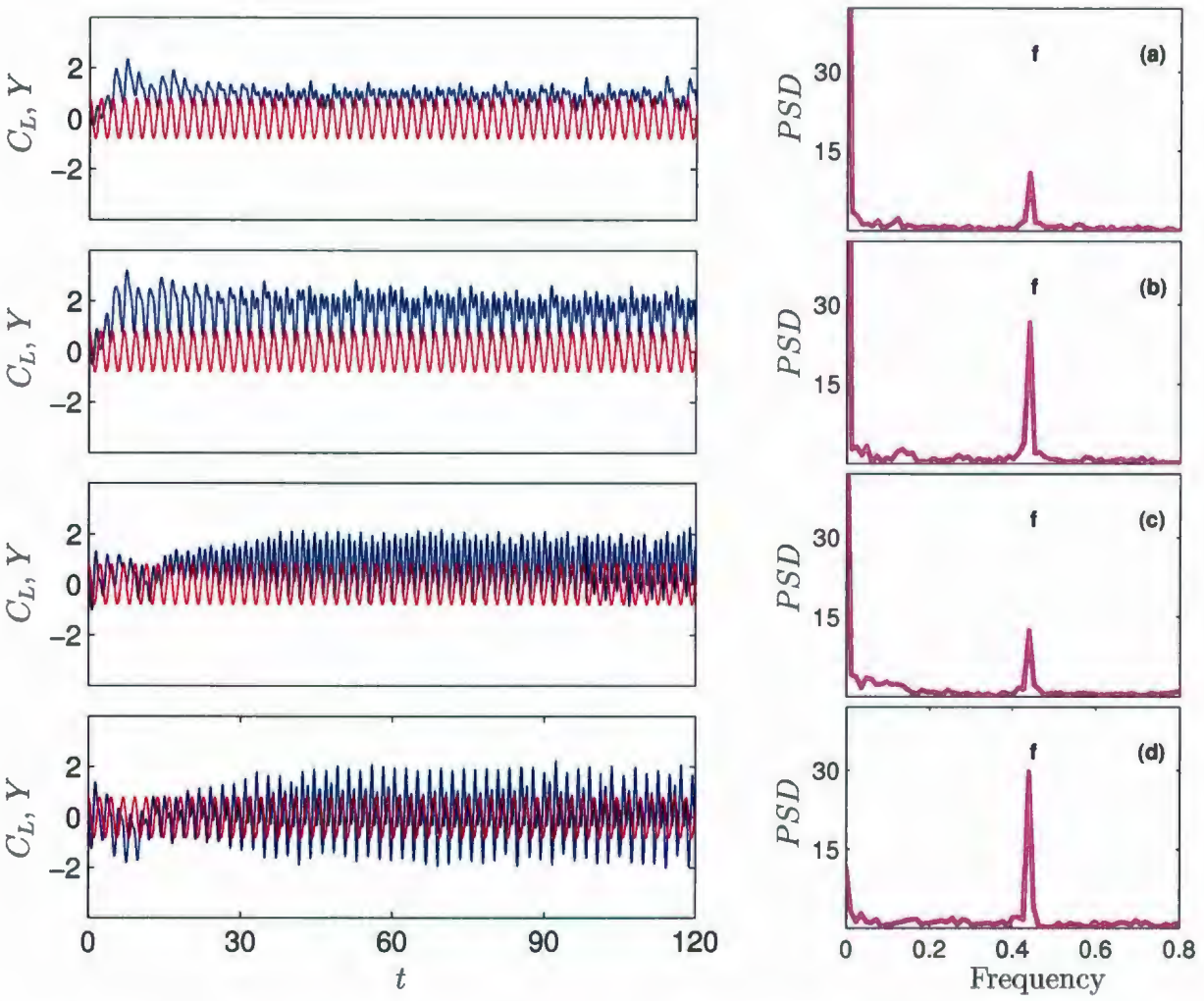

Figure 6.21: The time variation of C_L (—) with respect to cylinder displacement, Y (—) and the Fourier analysis of the lift coefficient PSD (-) for the combined (2-DoF) in-line and rotational oscillation case ($\eta = 0^o$, $\Theta_m \neq 0$) when $R = 855$, $A = 0.26$ and $f/f_0 = 4.0$: (a) $\Theta_m = 15^o$; (b) $\Theta_m = 30^o$; (c) $\Theta_m = 60^o$ and (d) $\Theta_m = 75^o$.

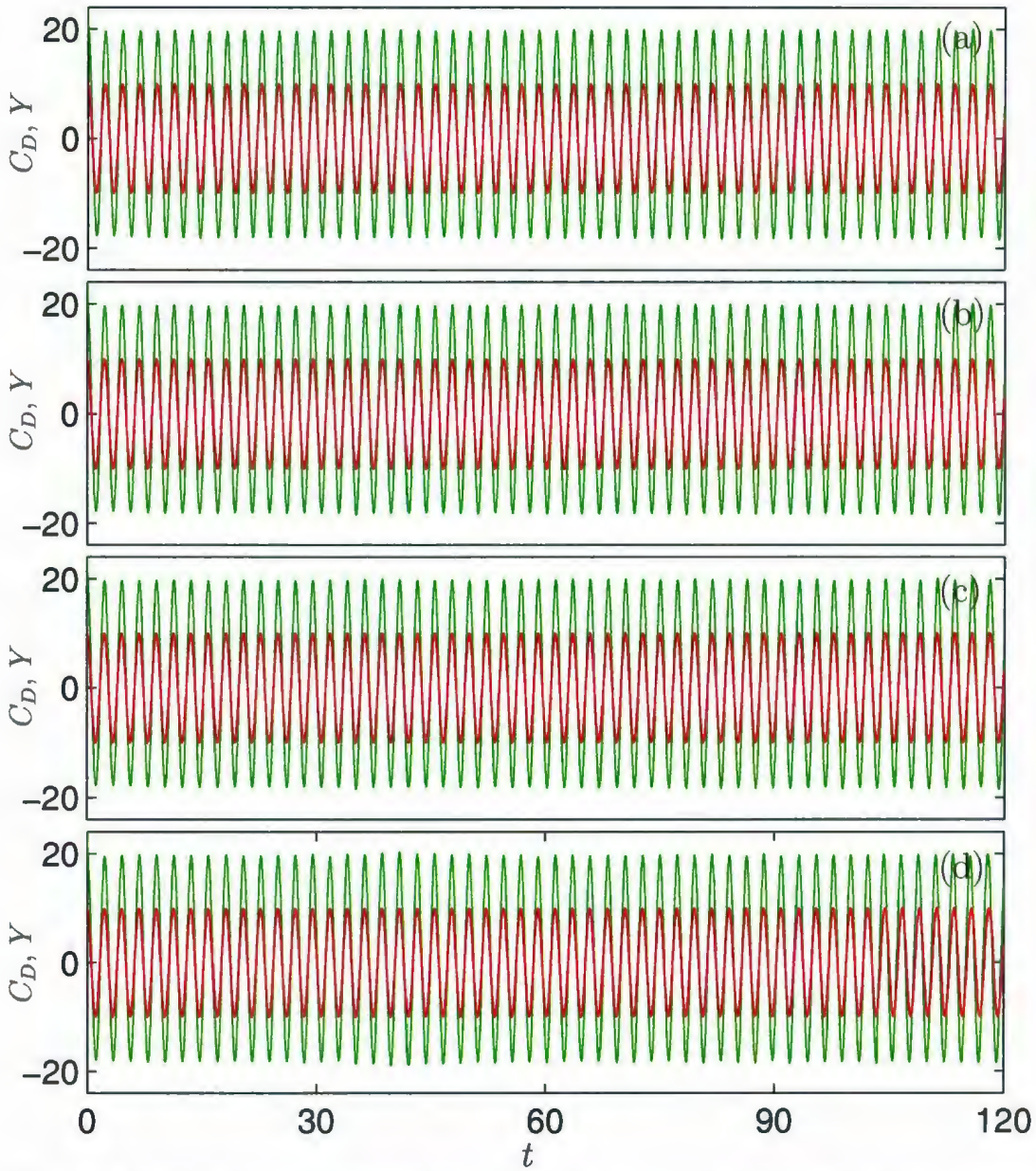

Figure 6.22: The time variation of C_D (—) with respect to cylinder displacement, Y (—) for the combined (2-DoF) in-line and rotational oscillation case ($\eta = 0^o$, $\Theta_m \neq 0$) when $R = 855$, $A = 0.26$ and $f/f_0 = 4.0$: (a) $\Theta_m = 15^o$; (b) $\Theta_m = 30^o$; (c) $\Theta_m = 60^o$ and (d) $\Theta_m = 75^o$.

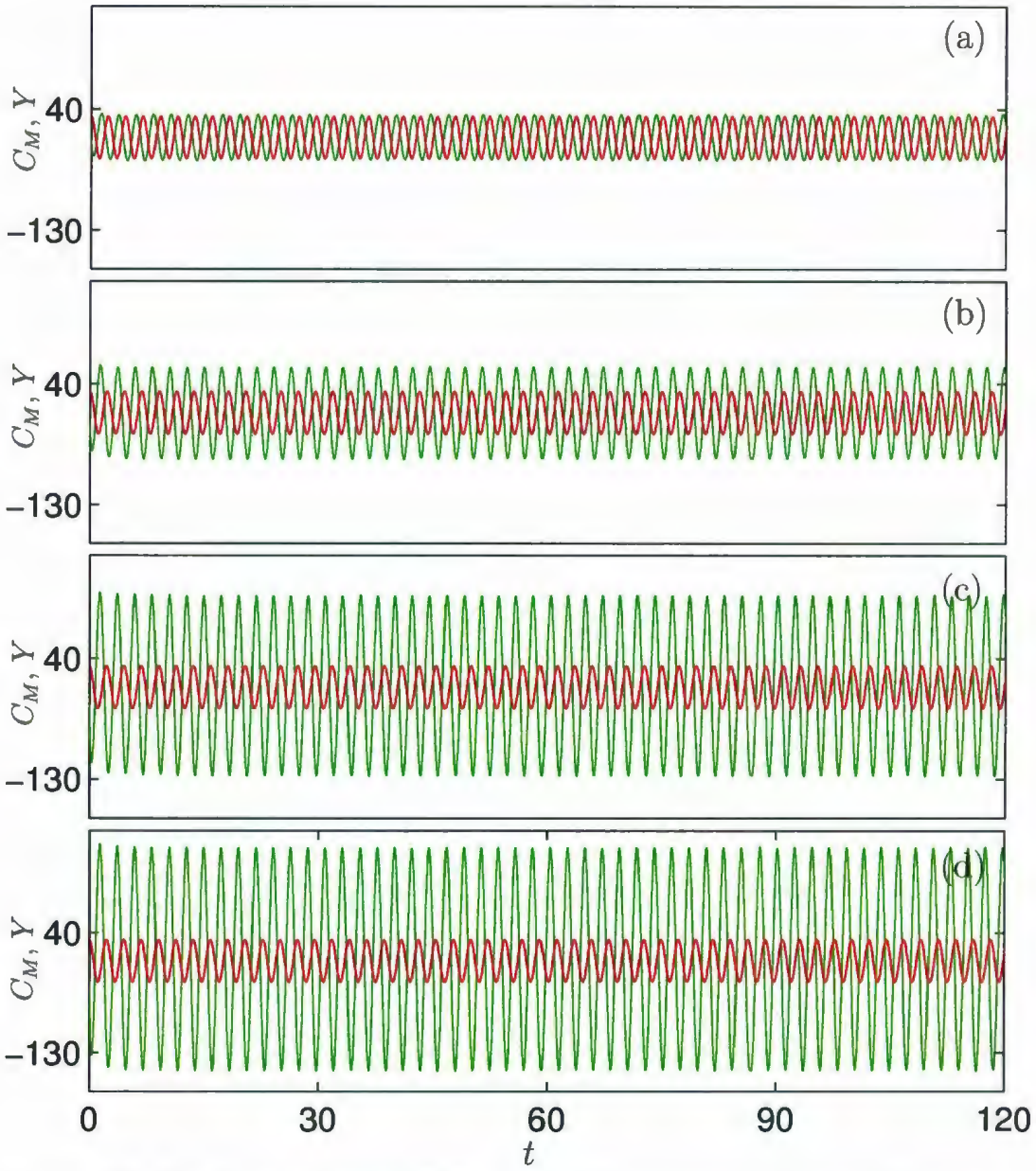

Figure 6.23: The time variation of C_M (—) with respect to cylinder displacement, Y (—) for the combined (2-DoF) in-line and rotational oscillation case ($\eta = 0^o$, $\Theta_m \neq 0$) when $R = 855$, $A = 0.26$ and $f/f_0 = 4.0$: (a) $\Theta_m = 15^o$; (b) $\Theta_m = 30^o$; (c) $\Theta_m = 60^o$ and (d) $\Theta_m = 75^o$.

$C_{L,max}$, the minimum lift coefficient $C_{L,min}$, the lift amplitude $C_{L,amp}$, the maximum drag coefficient $C_{D,max}$, the minimum drag coefficient $C_{D,min}$, the drag amplitude $C_{D,amp}$ and the time-averaged drag coefficient $\bar{C}_D$. These quantities are calculated over two periods of cylinder oscillation for $f/f_0 = 0.5$ and over four periods for $1 \leq f/f_0 \leq 4$. The value of $C_{L,min}$ decreases as Θ_m increases beyond 30^o and at $f/f_0 = 3$ and 4. The value of $C_{L,amp}$ tends to increase as Θ_m increases at high values of the frequencies, $f/f_0 \geq 2$. Increasing f/f_0, rather than increasing Θ_m, has a greater affect on the maximum value of the drag, $C_{D,max}$. On the other hand, increasing Θ_m beyond 30^o at high frequency causes a reduction in the value of $C_{D,min}$ and an increase in the value of $C_{D,amp}$. The value of $\bar{C}_D$ tends to decrease as Θ_m increases beyond 30^o.

f/f_0 \ Θ_m	15^o	30^o	60^o	75^o
0.5	1.2910	1.2144	1.6281	1.6049
1.0	1.3990	1.7470	1.4330	1.5101
2.0	2.3184	2.0227	2.1918	2.1565
3.0	1.3229	2.1158	2.8324	2.8338
4.0	1.2354	2.8470	2.0837	1.9279

Table 6.3: The effect of f/f_0 and Θ_m on $C_{L_{max}}$ for the combined (2-DoF) in-line and rotational oscillation case ($\eta = 0^o$, $\Theta_m \neq 0$) when $R = 855$, $A = 0.26$.

f/f_0 \ Θ_m	15^o	30^o	60^o	75^o
0.5	-1.6860	-1.8971	-2.1425	-2.4967
1.0	-1.3062	-1.5949	-0.9040	-0.8116
2.0	-1.0754	0.3670	0.4419	0.3182
3.0	0.4020	0.3856	0.3855	0.3534
4.0	0.4070	0.5239	-0.5461	-1.7535

Table 6.4: The effect of f/f_0 and Θ_m on $C_{L_{min}}$ for the combined (2-DoF) in-line and rotational oscillation case ($\eta = 0^o$, $\Theta_m \neq 0$) when $R = 855$, $A = 0.26$.

f/f_0 \ Θ_m	15^o	30^o	60^o	75^o
0.5	2.9769	3.1114	3.7706	4.1016
1.0	2.7052	3.3419	2.3371	2.3217
2.0	3.3937	1.6557	1.7500	1.8383
3.0	0.9209	1.7302	2.4469	2.4804
4.0	0.8285	2.3231	2.6297	3.6815

Table 6.5: The effect of f/f_0 and Θ_m on $C_{L_{amp}}$ for the combined (2-DoF) in-line and rotational oscillation case ($\eta = 0^o$, $\Theta_m \neq 0$) when $R = 855$, $A = 0.26$.

6.3 Combined (2-DoF) in-line and rotational oscillations versus an in-line-only and rotational-only (1-DoF) cylinder oscillations: wake modes

In this section a series of 1-DoF forced in-line or rotational cylinder oscillations in a steady uniform flow is analyzed under the same oscillation conditions of this chapter to better understand what differences result from the addition of these 1-DoF oscillatory motions. The simulations for the (1-DoF) oscillatory motion cases are carried

f/f_0 \ Θ_m	15^o	30^o	60^o	75^o
0.5	1.7838	1.7304	1.9715	2.0243
1.0	2.6253	2.8454	2.9363	2.7911
2.0	5.8234	5.6478	5.4424	5.3762
3.0	11.4084	11.2609	11.4113	11.1703
4.0	19.8505	19.7369	19.7762	19.9170

Table 6.6: The effect of f/f_0 and Θ_m on $C_{D_{max}}$ for the combined (2-DoF) in-line and rotational oscillation case ($\eta = 0^o$, $\Theta_m \neq 0$) when $R = 855$, $A = 0.26$.

f/f_0 \ Θ_m	15^o	30^o	60^o	75^o
0.5	0.9909	1.0282	0.7899	0.7123
1.0	-0.0893	0.0165	0.0985	0.1401
2.0	-2.9827	-3.1597	-3.4896	-3.9150
3.0	-9.4400	-9.3093	-9.8725	-10.1878
4.0	-17.9402	-17.7486	-18.2588	-18.5076

Table 6.7: The effect of f/f_0 and Θ_m on $C_{D,min}$ for the combined (2-DoF) in-line and rotational oscillation case ($\eta = 0^o$, $\Theta_m \neq 0$) when $R = 855$, $A = 0.26$.

out by using the same set of numerical parameters that used for the combined (2-DoF) in-line and rotational oscillation case. The results for in-line-only simulations are obtained by setting maximum angular displacement and angle of inclination to $\Theta_m = 0$, $\eta = 0^o$, respectively. The results for rotational-only simulations are obtained by setting recti-linear oscillatory velocity to $V(t) = 0$. A summary of the vortex shedding modes and their periods for the 1-DoF forced in-line oscillation are displayed in Table 6.10.

Overview of equivorticity lines for 1-DoF and 2-DoF motions under consideration is

f/f_0 \ Θ_m	15^o	30^o	60^o	75^o
0.5	0.7929	0.7022	1.1816	1.3119
1.0	2.7146	2.8288	2.8378	2.6510
2.0	8.8061	8.8075	8.9320	9.2912
3.0	20.8484	20.5702	21.2838	21.3581
4.0	37.7907	37.4855	38.0350	38.4246

Table 6.8: The effect of f/f_0 and Θ_m on $C_{D,amp}$ for the combined (2-DoF) in-line and rotational oscillation case ($\eta = 0^o$, $\Theta_m \neq 0$) when $R = 855$, $A = 0.26$.

f/f_0 \ Θ_m	15^o	30^o	60^o	75^o
0.5	1.4159	1.3908	1.4530	1.3722
1.0	1.2904	1.6538	1.4563	1.4408
2.0	1.6200	1.2313	0.9712	0.8827
3.0	0.6982	0.6106	0.4040	0.3609
4.0	1.7324	1.8364	1.4768	1.4286

Table 6.9: The effect of f/f_0 and Θ_m on $\bar{C}_D$ for the combined (2-DoF) in-line and rotational oscillation case ($\eta = 0^o$, $\Theta_m \neq 0$) when $R = 855$, $A = 0.26$.

presented, in Figures 6.24-6.28, at $f/f_0 = 0.5$, 1, 2, 3 and 4. In each figure, the top row of snapshots corresponds to the 1-DoF rotational oscillation case, taken at the maximum negative angular displacement, $-\Theta_m$, with amplitudes $\Theta_m = 15^o$, 30^o, 60^o and 75^o. In the middle row we display a series of the same snapshot for the 1-DoF in-line oscillation case taken at the maximum positive displacement, A. The bottom row exhibits snapshots of the combined (2-DoF) in-line and rotational oscillations at the instant corresponding to $-\Theta_m$. The instantaneous rotational and in-line speeds of the cylinder are zero at these positions.

f/f_0	Mode	Period
0.5	**2S** •	T/2
1	**2S** •	T
2	**S+P** •	2T
3	**2S** •	T
4	**2S** •	T

Table 6.10: The effects of f/f_0 and Θ_m on the vortex shedding modes and their periods for the in-line-only oscillations ($\eta = 0^o$, $\Theta_m = 0^o$) when $R = 855$, $A = 0.26$: • lock-on mode; • non-lock mode.

In fact, increasing the frequency ratio f/f_0 affects both the rotational and in-line oscillatory velocities at the same rates while increasing Θ_m affects only the rotational oscillation velocity. Essentially, the total speeds of the upper and lower parts of the cylinder at any instant are not equal which causes a different effect on the fluid in the bottom and top parts of the cylinder. For instance, in the case of counterclockwise rotation, the maximum relative velocities of the fluid compared with that of the wall are achieved at $t = T/4$ and given by $(2 - 2\pi f\Theta_m - 2\pi fA)$ and $(2 + 2\pi f\Theta_m - 2\pi fA)$ for $\theta = \mp 90^o$, respectively, however, in the clockwise rotation case, these relative velocities are achieved at the instant $t = 3T/4$ and equal to $(2 + 2\pi f\Theta_m + 2\pi fA)$ and $(2 - 2\pi f\Theta_m + 2\pi fA)$ for $\theta = \mp 90^o$. Thus, these differences cause breaking up the near-wake vorticity in both sides of the cylinder into different modes. In addition, the vortex shedding from both sides of the cylinder can be controlled by different frequencies according to the dominant oscillatory motion in the flow.

The vortex shedding modes and their periods at $f/f_0 = 0.5$ for the combined (2-DoF) in-line and rotational oscillation case are similar to that for the in-line-only and rotational-only (1-DoF) oscillations as shown in Tables 5.10 and 6.10. However,

Figure 6.24 shows that the (1-DoF) in-line-only oscillation is the dominant motion at $\Theta_m = 15^o$. However, the high competition between the in-line-only and rotational-only (1-DoF) oscillations is observed at $30^o \leq \Theta_m \leq 75^o$ which produces different near-wake structure than that for the combined (2-DoF) in-line and rotational oscillation. This may be attributed to the dominant uniform stream velocity.

At $f/f_0 = 1$, the vortex shedding modes and their periods for combined (2-DoF) in-line and rotational oscillation case are similar to that for the cases of (1-DoF) oscillatory motions as seen in Tables 5.10 and 6.10. However, comparing the bottom row with the middle and top rows of Figure 6.25 we conclude that the near-wake region for the combined (2-DoF) in-line and rotational oscillation is similar to that of the in-line-only (1-DoF) oscillation case for $\Theta_m = 15^o$ whereas for $30^o \leq \Theta_m \leq 75^o$ is similar to that for the rotational-only (1-DoF) oscillation case. A remarkable result observed at $\Theta_m = 15^o$ is that the synchronization of the vortex shedding to the cylinder motion reflects the effect of the rotational-only (1-DoF) oscillation. Typical equivorticity lines for 1-DoF and 2-DoF motions under consideration is presented at $f/f_0 = 1$, in Figure 6.29, over one period of cylinder oscillations, T. Thus, the rotational-only (1-DoF) oscillation play a crucial role in obtaining the vortex lock-on regimes. Further, the effect of the in-line-only (1-DoF) oscillation reduces the vortex formation length in the near-wake region.

The vortex shedding modes and their periods for combined (2-DoF) in-line and rotational oscillation case at $f/f_0 = 2$ show a competition between the two 1-DoF oscillatory motions (rotational and in-line) in different rates according to the values

of Θ_m. For $\Theta_m = 15^o$, the vortex shedding mode and their periods for the combined (2-DoF) in-line and rotational oscillation case is similar to that of the in-line-only (1-DoF) oscillation case as shown in Figure 6.26, Tables 5.10 and 6.10. Further, the effect of the rotational-only (1-DoF) oscillation is still evident especially in developing the weak vortex on the top of the cylinder. Typical equivorticity lines for 1-DoF and 2-DoF motions under consideration are presented, in Figure 6.30, at $f/f_0 = 2$ over two periods of cylinder oscillations, $2T$. For $\Theta_m = 30^o$, a high competition between the 1-DoF oscillatory motions is observed. For $\Theta_m = 60^o, 75^o$, the vortex shedding is characterized by a synchronized asymmetric **2S** mode, per T, which is similar to that observed for the rotational-only (1-DoF) oscillation case at the same values of Θ_m.

At $f/f_0 = 3.0$ and 4.0, the in-line-only (1-DoF) oscillation is more dominant on the vortex shedding modes and their periods for $\Theta_m = 15^o$. However, the rotational-only (1-DoF) oscillation play a crucial role in destroying the symmetry of the 1-DoF in-line oscillation as seen in Figure 6.31. For $\Theta_m \geq 3^o$, the effect of the 1-DoF oscillatory motion on the vortex shedding is not standard on both sides of the cylinder but still the effect of the rotational-only (1-DoF) oscillation is dominant on the vortex shedding structure in the near-wake region.

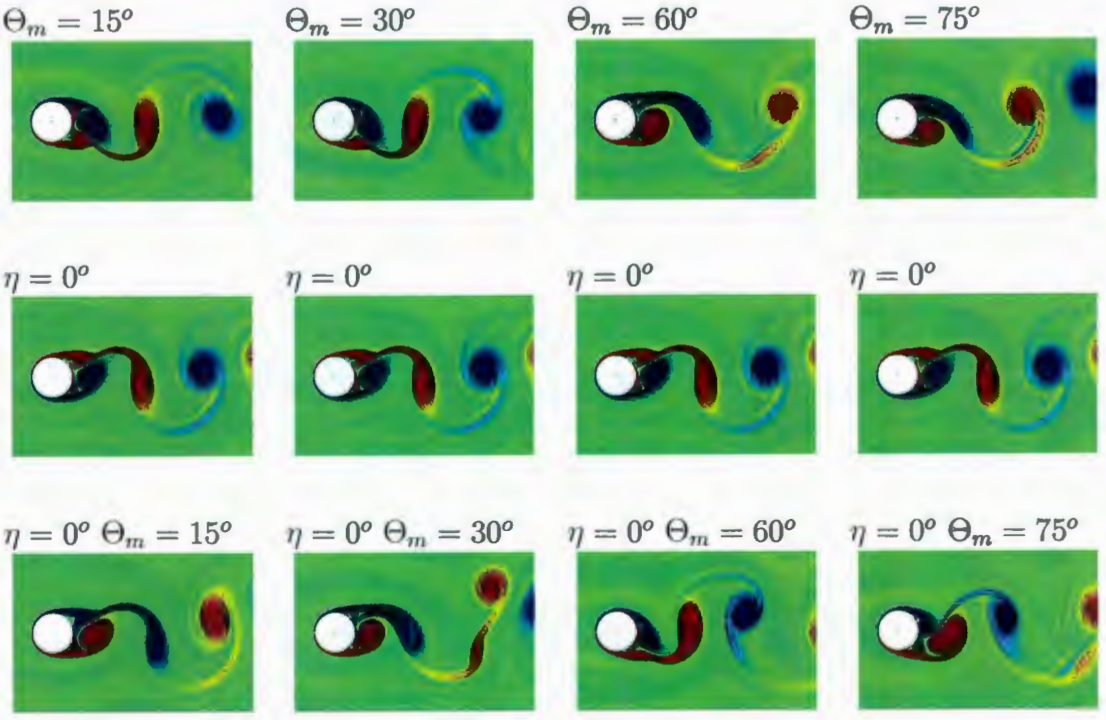

Figure 6.24: A rotational-only or in-line-only (1-DoF) cylinder oscillation (top or middle) versus combined (2-DoF) in-line and rotational oscillation (bottom): overview of near-wake structure for $R = 855$, $A = 0.26$ and $f/f_0 = 0.5$ when $\Theta_m = 15^o$, $\Theta_m = 30^o$, $\Theta_m = 60^o$ and $\Theta_m = 75^o$. All snapshots in the top and bottom rows are taken at the instant corresponding to maximum negative angular displacement, $-\Theta_m$, while the middle row corresponds to maximum positive cylinder displacement A.

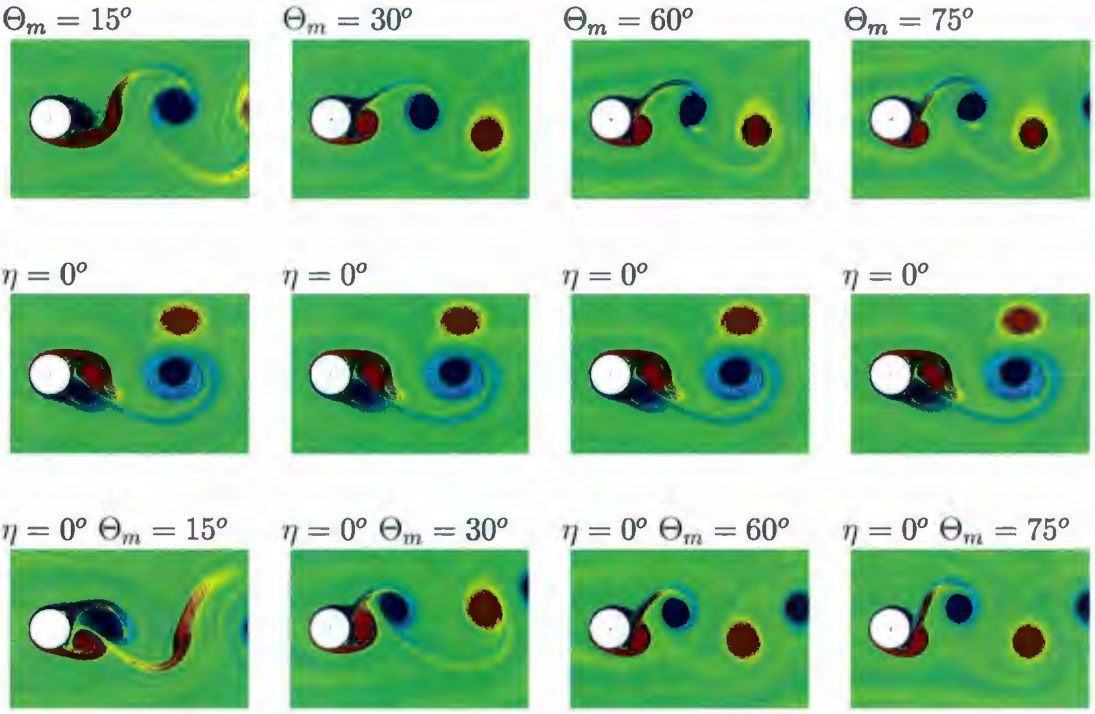

Figure 6.25: A rotational-only or in-line-only (1-DoF) cylinder oscillation (top or middle) versus combined (2-DoF) in-line and rotational oscillation (bottom): overview of near-wake structure for $R = 855$, $A = 0.26$ and $f/f_0 = 1$ when $\Theta_m = 15^o$, $\Theta_m = 30^o$, $\Theta_m = 60^o$ and $\Theta_m = 75^o$. All snapshots in the top and bottom rows are taken at the instant corresponding to maximum negative angular displacement, $-\Theta_m$, while the middle row corresponds to maximum positive cylinder displacement A.

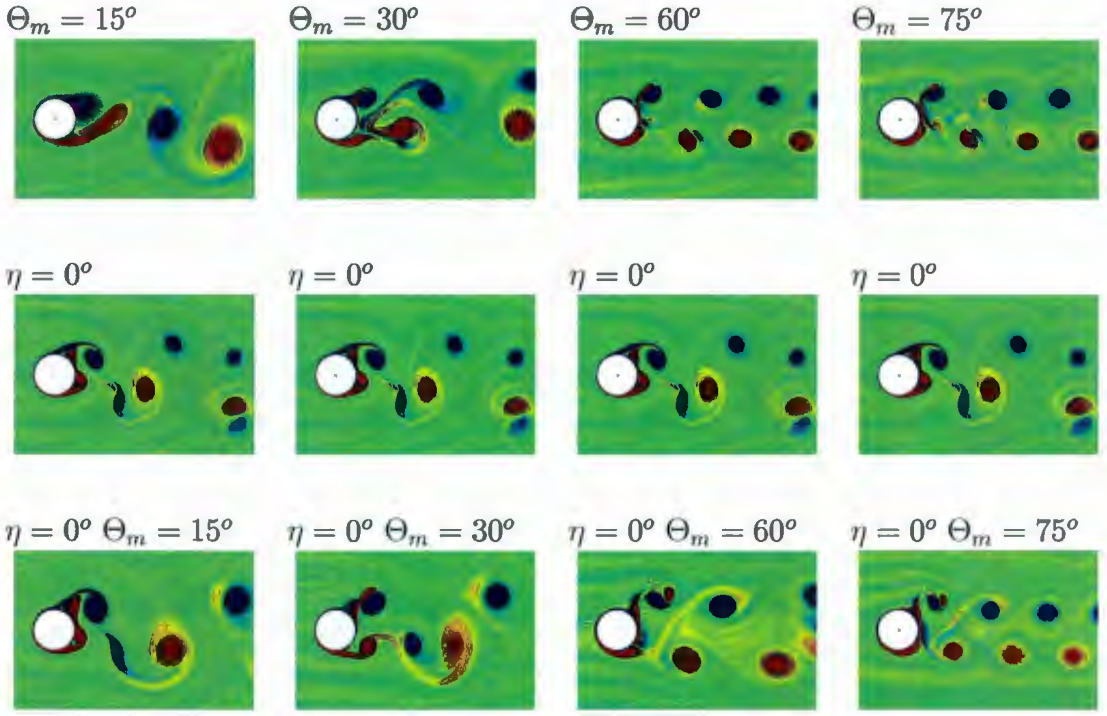

Figure 6.26: A rotational-only or in-line-only (1-DoF) cylinder oscillation (top or middle) versus combined (2-DoF) in-line and rotational oscillation (bottom): overview of near-wake structure for $R = 855$, $A = 0.26$ and $f/f_0 = 2$ when $\Theta_m = 15^o$, $\Theta_m = 30^o$, $\Theta_m = 60^o$ and $\Theta_m = 75^o$. All snapshots in the top and bottom rows are taken at the instant corresponding to maximum negative angular displacement, $-\Theta_m$, while the middle row corresponds to maximum positive cylinder displacement A.

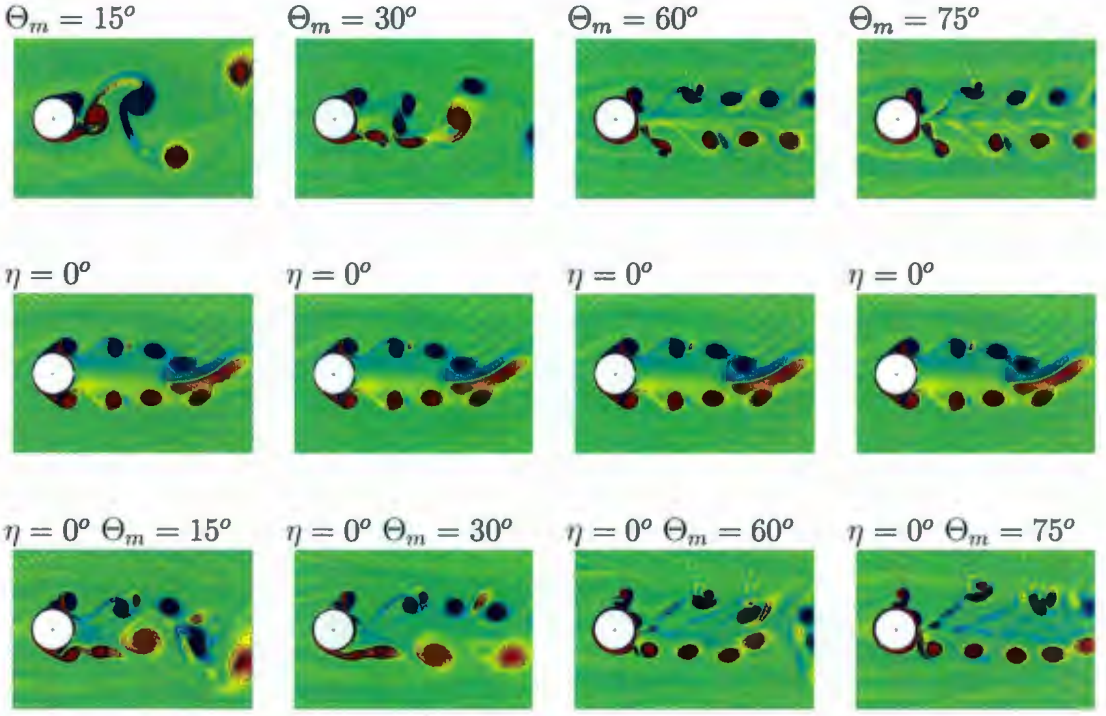

Figure 6.27: A rotational-only or in-line-only (1-DoF) cylinder oscillation (top or middle) versus combined (2-DoF) in-line and rotational oscillation (bottom): overview of near-wake structure for $R = 855$, $A = 0.26$ and $f/f_0 = 3$ when $\Theta_m = 15^o$, $\Theta_m = 30^o$, $\Theta_m = 60^o$ and $\Theta_m = 75^o$. All snapshots in the top and bottom rows are taken at the instant corresponding to maximum negative angular displacement, $-\Theta_m$, while the middle row corresponds to maximum positive cylinder displacement A.

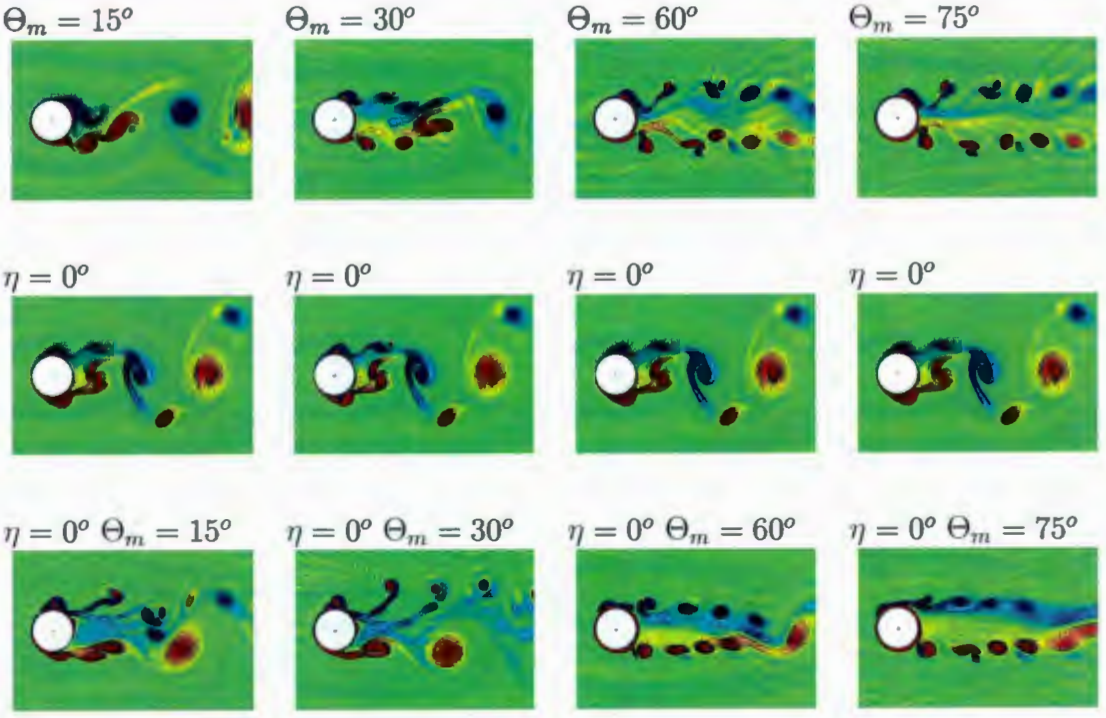

Figure 6.28: A rotational-only or in-line-only (1-DoF) cylinder oscillation (top or middle) versus combined (2-DoF) in-line and rotational oscillation (bottom): overview of near-wake structure for $R = 855$, $A = 0.26$ and $f/f_0 = 4$ when $\Theta_m = 15^o$, $\Theta_m = 30^o$, $\Theta_m = 60^o$ and $\Theta_m = 75^o$. All snapshots in the top and bottom rows are taken at the instant corresponding to maximum negative angular displacement, $-\Theta_m$, while the middle row corresponds to maximum positive cylinder displacement A.

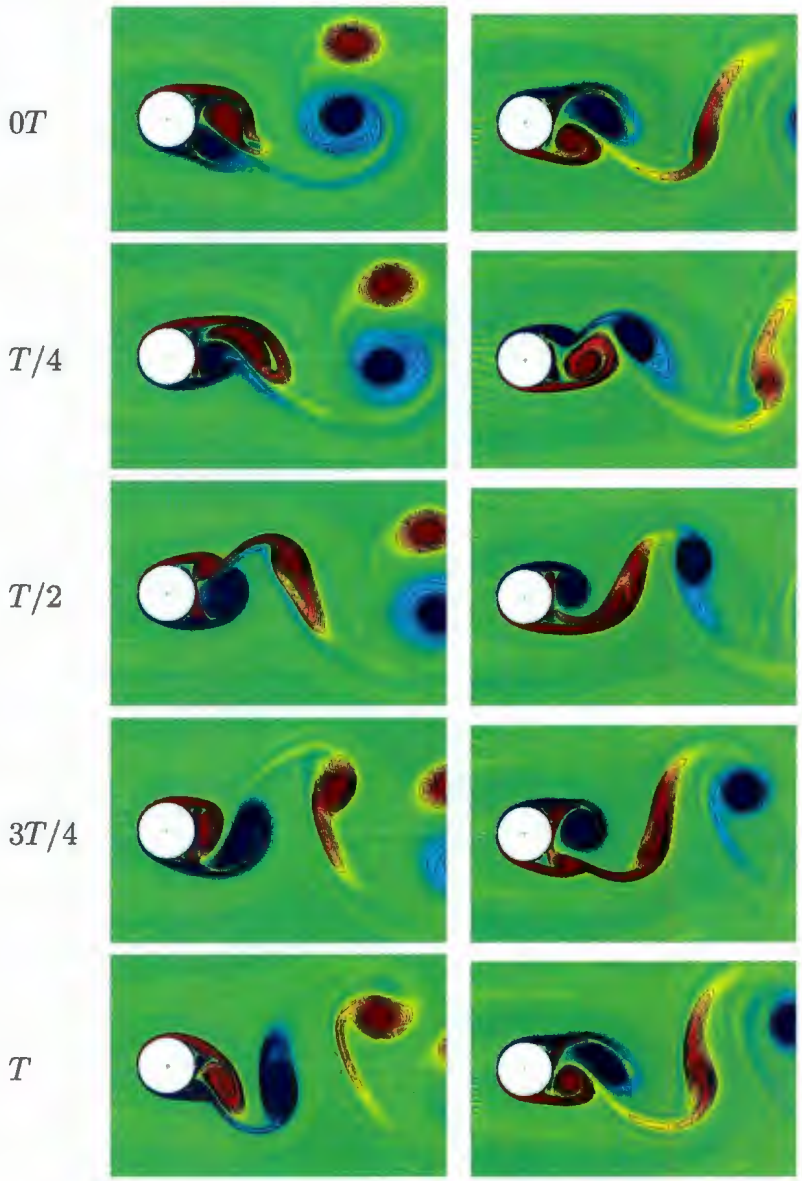

Figure 6.29: Equivorticity lines over one period of oscillation, T, for in-line-only (1-DoF) oscillation case (left); combined in-line and rotational (2-DoF) oscillation case (right) when $R = 855$, $A = 0.26$: $\Theta_m = 15^o$ and $f/f_0 = 1$ ($T = 9.09$, $81.82 \leq t \leq 90.91$).

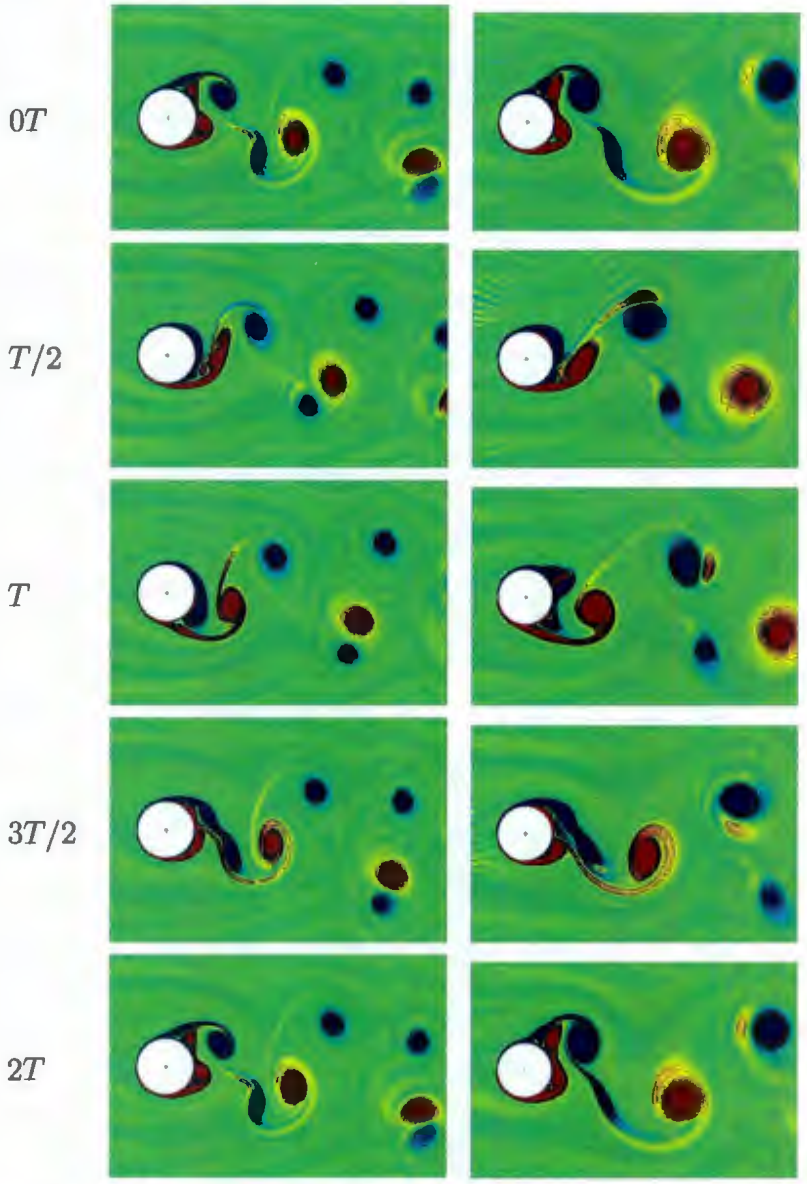

Figure 6.30: Equivorticity lines over two periods of oscillation, $2T$, for in-line-only (1-DoF) oscillation case (left); combined in-line and rotational (2-DoF) oscillation case (right) when $R = 855$, $A = 0.26$: $\Theta_m = 15^o$ and $f/f_0 = 2$ ($T = 4.55$, $90.9 \leq t \leq 95.45$).

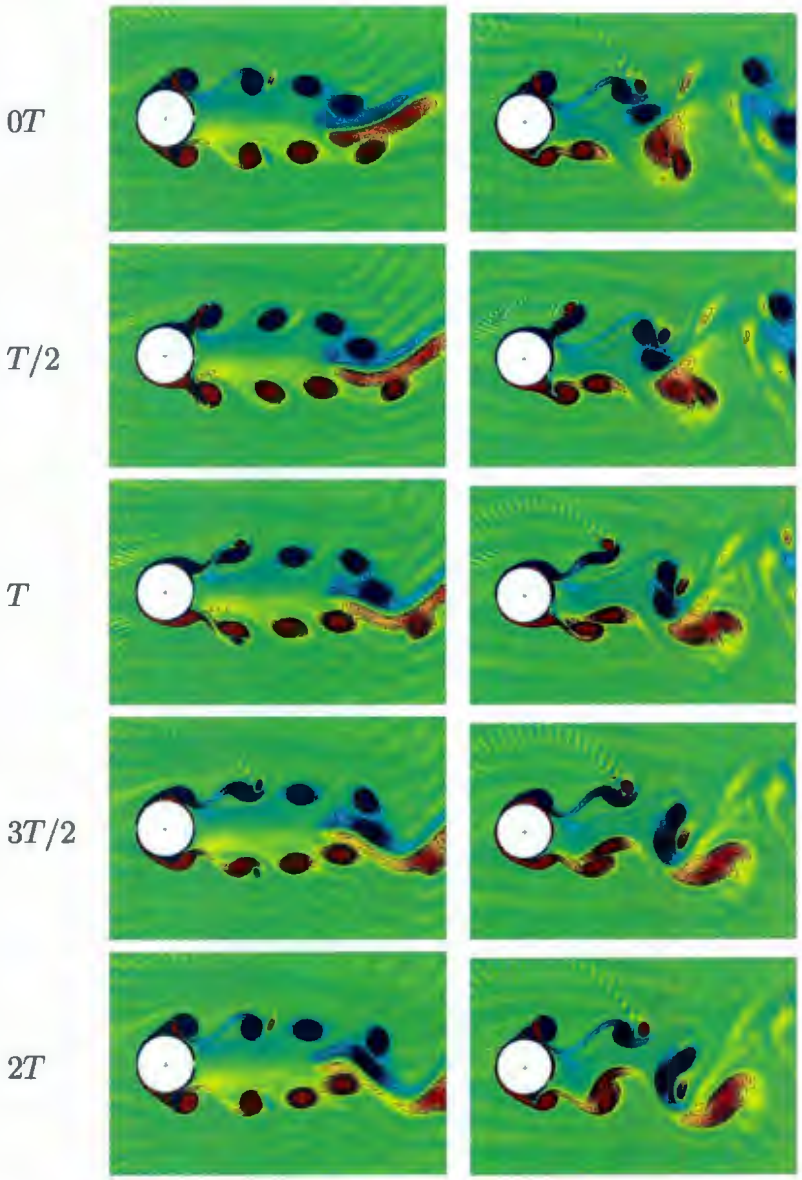

Figure 6.31: Equivorticity lines over three periods of oscillation, $3T$, for in-line-only (1-DoF) oscillation case (left); combined in-line and rotational (2-DoF) oscillation case (right) when $R = 855$, $A = 0.26$: $\Theta_m = 15^o$ and $f/f_0 = 3$ ($T = 3.03$, $90.9 \leq t \leq 93.94$).

Chapter 7

Summary and Conclusions

The present thesis deals with analysis and numerical simulation of a new class of wake flows created in a steady uniform flow by combining translational (in-line or transverse) and rotational oscillation of a circular cylinder. The flow is incompressible and two-dimensional, and recti-linear and rotational oscillations are harmonic. Specifically, the dimensionless recti-linear and rotational oscillatory velocities have the form $V(t) = -2\pi f A \sin(2\pi f t)$ and $\Omega(t) = 2\pi f_\theta \Theta_m \sin(2\pi f_\theta t)$, respectively. Here t is the time; A and θ_m are the amplitudes of two simple harmonic motions; f and f_θ are the forced frequencies of two oscillatory motions. It is further supposed that the instantaneous translation and rotation start at the same moment and the development of the flow is studied in a coordinate frame which moves with the cylinder but does not rotate. For the motion we have described, analysis is carried out for combined phase-locked translation and rotation with a single frequency, i.e., $f = f_\theta$. The motion is assumed to be laminar and governed by the unsteady Navier-Stokes equations and the mass conservation equation. The associated conditions are no-slip and impermeability conditions on the cylinder surface and free stream conditions far

away from the surface.

The method of analysis adopted here is based on the use of truncated Fourier representations for the stream function and vorticity in the angular polar coordinate. Two types of solutions are obtained. A series expansion for small times is developed. The Navier-Stokes equations are also integrated for large values of the time using an implicit time-marching scheme. The vorticity is determined using conditions of an integral character deduced from the no-slip and impermeability conditions on the cylinder surface and free stream conditions at large distances, together with the mass conservation equation. The integral conditions are used both in obtaining the analytical solutions of the governing equations using Fourier, or spectral, analysis and implementing finite difference method in the two-dimensional numerical solution procedure. This eliminates the use of local finite-difference approximations to link discretized values of the stream function and vorticity on and near boundaries in the solution domain. It is shown that the correct satisfaction of integral conditions is the required condition to ensure that the pressure in the fluid is periodic. Thus, this is considered as a very important part of the solution procedure since they ensure both the free stream is approached far from the cylinder and satisfaction of the physically essential results for the existence of the flow. Special care is taken to account for the impulsive start of the motion. This is done by implementing the special starting procedure using similarity coordinates later replaced by physical coordinates. The analytical and numerical techniques employed are a direct extension of those which were used by Collins (1971), Collins and Dennis (1973a) (analytical); Collins and

Dennis (1973b) and Badr and Dennis (1985)(numerical). In the present thesis numerical solutions of the Navier-Stokes equations are obtained for large values of the time rather than moderate values of the time obtained by various researchers using the same method for solving problems of uniform flow past a stationary cylinder; a steadily rotating cylinder; a cylinder undergoing (1-DoF) forced (recti-linear or rotational) oscillations.

The numerical scheme is verified by applying it to the special cases of uniform flow past (i) a stationary cylinder (no forced oscillations) at $R = 100,\ 106,\ 10^3$; (ii) a steadily rotating cylinder (no forced oscillations) for the constant rotating rates $\Omega = 1,\ 3$ at $R = 500,\ 10^3$; (iii) a cylinder undergoing 1-DoF forced recti-linear oscillations, at angles of 0^0, 60^0, 90^0 with respect to the uniform free-stream ($R = 855$ and $A = 0.26$: $0.5 \leq f/f_0 \leq 4$). Furthermore, the simulations of the start-up flow for the case of combined (2-DoF) forced recti-linear and rotational cylinder oscillations at a Reynolds number of $R = 855$ are consistent with the results of the analytical solution. The surface pressure distribution is also calculated for the same case of 2-DoF motion to verify the correct implementation of the surface pressure periodicity in the numerical scheme for large values of the time. Exceptionally good comparisons with previous experimental and numerical results are obtained, not only in the detailed formation of the wake but also development with time of velocity profiles and various other properties of the above mentioned flows. In fact, the general evidence of the comparisons is that the previous (experimental and numerical) and present (numerical) treatments the problem in the three special cases mentioned earlier are almost identical and give the same physical development of the flow in every respect.

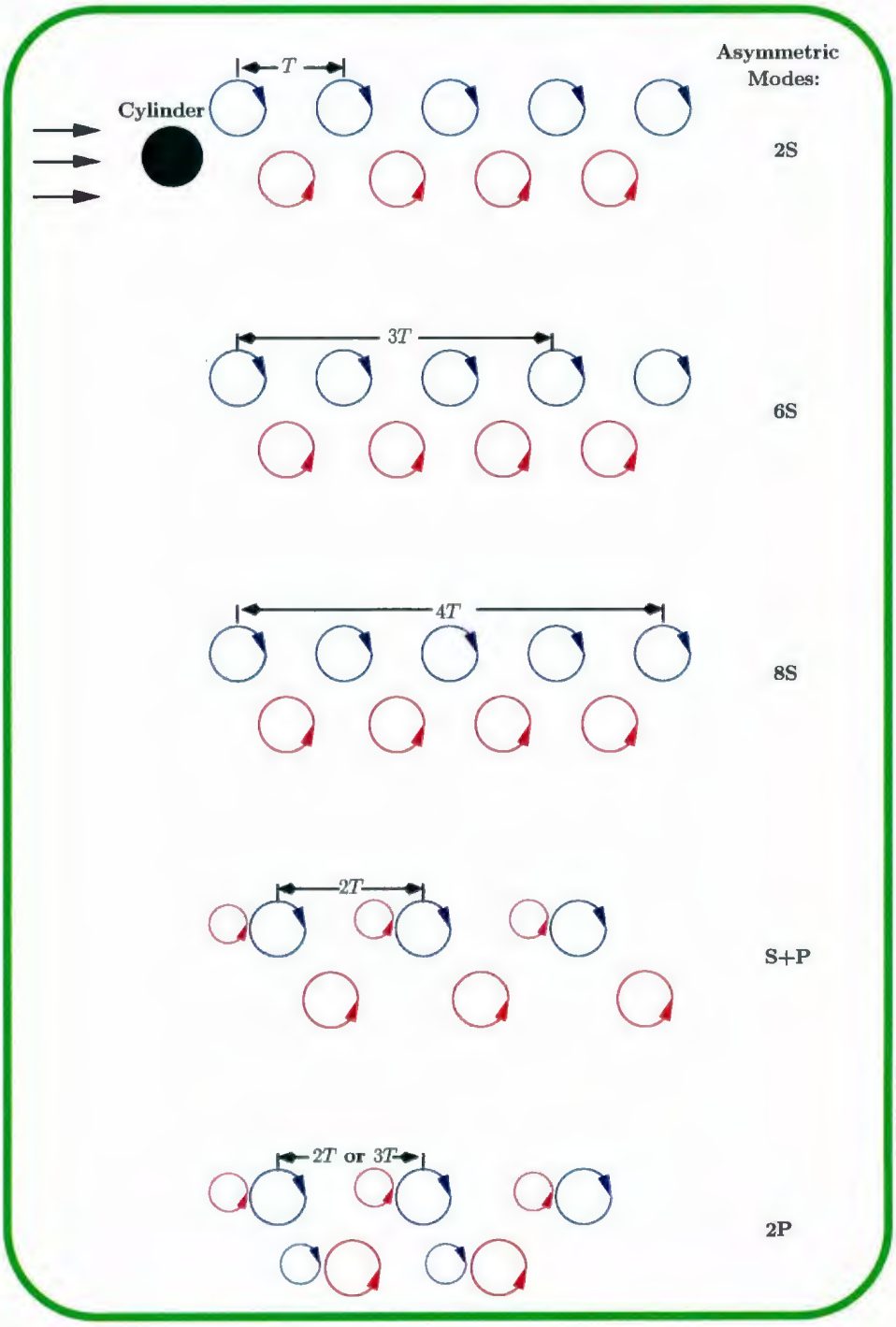

Figure 7.1: Representation of basic modes of vortex formation from cylinder undergoing combined (2-DoF) recti-linear and rotational oscillation.

In the present thesis two types of 2-DoF forced oscillation of a circular cylinder simulations are performed for the first time. In the first, the cylinder is forced to move by combined transverse (cross-stream) and rotational oscillation ($\eta = 90^o$, $\Theta_m \neq 0$). In the second, the cylinder is forced to move by combined in-line (streamwise) and rotational oscillation ($\eta = 0^o$, $\Theta_m \neq 0$). Calculations are carried out for fixed values of Reynolds number, $R = 855$, and amplitude of translational (in-line or transverse) oscillatory motion, $A = 0.26$, respectively, in the cases $f/f_0 = 0.5$, 1, 2, 3, 4 and $\Theta_m = 15^o$, 30^o, 60^o, 75^o. The effects of f/f_0 and Θ_m on the vortex formation modes as well as the fluid forces acting on the cylinder are examined. Results show that five basic asymmetric modes of vortex formation synchronized with the body motions in the near-wake region. Four of these asymmetric modes show period doubling; doubling or tripling; tripling and quadrupling relative to the classical Kármán mode. These modes are schematically portrayed in Figure 7.1. The asymmetric **2S** and **S+P** modes occur for both types of 2-DoF forced oscillation; the asymmetric **6S**, **8S** and **2P** modes occur only for combined (2-DoF) transverse and rotational oscillation case:

Combined (2-DoF) transverse and rotational cylinder oscillations: Overview of wake modes and fluid forces

When the forcing frequency is $f/f_0 = 1$, the classical asymmetric **2S** mode over one oscillation cycle is the dominant mode for all values of Θ_m since the maximum oscillatory speeds of both motions are less than the uniform flow speed. In the range of the frequency ratios when $f/f_0 \geq 2$, the vortex shedding becomes more complicated due

to the strong interaction between the cylinder motion and the shed vortices. Breaking up of the near-wake vortices and coalescence of these vortices occur in the region very close to the cylinder surface. This coalescence phenomenon produces an interesting repeatable patterns in the near-wake region. It seems that the translational oscillation plays an important role in activating the periodic coalesce phenomenon at high values of the frequency ratio. The asymmetric **S+P** mode occur over two oscillation cycles only for $f/f_0 = 2 : \Theta_m = 15^o$. The asymmetric **2P** mode occurs over two and three cycles of oscillation when $f/f_0 = 2 : \Theta_m = 30^o$ and $f/f_0 = 3 : \Theta_m = 15^o$, respectively. The asymmetric **6S** and **8S** modes occur over three and four oscillation cycles for $f/f_0 = 3 : \Theta_m = 30^o$; $f/f_0 = 4 : \Theta_m = 60^o$ and $f/f_0 = 4 : \Theta_m = 15^o, 30^o$, respectively. Period doubling; tripling; quadrupling relative to the classical Kármán mode occur in the cases $f/f_0 = 2 : \Theta_m = 15^o, 30^o$; $f/f_0 = 3 : \Theta_m = 30^o$ and $f/f_0 = 4 : \Theta_m = 60^o$; $f/f_0 = 4 : \Theta_m = 15^o, 30^o$, respectively. Thus, the vortex shedding period is increasing proportionally with f/f_0. The effect of increasing the oscillation frequency ratio seems to magnify the amplitude of the lift coefficient which is consistent with the results observed for the transverse-only oscillations by the previous researchers and in the present study. On the other hand, the time-averaged drag coefficient, shows its maximum value at $f/f_0 = 1$ for all values of the rotational oscillation amplitude. In all the cases considered C_L and C_M curves oscillate with the frequency of cylinder oscillation whereas a switch over in the nature of the fluctuations of the drag coefficient is observed with the increase of the oscillation frequency ratio. In addition, C_L is in phase with the cylinder motion whereas both C_D and C_M are out of phase with the cylinder motion for all values of f/f_0 and Θ_m.

It seems that the effect of increasing the rotational oscillation amplitude is to reduce the vortex shedding period. The location of the developing vortices increases vertically on the cylinder surface as Θ_m increases. Thus, the angle of separation is increasing as Θ_m increases which is consistent with the results observed for rotational-only oscillations case. The amplitude of the lift coefficient is decreasing as Θ_m increases in the range of $f/f_0 \geq 1$. Furthermore, as a result of increasing Θ_m, $\bar{C}_D$ is decreasing at all values of f/f_0.

The vortex lock-on phenomenon is observed for all values of $f/f_0 \geq 1$, when $15^o \leq \Theta_m \leq 75^o$. An interesting result related to the lock-on phenomenon is observed at $f/f_0 = 4$ and $\Theta_m = 15^o$ in which the vortex shedding in both transverse-only and rotational-only (1-DoF) oscillation cases is not lock-on while it produces vortex lock-on for the case of combined (2-DoF) transverse and rotational oscillations. This leads to the fact that when the maximum oscillatory speeds of both motions is close to each other it is difficult to track the dominant motion in the flow unlike when the difference between these maximum speeds is relatively high.

Finally, when the maximum oscillatory speeds of both motions are close to each other the rotational oscillation has more significant effect than the transverse oscillation for all values of f/f_0 except $f/f_0 = 0.5$.

Combined (2-DoF) in-line and rotational cylinder oscillations: Overview of wake modes and fluid forces

The classical asymmetric **2S** mode over one period of oscillation cycle is the dominant mode for all values of f/f_0 and Θ_m except $f/f_0 = 2 : \Theta_m = 15^o, 30^o$. This vortex shedding mode is consistent with the in-line-only (1-DoF) oscillation case at $f/f_0 = 2$, 3 and has three different occurrences than that of the ones observed previously. In the first one, we observe a small counter-rotating vortex accompany the large shed vortex from the upper side of the cylinder until a limited distance in the downstream. In the second occurrence this counter-rotating vortex accompany the shed vortex from the bottom of the cylinder. Finally, in the third occurrence each shed vortex is accompanied by counter-rotating vortex. An interesting result observed at $f/f_0 = 4$ and $\Theta_m = 60^o$ is that asymmetrical **2S** vortex formation mode decays a symmetrical mode as vortices move downstream. Moreover, the existence of the asymmetric **S+P** mode which is observed at $f/f_0 = 2$ when $\Theta_m \leq 30^o$ is consistent with the results of the previous experimental and numerical studies for the case of in-line-only (1-DoF) oscillation at the same value of f/f_0. It seems that the effect of increasing the oscillation frequency ratio magnifies the amplitude of the drag coefficient which is also consistent with the results observed for the in-line-only oscillations by the previous researchers and the in present study.

At $\Theta_m = 15^o$ when the maximum oscillatory speeds of both motions are close to each other, the in-line-only (1-DoF) oscillation has a significant effect on the vortex shedding modes and their periods. An interesting result observed at $f/f_0 = 1$ when $\Theta_m = 15^o$: vortex lock-on is controlled by the rotational oscillation whereas the near-wake structure is similar to that of the in-line-only oscillations. It is also noted that the vortex shedding period is affected more by the in-line oscillation rather than the

rotational oscillation especially in the range $\Theta_m \leq 30^o$. The lock-on phenomenon is reported at all values of $f/f_0 \geq 1$ when $15^o \leq \Theta_m \leq 75^o$. An interesting repeatable phenomena is observed at $f/f_0 \geq 3$ when $\Theta_m \leq 30^o$: the shed vortices from the bottom of the cylinder are coalesce to form one large vortex as vortices move downstream.

In all the cases considered C_D, C_L and C_M curves oscillate with the frequency of cylinder oscillation. Both C_D and C_L are in phase with the cylinder motion whereas C_M is out of phase with the cylinder motion for all values of f/f_0 and Θ_m.

Appendix A

Appendix for Chapter 2

A.1 Determination of $\omega(z,\theta,0)$ and $\Psi(z,\theta,0)$

The initial solutions for ω and Ψ are determined by solving equations (2.2.19) and (2.2.20) subject to (2.2.21)-(2.2.24) at $t = 0$. The solution for $\omega(z,\theta,0)$ can be represented by the Fourier expansion as

$$\omega(z,\theta,0) = \frac{1}{2}G_{0,0}(z) + \sum_{j=1}^{\infty}\left[G_{0,j}(z)\cos(j\theta) + g_{0,j}(z)\sin(j\theta)\right]. \tag{A.1.1}$$

The general solution for $\omega(z,\theta,0)$ has been obtained by using the method of reduction of order after substituting (A.1.1) into (2.2.19); its expression is given by

$$\omega(z,\theta,0) = \sum_{j=0}^{\infty}\left[(C_j\, e^{-z^2} + c_j\, e^{-z^2}\,\mathrm{erfi}(z))\cos(j\theta) + (D_j\, e^{-z^2} + d_j\, e^{-z^2}\,\mathrm{erfi}(z))\sin(j\theta)\right] \tag{A.1.2}$$

where $\mathrm{erfi}(z)$ is the imaginary error function defined by

$$\mathrm{erfi}(z) = \frac{2}{\sqrt{\pi}}\int_0^z e^{s^2}\,ds,$$

and C_j, D_j, c_j and d_j are constants.

The integral condition (2.2.24) is used to show that C_j, D_j, c_j and d_j are identically zeros for all $j > 1$. The approximation

$$e^{-z^2}\,\mathrm{erfi}(z) \;\sim\; \frac{\sqrt{\pi}}{4\,z}$$

can be used to conclude that

$$\int_0^{\infty} c_1\, e^{-z^2}\,\mathrm{erfi}(z)\,dz \;\sim\; \int_0^{\infty} c_1\,\frac{\sqrt{\pi}}{4\,z}\,dz \;=\; c_1\,\frac{\sqrt{\pi}}{4}\,\ln(z)\Big|_{z=0}^{z=\infty}. \tag{A.1.3}$$

Since $\ln(z)$ is an unbounded function, (A.1.3) gives that c_1 should be zero. Following the same procedure we also conclude that d_1 is zero. Finally the constants C_0, C_1 and D_1 can easily be determined from the integral conditions (3.3.9), these constants are

$$C_0 = \frac{2}{\sqrt{\pi}}\,\alpha_0$$

$$C_1 = -\frac{4}{\sqrt{\pi}}\,\sigma_0 \sin(\eta)$$

$$D_1 = \frac{4}{\sqrt{\pi}}\,(\sigma_0\cos(\eta) + 1).$$

where $\alpha_0 = \Omega(0)$, $\sigma_0 = V(0)$. Consequently $\omega(z,\theta,0)$ is given by

$$\omega(z,\theta,0) \;=\; \frac{2\,e^{-z^2}}{\sqrt{\pi}}\,\left(\Omega(0) - 2\,V(0)\sin(\eta)\cos(\theta) + 2\,(V(0)\cos(\eta)+1)\sin(\theta)\right). \tag{A.1.4}$$

The corresponding solution for $\Psi(z,\theta,0)$ is obtained by direct substitution of (A.1.4) into (2.2.20) and integrating twice with respect to z subject to (2.2.21). The final result is given by

$$\begin{aligned}\Psi(z,\theta,0) \;&= [2\,V(0)\sin(\eta)\cos(\theta) - 2\,(V(0)\cos(\eta)+1)\sin(\theta) - \Omega(0)]\left[\frac{1-e^{-z^2}}{\sqrt{\pi}} - z\,\mathrm{erf}(z)\right] \\ &\quad -z\,\Omega(0)\end{aligned} \tag{A.1.5}$$

where $\mathrm{erf}(z)$ is the error function defined by

$$\mathrm{erf}(z) = \frac{2}{\sqrt{\pi}} \int_0^z e^{-s^2} ds.$$

A.2 Mathematical derivation of formulas for drag, lift and moment coefficients

In this appendix, formulas for drag, lift, pressure and moment coefficients are derived. In what follows, a represents the radius of the cylinder, U the uniform stream velocity and ρ, μ are the density and viscosity respectively.

The drag and lift forces exerting on the cylinder are determined by integrating the normal (σ) and shear (τ) stresses around a closed contour C that contains the cylinder. The dimensional viscous stresses are defined according to Stokes relations, see Potter *et al.* (1996), and given by

$$\begin{aligned} \sigma_{xx} &= \rho U^2 \left(-p + \frac{4}{R} \frac{\partial u}{\partial x} \right), \\ \sigma_{yy} &= \rho U^2 \left(-p + \frac{4}{R} \frac{\partial u}{\partial y} \right), \\ \tau_{xy} = \tau_{yx} &= \frac{2\,\rho\,U^2}{R} \left(\frac{\partial u}{\partial y} + \frac{\partial v}{\partial x} \right). \end{aligned} \tag{A.2.1}$$

The dimensional forces per unit length acting on the cylinder in the x, y directions are given, respectively, by

$$D = a \oint_C \left[\sigma_{xx} l + \tau_{xy} m - \rho U^2 (u^2 l + uvm) \right] ds, \tag{A.2.2}$$

$$L = a \oint_C \left[\sigma_{yy} m + \tau_{xy} l - \rho U^2 (v^2 m + uvl)\right] ds, \tag{A.2.3}$$

where l and m are the direction cosines of the outward normal to C given by

$$l = \frac{dy}{ds}, \qquad m = -\frac{dx}{ds}.$$

Substitution of σ_{xx}, σ_{yy} and τ_{xy} from (A.2.1) into (A.2.2) and (A.2.3) gives

$$D = a\rho U^2 \oint_C \left[-l\frac{p}{2} + l\frac{4}{R}\frac{\partial u}{\partial x} + m\frac{2}{R}\frac{\partial u}{\partial y} + m\frac{2}{R}\frac{\partial v}{\partial x} - lu^2 - muv\right] ds, \tag{A.2.4}$$

$$L = a\rho U^2 \oint_C \left[-m\frac{p}{2} + m\frac{4}{R}\frac{\partial v}{\partial y} + l\frac{2}{R}\frac{\partial u}{\partial y} + l\frac{2}{R}\frac{\partial v}{\partial x} - mv^2 - luv\right] ds. \tag{A.2.5}$$

By using the continuity equation we conclude that

$$l\frac{4}{R}\frac{\partial u}{\partial x} + m\frac{2}{R}\frac{\partial u}{\partial y} + m\frac{2}{R}\frac{\partial v}{\partial x} = \frac{2}{R}\left(m\zeta + 2\left(m\frac{\partial v}{\partial x} - l\frac{\partial v}{\partial y}\right)\right), \tag{A.2.6}$$

and

$$m\frac{4}{R}\frac{\partial v}{\partial y} + l\frac{2}{R}\frac{\partial u}{\partial y} + l\frac{2}{R}\frac{\partial v}{\partial x} = \frac{2}{R}\left(-l\zeta + 2\left(-m\frac{\partial u}{\partial x} + l\frac{\partial u}{\partial y}\right)\right), \tag{A.2.7}$$

where $\zeta = \partial u/\partial y - \partial v/\partial x$ represents the vorticity. Thus, substituting (A.2.6) and (A.2.7) into (A.2.4) and (A.2.5) we obtain

$$\mathrm{D} = a\rho U^2 \oint_C \left[-l\frac{p}{2} + m\frac{2}{R}\zeta - lu^2 - muv\right] ds \tag{A.2.8}$$

$$\mathrm{L} = a\rho U^2 \oint_C \left[-m\frac{p}{2} - l\frac{2}{R}\zeta - mv^2 - luv\right] ds. \tag{A.2.9}$$

By assuming that C ($\equiv C_0$) is concentric with the cylinder surface and using the fact that the normal fluid velocity on the cylinder surface is zero, we may rewrite (A.2.8) and (A.2.9) as follow

$$\begin{aligned} D &= a\rho U^2 \oint_{C_0} \left[-l\frac{p}{2} + m\frac{2}{R}\zeta\right] ds \\ &= a\rho U^2 \oint_{C_0} \left[-\frac{p}{2}dy - \frac{2}{R}\zeta dx\right], \end{aligned} \tag{A.2.10}$$

$$\begin{aligned} L &= a\rho U^2 \oint_{C_0} \left[-m\frac{p}{2} - l\frac{2}{R}\zeta \right] ds \\ &= a\rho U^2 \oint_{C_0} \left[\frac{p}{2}dx - \frac{2}{R}\zeta dy \right]. \end{aligned} \tag{A.2.11}$$

Since $x = e^{\xi}\cos(\theta)$ and $y = e^{\xi}\sin(\theta)$ then $dx = -\sin(\theta)\,d\theta$ and $dy = \cos(\theta)d\theta$ on the surface of the cylinder. Consequently (A.2.10) and (A.2.11) can be rewritten at $\xi = 0$ as follows

$$D = a\rho U^2 \int_0^{2\pi} \left(-\frac{p}{2}\Big|_{\xi=0} \cos(\theta) + \frac{2}{R}\,\zeta|_{\xi=0} \sin(\theta) \right) d\theta, \tag{A.2.12}$$

$$L = a\rho U^2 \int_0^{2\pi} \left(-\frac{p}{2}\Big|_{\xi=0} \sin(\theta) - \frac{2}{R}\,\zeta|_{\xi=0} \cos(\theta) \right) d\theta. \tag{A.2.13}$$

Integrating the pressure term in (A.2.12) and (A.2.13) by parts with respect to θ we obtain

$$D = a\rho U^2 \left(\frac{1}{2}\int_0^{2\pi} \frac{\partial p}{\partial \theta}\Big|_{\xi=0} \sin(\theta) d\theta + \frac{2}{R}\int_0^{2\pi} \zeta|_{\xi=0} \sin(\theta)\,d\theta \right) \tag{A.2.14}$$

and

$$L = a\rho U^2 \left(-\frac{1}{2}\int_0^{2\pi} \frac{\partial p}{\partial \theta}\Big|_{\xi=0} \cos(\theta) d\theta - \frac{2}{R}\int_0^{2\pi} \zeta|_{\xi=0} \cos(\theta)\,d\theta \right) \tag{A.2.15}$$

By substituting the expression for $\partial p/\partial\theta$ at $\xi = 0$ given in (2.3.1) into (A.2.14) we obtain

$$D = a\rho U^2 \left(\frac{-2}{R}\int_0^{2\pi} \frac{\partial \zeta}{\partial \xi}\Big|_{\xi=0} \sin(\theta) d\theta + \frac{2}{R}\int_0^{2\pi} \zeta|_{\xi=0} \sin(\theta)\,d\theta - \pi\,\dot{V}(t)\cos(\eta) \right), \tag{A.2.16}$$

and

$$L = a\rho U^2 \left(\frac{2}{R}\int_0^{2\pi} \frac{\partial w}{\partial \xi}\Big|_{\xi=0} \cos(\theta) d\theta - \frac{2}{R}\int_0^{2\pi} \zeta|_{\xi=0} \cos(\theta)\,d\theta - \pi\,\dot{V}(t)\sin(\eta) \right). \tag{A.2.17}$$

Finally the dimensionless drag and lift coefficients are given by

$$C_D = \frac{D}{a\rho U^2} = \frac{2}{R}\int_0^{2\pi} \zeta|_{\xi=0} \sin\theta d\theta - \frac{2}{R}\int_0^{2\pi} \left.\frac{\partial\zeta}{\partial\xi}\right|_{\xi=0} \sin\theta d\theta - \pi\dot{V}(t)\cos(\eta)$$

$$C_L = \frac{L}{a\rho U^2} = -\frac{2}{R}\int_0^{2\pi} \zeta|_{\xi=0} \cos\theta d\theta + \frac{2}{R}\int_0^{2\pi} \left.\frac{\partial\zeta}{\partial\xi}\right|_{\xi=0} \cos\theta d\theta - \pi\dot{V}(t)\sin(\eta).$$

The moment exerted on the cylinder surface by the fluid can be obtained by integrating the torque around a contour C enclosing the cylinder surface. The dimensional moment is given by

$$M = a \oint_C (x\, d\, L - y\, d\, D) \tag{A.2.18}$$

where L and D are dimensional forces in the x, y directions given in (A.2.2) and (A.2.3). Substituting equations (A.2.2) and (A.2.3) into (A.2.18) and using the continuity equation gives

$$\begin{aligned} M &= a^2\rho U^2 \left\{ \oint_C p(xdx + ydy) + \frac{2}{R}\oint_C \zeta(ydx - xdy) \right. \\ &- \oint_C uv(xdy + ydx) + \oint_C v^2 xdx + \oint_C u^2 ydy \\ &+ \left. \frac{4}{R}\oint_C (x\frac{\partial u}{\partial y} + y\frac{\partial v}{\partial y})dy + \frac{4}{R}\oint_C (x\frac{\partial u}{\partial x} + y\frac{\partial v}{\partial x})dx \right\}. \end{aligned} \tag{A.2.19}$$

The dimensionless velocity components u and v are related to the dimensionless stream function

$$u = \frac{\partial\psi}{\partial y} = e^{-\xi}\, \sin(\theta)\, \frac{\partial\psi}{\partial\xi} + e^{-\xi}\, \cos(\theta)\, \frac{\partial\psi}{\partial\theta}, \tag{A.2.20}$$

$$v = -\frac{\partial\psi}{\partial x} = -e^{-\xi}\, \cos(\theta)\, \frac{\partial\psi}{\partial\xi} + e^{-\xi}\, \sin(\theta)\, \frac{\partial\psi}{\partial\theta}. \tag{A.2.21}$$

Thus, taking the contour C to be a circle concentric with the cylinder and using the modified polar coordinate to rewrite all the variables in equation A.2.19, we obtain

$$M = a^2\rho U^2 \left(\int_0^{2\pi} (-\frac{2}{R}e^{2\xi}\zeta + \frac{\partial\psi}{\partial\xi}\frac{\partial\psi}{\partial\theta})d\theta + \frac{4}{R}\int_0^{2\pi} \frac{\partial\psi}{\partial\xi}d\theta \right). \tag{A.2.22}$$

On the cylinder surface, when $\xi = 0$, the expression (A.2.22) can be simplified, after making use of the conditions $\partial\psi/\partial\theta = 0$ and $\partial\psi/\partial\xi = -\Omega(t)$ when $\xi = 0$, to

$$M = a^2\rho U^2 \left(-\frac{2}{R}\int_0^{2\pi} \zeta|_{\xi=0} d\theta - \frac{8\pi\Omega(t)}{R}\right). \tag{A.2.23}$$

The dimensionless moment coefficient is defined by

$$C_M = \frac{M}{4\pi\mu a^2 f_\theta}. \tag{A.2.24}$$

where $f_\theta = a\ f_\theta^*/U$ is the dimensionless frequency. By combining (A.2.23) and (A.2.24), we obtain

$$C_M = -\frac{1}{4\pi f_\theta}\int_0^{2\pi} \zeta|_{\xi=0} d\theta - \frac{\Omega(t)}{f_\theta}. \tag{A.2.25}$$

Appendix B

Appendix for Chapter 3

B.1 List of formulas used in obtaining component form of $\omega_{n,m}(z,\theta)$ and $\Psi_{n,m}(z,\theta)$

$$(i)\quad \Big(\sum_{r=1}^{N_1} F_r\cos(r\theta)\Big)\Big(\sum_{s=1}^{N_2} G_s\cos(s\theta)\Big) = \frac{1}{2}\sum_{u=2}^{N_1+N_2}\left(\sum_{s=\max(1,u-N_1)}^{\min(u-1,N_2)} F_{u-s}\,G_s\right)\cos(u\,\theta) + \frac{1}{2}\sum_{u=1-N_2}^{N_1-1}\left(\sum_{s=\max(1-u,1)}^{\min(N_2,N_1-u)} F_{u+s}\,G_s\right)\cos(u\,\theta)$$

$$(ii)\quad \Big(\sum_{r=1}^{N_1} F_r\cos(r\theta)\Big)\Big(\sum_{s=1}^{N_2} G_s\sin(s\theta)\Big) = \frac{1}{2}\sum_{u=2}^{N_1+N_2}\left(\sum_{s=\max(1,u-N_1)}^{\min(u-1,N_2)} F_{u-s}\,G_s\right)\sin(u\,\theta) - \frac{1}{2}\sum_{u=1-N_2}^{N_1-1}\left(\sum_{s=\max(1-u,1)}^{\min(N_2,N_1-u)} F_{u+s}\,G_s\right)\sin(u\,\theta)$$

$$(iii)\quad \Big(\sum_{r=1}^{N_1} F_r\sin(r\theta)\Big)\Big(\sum_{s=1}^{N_2} G_s\sin(s\theta)\Big) = -\frac{1}{2}\sum_{u=2}^{N_1+N_2}\left(\sum_{s=\max(1,u-N_1)}^{\min(u-1,N_2)} F_{u-s}\,G_s\right)\cos(u\,\theta) + \frac{1}{2}\sum_{u=1-N_2}^{N_1-1}\left(\sum_{s=\max(1-u,1)}^{\min(N_2,N_1-u)} F_{u+s}\,G_s\right)\cos(u\,\theta)$$

$$(iv)\quad \sum_{j=0}^{N_1-1}\left\{\sum_{r=1}^{j+1}F_{j,r}\sin(r\theta)+\sum_{s=1}^{N_1-j}G_{j,s}\sin(s\theta)\right\}=\sum_{r=1}^{N_1}\left\{\sum_{i=r-1}^{N_1-1}F_{i,r}+\sum_{i=0}^{N_1-r}G_{i,r}\right\}\sin(r\theta)$$

$$(v)\quad \sum_{j=0}^{N_1-1}\left\{\sum_{r=1}^{j+1}F_{j,r}\cos(r\theta)+\sum_{s=1}^{N_1-j}G_{j,s}\cos(s\theta)\right\}=\sum_{r=1}^{N_1}\left\{\sum_{i=r-1}^{N_1-1}F_{i,r}+\sum_{i=0}^{N_1-r}G_{i,r}\right\}\cos(r\theta)$$

$$(vi)\quad \sum_{j=0}^{N_1-1}\left\{\sum_{r=j-m+1}^{j}F_{j,r}\cos(r\theta)\right\}=\sum_{r=1}^{N_1-1}\left\{\sum_{i=r}^{N_1-1}F_{i,r}+\sum_{i=0}^{N_1-r-1}F_{i,-r}\right\}\sin(r\theta)+\sum_{j=0}^{N_1-1}F_{j,0}$$

$$(vii)\quad \sum_{j=0}^{N_1-1}\left\{\sum_{r=j-m+1}^{j}F_{j,r}\sin(r\theta)\right\}=\sum_{r=1}^{N_1-1}\left\{\sum_{i=r}^{N_1-1}F_{i,r}-\sum_{i=0}^{N_1-r-1}F_{i,-r}\right\}\sin(r\theta)$$

where r, N_1 and N_2 are integers.

B.2 List of differential equations and required conditions satisfied by Fourier components for the scaled vorticity $\omega(z,\theta)$

$$\frac{d^2G^0_{0,0}}{dz^2}+2z\frac{dG^0_{0,0}(z)}{dz}+2G^0_{0,0}(z)=0, \tag{B.2.1}$$

$$\int_0^\infty G^0_{0,0}(z)dz=2\alpha_0,\qquad G^0_{0,0}\to 0 \text{ when } z\to\infty \tag{B.2.1a}$$

$$\frac{d^2G^1_{0,0}}{dz^2}+2z\frac{dG^1_{0,0}(z)}{dz}+2G^1_{0,0}(z)=0, \tag{B.2.2}$$

$$\int_0^\infty G^1_{0,0}(z)dz=-2\sigma_0\sin(\eta),\qquad G^1_{0,0}\to 0 \text{ when } z\to\infty \tag{B.2.2a}$$

$$\frac{d^2g^1_{0,0}}{dz^2}+2z\frac{dg^1_{0,0}(z)}{dz}+2g^1_{0,0}(z)=0, \tag{B.2.3}$$

$$\int_0^\infty g^1_{0,0}(z)dz = 2[\sigma_0 \cos(\eta) + 1], \qquad g^1_{0,0} \to 0 \text{ when } z \to \infty \tag{B.2.3a}$$

$$\frac{d^2G^0_{0,1}}{dz^2} + 2z\frac{dG^0_{0,1}(z)}{dz} - 2G^0_{0,1}(z) = \mathrm{RC}^0_{0,1}(z), \tag{B.2.4}$$

$$\int_0^\infty G^0_{0,1}(z)dz = 2\alpha_1 \qquad G^0_{0,1} \to 0 \text{ when } z \to \infty \tag{B.2.4a}$$

$$\frac{d^2G^1_{0,1}}{dz^2} + 2z\frac{dG^1_{0,1}(z)}{dz} - 2G^1_{0,1}(z) = \mathrm{RC}^1_{0,1}(z), \tag{B.2.5}$$

$$\int_0^\infty G^1_{0,1}(z)dz = -2\sin(\eta)\sigma_1, \qquad G^1_{0,1} \to 0 \text{ when } z \to \infty \tag{B.2.5a}$$

$$\frac{d^2G^2_{0,1}}{dz^2} + 2z\frac{dG^2_{0,1}(z)}{dz} - 2G^2_{0,1}(z) = \mathrm{RC}^2_{0,1}(z), \tag{B.2.6}$$

$$\int_0^\infty G^2_{0,1}(z)dz = 0, \qquad G^2_{0,1} \to 0 \text{ when } z \to \infty \tag{B.2.6a}$$

$$\frac{d^2g^1_{0,1}}{dz^2} + 2z\frac{dg^1_{0,1}(z)}{dz} - 2g^1_{0,1}(z) = \mathrm{RS}^1_{0,1}(z), \tag{B.2.7}$$

$$\int_0^\infty g^1_{0,1}(z)dz = 2\cos(\eta)\sigma_1, \qquad g^1_{0,1} \to 0 \text{ when } z \to \infty. \tag{B.2.7a}$$

$$\frac{d^2g^2_{0,1}}{dz^2} + 2z\frac{dg^2_{0,1}(z)}{dz} - 2g^2_{0,1}(z) = \mathrm{RS}^2_{0,1}(z), \tag{B.2.8}$$

$$\int_0^\infty g^2_{0,1}(z)dz = 0, \qquad g^2_{0,1} \to 0 \text{ when } z \to \infty. \tag{B.2.8a}$$

$$\frac{d^2G^0_{0,2}}{dz^2} + 2z\frac{dG^0_{0,2}(z)}{dz} - 6G^0_{0,2}(z) = \mathrm{RC}^0_{0,2}(z), \tag{B.2.9}$$

$$\int_0^\infty G^0_{0,2}(z)dz = 2\alpha_2 \qquad G^0_{0,2} \to 0 \text{ when } z \to \infty \tag{B.2.9a}$$

$$\frac{d^2G^2_{0,2}}{dz^2} + 2z\frac{dG^1_{0,2}(z)}{dz} - 6G^1_{0,2}(z) = \mathrm{RC}^1_{0,2}(z), \tag{B.2.10}$$

$$\int_0^\infty G^1_{0,2}(z)dz = -2\sin(\eta)\sigma_2, \qquad G^1_{0,2} \to 0 \text{ when } z \to \infty \tag{B.2.10a}$$

$$\frac{d^2G^2_{0,2}}{dz^2} + 2z\frac{dG^2_{0,2}(z)}{dz} - 6G^2_{0,2}(z) = \mathrm{RC}^2_{0,2}(z), \tag{B.2.11}$$

$$\int_0^\infty G^2_{0,2}(z)dz = 0, \qquad G^2_{0,2} \to 0 \text{ when } z \to \infty \tag{B.2.11a}$$

$$\frac{d^2G^3_{0,2}}{dz^2} + 2z\frac{dG^3_{0,2}(z)}{dz} - 6G^3_{0,2}(z) = \mathrm{RC}^3_{0,2}(z), \tag{B.2.12}$$

$$\int_0^\infty G^3_{0,2}(z)dz = 0, \qquad G^3_{0,2} \to 0 \text{ when } z \to \infty \tag{B.2.12a}$$

$$\frac{d^2g^1_{0,2}}{dz^2} + 2z\frac{dg^1_{0,2}(z)}{dz} - 6g^1_{0,2}(z) = \mathrm{RS}^1_{0,2}(z), \tag{B.2.13}$$

$$\int_0^\infty g^1_{0,2}(z)dz = 2\cos(\eta)\sigma_2, \qquad g^1_{0,2} \to 0 \text{ when } z \to \infty. \tag{B.2.13a}$$

$$\frac{d^2 g^2_{0,2}}{dz^2} + 2z\frac{dg^2_{0,2}(z)}{dz} - 6g^2_{0,2}(z) = \mathrm{RS}^2_{0,2}(z), \tag{B.2.14}$$

$$\int_0^\infty g^2_{0,2}(z)dz = 0, \qquad g^2_{0,2} \to 0 \text{ when } z \to \infty. \tag{B.2.14a}$$

$$\frac{d^2 g^3_{0,2}}{dz^2} + 2z\frac{dg^3_{0,2}(z)}{dz} - 6g^3_{0,2}(z) = \mathrm{RS}^3_{0,2}(z), \tag{B.2.15}$$

$$\int_0^\infty g^3_{0,2}(z)dz = 0, \qquad g^3_{0,2} \to 0 \text{ when } z \to \infty. \tag{B.2.15a}$$

$$\frac{d^2 G^0_{1,0}}{dz^2} + 2z\frac{dG^0_{1,0}(z)}{dz} = \mathrm{RC}^0_{1,0}(z), \tag{B.2.16}$$

$$\int_0^\infty [2zG^0_{0,0}(z) + G^0_{1,0}(z)]dz = 0, \qquad G^0_{1,0} \to 0 \text{ when } z \to \infty \tag{B.2.16a}$$

$$\frac{d^2 G^1_{1,0}}{dz^2} + 2z\frac{dG^1_{1,0}(z)}{dz} = \mathrm{RC}^1_{1,0}(z), \tag{B.2.17}$$

$$\int_0^\infty [zG^1_{0,0}(z) + G^1_{1,0}(z)]dz = 0, \qquad G^1_{1,0} \to 0 \text{ when } z \to \infty \tag{B.2.17a}$$

$$\frac{d^2 g^1_{1,0}}{dz^2} + 2z\frac{dg^1_{1,0}(z)}{dz} = \mathrm{RS}^1_{1,0}(z), \tag{B.2.18}$$

$$\int_0^\infty [zg^1_{0,0}(z) + g^1_{1,0}(z)]dz = 0, \qquad g^1_{1,0} \to 0 \text{ when } z \to \infty \tag{B.2.18a}$$

$$\frac{d^2G^0_{1,1}}{dz^2} + 2z\frac{dG^0_{1,1}(z)}{dz} - 4G^0_{1,1}(z) = \mathrm{RC}^0_{1,1}(z), \tag{B.2.19}$$

$$\int_0^\infty [2zG^0_{0,1}(z) + G^0_{1,1}(z)]dz = 0, \qquad G^0_{1,1} \to 0 \text{ when } z \to \infty \tag{B.2.19a}$$

$$\frac{d^2G^1_{1,1}}{dz^2} + 2z\frac{dG^1_{1,1}(z)}{dz} - 4G^1_{1,1}(z) = \mathrm{RC}^1_{1,1}(z), \tag{B.2.20}$$

$$\int_0^\infty [zG^1_{0,1}(z) + G^1_{1,1}(z)]dz = 0, \qquad G^1_{1,1} \to 0 \text{ when } z \to \infty \tag{B.2.20a}$$

$$\frac{d^2G^2_{1,1}}{dz^2} + 2z\frac{dG^2_{1,1}(z)}{dz} - 4G^2_{1,1}(z) = \mathrm{RC}^2_{1,1}(z), \tag{B.2.21}$$

$$\int_0^\infty G^2_{1,1}(z)dz = 0, \qquad G^2_{1,1} \to 0 \text{ when } z \to \infty \tag{B.2.21a}$$

$$\frac{d^2g^1_{1,1}}{dz^2} + 2z\frac{dg^1_{1,1}(z)}{dz} - 4G^1_{1,1}(z) = \mathrm{RS}^1_{1,1}(z), \tag{B.2.22}$$

$$\int_0^\infty [zg^1_{0,1}(z) + g^1_{1,1}(z)]dz = 0, \qquad g^1_{1,1} \to 0 \text{ when } z \to \infty \tag{B.2.22a}$$

$$\frac{d^2g^2_{1,1}}{dz^2} + 2z\frac{dg^2_{1,1}(z)}{dz} - 4g^2_{1,1}(z) = \mathrm{RS}^2_{1,1}(z), \tag{B.2.23}$$

$$\int_0^\infty g^2_{1,1}(z)dz = 0, \qquad g^2_{1,1} \to 0 \text{ when } z \to \infty \tag{B.2.23a}$$

$$\frac{d^2G^0_{1,2}}{dz^2} + 2z\frac{dG^0_{1,2}(z)}{dz} - 8G^0_{1,2}(z) = \mathrm{RC}^0_{1,2}(z), \tag{B.2.24}$$

$$\int_0^\infty [2zG^0_{0,2}(z) + G^0_{1,2}(z)]dz = 0, \qquad G^0_{1,2} \to 0 \text{ when } z \to \infty \tag{B.2.24a}$$

$$\frac{d^2G^1_{1,2}}{dz^2} + 2z\frac{dG^1_{1,2}(z)}{dz} - 8G^1_{1,2}(z) = \mathrm{RC}^1_{1,2}(z), \tag{B.2.25}$$

$$\int_0^\infty [zG^1_{0,2}(z) + G^1_{1,2}(z)]dz = 0, \qquad G^1_{1,2} \to 0 \text{ when } z \to \infty \tag{B.2.25a}$$

$$\frac{d^2G^2_{1,2}}{dz^2} + 2z\frac{dG^2_{1,2}(z)}{dz} - 8G^2_{1,2}(z) = \mathrm{RC}^2_{1,2}(z), \tag{B.2.26}$$

$$\int_0^\infty G^2_{1,2}(z)dz = 0, \qquad G^2_{1,2} \to 0 \text{ when } z \to \infty \tag{B.2.26a}$$

$$\frac{d^2G^3_{1,2}}{dz^2} + 2z\frac{dG^3_{1,2}(z)}{dz} - 8G^3_{1,2}(z) = \mathrm{RC}^3_{1,2}(z), \tag{B.2.27}$$

$$\int_0^\infty [-zG^3_{0,2}(z) + G^3_{1,2}(z)]dz = 0, \qquad G^3_{1,2} \to 0 \text{ when } z \to \infty \tag{B.2.27a}$$

$$\frac{d^2g^1_{1,2}}{dz^2} + 2z\frac{dg^1_{1,2}(z)}{dz} - 8g^1_{1,2}(z) = \mathrm{RS}^1_{1,2}(z), \tag{B.2.28}$$

$$\int_0^\infty [zg^1_{0,2}(z) + g^1_{1,2}(z)]dz = 0, \qquad g^1_{1,2} \to 0 \text{ when } z \to \infty \tag{B.2.28a}$$

$$\frac{d^2 g^2_{1,2}}{dz^2} + 2z\frac{dg^2_{1,2}(z)}{dz} - 8g^2_{1,2}(z) = \mathrm{RS}^2_{1,2}(z), \tag{B.2.29}$$

$$\int_0^\infty g^2_{1,2}(z)dz = 0, \qquad g^2_{1,2} \to 0 \text{ when } z \to \infty \tag{B.2.29a}$$

$$\frac{d^2 g^3_{1,2}}{dz^2} + 2z\frac{dg^3_{1,2}(z)}{dz} - 8g^3_{1,2}(z) = \mathrm{RS}^3_{1,2}(z), \tag{B.2.30}$$

$$\int_0^\infty [-zg^3_{0,2}(z) + g^3_{1,2}(z)]dz = 0, \qquad g^3_{1,2} \to 0 \text{ when } z \to \infty \tag{B.2.30a}$$

$$\frac{d^2 G^0_{2,0}}{dz^2} + 2z\frac{dG^0_{2,0}(z)}{dz} - 2G^0_{2,0}(z) = \mathrm{RC}^0_{2,0}(z), \tag{B.2.31}$$

$$\int_0^\infty [2z^2 G^0_{0,0}(z) + 2zG^0_{1,0}(z) + G^0_{2,0}(z)]dz = 0, \qquad G^0_{2,0} \to 0 \text{ when } z \to \infty \tag{B.2.31a}$$

$$\frac{d^2 G^1_{2,0}}{dz^2} + 2z\frac{dG^1_{2,0}(z)}{dz} - 2G^1_{2,0}(z) = \mathrm{RC}^1_{2,0}(z), \tag{B.2.32}$$

$$\int_0^\infty [\frac{1}{2}z^2 G^1_{0,0}(z) + zG^1_{1,0}(z) + G^1_{2,0}(z)]dz = 0, \qquad G^1_{2,0} \to 0 \text{ when } z \to \infty \tag{B.2.32a}$$

$$\frac{d^2 g^1_{2,0}}{dz^2} + 2z\frac{dg^1_{2,0}(z)}{dz} - 2g^1_{2,0}(z) = \mathrm{RS}^1_{2,0}(z), \tag{B.2.33}$$

$$\int_0^\infty [\frac{1}{2}z^2 g^1_{0,0}(z) + zg^1_{1,0}(z) + g^1_{2,0}(z)]dz = 0, \qquad g^1_{2,0} \to 0 \text{ when } z \to \infty \tag{B.2.33a}$$

$$\frac{d^2G^0_{2,1}}{dz^2} + 2z\frac{dG^0_{2,1}(z)}{dz} - 6G^0_{2,1}(z) = \mathrm{RC}^0_{2,1}(z), \tag{B.2.34}$$

$$\int_0^\infty [2z^2G^0_{0,1}(z) + 2zG^0_{1,1}(z) + G^0_{2,1}(z)]dz = 0, \qquad G^0_{2,1} \to 0 \text{ when } z \to \infty \tag{B.2.34a}$$

$$\frac{d^2G^1_{2,1}}{dz^2} + 2z\frac{dG^1_{2,1}(z)}{dz} - 2G^1_{2,1}(z) = \mathrm{RC}^1_{2,1}(z), \tag{B.2.35}$$

$$\int_0^\infty [\frac{1}{2}z^2G^1_{0,1}(z) + zG^1_{1,1}(z) + G^1_{2,1}(z)]dz = 0, \qquad G^1_{2,1} \to 0 \text{ when } z \to \infty \tag{B.2.35a}$$

$$\frac{d^2G^2_{2,1}}{dz^2} + 2z\frac{dG^2_{2,1}(z)}{dz} - 2G^2_{2,1}(z) = \mathrm{RC}^2_{2,1}(z), \tag{B.2.36}$$

$$\int_0^\infty G^2_{2,1}(z)dz = 0, \qquad G^2_{2,1} \to 0 \text{ when } z \to \infty \tag{B.2.36a}$$

$$\frac{d^2g^1_{2,1}}{dz^2} + 2z\frac{dg^1_{2,1}(z)}{dz} - 2g^1_{2,1}(z) = \mathrm{RS}^1_{2,1}(z), \tag{B.2.37}$$

$$\int_0^\infty [\frac{1}{2}z^2g^1_{0,1}(z) + zg^1_{1,1}(z) + g^1_{2,1}(z)]dz = 0, \qquad g^1_{2,1} \to 0 \text{ when } z \to \infty \tag{B.2.37a}$$

$$\frac{d^2g^2_{2,1}}{dz^2} + 2z\frac{dg^2_{2,1}(z)}{dz} - 2g^2_{2,1}(z) = \mathrm{RC}^2_{2,1}(z), \tag{B.2.38}$$

$$\int_0^\infty g^2_{2,1}(z)dz = 0, \qquad g^2_{2,1} \to 0 \text{ when } z \to \infty \tag{B.2.38a}$$

B.3 The non-homogenous terms in (3.1.2) given by (3.1.4)

The non-homogenous term of the differential equation (3.1.4) when $n = 0$ and $m = 2$ is given by

$$
\begin{aligned}
R_{0,2} &= \frac{16}{3}(A_0B_1 - B_0A_1)\Big[-12\,\mathrm{erf}(z)\,z\mathrm{erfc}(z) + \{6\mathrm{erfc}(z) + [(-9-4z^4)\,\mathrm{erfc}(z) \\
&+ 6z^2+3]\,e^{-z^2}\}\pi^{-\frac{1}{2}} + [-4ze^{-z^2} + (-2z+4z^3)e^{-2z^2}]\pi^{-1}\Big] - \frac{8}{9}({B_0}^2 + {A_0}^2) \\
&\times \alpha_0\Big[-36\,z\,\mathrm{erf}(z)^2\,\mathrm{erfc}(z) + \{18\,\mathrm{erf}(z)\,\mathrm{erfc}(z) + [(36+48\,z^4-36\,z^2)\,\mathrm{erf}(z)^2 \\
&+ (-12z^4-27)\mathrm{erf}(z)]e^{-z^2}\}\pi^{-\frac{1}{2}} + \{ -48\mathrm{erf}(z)z\mathrm{erfc}(z) + [(6z-84\,z^3)\,\mathrm{erf}(z) \\
&+ 48z\sqrt{2}\mathrm{erf}(\sqrt{2}z) + 12z]e^{-z^2} + ((-120z+96z^3)\,\mathrm{erf}(z) + 6\,z - 12z^3)e^{-2z^2}\} \\
&\times \pi^{-1} + \{24\,\mathrm{erfc}(z) + [(-36-16\,z^4)\,\mathrm{erfc}(z) + 48\,z^2]\,e^{-z^2} + (-84\,z^2+48) \\
&\times e^{-2z^2} + (-36+48\,z^2)\,e^{-3z^2}\}\pi^{-3/2} + [-16\,z\,e^{-z^2} + (-8\,z+16\,z^3)\,e^{-2z^2}] \\
&\times \pi^{-2}\Big] + \Big[-16z\,\mathrm{erf}(z)\,\mathrm{erfc}(z)^2 + \{[(32z^2-8-\frac{32}{3}z^4)\mathrm{erfc}(z)^2 + (8-32z^2 \\
&+ \frac{32}{3}\,z^4)\,\mathrm{erfc}(z)]\,e^{-z^2}\}\pi^{-\frac{1}{2}} + \frac{1}{3}\{-64\,z\,\mathrm{erfc}(z)^2 - 128\,z\,(-1+\sqrt{2}\,\mathrm{erf}(\sqrt{2}\,z)) \\
&\times e^{-z^2} + [(224\,z-64\,z^3)\,\mathrm{erf}(z) - 112z + 32\,z^3]e^{-2z^2}\}\pi^{-1} + [\frac{1}{9}(192+128z^4 \\
&+ 192\,z^2)\,\mathrm{erfc}(z)\,e^{-z^2} - \frac{32}{3}z^2e^{-3z^2}]\pi^{-3/2} + [\frac{128}{9}z\,e^{-z^2} - \frac{128}{9}(z+z^3)e^{-2z^2}] \\
&\times \pi^{-2}\Big]\,(-A_0\cos(\theta) + B_0\sin(\theta))\alpha_0{}^2 + \{-32\mathrm{erf}(z)z\mathrm{erfc}(z) + [32\mathrm{erfc}(z) + (32z^2 \\
&- 16)\,\mathrm{erfc}(z)\,e^{-z^2}]\pi^{-\frac{1}{2}} - 32\,z\,e^{-2z^2}\pi^{-1}\}(B_0\cos(\theta) + A_0\sin(\theta))\,\alpha_1 + \Big[-32\,z \\
&\times \mathrm{erfc}(z)^2 - \frac{32}{3}\{[(-2\,z^4-3)\,\mathrm{erfc}(z) + 3z^2\mathrm{erf}(z)]e^{-z^2}\}\pi^{-\frac{1}{2}} + \frac{64}{3}[ze^{-z^2} + (-z^3 \\
&- z)\,e^{-2z^2}]\pi^{-1}\Big]\,\alpha_0(\cos(\theta)\,B_1 + \sin(\theta)\,A_1) + \Big[-48\mathrm{erf}(z)\,z(\mathrm{erf}(z)+2)\mathrm{erfc}(z)
\end{aligned}
$$

$$
\begin{aligned}
&+ \{32 - 16\,\mathrm{erf}(z) - 16\,\mathrm{erf}(z)^2 + [(-64z^2 + 40 + \frac{160}{3}z^4)\mathrm{erf}(z)^2 + (\frac{64}{3}z^4 + 16z^2 \\
&+ 40)\,\mathrm{erf}(z) - \frac{128}{3}\,z^4 + 32\,z^2 - 32]e^{-z^2}\}\pi^{-\frac{1}{2}} + \{-64\mathrm{erf}(z)\,z\mathrm{erfc}(z) + \frac{1}{3}[(16z \\
&- 224\,z^3)\,\mathrm{erf}(z) - 64\,z + 256\,z\sqrt{2}\mathrm{erf}(\sqrt{2}\,z)]e^{-z^2} + \frac{1}{3}[(-544z + 320z^3)\mathrm{erf}(z) \\
&+ 64\,z^3 + 16\,z]\,e^{-2z^2}\}\pi^{-1} + \frac{1}{9}\{192\,\mathrm{erfc}(z) + [(-192\,z^2 - 256\,z^4 - 480)\,\mathrm{erfc}(z) \\
&+ 192 + 384\,z^2]\,e^{-z^2} + (-672\,z^2 + 384)\,e^{-2z^2} + (480\,z^2 - 288)\,e^{-3z^2}\}\pi^{-3/2} \\
&+ \frac{1}{9}\,[-256\,z\,e^{-z^2} + (256\,z^3 + 64\,z)\,e^{-2z^2}]\pi^{-2}\Big]\,(B_0{}^2 + A_0{}^2)\,(A_0\cos(\theta) - B_0 \\
&\times \sin(\theta)) + \Big[\{-32\mathrm{erfc}(z) + [(-16 - 64z^2 - \frac{64}{3}z^4)\mathrm{erfc}(z) + 48 + 32z^2]e^{-z^2}\} \\
&\times \pi^{-\frac{1}{2}} + [-\frac{64}{3}ze^{(-z^2)} + \frac{1}{3}(160z + 64\,z^3)e^{-2z^2}]\pi^{-1}\Big]\,[(A_0B_1 + B_0A_1)\cos(2\theta) \\
&+ (-B_0\,B_1 + A_0\,A_1)\sin(2\,\theta)] - \frac{8}{3}[(A_0{}^2 - B_0{}^2)\cos(2\,\theta) - 2\,A_0\,B_0\sin(2\,\theta)]\,\alpha_0 \\
&\times (12\,z\,(\mathrm{erf}(z) + 2)\,\mathrm{erfc}(z)^2 + [-6\,\mathrm{erf}(z)\,\mathrm{erfc}(z) + (-36\,\mathrm{erf}(z)^2z^2 + (4\,z^4 + 15 \\
&+ 36\,z^2)\,\mathrm{erf}(z) - 16\,z^4 - 12)\,e^{-z^2}]\pi^{-\frac{1}{2}} + [16z\,\mathrm{erfc}(z)^2 + ((-2\,z + 28\,z^3)\mathrm{erf}(z) \\
&+ 48\,z\sqrt{2}\,\mathrm{erf}(\sqrt{2}\,z) - 44\,z)\,e^{-z^2} + (4\,z^3 - 72\,\mathrm{erf}(z)\,z + 34\,z)e^{-2z^2}]\pi^{-1} + [-8 \\
&\times \mathrm{erfc}(z) + [(-32\,z^2 - 16\,z^4 - 20)\,\mathrm{erfc}(z) - 16\,z^2 + 16]\,e^{-z^2} + (-16 + 28\,z^2) \\
&\times e^{-2z^2} + 12\,e^{-3z^2}]\pi^{-\frac{3}{2}} + [-16\,z\,e^{-z^2} + (24\,z + 16\,z^3)\,e^{-2z^2}]\pi^{-2}) + \Big[-16 \\
&\times \mathrm{erf}(z)\,z(\mathrm{erf}(z) + 2)\mathrm{erfc}(z) + [-16(\mathrm{erf}(z) + 2)\mathrm{erfc}(z) + ((-8 - 64z^2 - \frac{32}{3}z^4) \\
&\times \mathrm{erf}(z)^2 + (24 + 48\,z^2 + \frac{64}{3}\,z^4)\,\mathrm{erf}(z) - 32\,z^2 - \frac{128}{3}\,z^4 + 32)e^{-z^2}]\pi^{-\frac{1}{2}} + \frac{1}{3} \\
&\times \{-64\,\mathrm{erf}(z)\,z\,\mathrm{erfc}(z) + [(-16\,z + 224\,z^3)\,\mathrm{erf}(z) - 64\,z + 256\,z\sqrt{2}\,\mathrm{erf}(\sqrt{2}\,z)] \\
&\times e^{-z^2} + (64\,z^3\ \mathrm{erfc}(z) + 112\,z - 352\ \mathrm{erf}(z)\,z)\,e^{-2z^2}\}\,\pi^{-1} + \{-\frac{64}{3}\ \mathrm{erfc}(z)
\end{aligned}
$$

$$
\begin{aligned}
&+ \left[(-32 - 64z^2 - \frac{256}{9}z^4)\,\mathrm{erfc}(z) - \frac{128}{3}\,z^2 + 64\right]e^{-z^2} + \frac{1}{3}(224z^2 - 128)e^{-2\,z^2} \\
&+ \left.\frac{1}{3}(-32\,z^2 + 96)e^{-3z^2}\right\}\pi^{-\frac{3}{2}} + \left[-\frac{256}{9}\,z\,e^{-z^2} + \frac{1}{9}\,(256\,z^3 + 448\,z)\,e^{-2\,z^2}\right]\pi^{-2}\Bigg] \\
&\times \left[(A_0{}^3 - 3\,B_0{}^2\,A_0)\cos(3\,\theta) + (B_0{}^3 - 3\,A_0{}^2\,B_0)\sin(3\,\theta)\right]. \qquad \text{(B.3.1)}
\end{aligned}
$$

where A_0 B_0 and A_1, B_1 are given in (3.3.13) and (3.3.16) respectively.

The non-homogenous term of the differential equation (3.1.4) when $n = m = 1$ is given by

$$
\begin{aligned}
\mathrm{R}_{1,1} &= -16\,z\,(-\alpha_1 + 2\cos(\theta)\,A_1 - 2\sin(\theta)\,B_1)\,e^{-z^2}\pi^{-\frac{1}{2}} + \Big\{4\mathrm{erfc}(z)^2 + 4\,z[(16\,z^4 \\
&- 1 + 6\,z^2)\,\mathrm{erf}(z) - 14\,z^2]\,e^{-z^2}\pi^{-\frac{1}{2}} + [-\frac{224}{3}\,e^{-z^2}\,z^4 + (64\,z^4 - 8\,z^2)\,e^{-2\,z^2}] \\
&\times \pi^{-1} - \frac{64}{3}\,e^{-z^2}\,z\pi^{-\frac{3}{2}}\Big\}\,(\cos(\theta)\,B_0 + \sin(\theta)A_0)\,\alpha_0 + \Big\{-4\mathrm{erf}(z)\mathrm{erfc}(z) + [(24 \\
&\times z^3 + 64\,z^5 - 4\,z)\,\mathrm{erf}(z) - 24\,z - 8\,z^3]\,e^{-z^2}\pi^{-\frac{1}{2}} + [-\frac{224}{3}\,e^{-z^2}\,z^4 + (64\,z^4 \\
&- 8\,z^2)\,e^{-2\,z^2}]\pi^{-1} - \frac{64}{3}\,e^{-z^2}\,z\pi^{-\frac{3}{2}}\Big\}\,[(B_0{}^2 - A_0{}^2)\sin(2\,\theta) \qquad \text{(B.3.2)} \\
&- 2\,A_0\,B_0\cos(2\,\theta)].
\end{aligned}
$$

where A_0 B_0 and A_1, B_1 are given in (3.3.13) and (3.3.16) respectively.

The non-homogenous term of the differential equation (3.1.4) when $n = 1$ and $m = 2$ is not presented due to its lengthly expression.

The non-homogenous term of the differential equation given by (3.1.4) when $n = 2$

and $m = 1$ is

$$
\begin{aligned}
\mathrm{R}_{2,1} &= 8\,(-1+4\,z^4-2\,z^2)\,e^{-z^2}\,(-\sin(\theta)\,B_1+\cos(\theta)\,A_1)\pi^{-\frac{1}{2}}+[-4\,z\,\mathrm{erfc}(z)\\
&+ (-16\,z^4+8\,z^2)\,e^{-z^2}\pi^{-\frac{1}{2}}]\,\alpha_1+\Big\{z\,\mathrm{erfc}(z)\,(6\,\mathrm{erf}(z)+64\,\sqrt{2}-67)-\frac{1}{3}\\
&\times [-12\,z^2\,\mathrm{erfc}(z)+(-136\,z^6+144\,z^8+3-36\,z^4)\,\mathrm{erf}(z)+24\,z^2-160\,z^6\\
&+ 128\,z^4+3]e^{-z^2}\pi^{-\frac{1}{2}}+[(\frac{76}{15}\,z+\frac{92}{5}\,z^3+\frac{176}{3}\,z^7-\frac{264}{5}\,z^5)\,e^{-z^2}+(\frac{208}{3}\\
&\times z^5-\frac{50}{3}z-\frac{44}{3}z^3-48z^7)e^{-2z^2}]\pi^{-1}+\frac{16}{3}(-1+4\,z^4-2\,z^2)e^{-z^2}\pi^{-\frac{3}{2}}\Big\}\\
&\times (A_0\sin(\theta)+\cos(\theta)\,B_0)\,\alpha_0+\Big\{-z\,\mathrm{erfc}(z)\,(18\,\mathrm{erf}(z)-47+96\,\sqrt{2})+\frac{1}{3}\\
&\times [(21-136z^6-24z^2+144z^8-36z^4)\mathrm{erf}(z)-68z^4+54z^2+48-40z^6]\\
&\times e^{-z^2}\pi^{-\frac{1}{2}}+[-\frac{16}{3}\,z\,\mathrm{erfc}(z)+(-\frac{92}{5}\,z^3-\frac{176}{3}\,z^7+\frac{44}{15}\,z+\frac{264}{5}\,z^5)\,e^{-z^2}\\
&+ (\frac{14}{3}z-\frac{208}{3}z^5+\frac{44}{3}z^3+48\,z^7)e^{-2z^2}]\pi^{-1}-\frac{32}{3}(2z^4-2-z^2)e^{-z^2}\pi^{-\frac{3}{2}}\Big\}\\
&\times [({A_0}^2-{B_0}^2)\sin(2\,\theta)+2\,A_0\,B_0\cos(2\,\theta)]. \qquad \text{(B.3.3)}
\end{aligned}
$$

where A_0 B_0 and A_1, B_1 are given in (3.3.13) and (3.3.16) respectively.

B.4 The solutions for scaled stream function components: $\Psi_{0,2}(z,\theta)$, $\Psi_{1,1}(z,\theta)$, $\Psi_{2,1}(z,\theta)$

The solution for $\Psi_{0,2}(z,\theta)$ is obtained by solving the differential equation (3.1.3) subject to (3.1.6) (when $n=0$ and $m=2$) and given by

$$
\begin{aligned}
\Psi_{0,2} &= \frac{1}{15}\Big\{ (-4z^5 - 20\,z^3 - 15\,z)\,\mathrm{erfc}(z) + [-8 + (4\,z^4 + 8 + 18\,z^2)e^{-z^2}]\pi^{-\frac{1}{2}} \Big\} \\
&\times \alpha_2 + \Bigg\{ \frac{1}{60}\,z\,\mathrm{erf}(z)\,\mathrm{erfc}(z)\,[(24\,z^4 + 40\,z^2 + 30)\,\mathrm{erf}(z) + 4\,z^4 + 15 + 20\,z^2] \\
&+ \{\frac{1}{15}\,[10 - 20\,z^2 + (-18\,z^4 - 11\,z^2 + 4)\,e^{-z^2}]\,\mathrm{erf}(z)^2 + \frac{1}{60}\,[24 + 80\,z^2 \\
&- 64\sqrt{2}\mathrm{erf}(\sqrt{2}z) + (5 + 40z^4 + 10z^2)e^{-z^2}]\mathrm{erf}(z) - \frac{2}{15} + \frac{1}{30}(4 + 9z^2 + 2z^4) \\
&\times e^{-z^2}\}\pi^{-\frac{1}{2}} + \Big\{ (\frac{27}{25}\,z^5\sqrt{3} + \frac{27}{5}z^3\sqrt{3} + \frac{81}{20}\sqrt{3}\,z)\,\mathrm{erf}(\sqrt{3}\,z) + (-\frac{4}{9}z^5 - \frac{4}{9}z^3 \\
&- \frac{1}{3}\,z)\,\mathrm{erf}(z)^2 + [(\frac{76}{75} - \frac{27}{25}\sqrt{3})\,z^5 + (\frac{148}{45} - \frac{27}{5}\sqrt{3})\,z^3 + (-\frac{81}{20}\sqrt{3} + \frac{37}{15})\,z \\
&- 4\,z\,e^{-z^2} + (\frac{8}{15}\,z - \frac{6}{5}\,z^3)\,e^{-2z^2}]\mathrm{erf}(z) - \frac{128}{225}z^5 - \frac{128}{45}\,z^3 - \frac{32}{15}z + \frac{4}{3}ze^{-z^2} \\
&+ (\frac{1}{3}\,z^3 - \frac{1}{6}\,z)\,e^{-2z^2} \Big\}\pi^{-1} + \Big\{ [-\frac{8}{15} - \frac{16}{9}\,z^2 + (-\frac{8}{9}\,z^4 - \frac{2}{9}\,z^2 - \frac{1}{9})\,e^{-z^2}] \\
&\times \mathrm{erf}(z) - \frac{43}{15} + \frac{54}{25}\sqrt{3} + \frac{16}{9}\,z^2 + [(\frac{76}{75} - \frac{27}{25}\sqrt{3})\,z^4 + (-\frac{243}{50}\sqrt{3} + \frac{64}{25})z^2 \\
&- \frac{54}{25}\sqrt{3} + \frac{127}{75}]\,e^{-z^2} - \frac{8}{3}\,e^{-2z^2} + (\frac{27}{25}\,z^4 + \frac{241}{50}\,z^2 + \frac{96}{25})\,e^{-3z^2} \Big\}\pi^{-3/2} \\
&+ \Big[(\frac{128}{45}\,z + \frac{512}{135}z^3 + \frac{512}{675}z^5)\,\mathrm{erfc}(z) - \frac{16}{9}z\,e^{-z^2} + (-\frac{4}{9}\,z^3 + \frac{2}{9}z)\,e^{-2z^2} \Big] \\
&\times \pi^{-2} + [\frac{1024}{675} + (-\frac{1024}{675} - \frac{256}{75}z^2 - \frac{512}{675}z^4)\,e^{-z^2}]\pi^{-5/2} \Big\}\alpha_0({A_0}^2 + {B_0}^2) \\
&+ \Bigg\{ -\frac{1}{6}\,\mathrm{erf}(z)\,z\,(4\,z^2 + 4\,z^4 + 3)\,\mathrm{erfc}(z) + \Big\{ [-\frac{4}{5} - \frac{8}{3}\,z^2 + (-\frac{1}{3}\,z^2 - \frac{1}{6}
\end{aligned}
$$

$$
\begin{aligned}
&- \frac{4}{3}z^4)\,e^{-z^2}]\,\mathrm{erfc}(z) + \frac{29}{30} + (\frac{2}{3}z^4 + \frac{1}{3}z^2)\,e^{-z^2}\Big\}\,\pi^{-\frac{1}{2}} + \Big[\,(-\frac{64}{15}z - \frac{256}{225}z^5 \\
&- \frac{256}{45}z^3)\,\mathrm{erfc}(z) + \frac{8}{3}z\,e^{-z^2} + (\frac{2}{3}z^3 - \frac{1}{3}z)e^{-2z^2}\Big]\,\pi^{-1} + (-\frac{512}{225} + (\frac{256}{225}z^4 \\
&+ \frac{512}{225} + \frac{128}{25}z^2)\,e^{-z^2})\pi^{-3/2}\Big\}\,(-A_1\,B_0 + B_1\,A_0) + \{[-\frac{8}{3}z^3 - 2z - \frac{8}{15}z^5] \\
&\times \mathrm{erfc}(z) + 2z + \frac{1}{15}\,[-16 + (16 + 8z^4 + 36z^2)\,e^{-z^2}]\pi^{-\frac{1}{2}}\}(\sin(\theta)\,B_2 - A_2 \\
&\times \cos(\theta)) + \Big\{\frac{1}{30}\,z\,\mathrm{erfc}(z)\,[(12z^4 + 20z^2 - 15)\,\mathrm{erf}(z) - 8z^4] + \{-\frac{32}{15}\beta_2(z) \\
&+ \frac{8}{15}\,\mathrm{erf}(z) + \frac{3}{2} + [(-\frac{4}{5}z^4 - \frac{3}{5}z^2 + \frac{29}{10})\,\mathrm{erf}(z) - \frac{3}{2} + \frac{2}{3}z^4]\,e^{-z^2}\}\pi^{-\frac{1}{2}} \\
&+ [(\frac{32}{15}z^3 + \frac{32}{75}z^5 + \frac{8}{5}z)\,\mathrm{erfc}(z) + (-\frac{2}{5}z^3 + \frac{1}{15}z)\,e^{-2z^2}]\pi^{-1} + [\frac{64}{75} - (\frac{64}{75} \\
&+ \frac{32}{75}z^4 + \frac{48}{25}z^2)\,e^{-z^2}]\pi^{-3/2}\Big\}\,\alpha_0\,(\sin(\theta)\,A_1 + \cos(\theta)\,B_1) + \Big\{-\frac{1}{15}\,\mathrm{erf}(z) \\
&\times z\,\mathrm{erfc}(z)\,[(15 + 8z^4 + 10z^2)\,\mathrm{erf}(z) + 16z^4 + 15 + 20z^2] + [(\frac{4}{3}z^2 - \frac{2}{3}) \\
&\times \mathrm{erf}(z)^2 + (\frac{4}{3}z^2 + \frac{2}{15} + \frac{32}{15}\sqrt{2}\,\mathrm{erf}(\sqrt{2}\,z))\,\mathrm{erf}(z) - \frac{8}{15} - \frac{8}{3}z^2 + \frac{16}{15}\sqrt{2} \\
&\times \mathrm{erf}(\sqrt{2}\,z) + [(\frac{8}{5}z^4 + \frac{11}{30}z^2 + \frac{97}{60})\,\mathrm{erf}(z)^2 + (\frac{7}{15}z^2 - \frac{41}{30})\,\mathrm{erf}(z) + \frac{8}{15} \\
&- \frac{2}{15}z^2 - \frac{16}{15}z^4\,\mathrm{erfc}(z)]\,e^{-z^2}]\pi^{-\frac{1}{2}} + [(\frac{8}{9}z^3 + \frac{32}{45}z^5)\,\mathrm{erf}(z)^2 + ((\frac{63}{50}\sqrt{3} \\
&+ \frac{16}{225})\,z^5 + (\frac{136}{45} + \frac{63}{10}\sqrt{3})\,z^3 + (\frac{189}{40}\sqrt{3} + \frac{44}{15})\,z + 4z\,e^{-z^2} + (-\frac{19}{15}z \\
&+ \frac{8}{5}z^3)e^{-2z^2})\mathrm{erf}(z) + (-\frac{189}{40}\sqrt{3}z - \frac{63}{10}z^3\sqrt{3} - \frac{63}{50}z^5\sqrt{3})\mathrm{erf}(\sqrt{3}\,z) - \frac{72}{5}\beta_1(z) \\
&- \frac{176}{225}z^5 - \frac{176}{45}z^3 + (-\frac{44}{15} + \frac{4}{3}e^{-z^2})\,z + (\frac{8}{15}z^3 - \frac{1}{5}z)\,e^{-2z^2}]\pi^{-1} + [-\frac{16}{9} \\
&\times z^2\,\mathrm{erfc}(z) - \frac{63}{25}\sqrt{3} + \frac{8}{45}\mathrm{erf}(z) + \frac{64}{45}\sqrt{2}\mathrm{erf}(\sqrt{2}\,z) - \frac{38}{75} + (\frac{1}{45}\,(28z^2 - 82
\end{aligned}
$$

$$
\begin{aligned}
&+ \; 64\,z^4)\,\mathrm{erf}(z) + (\frac{16}{225} + \frac{63}{50}\sqrt{3})\,z^4 + (\frac{567}{100}\sqrt{3} + \frac{772}{225})\,z^2 + \frac{63}{25}\sqrt{3} + \frac{194}{75}) \\
&\times \; e^{-z^2} + \frac{8}{3}e^{-2z^2} + (-\frac{1667}{300}z^2 - \frac{63}{50}z^4 - \frac{356}{75})\,e^{-3z^2}]\pi^{-3/2} - [(\frac{176}{45}z + \frac{704}{135} \\
&\times \; z^3 + \frac{704}{675}\,z^5)\,\mathrm{erfc}(z) + \frac{16}{9}\,z\,e^{-z^2} + (\frac{32}{45}\,z^3 - \frac{4}{15}\,z)\,e^{-2\,z^2}]\pi^{-2} + [-\frac{1408}{675} \\
&+ \; (\frac{1408}{675} + \frac{704}{675}z^4 + \frac{352}{75}z^2)e^{-z^2}]\pi^{-\frac{5}{2}} \Big\}\,({A_0}^2 + {B_0}^2)(\cos(\theta)A_0 - \sin(\theta)B_0) \\
&+ \; \Big\{ -\frac{1}{15}\,\mathrm{erf}(z)\,(4\,z^5 + 15\,z)\,\mathrm{erfc}(z) + \{-\frac{8}{3}\,z^2\,\mathrm{erfc}(z) + \frac{4}{3}\,\mathrm{erf}(z) - \frac{32}{15}\,\beta_2(\mathrm{z}) \\
&+ \; \frac{28}{15} + [(-\frac{46}{15} + \frac{4}{15}\,z^2 - \frac{8}{15}\,z^4)\,\mathrm{erfc}(z) + \frac{6}{5} - \frac{2}{15}\,z^2 + \frac{4}{15}\,z^4]\,e^{-z^2}\}\pi^{-\frac{1}{2}} \\
&+ \; [(-\frac{32}{45}\,z^5 - \frac{8}{3}\,z - \frac{32}{9}\,z^3)\,\mathrm{erfc}(z) + \frac{8}{3}\,z\,e^{-z^2} + (\frac{4}{15}\,z^3 - \frac{4}{15}\,z)\,e^{-2\,z^2}]\pi^{-1} \\
&+ \; \frac{1}{45}\,[-64 + (32\,z^4 + 64 + 144\,z^2)\,e^{-z^2}]\pi^{-\frac{3}{2}} \Big\}\,(B_0\cos(\theta) + A_0\sin(\theta))\,\alpha_1 \\
&+ \; \Big\{ \frac{1}{60}\,z\,\mathrm{erf}(z)\,\mathrm{erfc}(z)[(30 + 8z^4)\mathrm{erf}(z) - 15 + 20\,z^2 - 4z^4] + \{(\frac{16}{15} - \frac{16}{15}\beta_2(\mathrm{z})) \\
&\times \; \mathrm{erf}(z) - \frac{8}{5}\beta_2(\mathrm{z}) + \frac{7}{15} + [(\frac{11}{30}z^2 - \frac{113}{60} - \frac{2}{5}z^4)\,\mathrm{erf}(z)^2 + (\frac{2}{5}z^4 + \frac{133}{60} - \frac{31}{30}\,z^2) \\
&\times \; \mathrm{erf}(z) + \frac{11}{30}\,z^2 - \frac{7}{15} - \frac{1}{15}\,z^4]e^{-z^2}\}\pi^{-\frac{1}{2}} + \{(\frac{1}{3}\,z - \frac{4}{15}\,z^5 - \frac{4}{9}\,z^3)\,\mathrm{erf}(z)^2 \\
&+ \; [(\frac{12}{25} - \frac{9}{50}\sqrt{3})\,z^5 + (-\frac{9}{10}\sqrt{3} + \frac{28}{45})\,z^3 + (-\frac{27}{40}\sqrt{3} - \frac{13}{15})\,z + (\frac{11}{15}\,z - \frac{2}{5}\,z^3) \\
&\times \; e^{-2\,z^2}]\mathrm{erf}(z) + (\frac{9}{50}\,z^5\sqrt{3} + \frac{27}{40}\sqrt{3}\,z + \frac{9}{10}\,z^3\sqrt{3})\,\mathrm{erf}(\sqrt{3}\,z) + \frac{8}{15}\,z - \frac{16}{75}\,z^5 \\
&- \; \frac{8}{45}\,z^3 + (-\frac{7}{10}\,z + \frac{1}{5}\,z^3)\,e^{-2\,z^2} + \frac{72}{5}\,\beta_1(\mathrm{z})\}\pi^{-1} + \{\frac{17}{15} - \frac{64}{45}\,\beta_2(\mathrm{z}) + \frac{9}{25}\sqrt{3} + \frac{16}{45} \\
&\times \; \mathrm{erf}(z) + [(\frac{29}{15} - \frac{2}{5}z^2 - \frac{8}{15}z^4)\mathrm{erf}(z) + (-\frac{9}{50}\sqrt{3} + \frac{12}{25})z^4 + (-\frac{81}{100}\sqrt{3} + \frac{4}{25}) \\
&\times \; z^2 - \frac{9}{25}\sqrt{3} - \frac{51}{25}]e^{-z^2} + (\frac{9}{50}\,z^4 + \frac{68}{75} + \frac{221}{300}\,z^2)\,e^{-3z^2}\}\pi^{-\frac{3}{2}} + [(\frac{16}{15}z + \frac{64}{45}z^3 \\
&+ \; \frac{64}{225}\,z^5)\,\mathrm{erfc}(z) - \frac{2}{45}\,z\,(-1 + 6\,z^2)\,e^{-2\,z^2}]\pi^{-2} + \frac{1}{225}\,[128 + (-64z^4 - 288z^2
\end{aligned}
$$

$$
\begin{aligned}
&- \ 128)e^{-z^2}]\pi^{-\frac{5}{2}} \Big\} (\sin(\theta)B_0 - \cos(\theta)A_0)\alpha_0{}^2 + \Big\{ -\frac{1}{60} z\,\mathrm{erfc}(z)[(8z^4 - 40z^2 \\
&+ \ 90)\,\mathrm{erf}(z)^2 + (-15 + 60\,z^2 + 28\,z^4)\,\mathrm{erf}(z) - 32\,z^4] + [(\frac{2}{3} - \frac{4}{3}\,z^2)\,\mathrm{erf}(z)^2 \\
&+ \ (\frac{4}{3}\,z^2 - \frac{34}{15} + \frac{16}{5}\,\sqrt{2}\,\mathrm{erf}(\sqrt{2}\,z))\,\mathrm{erf}(z) + \frac{16}{3}\,\sqrt{2}\,\mathrm{erf}(\sqrt{2}\,z) - \frac{7}{3} + [(-\frac{11}{5}\,z^2 \\
&+ \ \frac{2}{5}\,z^4 + \frac{39}{5})\,\mathrm{erf}(z)^2 + (\frac{17}{6}\,z^2 - \frac{29}{4} + \frac{2}{3}\,z^4)\,\mathrm{erf}(z) + \frac{1}{6}\,z^2 - z^4 + \frac{7}{3}]\,e^{-z^2}] \\
&\times \ \pi^{-\frac{1}{2}} + [(\frac{28}{45}\,z^5 - \frac{5}{3}z + \frac{4}{3}z^3)\mathrm{erf}(z)^2 + ((-\frac{9}{25}\sqrt{3} - \frac{4}{75})z^5 + (\frac{148}{45} - \frac{9}{5}\sqrt{3})z^3 \\
&+ \ (-\frac{27}{20}\sqrt{3} + \frac{97}{15})z - 4ze^{-z^2} + (\frac{2}{5}\,z^3 - \frac{12}{5}\,z)\,e^{-2\,z^2})\mathrm{erf}(z) + (\frac{9}{25}\,z^5\,\sqrt{3} + \frac{27}{20} \\
&\times \ \sqrt{3}\,z + \frac{9}{5}\,z^3\,\sqrt{3})\,\mathrm{erf}(\sqrt{3}\,z) - \frac{128}{225}\,z^5 - \frac{24}{5}\,z - \frac{288}{5}\,\beta_1(z) - \frac{208}{45}\,z^3 + \frac{4}{3}\,z\,e^{-z^2} \\
&+ \ \frac{1}{6}(7z + 2z^3)e^{-2z^2}]\pi^{-1} + \{\frac{16}{9}z^2\mathrm{erfc}(z) - \frac{1649}{225} + \frac{256}{45}\sqrt{2}\,\mathrm{erf}(\sqrt{2}\,z) + \frac{18}{25}\sqrt{3} \\
&- \ \frac{88}{45}\,\mathrm{erf}(z) + [(-\frac{353}{45} + \frac{56}{45}\,z^4 + \frac{62}{45}\,z^2)\,\mathrm{erf}(z) + (-\frac{9}{25}\,\sqrt{3} - \frac{4}{75})\,z^4 + (\frac{896}{225} \\
&- \ \frac{81}{50}\,\sqrt{3})\,z^2 - \frac{18}{25}\,\sqrt{3} + \frac{2201}{225}]e^{-z^2} - \frac{8}{3}e^{-2z^2} + (\frac{281}{150}\,z^2 + \frac{9}{25}z^4 + \frac{16}{75})e^{-3z^2}\} \\
&\times \ \pi^{-3/2} + [(-\frac{256}{675}\,z^5 - \frac{256}{135}\,z^3 - \frac{64}{45}\,z)\,\mathrm{erfc}(z) - \frac{16}{9}\,z\,e^{-z^2} + (\frac{2}{45}\,z + \frac{28}{45}\,z^3) \\
&\times \ e^{-2\,z^2}]\pi^{-2} + \frac{1}{675}[-512 + (256\,z^4 + 512 + 1152\,z^2)\,e^{-z^2}]\pi^{-\frac{5}{2}} \Big\} [(B_0{}^2 - A_0{}^2) \\
&\times \ \cos(2\,\theta) + 2\,A_0 B_0 \sin(2\,\theta)]\alpha_0 + \Big\{ -\frac{1}{30}\,z\,\mathrm{erfc}(z)\,[(20\,z^2 + 4\,z^4 - 45)\,\mathrm{erf}(z) \\
&+ \ 16\,z^4 + 80\,z^2] + \{[\frac{8}{3}\,z^2 + \frac{28}{15} + (-\frac{13}{15}\,z^2 + \frac{179}{30} - \frac{4}{15}\,z^4)\,e^{-z^2}]\,\mathrm{erfc}(z) + \frac{64}{15} \\
&\times \ \sqrt{2}\,\mathrm{erf}(\sqrt{2}\,z) - \frac{9}{2} + \frac{1}{3}(2z^4 - 10 + 9z^2)e^{-z^2}\}\pi^{-\frac{1}{2}} + [(\frac{16}{15}z + \frac{64}{45}z^3 + \frac{64}{225}z^5) \\
&\times \ \mathrm{erfc}(z) - \frac{8}{3}ze^{-z^2} + (\frac{1}{5}z + \frac{2}{15}z^3)e^{-2\,z^2}]\pi^{-1} + \frac{1}{225}\,[128 + (-64\,z^4 - 288\,z^2 \\
&- \ 128)\,e^{-z^2}]\pi^{-\frac{3}{2}} \Big\} [(B_1\,A_0 + A_1\,B_0)\cos(2\,\theta) + (-B_0\,B_1 + A_1\,A_0)\sin(2\,\theta)]
\end{aligned}
$$

$$
\begin{aligned}
+ \quad & \Bigg\{ -\frac{1}{15} z\,\mathrm{erf}(z)\mathrm{erfc}(z)[(-10z^2+15)\mathrm{erf}(z)+4z^4] + [(\frac{32}{15}\sqrt{2}\mathrm{erf}(z)+\frac{16}{5}\sqrt{2}) \\
\times \quad & \mathrm{erf}(\sqrt{2}\,z) + (\frac{2}{3}-\frac{4}{3}z^2)\mathrm{erf}(z)^2 + (-\frac{4}{3}z^2-\frac{6}{5})\mathrm{erf}(z) - \frac{14}{5}+\frac{8}{3}z^2 + ((-\frac{11}{6}z^2 \\
+ \quad & \frac{71}{12})\,\mathrm{erf}(z)^2 + (\frac{11}{15}\,z^2 - \frac{133}{30} + \frac{8}{15}z^4)\,\mathrm{erf}(z) + \frac{14}{5} - \frac{4}{15}\,z^4 + \frac{4}{5}z^2)e^{-z^2}]\pi^{-\frac{1}{2}} \\
+ \quad & \{(-\frac{4}{3}\,z + \frac{8}{9}\,z^3 + \frac{16}{45}\,z^5)\,\mathrm{erf}(z)^2 + [(-\frac{64}{225} - \frac{27}{50}\sqrt{3})\,z^5 + (-\frac{27}{10}\sqrt{3} - \frac{8}{15})\,z^3 \\
+ \quad & (\frac{8}{5} - \frac{81}{40}\sqrt{3})\,z]\mathrm{erf}(z) + (\frac{81}{40}\sqrt{3}z + \frac{27}{10}z^3\sqrt{3} + \frac{27}{50}z^5\sqrt{3})\mathrm{erf}(\sqrt{3}\,z) - \frac{216}{5}\beta_1(z) \\
- \quad & \frac{4}{15}\,z - \frac{16}{225}\,z^5 - \frac{16}{45}\,z^3 + (-4\,z\,\mathrm{erf}(z) - \frac{4}{3}\,z)\,e^{-z^2} + (\frac{1}{15}\,z + \frac{4}{15}\,z^3 - \frac{5}{3}\,z \\
\times \quad & \mathrm{erf}(z))e^{-2z^2}\}\pi^{-1} + \{(-\frac{8}{5} - \frac{16}{9}z^2)\mathrm{erf}(z) - \frac{874}{225} + \frac{27}{25}\sqrt{3} + \frac{16}{9}z^2 + \frac{64}{15}\sqrt{2} \\
\times \quad & \mathrm{erf}(\sqrt{2}\,z) + [(\frac{32}{45}\,z^4 - \frac{266}{45} + \frac{44}{45}\,z^2)\,\mathrm{erf}(z) + (-\frac{64}{225} - \frac{27}{50}\sqrt{3})\,z^4 + (\frac{4}{75} \\
- \quad & \frac{243}{100}\sqrt{3})z^2 + \frac{1222}{225} - \frac{27}{25}\sqrt{3}]e^{-z^2} - \frac{8}{3}e^{-2z^2} + (\frac{28}{25} + \frac{261}{100}z^2 + \frac{27}{50}z^4)e^{-3z^2}\} \\
\times \quad & \pi^{-\frac{3}{2}} + [(-\frac{64}{135}\,z^3 - \frac{16}{45}\,z - \frac{64}{675}\,z^5)\,\mathrm{erfc}(z) - \frac{16}{9}\,z\,e^{-z^2} + (\frac{16}{45}\,z^3 + \frac{4}{45}\,z) \\
\times \quad & e^{-2\,z^2}]\pi^{-2} + \frac{1}{675}\,[-128 + (64\,z^4 + 288\,z^2 + 128)\,e^{-z^2}]\pi^{-\frac{5}{2}}\Bigg\}\,[(-3\,A_0\,{B_0}^2 \\
+ \quad & {A_0}^3)\cos(3\,\theta) + ({B_0}^3 - 3\,B_0\,{A_0}^2)\sin(3\,\theta)] \qquad \text{(B.4.1)}
\end{aligned}
$$

where A_0 B_0 and A_1, B_1 are given in (3.3.13) and (3.3.16), respectively, and

$$\beta_1(z) = \int \frac{\mathrm{erf}(z)}{(e^{(z^2)})^2}\,dz, \quad \beta_2(z) = \sqrt{2}\,\mathrm{erf}(\sqrt{2}\,z).$$

The solution for $\Psi_{1,1}(z,\theta)$ is obtained by solving the differential equation (3.1.3) subject to (3.1.6) (when $n=1$ and $m=1$) and given by

$$
\begin{aligned}
\Psi_{1,1} \quad = \quad & \frac{1}{16}\,[(-4\,z^2 - 12\,z^4 - 1)\,\mathrm{erfc}(z) + 1 + (12\,z^3 - 2\,z)e^{-z^2}\pi^{\frac{-1}{2}}]\alpha_1 + \{\frac{1}{6}(-3z^2 \\
& +7z^4)\mathrm{erfc}(z) + \frac{1}{8}\mathrm{erf}(z) + \frac{1}{12}[-16z + (-14z^3 + 13z)e^{-z^2}]\pi^{-\frac{1}{2}}\}(A_1\cos(\theta)
\end{aligned}
$$

$$
\begin{aligned}
&-B_1\sin(\theta))+\left\{\frac{1}{48}\operatorname{erfc}(z)\,(24\operatorname{erf}(z)-57+64\sqrt{2})\,z^4+\frac{1}{16}\,(64\sqrt{2}-65)\,z^2\right.\\
&\times\operatorname{erfc}(z)+\frac{1}{64}\operatorname{erf}(z)\,(-64\sqrt{2}+104\operatorname{erf}(z)+9)+[\frac{2}{3}z(-7+8\sqrt{2}+3\operatorname{erf}(z)\\
&-4\sqrt{2}\operatorname{erf}(\sqrt{2}\,z))+(-\frac{1}{6}\,(12z^3+19z)\operatorname{erf}(z)+(\frac{27}{16}-\frac{4}{3}\sqrt{2})z^3+\frac{421}{96}z-\frac{10}{3}\\
&\times\sqrt{2}\,z)\,e^{-z^2}]\pi^{-\frac{1}{2}}+\left[\frac{1}{9}z^2(-3+7z^2)\operatorname{erfc}(z)+\frac{16}{15}+\frac{1}{12}\operatorname{erf}(z)+(\frac{4}{3}z^2+\frac{64}{15})\right.\\
&\left.\left.\times e^{-z^2}+(-\frac{16}{3}-\frac{3}{2}\,z^2)\,e^{-2z^2}\right]\pi^{-1}+\frac{1}{18}\,[-16\,z+(-14\,z^3+13\,z)e^{-z^2}]\pi^{-\frac{3}{2}}\right\}\\
&\times(\sin(\theta)\,A_0+B_0\cos(\theta))\,\alpha_0+\left\{(-\frac{13}{8}+\frac{1}{2}\,z^4)\operatorname{erf}(z)^2+[(-2\sqrt{2}+\frac{37}{48})\,z^4\right.\\
&+(\frac{77}{16}-6\sqrt{2})z^2+\frac{45}{64}-\frac{3}{2}\sqrt{2}]\operatorname{erfc}(z)-\frac{45}{64}-\frac{1}{2}\,z^4+\frac{3}{2}\sqrt{2}+\left\{\frac{2}{3}z(-3\operatorname{erf}(z)\right.\\
&-12\sqrt{2}+9+4\sqrt{2}\operatorname{erf}(\sqrt{2}\,z))+[(\frac{19}{6}\,z+2\,z^3)\operatorname{erf}(z)+(-\frac{37}{48}+2\sqrt{2})\,z^3\\
&\left.\left.+(-\frac{147}{32}+5\sqrt{2})\,z]\,e^{-z^2}\right\}\pi^{-\frac{1}{2}}+\left[(-\frac{5}{9}z^4+z^2+\frac{1}{4})\operatorname{erfc}(z)-\frac{79}{60}+(-\frac{4}{3}z^2\right.\right.\\
&\left.\left.-\frac{64}{15})\,e^{-z^2}+(\frac{3}{2}\,z^2+\frac{16}{3})e^{-2z^2}\right]\pi^{-1}+\frac{1}{18}[32z+(-23z+10\,z^3)e^{-z^2}]\pi^{-\frac{3}{2}}\right\}\\
&\times(2\,A_0\,B_0\cos(2\,\theta)+(\,{A_0}^2-\,{B_0}^2)\sin(2\,\theta)). \qquad \text{(B.4.2)}
\end{aligned}
$$

The solution for $\Psi_{2,1}(z,\theta)$ is obtained by solving the differential equation (3.1.3) subject to (3.1.6) (when $n=2$ and $m=1$) and given by

$$
\begin{aligned}
\Psi_{2,1} \;=\;& \frac{1}{120}\,[-4\,(5\,z^3+16\,z^5)\operatorname{erfc}(z)+-3+(3+18\,z^2+64\,z^4)\,e^{-z^2}\pi^{-\frac{1}{2}}]\,\alpha_1\\
+\;& \left\{(-\frac{11}{30}\,z^5-\frac{1}{4}\,z^3+\frac{11}{8}\,z)\operatorname{erf}(z)^2+[(\frac{403}{240}-\frac{28}{15}\sqrt{2})\,z^5+(-\frac{19}{48}\right.\\
-\;& \left.\frac{4}{3}\sqrt{2})\,z^3+(\sqrt{2}-\frac{201}{64})\,z]\operatorname{erf}(z)+(-\frac{21}{16}+\frac{28}{15}\sqrt{2})\,z^5+(\frac{31}{48}\right.\\
+\;& \left.\frac{4}{3}\sqrt{2})\,z^3+\left\{(-\frac{101}{15}\sqrt{2}-\frac{4}{3}\,z^2\sqrt{2})\operatorname{erf}(\sqrt{2}\,z)+(\frac{2}{3}\,z^2+\frac{43}{12})\operatorname{erf}(z)\right.\\
-\;& \left.\frac{4}{15}\sqrt{2}+\frac{2}{3}\,z^2+\frac{427}{120}+[(\frac{1}{2}\,z^6+\frac{27}{20}\,z^4+\frac{68}{15}\,z^2+\frac{373}{40})\operatorname{erf}(z)\right.
\end{aligned}
$$

$$
\begin{aligned}
&+ \left(\frac{81}{80} - \frac{28}{15}\sqrt{2}\right) z^4 + \left(-\frac{2}{5}\sqrt{2} - \frac{1193}{480}\right) z^2 + \frac{4}{15}\sqrt{2} - \frac{427}{120}]e^{-z^2}\Big\}\pi^{-\frac{1}{2}} \\
&+ \Big[\left(\frac{1189}{315} z^3 + \frac{1889}{1575} z^5 + \frac{1189}{420} z\right)\operatorname{erfc}(z) - \frac{23}{20} z + \left(-\frac{2}{3} z^5 - \frac{82}{45} z^3\right. \\
&- \left.\frac{703}{210} z\right) e^{-z^2} + \left(\frac{1}{2} z^5 + \frac{22}{15} z^3 + \frac{167}{60} z\right) e^{-2z^2}\Big]\pi^{-1} + \left(\frac{4}{9} z^2 + \frac{509}{350}\right. \\
&+ \left.\left(-\frac{1889}{1575} z^4 - \frac{509}{350} - \frac{11051}{3150} z^2\right) e^{(-z^2)}\pi^{-\frac{3}{2}}\right\}\left(\sin(\theta)\, A_0 + B_0 \cos(\theta)\right)\alpha_0 \\
&+ \frac{1}{120}[(15\, z + 84\, z^5 + 20\, z^3)\operatorname{erfc}(z) - 40\, z^3 - 15\, z + (80\, z^2 - 2 \\
&+ (-38\, z^2 - 84\, z^4 + 2)\, e^{-z^2})\pi^{-\frac{1}{2}}] \times (A_1 \cos(\theta) - B_1 \sin(\theta)) + \Big\{\frac{1}{120} z \\
&\times (68\, z^4 - 30\, z^2 - 345)\operatorname{erf}(z)^2 + \frac{1}{79452960}(19 + 288\sqrt{2})[662108\, z^5 \\
&+ (-63080 + 956160\sqrt{2})\, z^3 + (-898125 + 1068480\sqrt{2})\, z]\operatorname{erf}(z) \\
&+ \left(-\frac{12}{5}\sqrt{2} - \frac{29}{40}\right) z^5 - \frac{20}{3} z^3 + \Big\{\left(\frac{16}{3} z^2\sqrt{2} + \frac{122}{15}\sqrt{2}\right)\operatorname{erf}(\sqrt{2}\, z) \\
&+ \left(-\frac{263}{60} - \frac{8}{3} z^2\right)\operatorname{erf}(z) - \frac{593}{120} - \frac{4}{3} z^2 + \frac{6}{5}\sqrt{2} + [\left(-\frac{1}{2} z^6 - \frac{19}{20} z^4 - \frac{86}{15} z^2\right. \\
&- \left.\frac{451}{40}\right)\operatorname{erf}(z) + \left(\frac{13}{40} + \frac{12}{5}\sqrt{2}\right) z^4 + \left(\frac{1901}{240} - \frac{6}{5}\sqrt{2}\right) z^2 - \frac{6}{5}\sqrt{2} \\
&+ \frac{593}{120}]e^{-z^2}\Big\}\pi^{-\frac{1}{2}} + [\left(-\frac{592}{315} z^5 - \frac{494}{63} z^3 - \frac{40}{7} z\right)\operatorname{erfc}(z) + \frac{79}{30} z \\
&+ \frac{1}{630}\left(420\, z^5 + 1148\, z^3 + 849\, z\right) e^{(-z^2)} - \frac{1}{60}\left(30\, z^5 + 76\, z^3 - 31\, z\right) \\
&\times e^{-2z^2}]\pi^{-1} + [-\frac{197}{70} - \frac{16}{9} z^2 + \left(\frac{592}{315} z^4 + \frac{2279}{315} z^2 + \frac{197}{70}\right) e^{-z^2}]\pi^{-\frac{3}{2}}\Big\} \\
&\times [({A_0}^2 - {B_0}^2)\sin(2\,\theta) + 2\, A_0\, B_0 \cos(2\,\theta)]. \qquad \text{(B.4.3)}
\end{aligned}
$$

Appendix C

Appendix for Chapter 4

C.1 Fourier Spectrum

In this appendix we give the outline of analyzing the spectrum of a data results, $g(t_j, g_j)_{j=0}^{N}$, viewed by the time domain in which the vertical deflection is the signals amplitude, and the horizontal deflection is the time variable. Here g is a discrete data results, $t_j = j\Delta t$ where Δt is a uniform time increment, N is the number of time sampling and g_j is the signals amplitude. The main idea in calculating the spectrum of these data is to transform, g, from the time domain to the frequency domain by using the discrete fourier transform (DFT). Thus, assume that the frequency domain is divided into N equal subintervals with radian-frequency interval $\Delta\omega = 2\pi/NT$. Then, the Fourier transform function, G, of the signal g is defined by

$$G(n\Delta\omega) = \sum_{j=0}^{N-1} g(j\Delta t) e^{-i\, j\Delta t\, n\Delta\omega}$$

where i is complex number.

C.2 Calculation of the Pressure distribution

The Poisson's equation for the pressure is given by

$$\frac{\partial^2 p}{\partial x^2} + \frac{\partial^2 p}{\partial y^2} = -4\left[\frac{\partial u}{\partial y}\frac{\partial v}{\partial x} - \frac{\partial v}{\partial y}\frac{\partial u}{\partial x}\right], \tag{C.2.1}$$

which can be rewritten in the (ξ, θ) coordinates as

$$\frac{\partial^2 p}{\partial \xi^2} + \frac{\partial^2 p}{\partial \theta^2} = -4\left[\frac{\partial v_\theta}{\partial \xi}\left(\frac{\partial u_\xi}{\partial \theta} + v_\theta\right) - \frac{\partial u_\xi}{\partial \xi}\left(u_\xi + \frac{\partial v_\theta}{\partial \theta}\right)\right]. \tag{C.2.2}$$

Hence, to determine the pressure distribution throughout the flow field we solve equation C.2.2 together with the angular and radial momentum equations given in (2.1.30) and (2.1.31). For more convenience, equations (C.2.2), (2.1.30) and (2.1.31) can be rewritten respectively as

$$\frac{\partial^2 p}{\partial \xi^2} + \frac{\partial^2 p}{\partial \theta^2} = H_1(\xi, \theta, t), \tag{C.2.3}$$

$$\frac{\partial p}{\partial \xi} = H_2(\xi, \theta, t), \tag{C.2.4}$$

$$\frac{\partial p}{\partial \theta} = H_3(\xi, \theta, t), \tag{C.2.5}$$

where H_1, H_2 and H_3 are assumed to be known functions.

By integrating equation (C.2.5) with respect to θ from 0 to θ, we obtain

$$p(\xi, \theta, t) = \int_0^\theta H_3(\xi, \theta, t)d\theta + p(\xi, 0, t). \tag{C.2.6}$$

By implementing the periodicity condition for the p, u_ξ, v_θ and ζ, they may rewrite some quantities in terms of Fourier expansion as follows

$$p(\xi, \theta, t) = \frac{1}{2}p_0(\xi, t) + \sum_{n=1}^{\infty}\left[p_n(\xi, t)\cos(n\theta) + q_n(\xi, t)\sin(n\theta)\right], \tag{C.2.7}$$

$$\int_0^\theta H_3(\xi,\theta,t)d\theta = \frac{1}{2}H_{30}^c(\xi,t) + \sum_{n=1}^{\infty}\left[H_{3n}^c(\xi,t)\cos(n\theta) + H_{3n}^s(\xi,t)\sin(n\theta)\right], \tag{C.2.8}$$

$$H_1(\xi,\theta,t) = \frac{1}{2}H_{10}^c(\xi,t) + \sum_{n=1}^{\infty}\left[H_{1n}^c(\xi,t)\cos(n\theta) + H_{1n}^s(\xi,t)\sin(n\theta)\right], \tag{C.2.9}$$

$$H_2(\xi,\theta,t) = \frac{1}{2}H_{20}^c(\xi,t) + \sum_{n=1}^{\infty}\left[H_{2n}^c(\xi,t)\cos(n\theta) + H_{2n}^s(\xi,t)\sin(n\theta)\right] \tag{C.2.10}$$

It can be easily seen that $p_n = H_{3n}^c$ and $q_n = H_{3n}^s$ for $n = 1, 2, \cdots$. Thus, p_0 is the only unknown in the Fourier series expansion for the pressure (C.2.7). In order to determine p_0 we substitute the expansion (C.2.7) into (C.2.3) and eliminate all the trigonometric terms in the resulting expression to obtain

$$\frac{\partial^2 p_0}{\partial \xi^2} = H_{10}^c(\xi,t). \tag{C.2.11}$$

The required boundary conditions for p_0 at the outer boundaries and the surface of the cylinder are determined from C.2.3 and C.2.4 after making use of the boundary conditions (2.1.34)-(2.1.36). These conditions are

$$\begin{aligned} &\frac{\partial p_0}{\partial \xi} = H_{20}^c(\xi,t) \quad \text{at } \xi = 0 \\ &\frac{\partial p_0}{\partial \xi} \to 0 \qquad\qquad \text{as } \xi \to \infty. \end{aligned} \tag{C.2.12}$$

Finally, the second order finite difference scheme is used to solve equation (C.2.11) subject (C.2.12) with the uniform grids $\Delta\xi$.

C.3 Transformation of frame of reference for potting streamlines

The stream function that plots the streamlines in a moving frame of reference with respect to both the translational and oscillation motions of the cylinder is defined by

$$\Psi_I(\xi,\theta,t) = \Psi(\xi,\theta,t) - e^{\xi}\sin(\theta) + 2\pi f A e^{\xi}(\sin(\eta)\sin(2\pi f t)\cos(\theta) - \cos(\eta)\sin(2\pi f t)\sin(\theta)) \tag{C.3.1}$$

where Ψ represents the stream function in the fixed frame of reference with respect to the translational and oscillation motions defined in (2.1.28).

Bibliography

Abramowitz, M. and Stegun, A., Ed., (1972). *Handbook of Mathematical Functions.* Dover Publications, New York.

Anagnostopoulos, P. (1997). Computer-aided flow visualization and vorticity balance in the laminar wake of a circular cylinder. *Journal of Fluids and Structures*, 11(1):33–72.

Anagnostopoulos, P. (2002). *Flow-Induced Vibrations in Engineering Practice.* WIT Press, Ashurst, UK.

Ascher, U. M., Mattheij, R. M. M., and Russell, R. D. (1995). *Numerical Solution of Boundary Value Problems for Ordinary Differential Equations.* SIAM, Philadelphia.

Ayyalasomayajula, H., Mutnuri, P. K., Ghia, K., and Ghia, U. (2003). Analysis of higher-order compact differencing scheme by studying flow past a circular cylinder. *Proceedings of the Second MIT conference on Computational Fluid and Solid Mechanics (Editor: K. J. Bathe)*, Elsevier Science, 1:830–833.

Badr, H. M., Coutanceau, M., Dennis, S. C. R., and Menard, C. (1990). Unsteady flow past a rotating circular cylinder at Reynolds numbers 10^3 and 10^4. *Journal of Fluid Mechanics*, 220:459–484.

Badr, H. M. and Dennis, S. C. R. (1985). Time-dependent viscous flow past an impulsively started rotating and translating circular cylinder. *Journal of Fluid Mechanics*, 158:447–488.

Badr, H. M., Dennis, S. C. R., and Kocabiyik, S. (1995a). The initial oscillatory flow

past a circular cylinder. *Journal of Engineering Mathematics*, 29:255–269.

Badr, H. M., Dennis, S. C. R., Kocabiyik, S., and Nguyen, P. (1995b). Viscous oscillatory flow about a circular cylinder at small to moderate Strouhal number. *Journal of Fluid Mechanics*, 303:215–232.

Badr, H. M., Dennis, S. C. R., and Young, P. J. S. (1989). Steady and unsteady flow past a rotating circular cylinder at low Reynolds numbers. *Computers and Fluids*, 17(4):579–609.

Baek, S.-J., Lee, S. B., and Sung, H. J. (2001). Response of a circular cylinder wake to superharmonic excitation. *Journal of Fluid Mechanics*, 422:67–88.

Baek, S.-J. and Sung, H. J. (1998). Numerical simulation of the flow behind a rotary oscillating circular cylinder. *Physics of Fluids*, 10(4):869–876.

Baek, S.-J. and Sung, H. J. (2000). Quasi-periodicity in the wake of a rotationally oscillating cylinder. *Journal of Fluid Mechanics*, 408:275–300.

Barkley, D. and Henderson, R. D. (1996). Three-dimensional floquent stability analysis of the wake of a circular cylinder. *Journal of Fluid Mechanics*, 322:215–241.

Bearman, P. W. (1984). Vortex shedding from oscillating bluff bodies. *Annual Review of Fluid Mechanics*, 16:195–222.

Bishop, R. E. D. and Hassan, A. (1964). The lift and drag forces on a circular cylinder oscillating in a flowing fluid. *Proceedings of the Royal Society (London)*, Series A 277:51–75.

Blackburn, H. M., Elston, J. R., and Sheridan, J. (1999). Bluff-body propulsion produced by combined rotary and translational oscillation. *Physics of Fluids*, 11(1):4-6.

Blackburn, H. M. and Henderson, R. D. (1999). A study of two-dimensional flow past an oscillating cylinder. *Journal of Fluid Mechanics*, 385:255-286.

Braza, M., Chassaing, P., and Minh, H. H. (1986). Numerical study and physical analysis of the pressure and velocity fields in the near wake of a circular cylinder. *Journal of Fluid Mechanics*, 165:79–130.

Carberry, J., Sheridan, J., and Rockwell, D. (2001). Forces and wake modes of an oscillating cylinder. *Journal of Fluids and Structures*, 15:523–532.

Cetiner, O. and Rockwell, D. (2001). Streamwise oscillations of a cylinder in a steady current. Part 1: Locked-on stages of vortex formation and loading. *Journal of Fluid Mechanics*, 427:1–28.

Cheng, M., Chew, Y. T., and Luo, S. C. (2001). Numerical investigation of a rotationally oscillating cylinder in mean flow. *Journal of Fluids and Structures*, 15(7):981–1007.

Chou, M.-H. (2000). Numerical study of vortex shedding from a rotating cylinder immersed in a uniform flow field. *International Journal for Numerical Methods in Fluids*, 32:545–567.

Collins, W. M. (1971). *Time-dependent viscous fluid flow past a circular cylinder.* PhD Thesis, The University of Western Ontario, London, Canada.

Collins, W. M. and Dennis, S. C. R. (1973a). The initial flow past an impulsively started circular cylinder. *The Quarterly Journal of Mechanics and Applied Mathematics*, 26(1):51–75.

Collins, W. M. and Dennis, S. C. R. (1973b). Flow past an impulsively started circular cylinder. *Journal of Fluid Mechanics*, 60:105–127.

Coutanceau, M. and Pineau, G. (1997). Some typical mechanisms in the early phase of the vortex-shedding process from particle-streak visualization. In: *Atlas of visualization III* (Edited by The Visualization Society of Japan), 43–68,. CRC Press.

Dennis, S. C. R. and Chang, G. Z. (1969). Numerical integration of the Navier-Stokes equations, Technical Summary Report No. 859. *Mathematical Research Center, University of Wisconsin.*

Dennis, S. C. R. and Kocabiyik, S. (1990). The solution of two-dimensional Oseen flow problems using integral conditions. *IMA Journal of Applied Mathematics*, 45(1):113.

Dennis, S. C. R. and Kocabiyik, S. (1991). An asymptotic matching condition for unsteady boundary-layer flows governed by the Navier-Stokes equations. *IMA Journal of Applied Mathematics*, 47:8198.

Dennis, S. C. R., Nguyen, P., and Kocabiyik, S. (2000). The flow induced by a rationally oscillating and translating circular cylinder. *Journal of Fluid Mechanics*, 407:123–144.

Dennis, S. C. R. and Quartapelle, L. (1983). Direct solution of the vorticity-stream function ordinary differential equations by a chebyshev approximation. *Journal of Computational Physics*, 52:448–463.

Dennis, S. C. R. and Quartapelle, L. (1989). Some used of Green's theorem in solving the Navier-Stokes equations. *International Journal for Numerical Methods in Fluids*, 9:871–890.

Dennis, S. C. R. and Walker, J. D. A. (1971). Calculation of the steady flow past a sphere at low and moderate Reynolds number. *Journal of Fluid Mechanics*, 48(4):771789.

Glowinski, R. and Pironneau, O. (1979). Numerical methods for the first biharmonic equation and the two-dimensional Stokes problem. *SIAM Review*, 21(2):167–212.

Griffin, O. M. and Hall, M. S. (1991). Review-vortex shedding lock-on and flow control in bluff body wakes. *Transactions of the ASME: Journal of Fluids Engineering*, 113:526–537.

Griffin, O. M. and Ramberg, S. E. (1976). Vortex shedding from a cylinder vibrating in line with incident uniform flow. *Journal of Fluid Mechanics*, 75:257–271.

Grosch, C. and Orszag, S. (1977). Numerical solution of problems in unbounded regions: Coordinate transforms. *Journal of Computational Physics*, 25:273–296.

Guilmineau, E. and Queutey, P. (2002). A numerical simulation of vortex shedding from an oscillating circular cylinder. *Journal of Fluids and Structures*, 16(6):773-794.

Hammache, M. and Gharib, M. (1991). An experimental study of the parallel and

oblique vortex shedding from circular cylinders. *Journal of Fluid Mechanics*, 232:567–590.

Herfjord, K. (1995). *A study of two-dimensional flow separated flow by a combination of finite element method and Navier-Stokes equations.* PhD Thesis, The Norwegian Institute of Technology, Trondhjem, Norway.

Honji, H. (1972). Starting flows past spheres and elliptic cylinders. *Reports of the Research Institute of Applied Mechanics, Kyushu University, Japan*, XIX(65).

Iliadis, G. and Anagnostopoulos, P. (1998). Viscous oscillatory flow around a circular cylinder at low Keulegan-Carpenter numbers and frequency parameters. *International Journal for Numerical Methods in Fluids*, 26(4):403–442.

Jordan, S. and Fromm, J. (1972). Oscillatory drag, lift and torque on a circular cylinder in a uniform flow. *Physics of Fluids*, 15:371–376.

Justesen, P. (1991). A numerical study of oscillating flow around a circular cylinder. *Journal of Fluid Mechanics*, 222:157–196.

Karanth, D., Rankin, G. W., and Sridhar, K. (1995). Computational study of flow past a cylinder with combined in-line and transverse oscillation. *Computational Mechanics*, 16:1–10.

Kim, B.-H. (2000). Quadratic nonlinear behavior of surface pressures on cylinders undergoing forced oscillations. M.Sc. Thesis, Illinois Institute of Technology, Chicago, U.S.A.

Kocabiyik, S. (1996a). An accelerated flow around a sphere. *Applied Mathematics Letters*, 9:41–46.

Kocabiyik, S. (1996b). Boundary layer on a sphere in an oscillating viscous flow. *Canadian Applied Mathematics Quarterly*, 4:97–107.

Kocabiyik, S. and Al-Mdallal, Q. (2003a). Numerical simulation of laminar flow past an oscillating circular cylinder. *Proceedings of the 11th Annual Conference of the Computational Fluid Dynamics Society of Canada*, 1:191–198.

Kocabiyik, S. and Al-Mdallal, Q. (2003b). A numerical study on rectilinear oscillations of a circular cylinder. *Proceedings of the International Union of Theoretical and Applied Mechanics Symposium on Integrated Modelling of Fully Coupled Fluid Structure Interactions Using Analysis, Computations and Experiments.* (edited by H. Benaroya and T. Wei). Kluwer Academic Publ., *163-173.* [In: *Fluid Mechanics and its Applications Series*, **75**, (edited by R. Moreau)].

Kocabiyik, S., Mahfouz, F. M., and Al-Mdallal, Q. (2004). Numerical simulation of the flow behind a circular cylinder subject to small-amplitude recti-linear oscillations. *Advances in Engineering software; in press*

Koopman, G. H. (1967). The vortex wakes of vibrating cylinders at low Reynolds numbers. *Journal of Fluid Mechanics*, 28:501–512.

Kravchenko, A. G., Moin, P., and Shariff, K. (1999). B-spline method and zonal grids for simulations of complex turbulent flows. *Journal of Computational Physics*, 151(2):757–789.

Lawrence, K. P. (2002). *Analysis of the initial flow past an accelerating cylinder*, Applied Mathematics Honors Dissertation. Memorial University of Newfoundland, St. John's, Canada.

Lu, X. and Dalton, C. (1996). Calculation of the timing of vortex formation from an oscillating circular cylinder,. *Journal of Fluids and Structures*, 10:527–541.

Lugt, H. J. and Haussling, H. J. (1974). Laminar flow past an abruptly accelerated elliptic cylinder at 45 incidence. *Journal of Fluid Mechanics*, 65:711–734.

Mahfouz, F. M. and Badr, H. M. (2000). Flow structure in the wake of a rotationally oscillating cylinder. *Transactions of the ASME: Journal of Fluids Engineering*, 122:290–301.

Martinez, G. and Hinh, H. H. (1978). *Proceedings of International Conference on Numerical Methods in Laminar and Turbulent Flow, Swansea*, Pineridge:105–127.

Matsumoto, M. (1999). Vortex shedding of bluff bodies: A review. *Journal of Fluids and Structures*, 13:791–811.

Meneghini, J. R. (1993). *Numerical simulation of bluff flow control using a discrete vortex method.* PhD Thesis, University of London, London, U.K.

Mittal, S. and Kumar, B. (1999). Finite element study of vortex-induced cross-flow and in-line oscillations of a circular cylinder at low Reynolds numbers. *International Journal For Numerical Methods in Fluids*, 31(7):1087–1120.

Ongoren, A. and Rockwell, D. (1988a). Flow structure from an oscillating cylinder Part 1: Mechanisms of phase shift and recovery in the near wake. *Journal of Fluid Mechanics*, 191:197–223.

Ongoren, A. and Rockwell, D. (1988b). Flow structure from an oscillating cylinder Part 2: Mode competition in the near wake. *Journal of Fluid Mechanics*, 191:225–245.

Panniker, P. K. G. and Lavan, Z. (1975). Flow past impulsively started bodies using Green's functions. *Journal of Computational Physics*, 18:46–65.

Peyret, R. and Taylor, T. D. (1983). *Computational Methods for Fluid Flow.* Springer-Verlag, New York.

Pier, B. and Huerre, P. (2001). Nonlinear self-sustained structures and fronts in spatially developing wake flows. *Journal of Fluid Mechanics*, 435:145–174.

Potter, M. C., Wiggert, D. C., and Hondzo, M. (1996). *Mechanics of Fluids.* Prentice Hall.

Quartapelle, L. and Napolitano, M. (1984). A method solving the factorized vorticity-stream function equations by finite elements. *International Journal for Numerical Methods in Fluids*, 4:109–125.

Quartapelle, L. and Valz-Gris, F. (1981). Projection conditions on the vorticity in viscous incompressible flows. *International Journal for Numerical Methods in Fluids*, 1:129–144.

Riley, N. (1991). Oscillating viscous flows II: Superposed oscillations. *Mathematika*, 38:203–216.

Roshko, A. (1954). On the development of turbulent wakes from vortex streets. *NACA*

Report 1191.

Sarpkaya, T. (1979). Vortex induced oscillations. *Journal of Applied Mechanics*, 46:241–258.

Sarpkaya, T. (2004). A critical review of the intrinsic nature of vortex induced vibrations. *Journal of Fluids and Structures*, 19(4):389–447.

Stansby, P. K. (1976). The locking-on of vortex shedding due to the cross-stream vibration of circular cylinders in uniform and shear flows. *Journal of Fluid Mechanics*, 74:641–655.

Sumer, B. M. and Fredsøe, J. (1997). *Hydrodynamics around Cylindrical Structures.* World Scientific.

Tatsuno, M. and Bearman, P. W. (1990). A visual study of the flow around an oscillating circular cylinder at low Keulegan-Karpenter numbers and low Stokes numbers. *Journal of Fluid Mechanics*, 211:157–182.

Tokumaru, P. and Dimotakis, P. (1991). Rotary oscillation control of a cylinder wake. *Journal of Fluid Mechanics*, 24:77–90.

Vretblad, A. (2003). *Fourier analysis and its applications.* Springer-Verlag, New York.

Wen, C. Y. and Lin, C. Y. (2001). Two dimensional vortex-shedding of a circular cylinder. *Physics of Fluids*, 13(3):557–560.

Williamson, C. H. K. (1985). Sinusoidal flow relative to circular cylinder. *Journal of Fluid Mechanics*, 155:141–174.

Williamson, C. H. K. (1989). Oblique and parallel modes of vortex shedding in the wake of a cylinder. *Journal of Fluid Mechanics*, 206:579–628.

Williamson, C. H. K. and Govardhan, R. (2004). Vortex-induced vibrations. *Annual Review of Fluid Mechanics*, 36:413–455.

Williamson, C. H. K. and Roshko, A. (1988). Vortex formation in the wake of an oscillating cylinder. *Journal of Fluids and Structures*, 2:355–381.

Zdravkovich, M. M. (1997). *Flow around Circular Cylinders: Vol. 1: Fundamentals.* Oxford University Press, Oxford.